Reza N. Jazar · Liming Dai *Editors*

Nonlinear Approaches in Engineering Applications 2

Springer

Nonlinear Approaches in Engineering Applications 2

Reza N. Jazar • Liming Dai
Editors

Nonlinear Approaches in Engineering Applications 2

Springer

Editors
Reza N. Jazar
Aerospace, Mechanical and Manufacturing
RMIT University
Bundoora, VIC, Australia

Liming Dai
Industrial Systems Engineering
University of Regina
Regina, SK, Canada

ISBN 978-1-4614-6876-9 ISBN 978-1-4614-6877-6 (eBook)
DOI 10.1007/978-1-4614-6877-6
Springer New York Heidelberg Dordrecht London

Library of Congress Control Number: 2011942901

Printed on acid-free paper

Springer is part of Springer Science+Business Media (www.springer.com)

Preface

Besides the idea from the first volume of this book which was focused on various methods to diagnose the complex behavior of nonlinear dynamic system, this volume will additionally take an insight into applying different control strategies to stabilize the complex behavior of the nonlinear dynamic system. The motivation of this volume is derived from the discussions among the researchers and engineers taking part in the ASME 2012 and 2011 Congress in the track of Dynamics Systems and Control, Optimal Approaches in Nonlinear Dynamics, which were organized by the editors. Processes in industries such as robotics and the aerospace industry typically have strong nonlinear dynamics. Nonlinear systems give rise to interesting phenomena such as limit cycle, bifurcation, and chaos. They are all harmful motions since an ideal system will require holding the set point and not oscillating around it. Therefore, these behaviors of dynamical systems need to be controlled to be stabilized. The usual objective of a control theory is to calculate solutions for the proper corrective action from the controller that result in system stability.

In the role of the editors as well as the chapter contributors of this book, we have tried to present a collection of chapters showing the theoretically and practically sound nonlinear approaches and their engineering applications in various areas, in hoping that this book may provide useful tools and comprehensible examples of solving, modeling, and simulating the nonlinear systems existing in the real world. The carefully selected chapters contained in this book reflect recent advances in nonlinear approaches and their engineering applications. The book intends to feature in particular the fundamental concepts and approaches of nonlinear science and their applications in engineering and physics fields. It is anticipated that this book may help to promote the development of nonlinear science and nonlinear dynamics in engineering, as well as to stimulate research and applications of nonlinear science and nonlinear dynamics in physics and engineering practices. It is also expected that the book will further enhance the comprehension of nonlinear science and stimulate interactions among scientists and engineers who are interested in nonlinear science and who find that nonlinearity and complexity of systems play an important role in their respective fields.

In control theory it is sometimes possible to linearize such classes of systems and apply linear techniques, but in many cases it can be necessary to devise from scratch theories permitting control of nonlinear systems. Differential geometry has been widely used as a tool for generalizing well-known linear control concepts to the nonlinear case, as well as showing the subtleties that make it a more challenging problem. Nonlinear control is the area of control engineering specifically involved with systems that are nonlinear, time-variant, or both. Many well-established analysis and design techniques exist for linear time-invariant (LTI) systems; however, one or both of the controller and the system under control in a general control system may not be a linear time-invariant system, and so these methods cannot necessarily be applied directly. Nonlinear control theory studies how to apply existing linear methods to these more general control systems. Additionally, it provides novel control methods that cannot be analyzed using linear time-invariant system theory. A nonlinear controller can have attractive characteristics though it usually requires more rigorous mathematical analysis to justify its conclusions.

In chaos theory, control of chaos is based on the fact that any chaotic attractor contains an infinite number of unstable periodic orbits. Control of chaos is the stabilization of one of these unstable periodic orbits, by means of small system perturbations. The perturbation must be tiny to avoid significant modification of the system's natural dynamics. Several techniques have been devised for chaos control, and most are developments that require a previous determination of the unstable periodic orbits of the chaotic system before the controlling algorithm can be designed.

With the theme of the book, *Nonlinear Approaches and Engineering Applications 2*, the book covers interdisciplinary studies on theories and methods of nonlinear science and their applications in complex systems such as those in nonlinear dynamics, nanotechnology, fluid dynamics, aerospace structure engineering, mechatronics engineering, control engineering, ocean engineering, offshore structure engineering, mechanical engineering, human body dynamics, and material science. Specifically, by modifying the linear conditions into the nonlinear practical model of shock absorbers, Chap. 1 analytically reviews the flat ride conditions of vehicles and provides design charts to satisfy the required conditions. In Chap. 2, the formulation of tracking mechanism used for a light-tracking system is presented to maximize the collected energy. Chapter 3 focuses on both diagnosing and controlling the nonlinear dynamic responses of a fluttering plate excited by a high-velocity air flow. The approaches presented have research and engineering application significances in the fields of aerodynamics, nonlinear dynamics, aircraft design, and design of space vehicles. Chapter 4 presents the development of a closed-form controller for the tracking control of uncertain real-life multibody systems, which are in general highly nonlinear and intrinsically hard to be modeled. In Chap. 5, the robustness of orthogonal eigenstructure control (OEC) to the failure of the actuators was investigated. It was shown that the control gain was capable of controlling the systems during an actuator failure, as OEC generates the control gain by maintaining the closed-loop eigenvectors within the achievable eigenvectors set. In Chap. 6, the highly nonlinear phenomenon of fluid–structure interaction is

discussed, including examples on aircraft flutter. Chapter 7 reports on a study that used computer dynamic simulation to analyze the energy absorption and damage in a new impact attenuator in both numerical modeling and experiment verification level. In Chap. 8, nonlinear Vehicle Seat buzz, squeak, and rattle (BSR) noise are characterized using CAE methodology and then can consequently be partly controlled by managing the seat structure resonant frequencies and mode shapes. Chapter 9 introduces a novel approach to calculate a first-order approximation for point distances from general nonlinear structures. It also proposes an accelerated sampling method for robust segmentation of multiple structures. Chapter 10 reviews mathematical models of mechanical and electromechanical parametric amplifiers.

Level of the Book

This book aims at engineers, scientists, researchers, and engineering and physics students of graduate levels, together with the interested individuals in engineering, physics, and mathematics. This chapter-book focuses on application of the nonlinear approaches representing a wide spectrum of disciplines of engineering and science. Throughout the book, great emphases are placed on engineering applications, physical meaning of the nonlinear systems, and methodologies of the approaches in analyzing and solving for the systems. Topics that have been selected are of high interest in engineering and physics. An attempt has been made to expose the engineers and researchers to a broad range of practical topics and approaches.

The topics contained in this book are of specific interest to engineers who are seeking expertise in nonlinear analysis, mathematical modeling of complex systems, optimization of nonlinear systems, nonclassical engineering problems, and future of engineering.

The primary audience of this book is the researchers, graduate students and engineers in mechanical engineering, engineering mechanics, civil engineering, aerospace engineering, ocean engineering, mathematics, and science disciplines. In particular, the book can be used as a research book for the graduate students to enhance their knowledge by taking a graduate course in the areas of nonlinear science, dynamics, vibration, structure dynamics, and engineering applications of nonlinear science. It can also be utilized as a guide to the readers' fulfillment in practices. The covered topics are also of interest to engineers who are seeking to expand their expertise in these areas.

Organization of the Book

The main structure of the book consists of two parts of analytical and practical nonlinearity, including ten chapters. Each of the chapters covers an independent topic along the line of nonlinear approach and engineering applications of nonlinear

science and control theory. The main concepts in nonlinear science and engineering applications are explained fully with necessary derivatives in detail. The book and each of the chapters are intended to be organized as essentially self-contained. All necessary concepts, proofs, mathematical background, solutions, methodologies, and references are supplied except for some fundamental knowledge well known in the general fields of engineering and physics. The readers may therefore gain the main concepts of each chapter with as less as possible the need to refer to the concepts of the other chapters. Readers may hence start to read one or more chapters of the book for their own interests.

Method of Presentation

The scope of each chapter is clearly outlined and the governing equations are derived with an adequate explanation of the procedures. The covered topics are logically and completely presented without unnecessary overemphasis. The topics are presented in a book form rather than in the style of a handbook. Tables, charts, equations, and references are used in abundance. Proofs and derivations are emphasized in such a way that they can be straightforwardly followed by the readers with fundamental knowledge of engineering science and university physics. The physical model and final results provided in the chapters are accompanied with necessary illustrations and interpretations. Specific information that is required in carrying out the detailed theoretical concepts and modeling processes has been stressed.

Prerequisites

This book is primarily intended for researchers, engineers, and graduate students, so the assumption is that the readers are familiar with the fundamentals of dynamics, calculus, and differential equations, as well as a basic knowledge of linear algebra and numerical methods. The presented topics are given in a way to establish as conceptual framework that enables the readers to pursue further advances in the field. Although the governing equations and modeling methodologies will be derived with adequate explanations of the procedures, it is assumed that the readers have a working knowledge of dynamics, university mathematics, and physics together with theory of linear elasticity.

Bundoora, VIC, Australia Reza N. Jazer
Regina, SK, Canada Liming Dai

Acknowledgments

This book is made available under the close and effective collaborations of all the enthusiastic chapter contributors who have the expertise and experience in various disciplines of nonlinear science and engineering applications. They deserve sincere gratitude for the motivation of creating such book, encouragement in completing the book, scientific and professional attitude in constructing each of the chapters of the book, and the continuous efforts toward improving the quality of the book. Without the collaboration and consistent efforts of the chapter contributors, the completion of this book would have been impossible. What we have at the end is a book that we have every reason to be proud of.

It has been gratifying to work with the staff of Springer through the development of this book. The assistance provided by the staff members has been valuable and efficient. We thank Springer for their production of an elegant book.

Contents

Part I Analytical Nonlinearity 1

1 Smart Flat Ride Tuning 3
Hormoz Marzbani and Reza N. Jazar

2 Light-Tracking Kinematics of Mobile Platform 37
Ahmad Salahuddin Mohd Harithuddin, Pavel M. Trivailo, and Reza N. Jazar

3 Diagnosis and Control of Nonlinear Oscillations of a Fluttering Plate 65
Liming Dai, Lu Han, Lin Sun, and Xiaojie Wang

4 A New Approach to the Tracking Control of Uncertain Nonlinear Multi-body Mechanical Systems 101
Firdaus E. Udwadia and Thanapat Wanichanon

5 Robustness of Orthogonal Eigenstructure Control to Actuators Failure 137
Mohammad Rastgaar and Nina Mahmoudian

Part II Practical Nonlinearity

6 Energy Harvesting from Flows Using Piezoelectric Patches 169
J.M. McCarthy, A. Deivasigamani, S. Watkins, S.J. John, and F. Coman

7 Experimental and Finite Element Nonlinear Dynamics Analysis of Formula SAE Impact Attenuator 213
Toh Yen Pang and Hoy Tristian

8 Nonlinear Vehicle Seat BSR Characterization Using CAE Methodology 231
M. Tatari, M. Fard, N. Nasrollahzadeh, and M. Mahjoob

9 Parametric Segmentation of Nonlinear Structures in Visual Data: An Accelerated Sampling Approach 257
Reza Hoseinnezhad and Alireza Bab-Hadiashar

10 Parametric Resonance: Application on Low Noise Mechanical and Electromechanical Amplifiers 277
Naser Nasrolahzadeh, Mohammad Fard, and Milad Tatari

Index 309

Part I
Analytical Nonlinearity 1

Chapter 1
Smart Flat Ride Tuning

Hormoz Marzbani and Reza N. Jazar

Abstract Flat ride is the condition that the unpleasant pitch oscillation of the vehicle body turns into more tolerable bounce oscillation, when a car hits a bump in forward motion. Based on experimental results, Maurice Olley discovered and introduced two conditions for flat ride:

1. The radius of gyration in pitch should be equal to the multiplication of the distance from the mass centers a_1, a_2 of the front and rear wheels of the car ($r^2 = a_1 a_2$).
2. The rear suspension should have around 20% higher rate than the front. The equation $r^2 = a_1 a_2$ makes the car to be considered as two separated uncoupled mass-spring systems of front and rear suspensions.

In this chapter, we will analytically review the flat ride conditions and provide design charts to satisfy the required conditions. The nonlinear practical model of shock absorbers modifies the conditions which were based on linear models.

1.1 Flat Ride Definition

The excitation inputs from the road to a straight moving car will affect the front wheels first and then, with a time lag, the rear wheels. The general recommendation was that the natural frequency of the front suspension should be lower than that of the rear. So, the rear part oscillates faster to catch up with the front to eliminate pitch and put the car in bounce before the vibrations die out by damping. This is what Olley called the *flat ride tuning* [4]. Maurice Olley (1889–1983) established guidelines, back in the 1930, for designing vehicles with better ride. These were

H. Marzbani • R.N. Jazar (✉)
School of Aerospace, Mechanical and Manufacturing Engineering, RMIT University, Melbourne, VIC, Australia
e-mail: hormoz.marzbani@rmit.edu.au; reza.jazar@rmit.edu.au

R.N. Jazar and L. Dai (eds.), *Nonlinear Approaches in Engineering Applications 2*,
DOI 10.1007/978-1-4614-6877-6_1,

derived from experiments with a modified car to allow variation of the pitch mass moment. Although the measures of ride were strictly subjective, those guidelines are considered as valid rules of thumb even for modern cars. What is known as Olley's flat ride not considering the other prerequisites can be put forward as:

The front suspension should have around 30% *lower rate than the rear.*

An important prerequisite for flat ride was the uncoupling condition, which was introduced by Rowell and Guest for the first time in 1923 [4, 9]. Rowell and Guest used the geometry of a bicycle car model to find the condition which sets the bounce and pitch centers of the model located on the springs. Having the condition, the front and rear spring systems of the vehicle can be regarded as two separate one degree-of-freedom (DOF) systems.

In this study, using analytical methods, we study the flat ride conditions which have been respected and followed by the car manufacturers' designers since they were introduced for the first time. This article will provide a more reliable scientific and mathematical approach for what are the flat ride design criteria in vehicle dynamic studies.

1.2 Uncoupling the Car Bicycle Model

Consider the two DOF system in Fig. 1.1. A beam with mass m and mass moment I about the mass center C is sitting on two springs k_1 and k_2 to model a car in bounce and pitch motions. The translational coordinate x of C and the rotational coordinate θ are the usual generalized coordinates that we use to measure the kinematics of the beam. The equations of motion and the mode shapes are functions of the chosen coordinates.

The free vibration equations of motion of the system are:

$$\begin{bmatrix} m & 0 \\ 0 & I \end{bmatrix} \begin{bmatrix} \ddot{x} \\ \ddot{\theta} \end{bmatrix} + \begin{bmatrix} k_1 + k_2 & a_2k_2 - a_1k_1 \\ a_2k_2 - a_1k_1 & a_2^2k_2 + a_1^2k_1 \end{bmatrix} \begin{bmatrix} x \\ \theta \end{bmatrix} = 0 \tag{1.1}$$

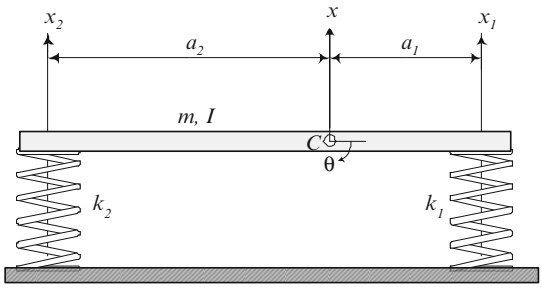

Fig. 1.1 The bicycle model of a car is a beam with mass m and mass moment I, sitting on two springs k_1 and k_2

To compare the mode shapes of the system practically, we employ the coordinates x_1 and x_2 instead of x and θ, as shown in Fig. 2.1. The equations of motion of the system would then be:

$$\begin{bmatrix} \frac{ma_2^2 + I}{a_1 + a_2{}^2} & \frac{ma_1a_2 - I}{a_1 + a_2{}^2} \\ \frac{ma_1a_2 - I}{a_1 + a_2{}^2} & \frac{ma_1^2 + I}{a_1 + a_2{}^2} \end{bmatrix} \begin{bmatrix} \ddot{x}_1 \\ \ddot{x}_2 \end{bmatrix} + \begin{bmatrix} k_1 & 0 \\ 0 & k_2 \end{bmatrix} \begin{bmatrix} x_1 \\ x_2 \end{bmatrix} = 0 \tag{1.2}$$

Let us define the following parameters:

$$I = mr^2 \tag{1.3}$$

$$\Omega_1^2 = \frac{k_1}{m}\beta \tag{1.4}$$

$$\Omega_2^2 = \frac{k_2}{m}\beta \tag{1.5}$$

$$\beta = \frac{l^2}{a_1a_2} \tag{1.6}$$

$$\alpha = \frac{r^2}{a_1a_2} \tag{1.7}$$

$$\gamma = \frac{a_2}{a_1} \tag{1.8}$$

$$l = a_1 + a_2 \tag{1.9}$$

and rewrite the equations as

$$\begin{bmatrix} \alpha + \gamma & 1 - \alpha \\ 1 - \alpha & \alpha + \frac{1}{\gamma} \end{bmatrix} \begin{bmatrix} \ddot{x}_1 \\ \ddot{x}_2 \end{bmatrix} + \begin{bmatrix} \Omega_1^2 & 0 \\ 0 & \Omega_2^2 \end{bmatrix} \begin{bmatrix} x_1 \\ x_2 \end{bmatrix} = 0 \tag{1.10}$$

Setting

$$\alpha = 1 \tag{1.11}$$

makes the equations decoupled

$$\begin{bmatrix} \alpha + \gamma & 0 \\ 0 & \alpha + \frac{1}{\gamma} \end{bmatrix} \begin{bmatrix} \ddot{x}_1 \\ \ddot{x}_2 \end{bmatrix} + \begin{bmatrix} \Omega_1^2 & 0 \\ 0 & \Omega_2^2 \end{bmatrix} \begin{bmatrix} x_1 \\ x_2 \end{bmatrix} = 0 \tag{1.12}$$

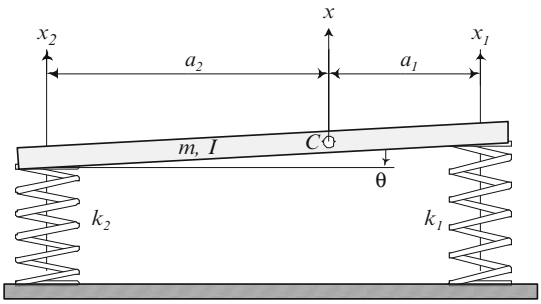

Fig. 1.2 The mode shape 1 for $\alpha = 1$ shows that only the front suspension is oscillating and the node is on the rear suspension

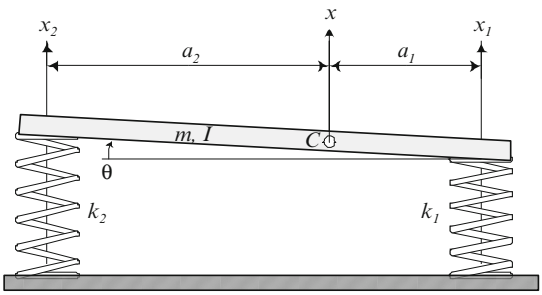

Fig. 1.3 The mode shape 2 for $\alpha = 1$ shows that only the rear suspension is oscillating and the node is on the front suspension

The natural frequencies ω_i and mode shapes u_i of the system are

$$\omega_1^2 = \frac{1}{\gamma + 1}\Omega_1^2 = \frac{l}{a_2}\frac{k_1}{m} \quad u_1 = \begin{bmatrix} 1 \\ 0 \end{bmatrix} \tag{1.13}$$

$$\omega_2^2 = \frac{\gamma}{\gamma + 1}\Omega_2^2 = \frac{l}{a_1}\frac{k_2}{m} \quad u_2 = \begin{bmatrix} 0 \\ 1 \end{bmatrix} \tag{1.14}$$

They show that the nodes of oscillation in the first and second modes are at the rear and front suspensions, respectively. Figures 1.2 and 1.3 illustrate the mode shapes of the bicycle car model for $\alpha = 1$.

The decoupling condition $\alpha = 1$ yields

$$r^2 = a_1 a_2 \tag{1.15}$$

which indicates that the pitch radius of gyration, r, must be equal to the multiplication of the distance of the mass center C from the front and rear axles. Therefore, by setting $\alpha = 1$, the nodes of the two modes of vibrations appear to be at the front and rear axles. As a result, the front wheel excitation will not alter the body at the rear axle and vice versa. For such a car, the front and rear parts of the car act independently. Therefore, the decoupling condition $\alpha = 1$ allows us to break

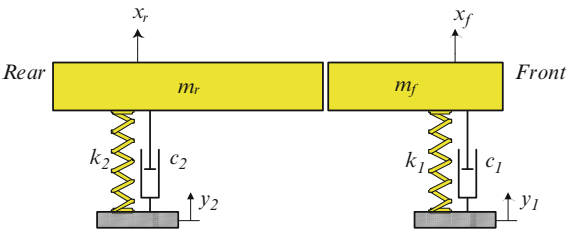

Fig. 1.4 Car bicycle model after decoupling

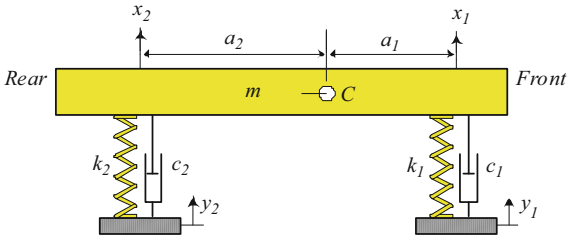

Fig. 1.5 Car bicycle model with damping

the initial two DOF system into two independent one DOF systems as illustrated in Fig. 1.4, where:

$$m_r = m\frac{a_1}{l} = m\varepsilon \tag{1.16}$$

$$m_f = m\frac{a_2}{l} = m(1-\varepsilon) \tag{1.17}$$

$$\varepsilon = \frac{a_1}{l} \tag{1.18}$$

The equations of motion of the independent systems will be:

$$m(1-\varepsilon)\ddot{x}_1 + c_1\dot{x}_1 + k_1x_1 = k_1y_1 + c_1\dot{y}_1 \tag{1.19}$$

$$m\varepsilon\ddot{x}_2 + c_2\dot{x}_2 + k_2x_2 = k_2y_2 + c_2\dot{y}_2 \tag{1.20}$$

The decoupling condition of undamped free system will not necessarily decouple the general damped system of Fig. 1.5. However, if there is no anti-pitch spring or anti-pitch damping between the front and rear suspensions, then equations of motion

$$\begin{bmatrix} \alpha+\gamma & 1-\alpha \\ 1-\alpha & \alpha+\frac{1}{\gamma} \end{bmatrix}\begin{bmatrix} \ddot{x}_1 \\ \ddot{x}_2 \end{bmatrix} + \begin{bmatrix} 2\xi_1\Omega_1 & 0 \\ 0 & 2\xi_2\Omega_2 \end{bmatrix}\begin{bmatrix} \dot{x}_1 \\ \dot{x}_2 \end{bmatrix} + \begin{bmatrix} \Omega_1^2 & 0 \\ 0 & \Omega_2^2 \end{bmatrix}\begin{bmatrix} x_1 \\ x_2 \end{bmatrix}$$
$$= \begin{bmatrix} 2\xi_1\Omega_1 & 0 \\ 0 & 2\xi_2\Omega_2 \end{bmatrix}\begin{bmatrix} \dot{y}_1 \\ \dot{y}_2 \end{bmatrix} + \begin{bmatrix} \Omega_1^2 & 0 \\ 0 & \Omega_2^2 \end{bmatrix}\begin{bmatrix} y_1 \\ y_2 \end{bmatrix} \tag{1.21}$$

$$2\xi_1\Omega_1 = \frac{c_1}{m}\beta \tag{1.22}$$

$$2\xi_2\Omega_2 = \frac{c_2}{m}\beta \tag{1.23}$$

will be decoupled by $\alpha = 1$

$$\begin{bmatrix} \alpha+\gamma & 0 \\ 0 & \alpha+\frac{1}{\gamma} \end{bmatrix} \begin{bmatrix} \ddot{x}_1 \\ \ddot{x}_2 \end{bmatrix} + \begin{bmatrix} c_1 & 0 \\ 0 & c_2 \end{bmatrix} \begin{bmatrix} \dot{x}_1 \\ \dot{x}_2 \end{bmatrix} + \begin{bmatrix} \Omega_1^2 & 0 \\ 0 & \Omega_2^2 \end{bmatrix} \begin{bmatrix} x_1 \\ x_2 \end{bmatrix}$$
$$= \begin{bmatrix} 2\xi_1\Omega_1 & 0 \\ 0 & 2\xi_2\Omega_2 \end{bmatrix} \begin{bmatrix} \dot{y}_1 \\ \dot{y}_2 \end{bmatrix} + \begin{bmatrix} \Omega_1^2 & 0 \\ 0 & \Omega_2^2 \end{bmatrix} \begin{bmatrix} y_1 \\ y_2 \end{bmatrix} \tag{1.24}$$

The equations of motion of the independent system of Fig. 1.4 may also be written as

$$m(1-\varepsilon)\ddot{x}_1 + c_1\dot{x}_1 + k_1x_1 = c_1\dot{y}_1 + k_1y_1 \tag{1.25}$$

$$m\varepsilon\ddot{x}_2 + c_2\dot{x}_2 + k_2x_2 = c_2\dot{y}_2 + k_2y_2 \tag{1.26}$$

which are consistent with the decoupled equations (1.24) because of

$$\varepsilon = \frac{1+\gamma}{\gamma\Omega_2^2} \tag{1.27}$$

To examine the effect of the decoupling condition and having independent front and rear model of a car, let us compare the responses of the model of Fig. 1.5 using (1.21) for different α.

Consider a car with the given characteristics in Table 1.1.

Table 1.1 Specification of a sample car

Specification	Nominalvalue
m (kg)	420
a_1 (m)	1.4
a_2 (m)	1.47
l (m)	2.87
k_1 (N/m)	10,000
k_2 (N/m)	13,000
c_1 (N s/m)	1,000
c_2 (N s/m)	1,000
β	4.00238
γ	1.05
Ω_1	95.2947
Ω_2	123.8832
ξ_1	0.05
ξ_2	0.0384

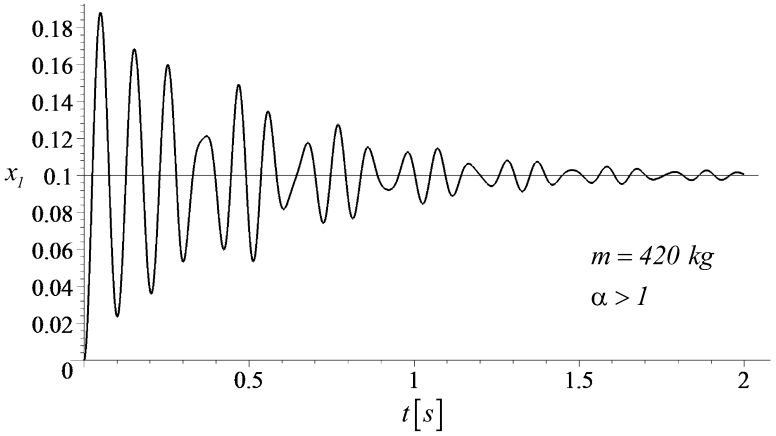

Fig. 1.6 Case 1: oscillations of the front of the car with $\alpha > 1$

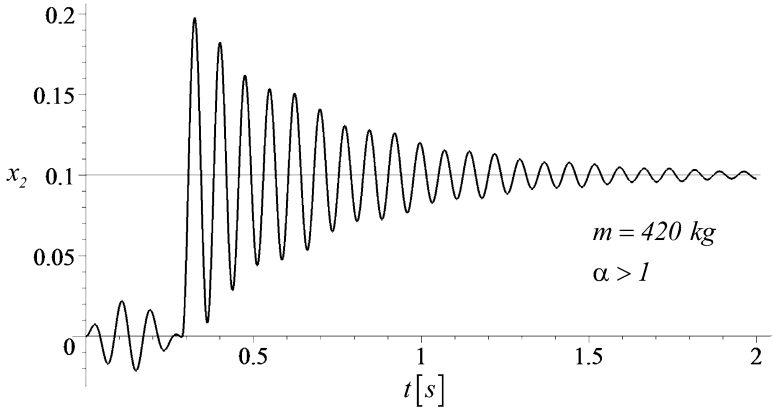

Fig. 1.7 Case 1: oscillations of the rear of the car with $\alpha > 1$

Figures 1.6–1.14 can be used for a comparison to show the effects of uncoupling the system when the car goes over a step

$$y_1 = 0.1\,\mathrm{m} \qquad y_1 = 0.1H\left(t - \frac{l}{v}\right)\,\mathrm{m} \tag{1.28}$$

where $H\,(x)$ is the Heaviside function

$$H\,(t-\tau) = \begin{cases} 0 & t \le \tau \\ 1 & t > \tau \end{cases} \tag{1.29}$$

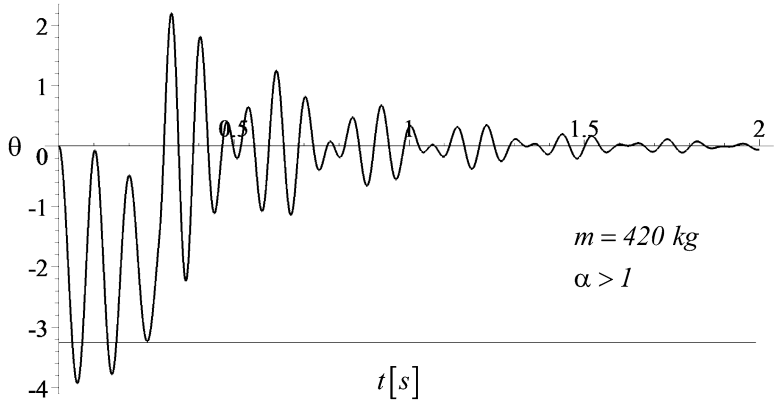

Fig. 1.8 Case 1: angular oscillations of the car with $\alpha > 1$

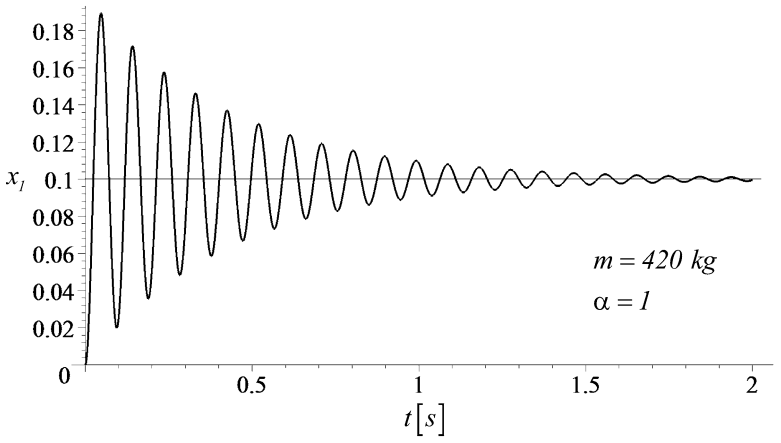

Fig. 1.9 Case 2: oscillations of the front of the car with $\alpha = 1$

Each set of three figures are for a value of α which varies from smaller than 1 to 1 and then bigger than 1.

- Case 1: $\alpha > 1$

$$\alpha = 1.2726\ ,\ r = 1.618\ ,\ I_y = 1100$$

- Case 2: $\alpha = 1$

$$\alpha = 1\ ,\ r = 1.434\ ,\ I_y = 864.36$$

- Case 3: $\alpha < 1$

$$\alpha = 0.8098 - r = 1.291 - I_y = 700$$

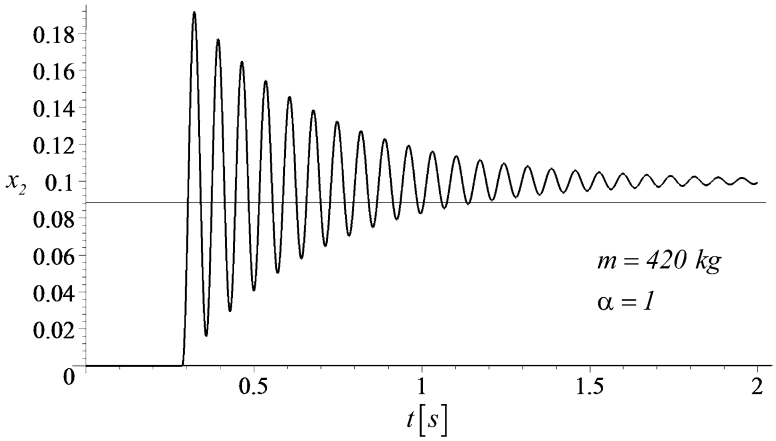

Fig. 1.10 Case 2: oscillations of the rear of the car with $\alpha = 1$

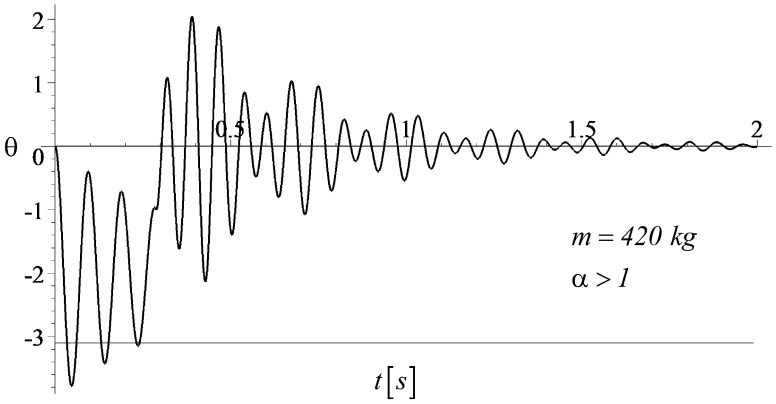

Fig. 1.11 Case 2: angular oscillations of the car with $\alpha = 1$

Figures 1.6–1.8 depict the oscillations of the front x_1, rear x_2, and pitch $\theta = (x_2 - x_1)/l$ for $\alpha = 1.2726 > 1$. Figures 1.9–1.11 show x_1, x_2, and θ for $\alpha = 1$, and Figs. 1.12–1.14 show x_1, x_2, and θ for $\alpha = 0.8098 < 1$.

Figures 1.6, 1.9, and 1.12 illustrate the oscillations of the front part of the vehicle after hitting the step for three different values of α. Similarly, Figs. 1.7, 1.10, and 1.13 illustrate the oscillations of the rear part of the vehicle after hitting the step for three different values of α. As it can be seen in Figs. 1.7 and 1.13 oscillations start with small amplitude, which does not exist in Fig. 1.10. The pitch vibrations behavior of the car for three different values of α can be compared in Figs. 1.8, 1.11, and 1.14.

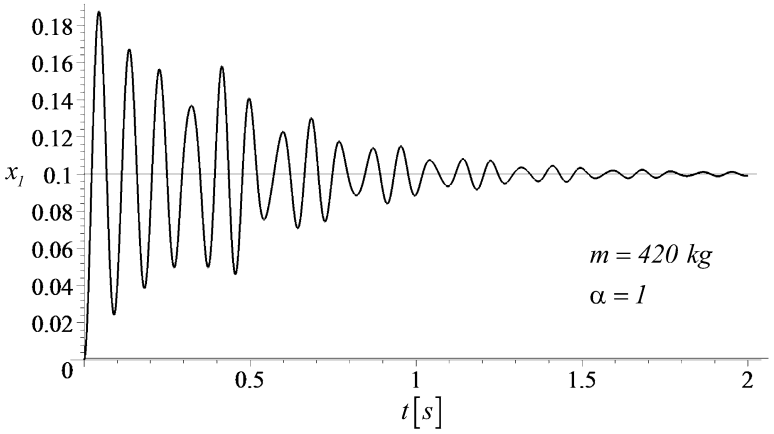

Fig. 1.12 Case 3: oscillations of the front of the car with $\alpha < 1$

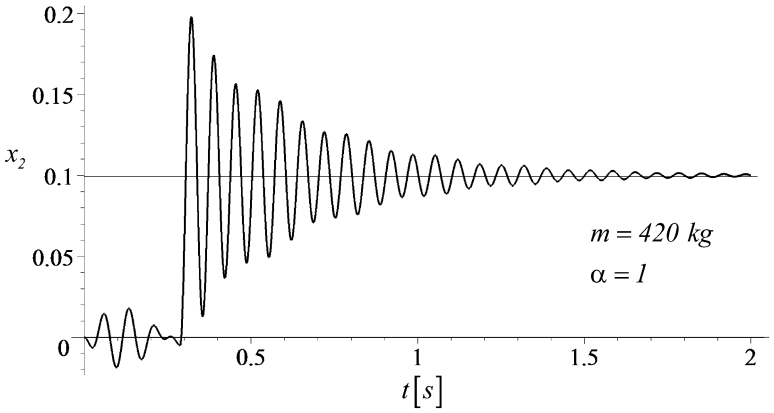

Fig. 1.13 Case 3: oscillations of the rear of the car with $\alpha < 1$

The delay in the oscillation of the rear of the vehicle is caused by the time lag between the front and the rear wheels hitting the step. This time lag is dependent to the wheelbase of the vehicle and also changes with the traveling speed shown by $\tau = \frac{l}{v}$.

Figure 1.10 shows the oscillation of the rear of a vehicle with $\alpha = 1$ and shows that in this case the oscillation of the front wheel, which has already started τ seconds ago, does not affect the oscillation of the rear part. That is a result of locating the vibration nodes of the vehicle at the rear and front springs, respectively, the condition for uncoupling.

However, considering Figs. 1.7 and 1.13 for values $\alpha > 1$ and $\alpha < 1$, respectively, the effect of the front oscillation on the rear, is observable in the form of small amplitude oscillations. The time lag oscillation in Fig. 1.7 starts off in the

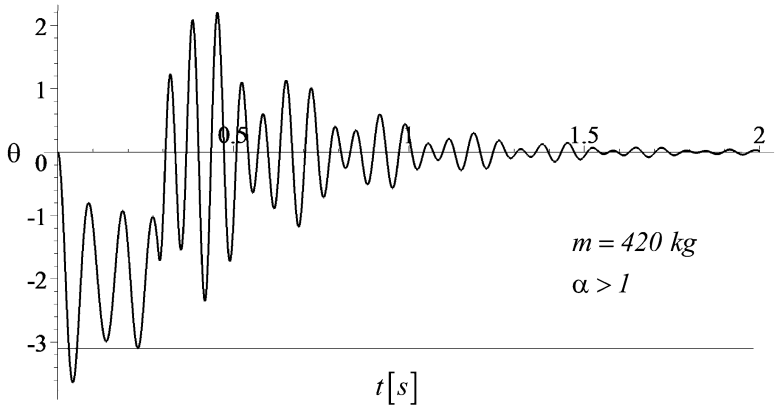

Fig. 1.14 Case 3: angular oscillations of the car with $\alpha < 1$

form of an upward motion which indicates that the oscillation node of the front wheel is located behind the rear wheel having $\alpha > 1$. The condition of the car is reverse for the values of $\alpha < 1$ in Fig. 1.13.

The same conclusions arises by comparing the set of figures which illustrate the pitch motion in the vehicles after hitting the step, Figs. 1.8, 1.11, and 1.14. The angle between the front and rear of the vehicle has been calculated and plotted by:

$$\theta = \frac{x_2 - x_1}{l} \tag{1.30}$$

Smaller pitch motion in Fig. 1.11 for $\alpha = 1$ makes it obvious that an uncoupled system provides a more comfortable ride compared to the pitch angle oscillation θ, in Figs. 1.8 and 1.14.

1.3 No Flat Ride Solution for Linear Suspension

The time lag between the front and rear suspension oscillations is a function of the wheelbase, l, and speed of the vehicle, v. Soon after the rear wheels have passed over a step, the vehicle is at the worst condition of pitching. Olley experimentally determined a recommendation for the optimum frequency ratio of the front and rear ends of cars. His suggestion for American cars and roads of 1950s was to have the natural frequency of the front approximately 80% of that of the rear suspension.

To examine Olley's experimental recommendation and possibly make an analytical base for flat ride, let us rewrite the equation of motion (1.25) and (1.26) as:

$$\ddot{x}_1 + 2\xi_1\dot{x}_1 + \frac{k_1}{m(1-\varepsilon)}x_1 = 2\xi_1\dot{y}_1 + \frac{k_1}{m(1-\varepsilon)}y_1 \tag{1.31}$$

$$\ddot{x}_2 + 2\xi\xi_1\dot{x}_2 + \frac{kk_1}{m\varepsilon}x_2 = 2\xi\xi_1 y_2 + \frac{kk_1}{m\varepsilon}y_2 \tag{1.32}$$

where

$$\xi = \frac{\xi_2}{\xi_1} = \frac{c_1}{c_2}\frac{\varepsilon}{1-\varepsilon} \tag{1.33}$$

$$k = \frac{k_2}{k_1} = \frac{k_1}{k_2}\frac{\varepsilon}{1-\varepsilon} \tag{1.34}$$

$$\xi_1 = \frac{c_1}{m(1-\varepsilon)} \tag{1.35}$$

$$\xi_2 = \frac{c_2}{m\varepsilon} \tag{1.36}$$

Parameters k and ξ are the ratio of the rear/front spring rates and damping ratios, respectively.

The necessity to achieve a flat ride provides that the rear system must oscillate faster to catch up with the front system at a reasonable time. At the time both systems must be at the same amplitude and oscillate together afterwards. Therefore, an ideal flat ride happens if the frequency of the rear system be higher than the front to catch up with the oscillation of the front at a certain time and amplitude. Then, the frequency of the rear must reduce to the value of the front frequency to oscillate in phase with the front. Furthermore, the damping ratio of the rear must also change to keep the same amplitude. Such a dual behavior is not achievable with any linear suspension. Therefore, theoretically, it is impossible to design linear suspensions to provide a flat ride, as the linearity of the front and rear suspensions keep their frequency of oscillation constant.

1.4 Near Flat Ride Solution for Linear Suspensions

To design the rear suspension parameters for a given set of front parameters to achieve a reasonable flat ride condition, we rephrase the problem by introducing a near flat ride condition. The rear suspension must have proper parameters and higher frequency to reach the same amplitude as the front suspension at a reasonable time before the oscillations die out. This brings the vehicle in a flat condition. Then the oscillation of the system dies out before the pitch mode significantly appears again. A near flat ride situation is shown in Fig. 1.15, for a car going over a unit step.

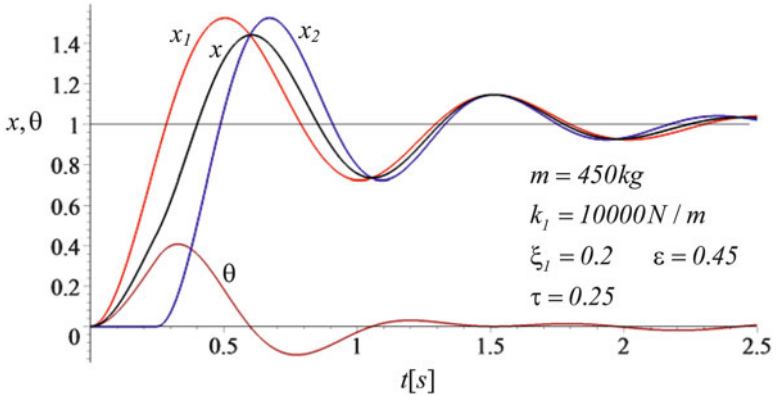

Fig. 1.15 Response of the front and rear suspensions of a near at ride car to a unit step

Solving the equations of motion (1.31) and (1.32) for x_1 and x_2 for a unit step input yields

$$x_1 = 1 - e^{\frac{-\xi_1 \omega t}{\sqrt{1-\varepsilon}}}\left(\cos\sqrt{\frac{1-\xi_1^2}{1-\varepsilon}}\omega t + \frac{\xi_1}{\sqrt{1-\xi_1^2}}\sin\sqrt{\frac{1-\xi_1^2}{1-\varepsilon}}\omega t\right) \qquad (1.37)$$

$$t \geq 0$$

$$x_2 = \begin{cases} 0 & t < 0 \\ 1 - e^{-\xi\xi_1\sqrt{\frac{k}{\varepsilon}}(t-\tau)}\left(\cos\sqrt{\frac{k(1-\xi^2\xi_1^2)}{\varepsilon}}\omega(t-\tau)\right. & \\ \left. \quad + \frac{\xi\xi_1}{\sqrt{1-\xi^2\xi_1^2}}\sin\sqrt{\frac{k(1-\xi^2\xi_1^2)}{\varepsilon}}\omega(t-\tau)\right) & t \geq 0 \end{cases} \qquad (1.38)$$

where

$$\omega = \sqrt{\frac{k_1}{m}} \qquad (1.39)$$

$$\tau = \frac{l}{v} \qquad (1.40)$$

As a reasonable catch up time, we search for the conditions such that both systems reach their third equal peak amplitude at the same time.

The third peak of x_1 happens at the time:

$$t_{p_1} = \frac{3\pi\sqrt{1-\varepsilon}}{\omega\sqrt{1-\xi_1^2}} \tag{1.41}$$

where its displacement is:

$$x_1 = 1 + exp(\frac{-3\pi\xi_1}{\sqrt{1-\xi_1^2}}) \tag{1.42}$$

The third peak of x_2 happens at

$$t_{p_2} = \tau + \frac{3\pi\sqrt{\frac{k}{\varepsilon}}}{\omega\sqrt{1-\xi^2\xi_1^2}} \tag{1.43}$$

where its displacement is

$$x_2 = 1 + exp(\frac{-3\pi\xi\xi_1}{\sqrt{1-\xi^2\xi_1^2}}). \tag{1.44}$$

The conditions that x_1 and x_2 meet after one and a half oscillations are:

$$x_1 = x_2 \tag{1.45}$$

$$t_{p_1} = t_{p_2} \tag{1.46}$$

which yield:

$$1 + exp(\frac{-3\pi\xi_1}{\sqrt{1-\xi_1^2}}) = 1 + exp(\frac{-3\pi\xi\xi_1}{\sqrt{1-\xi^2\xi_1^2}}) \tag{1.47}$$

$$\frac{3\pi\sqrt{1-\varepsilon}}{\omega\sqrt{1-\xi_1^2}} = \tau + \frac{3\pi\sqrt{\frac{k}{\varepsilon}}}{\omega\sqrt{1-\xi^2\xi_1^2}}. \tag{1.48}$$

Equation (1.47) is independent of the spring ratio k and can be solved for damping ratio ξ

$$\xi = 1. \tag{1.49}$$

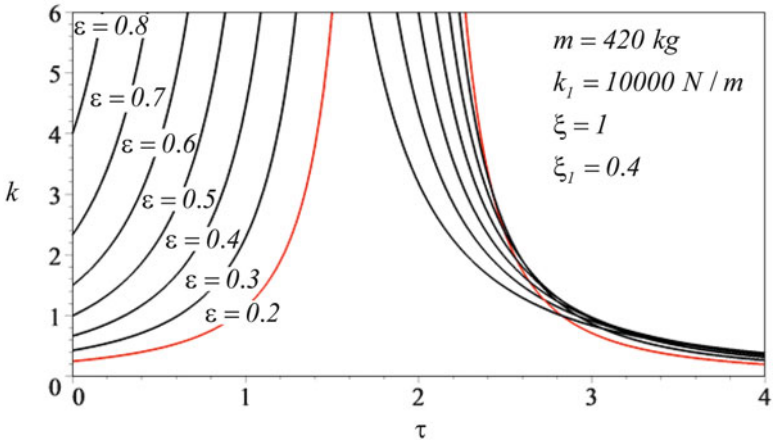

Fig. 1.16 Illustrates the plot of k versus τ, for different ε from 0.2 to 0.8

It indicates that the third peak of the motion of the front and rear of the car will be equal provided the damping coefficient of the front and rear suspensions are equal.

Solving (1.48) for spring ratio k yields:

$$k = \frac{Z_1}{Z_2\tau^2 + Z_3\tau + Z_4} \tag{1.50}$$

where

$$Z_1 = -9\varepsilon\pi^2 m(-1 + \xi_1^2) \tag{1.51}$$

$$Z_2 = (\xi^2\xi_1^4 - \xi^2\xi_1^2 + 1 - \xi_1^2)k_1 \tag{1.52}$$

$$Z_3 = 6\pi m(\xi^2\xi_1^2 - \varepsilon\xi^2\xi_1^2 - 1 + \varepsilon)\sqrt{-\frac{k_1(1-\xi_1^2)}{m(\varepsilon-1)}} \tag{1.53}$$

$$Z_4 = -9\pi^2 m(\varepsilon\xi^2\xi_1^2 - \varepsilon + 1 - \xi^2\xi_1^2) \tag{1.54}$$

Using a set of nominal values,

$$\xi = 1 \qquad m = 420 \qquad \xi_1 = 0.4 \qquad k_1 = 10000. \tag{1.55}$$

Figure 1.16 illustrates the plot of k versus τ, for different ε from 0.2 to 0.8. Using this graph, we can determine the value of spring ratio k for a given $\varepsilon = a_1/l$ and $\tau = l/v$. Because for a given car, the values of ε and l are fixed, the graph determines the required $k = k_2/k_1$ at any speed v.

Considering the existing designs of normal street vehicles, only a very small section of the horizontal axis of Fig. 1.16 should be investigated. The wheelbase

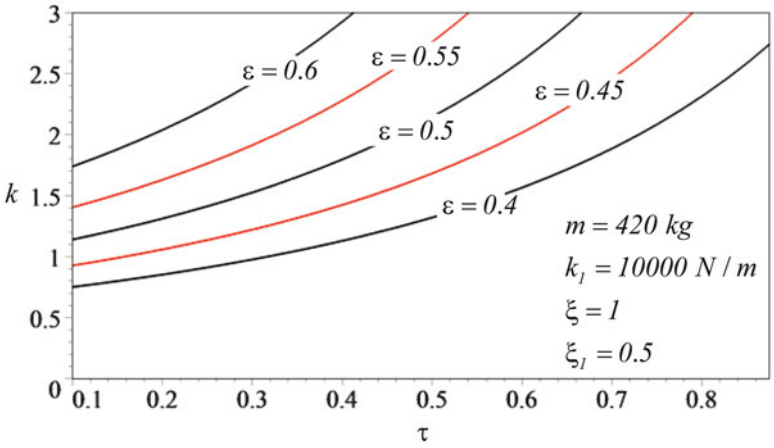

Fig. 1.17 Plots of k versus τ for $\xi_1 = 0.5$ and different ε in the domain $0.1 < \tau < 0.875$

for normal street vehicles is usually not less than 2 m or longer than 3.5 m. Let us assume that the speed of a car which goes over a step and is expected to show a flat ride, is between 4 and 20 m/s. Therefore, the practical domain of the time lag between the front and rear wheels would be $0.1 < \tau < 0.875$.

Furthermore, the mass center of street cars are normally in the front half of the wheelbase in order to provide understeer condition. Considering $0.4 < \varepsilon < 0.6$ will cover all street and sports cars. Figure 1.17 shows how k varies with τ for $\xi_1 = 0.5$ and different ε to provide a near flat ride. For any ε, the required stiffness ratio increases by increasing τ. Therefore, the ratio of rear to front stuffiness increases when the speed of the car decreases. It is because the frequency of the rear part must be higher to catch up with the oscillations of the front. Figure 1.18 illustrates the same information in the plane of (ε, τ). It shows that for a constant k, how the mass center of a car should change to provide a near flat ride. The value of ε is a decreasing function of τ and therefore, the mass center of a car should get closer to the front axle when the speed of the car increases. Ideally, the curves in both Figs. 1.17 and 1.18 must be horizontal to have a constant stiffness ratio to achieve a near flat ride at any speed. However, not only a flat ride is impossible to achieve, a near flat ride also is not achievable by linear suspensions.

Figures 1.19–1.26 depict the similar information of Figs. 1.17 and 1.18 for $\xi_1 = 0.4$, $\xi_1 = 0.3$, $\xi_1 = 0.2$, and $\xi_1 = 0.1$, respectively.

Let us consider having a vehicle with smart suspension, and the effect of change of traveling speed of the vehicle on the near flat ride, Figs. 1.18, 1.20, 1.22, 1.24, and 1.26 can be used as design charts. As an example, the average length of a sedan vehicle has been taken equal to 2.6 m with a normal weight distribution of a front differential vehicle 56/44 heavier at the front. Using the given information some other values can be calculated as: $a_1 = 1,144$ mm and $a_2 = 1,456$ mm which yields to $\varepsilon = 0.44$. Assuming that the front suspension of the car has a damping of

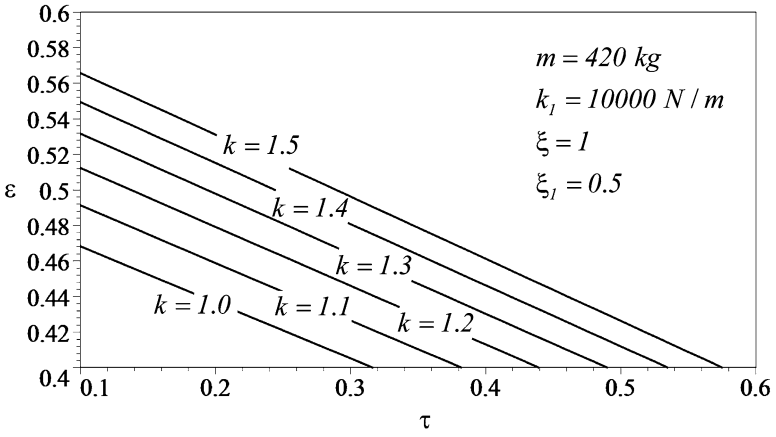

Fig. 1.18 τ versus ε for different spring rates

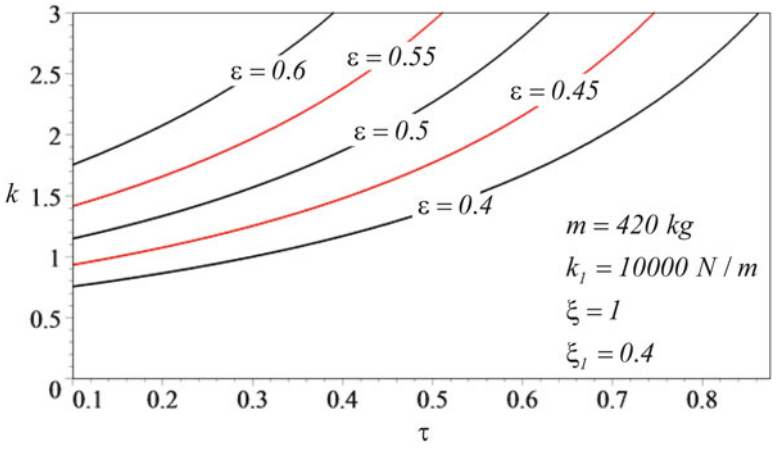

Fig. 1.19 Plots of k versus τ for $\xi_1 = 0.4$ and different ε in the domain $0.1 < \tau < 0.875$

$\xi_1 = 0.4$, the diagram in Fig. 1.20 can be used by the smart suspension to provide near flat ride in different speeds, by switching the spring rate to the required value. Continuous variation of k is illustrated in Fig. 1.21. The horizontal line in Fig. 1.27 is showing the values that the spring should be switching to as the traveling speed of the vehicle on the example changes, which is the ideal situation for near flat ride. To use the same chart for vehicles with passive suspension, a target speed needs to be chosen by the designer as the ideal speed for the vehicle to have a near flat ride. The point in Fig. 1.27 is indicating that for a car with passive suspension, with a wheelbase of 2.4 m, traveling speed of 29 km/h, to get a near flat ride a spring ratio of $k = 1.2$ is needed.

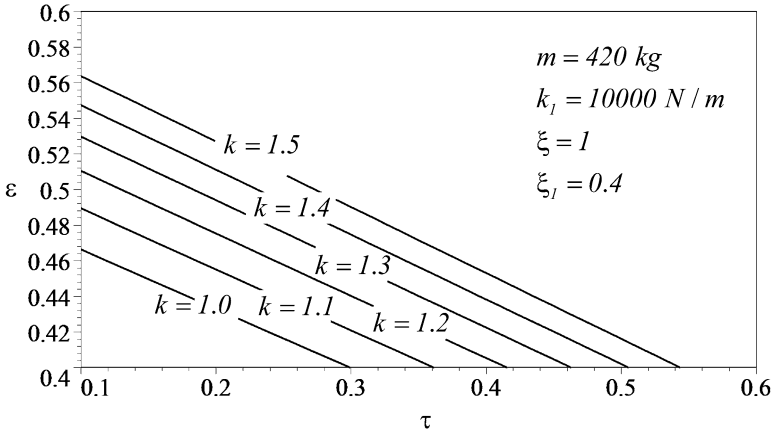

Fig. 1.20 τ versus ε for different spring rates for $\xi = 0.4$

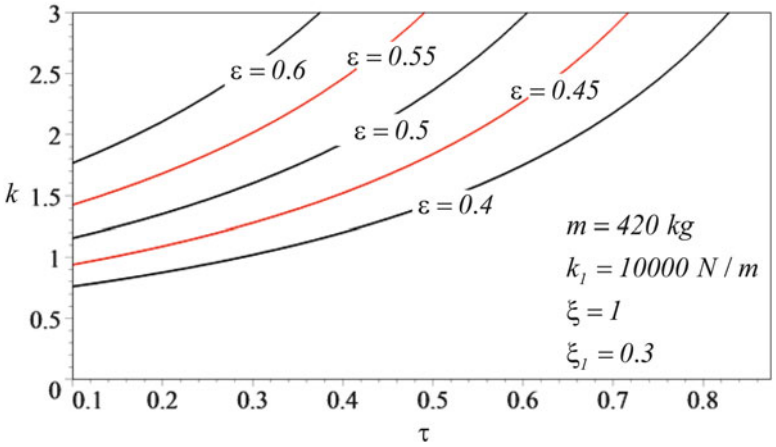

Fig. 1.21 Plots of k versus τ for $\xi_1 = 0.3$ and different ε in the domain $0.1 < \tau < 0.875$

1.5 Nonlinear Damper

The force–velocity characteristics of an actual shock absorber can be quite complex as is shown in Fig. 1.28. Although we may express the complex behavior using an approximate function, analytic calculation can be quite complicated with little design information. Furthermore, the representations of the exact shock absorber do not greatly affect the behavior of the system. The simplest linear viscous damper model is usually used for linear analytical calculation

$$F_D = cv_D, \tag{1.56}$$

where c is the damping coefficient of the damper.

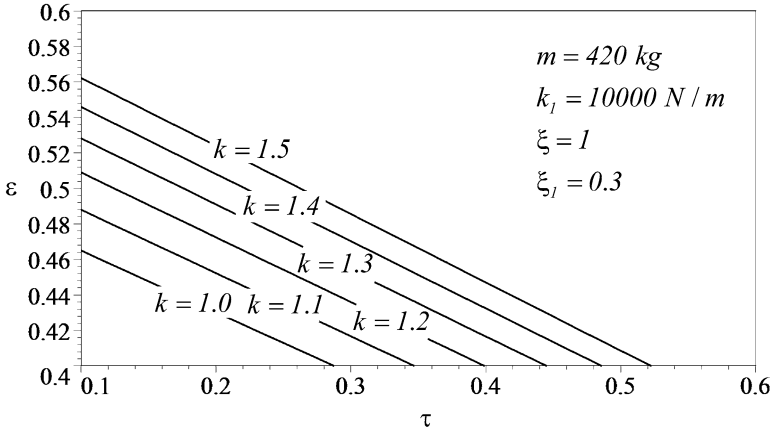

Fig. 1.22 τ versus ε for different spring rates for $\xi = 0.3$

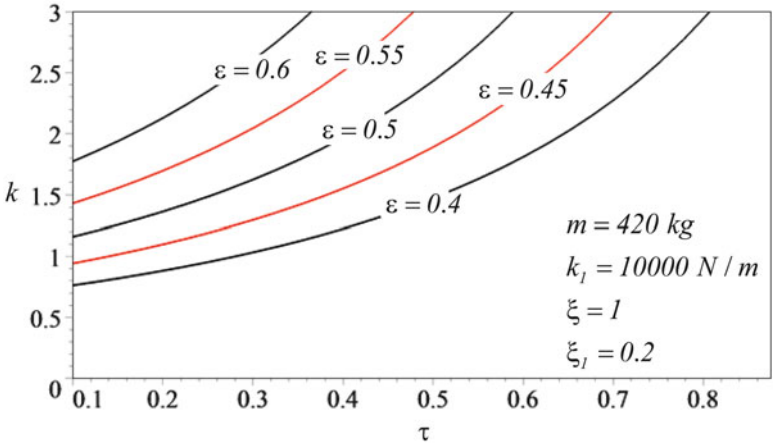

Fig. 1.23 Plots of k versus τ for $\xi_1 = 0.2$ and different ε in the domain $0.1 < \tau < 0.875$

As seen in Fig. 1.28 the bound and rebound forces of the damper are different, in other words the force–velocity characteristics diagram is not symmetric. Practically, a shock absorber compresses much easier than decompression. A reason is that during rebound in which the damper extends back, it uses up the stored energy in the spring. A high compression damping prevents to have enough spring compression to collect enough potential energy. That is why in order to get a more reliable and close to reality response for analysis on dampers, using bilinear dampers are suggested. It is similar to a linear damper but with different coefficients for the two directions [3]. The behavior of such damper models is illustrated in Fig. 1.29

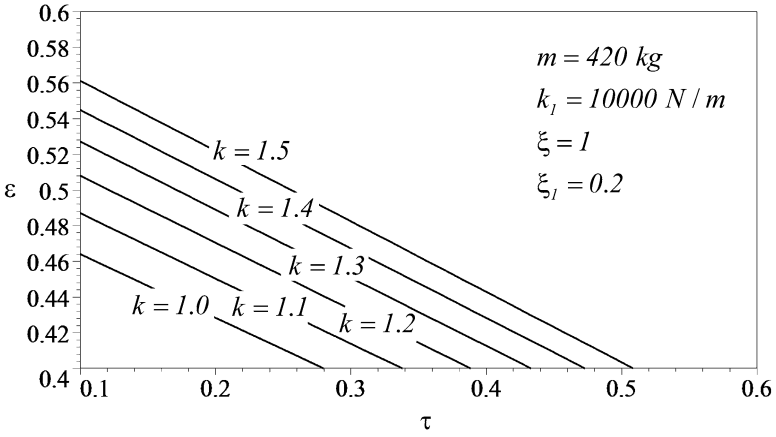

Fig. 1.24 τ versus ε for different spring rates for $\xi = 0.2$

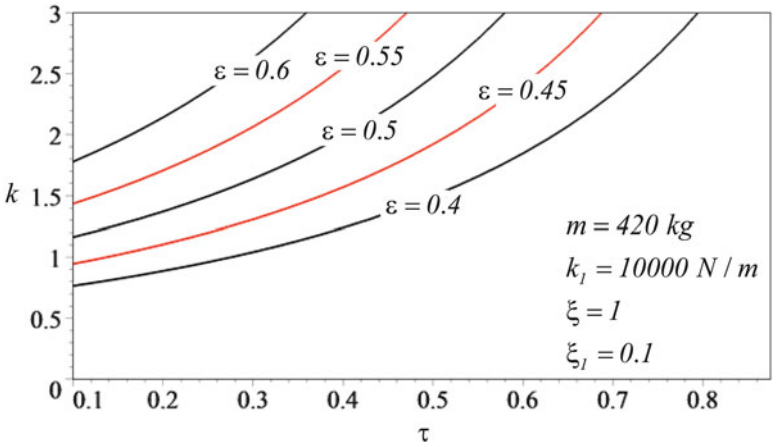

Fig. 1.25 Plots of k versus τ for $\xi_1 = 0.1$ and different ε in the domain $0.1 < \tau < 0.875$

$$F_D = \begin{cases} c_{DE} v_D & Extension \\ c_{DC} v_D & Compression \end{cases} \tag{1.57}$$

where c_{DE} is the damping coefficient when damper is extended and c_{DC} is the damping coefficient when the damper is compressed.

An ideal dual behavior damper is one which does not provide any damping while being compressed and, on the other hand, damps the motion while extending. Based on this model, the nonlinear damper model's behavior used for this study is illustrated in Fig. 1.30. Using the nonlinear damper model and following the same steps as the previous section, we can compare two systems to determine the effectiveness of damping on the flat ride.

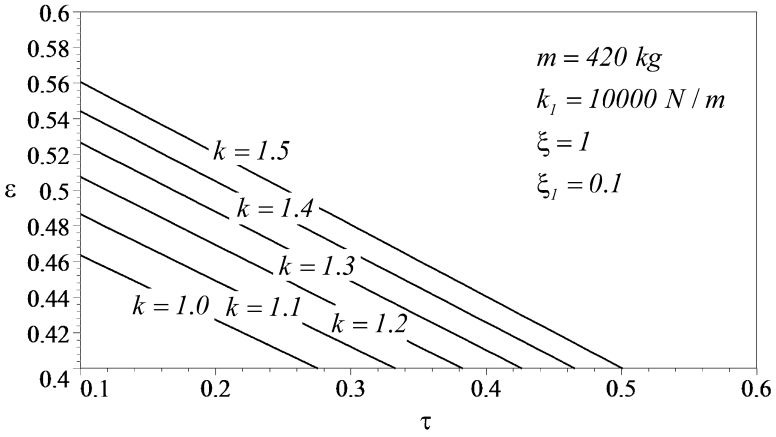

Fig. 1.26 τ versus ε for different spring rates for $\xi = 0.1$

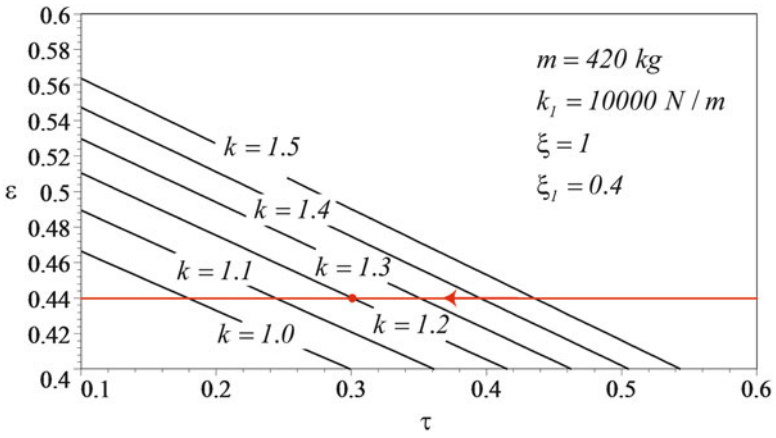

Fig. 1.27 Design chart for a smart suspension with a linear damper

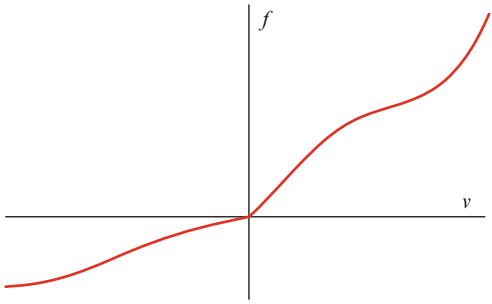

Fig. 1.28 The force–velocity characteristics of a real damper

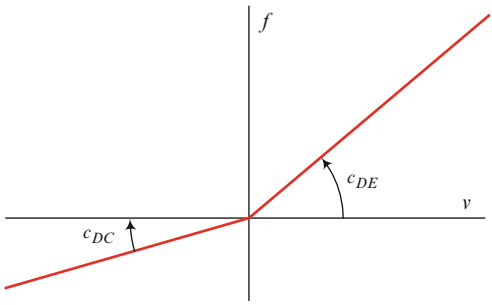

Fig. 1.29 Force–velocity characteristics of a bilinear damper

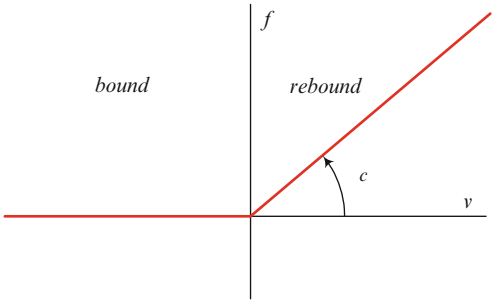

Fig. 1.30 Force–velocity characteristic of an ideal nonlinear damper model

Equations (1.37) and (1.38) have been used to get the motion of the front and rear of the vehicle after hitting a unit step. The only difference is that the motion is investigated in three steps for the front and same for the rear. Ideally, the unit step moves the ground up in no time and therefore the motion of the system begins when $y = 1$ and the suspension is compressed. The first step is right after the wheel hits the step and the damper starts extending which means the positive side of Fig. 1.30 would be in action. The second step is when the damper starts the compression phase, and according to the figure the damping coefficient would be equal to zero. The third step is when the damper starts extending again. Each of (1.37) and (1.38) should be solved for the three steps separately in order to find the time and amplitude of the third peak of the motion.

Figure 1.31 illustrates the behavior of the car equipped with a nonlinear damper when going over a unit step input. Figure 1.32 also illustrates the behavior of the same car if the damper was linear. Comparison of the behavior of the car for linear and nonlinear dampers is plotted in Figs. 1.33 and 1.34 for front and rear suspensions, respectively. The linear damper dissipates energy in both, bound and rebound cycles, while the nonlinear damper dissipates energy only in rebound cycle. Therefore, the linear damper is more effective in energy dissipation and damps the system faster. This fact can be seen in both Figs. 1.33 and 1.34.

To compare the behavior of a car with both cycle linear damper and one cycle nonlinear damper, we also analyze the opposite cycle nonlinear damper of Fig. 1.35. The response of the car to the opposite cycle nonlinear damper is illustrated in Fig. 1.36. Comparison of the linear and nonlinear dampers for the front and rear suspensions is plotted in Figs. 1.37 and 1.38, respectively.

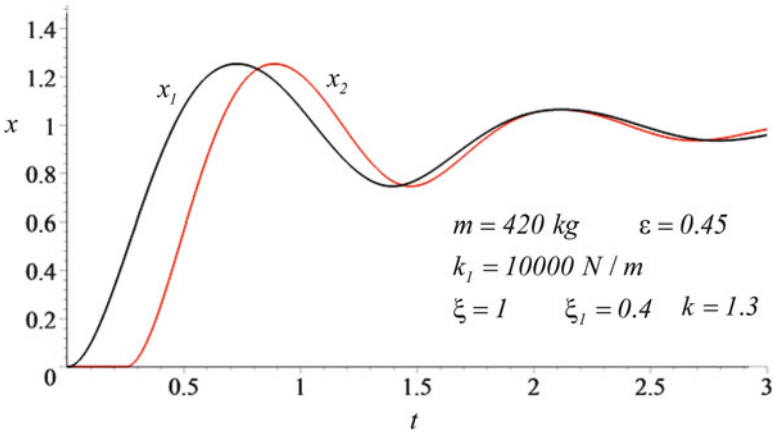

Fig. 1.31 Response of the front and rear suspensions of a near flat ride car with ideal nonlinear damper to a unit step

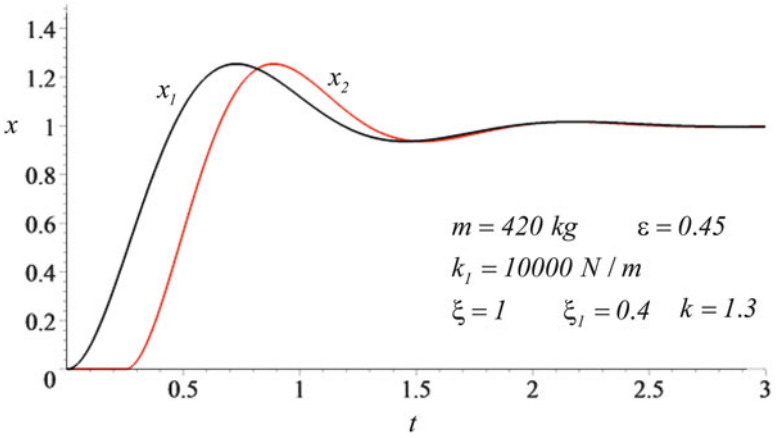

Fig. 1.32 Response of the front and rear suspensions of a car with linear damper to a unit step

1.6 Near Flat Ride Solution for Ideal, Nonlinear Damper

The conditions that x_1 and x_2 meet after one and a half oscillations are the same as (1.45) and (1.46). The equation resulted from $x_1 = x_2$ has got ξ and ξ_1 as its variables and could be plotted as an explicit function of the variables which interestingly shows that the value for $\xi = \xi_2/\xi_1$ must equal to 1 for any value for damping coefficient of the front suspension. Therefore, regardless of the value of ξ_1 the rear suspension should have an equal coefficient for the damper. The equation resulted from $t_{P_1} = t_{p_2}$ generates an equation to determine $k = k_2/k_1$. Figure 1.39

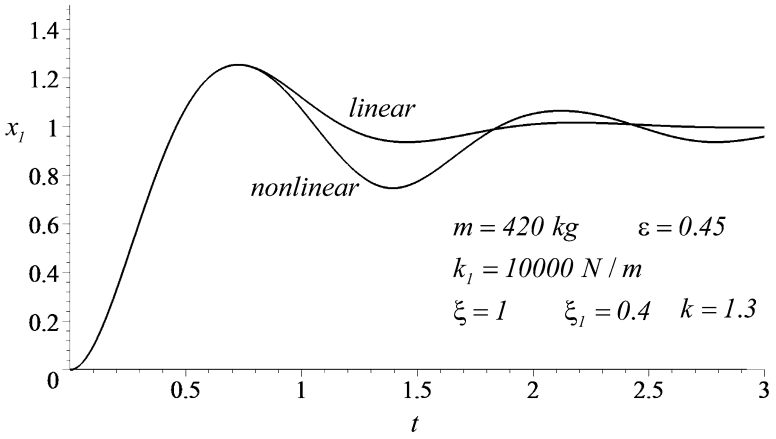

Fig. 1.33 Comparison of the behavior of the front suspensions of the car for linear and nonlinear dampers

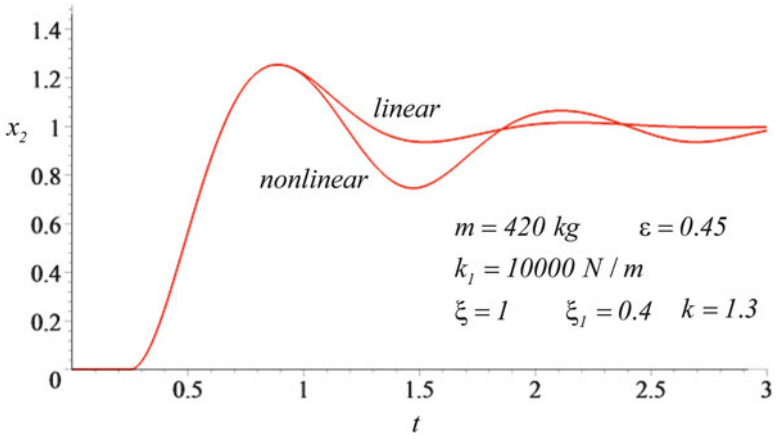

Fig. 1.34 Comparison of the behavior of the rear suspensions of the car for linear and nonlinear dampers

illustrates the spring ratio $k = k_2/k_1$ versus $\tau = l/v$, to have near flat ride with ideal nonlinear damping, for different $\varepsilon = a_1/l$.

Once again, considering the existing designs street vehicles, only the small section of $0.1 < \tau < 0.875$ of Fig. 1.39 is applied. The mass center of street cars is also limited to $0.4 < \varepsilon < 0.6$.

Figure 1.40 shows how k varies with τ for $\xi_1 = 0.5$ and different ε to provide a near flat ride with ideal nonlinear damper. For any ε, the required stiffness ratio increases by increasing τ. Therefore, the ratio of rear to front stuffiness increases when the speed of the car decreases. Figures 1.41–1.44 also provide the same design graphs for $\xi_1 = 0.4, 0.3, 0.2, 0.1$, respectively.

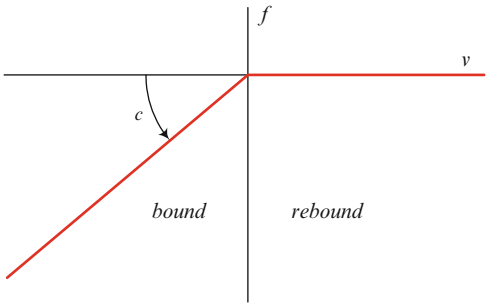

Fig. 1.35 Force–velocity characteristic of an opposite cycle nonlinear damper model

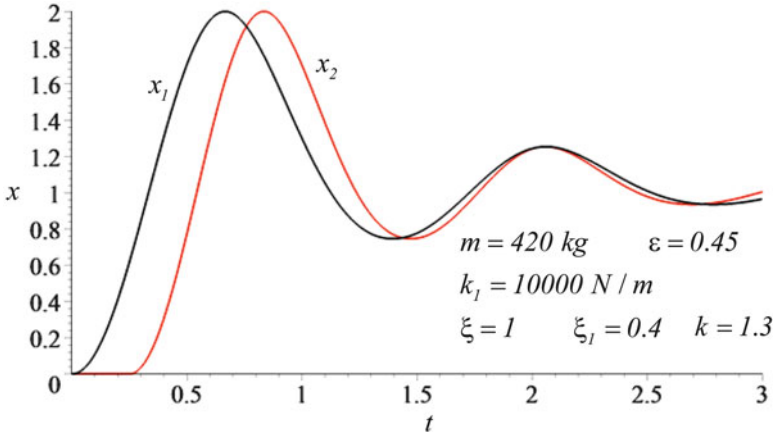

Fig. 1.36 Response of the front and rear suspensions of a near flat ride car with ideal nonlinear damper to a unit step

Using a nonlinear damper for studying Olley's flat ride tuning shows the same behavior as a linear damper. So, the same trend as for the linear case can be taken here. There will be a possibility of using the τ versus ε diagrams as a design chart.

1.7 The First Investigations

Maurice Olley was one of the first pioneers who introduced and studied the concept of flat ride in vehicle dynamics. He was an English engineer born in 1889, who during his life added a lot to the general knowledge of vehicle dynamics and is counted as one of the great automobile engineers of his era. He is one of the founders of modern vehicle dynamics. In his early career in the Rolls Royce design office, he worked under Sir Henry Royce but the majority of his career was spent at Cadillac in the USA and Vauxhall in England.

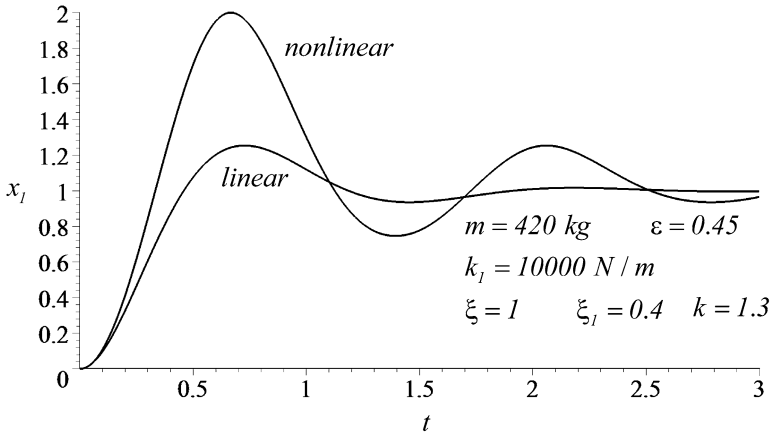

Fig. 1.37 Comparison of the behavior of the front suspensions of the car for linear and opposite cycle nonlinear dampers

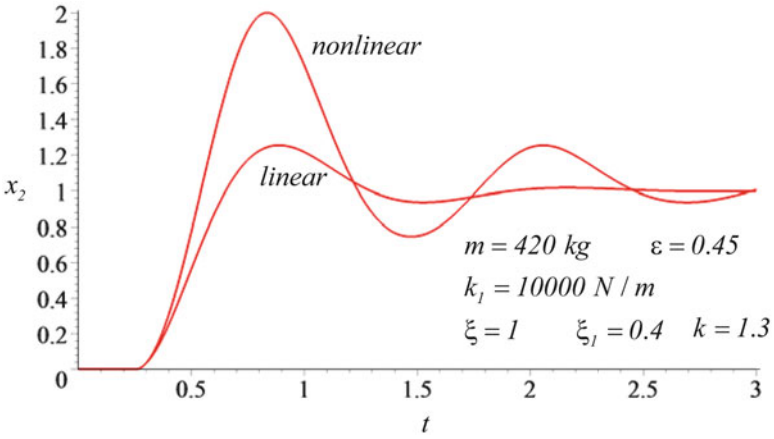

Fig. 1.38 Comparison of the behavior of the rear suspensions of the car for linear and opposite cycle nonlinear dampers

Olley worked directly for Sir Henry Royce and was in the United States for some 10 years struggling to get off the ground the manufacture of Rolls-Royce cars at Springfield, Massachusetts. The financial crash of 1929 put the skids under the operation. His first task after moving to the Cadillac company in 1930 was suspension and ride. He introduced the Rolls-Royce type of bump rig and began a full program of ride development. He studied the oscillation of wheels and tires and by applying some changes on the rig was soon studying the basic ride motions of the car. In his paper [6] he published the results taken from his experiments using the test rig for the first time.

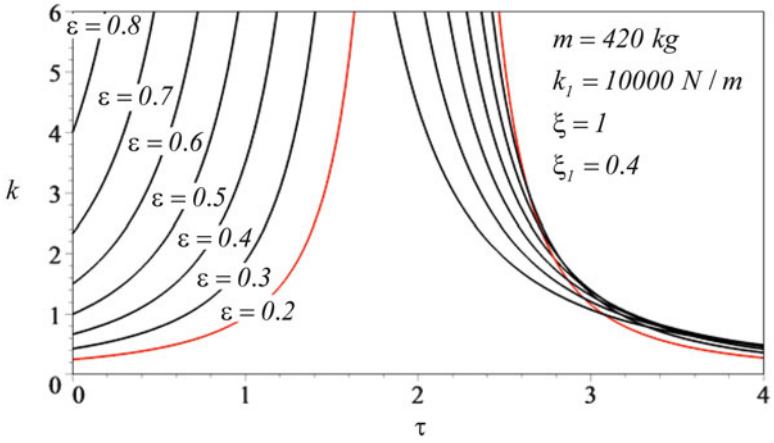

Fig. 1.39 The value of spring ratio $k = k_2/k_1$ versus $\tau = l/v$, to have near flat ride with ideal nonlinear damping, for different $\varepsilon = a_1/l$

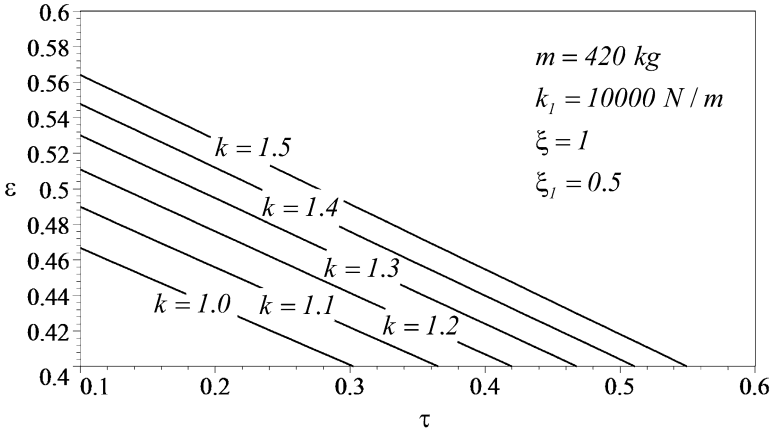

Fig. 1.40 ε versus τ, for different k for $\xi_1 = 0.5$ to have near flat ride with ideal nonlinear damping

He developed a bouncing table rig in General Motors proving grounds, on which humans were vibrated vertically at different frequencies and amplitudes. They would have increased the frequency till the person on the table begins to feel uncomfortable. Using this equipment Olley explained the relation between vertical acceleration and comfort over a range of frequencies. He generated a curve for passenger comfort, which is very similar to the current ISO2631 standard.

Olley as well as other investigators in well-established car companies realized that the pitch and roll modes of the car body are much more uncomfortable than the bounce mode. The investigators' effort focused on the suspension stiffness and damping rates to be experimentally adjusted to provide acceptable vertical

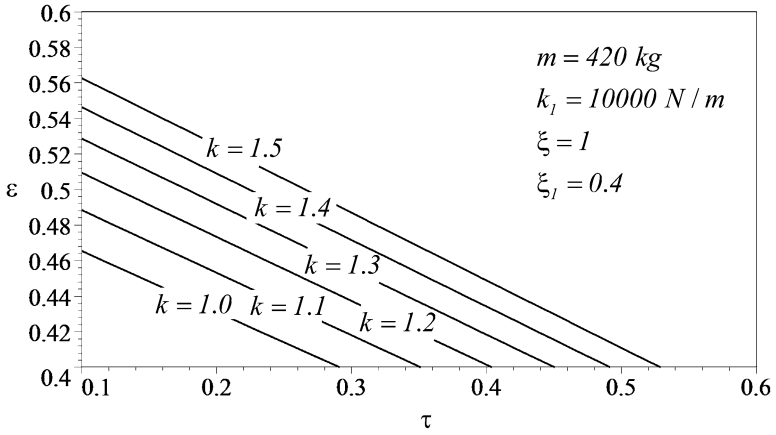

Fig. 1.41 ε versus τ, for different k for $\xi_1 = 0.4$ to have near flat ride with ideal nonlinear damping

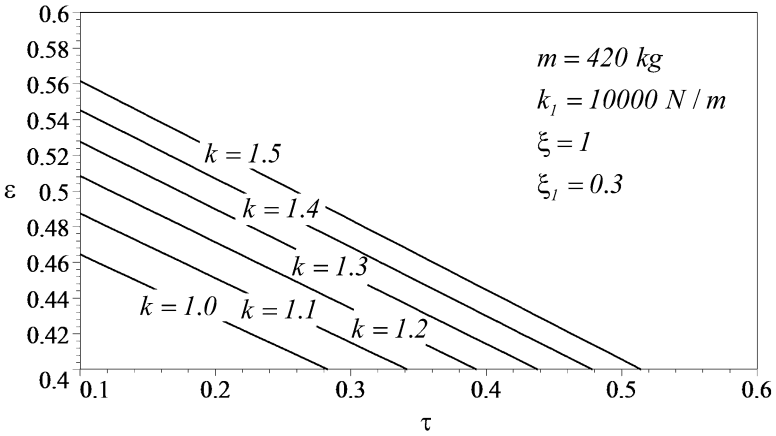

Fig. 1.42 ε versus τ, for different k for $\xi_1 = 0.3$ to have near flat ride with ideal nonlinear damping

vibrations. However, the strategy about roll and pitch modes was to transform them to bounce. Due to usual geometric symmetry of cars, as well as the symmetric excitation from the road, roll mode is being excited much less than pitch mode. Therefore, lots of investigations have been focused on adjustment of the front and rear suspensions such that pitch mode of vibration transform to the bounce.

In the early 1930s most cars were built with fairly stiff springs at the front and soft at the rear, with a $\frac{r^2}{a_1 a_2}$ ratio in pitch of about 0.8, where r is the pitch radius of gyration of the car and a_1 and a_2 are the distance of the mass center, C, from the front and rear axles, as shown in Fig. 1.45 [1]. However, based on what Olley discovered, such a choice was against the mode transfer desire.

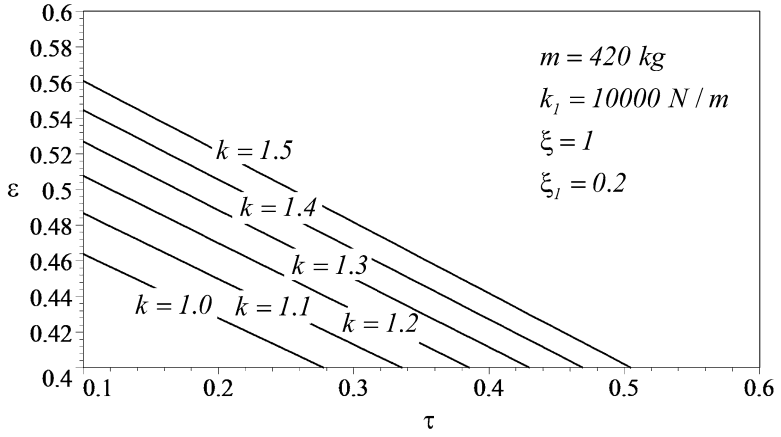

Fig. 1.43 ε versus τ, for different k for $\xi_1 = 0.2$ to have near flat ride with ideal nonlinear damping

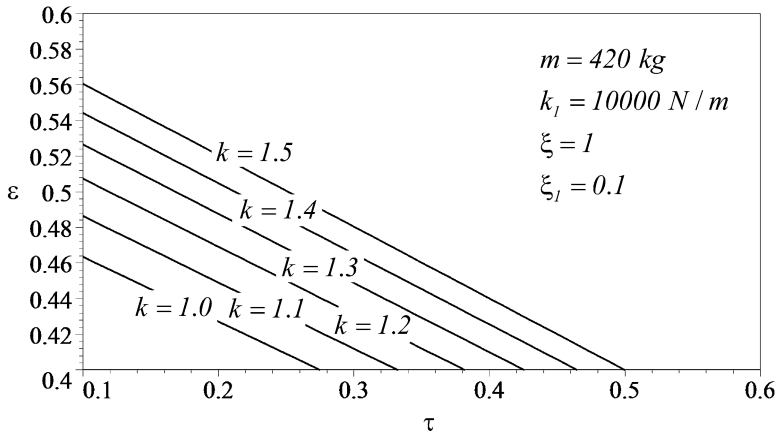

Fig. 1.44 ε versus τ, for different k for $\xi_1 = 0.1$ to have near flat ride with ideal nonlinear damping

Besides all the important facts that Olley discovered during his experiments, the principle known as the flat ride tuning or Olley's flat ride proved to be more industry approved and accepted. After his publications [6–8] in which he advocated this design practice, they became rules of practice.

We can summarize what has been said about ride and comfort in American passenger cars by Olley as the following:

1. The front spring should be softer than the rear for flat ride tuning. This will promote bouncing of the body rather than pitching motions at least for a greater majority of speeds and bump road situations. The front suspension should have

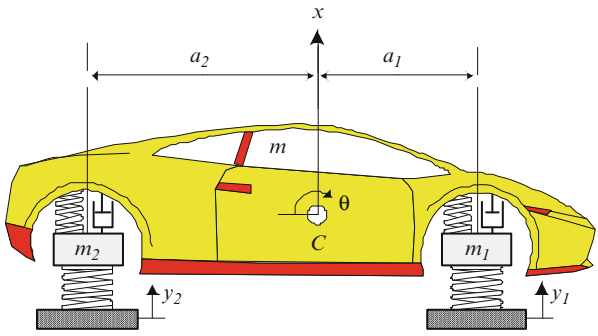

Fig. 1.45 Bicycle car model used for analyzing vibrations

a 30% lower ride rate than the rear suspension, or the spring center should be at least 6.5% of the wheelbase behind the center of gravity. Although this does not explicitly determine the front and rear natural frequencies, since the front-rear weight distribution on passenger cars is close to 50–50, it will generally assure that the rear frequency is greater than the front.

2. The ratio $\frac{r^2}{a_1.a_2}$ normally approaches unity. This reduces vibration interactions between front and rear because the two suspensions can now be considered as two separate systems. As a consequence there will be less resonant build-ups on the road and the pitching frequency will have a magnitude closer to that of bounce.
3. The pitch and bounce frequencies should be close together: the bounce frequency should be less than 1.2 times the pitch frequency. For higher ratios interference kicks resulting from the superposition of the two motions. This condition will be met for modern cars because the dynamic index is near unity with the wheels located near the forward and rearward extremes of the chassis.
4. Neither frequency should be greater than 1.3 Hz, which means that the effective static deflection of the vehicle should exceed roughly 6 in.
5. The roll frequency should be approximately equal to the pitch and bounce frequencies. To minimize roll vibrations the natural frequency in roll needs to be low just as for the bounce and pitch modes.

Rowell and Guest [9] in 1923 identified the value of $\frac{r^2}{a_1.a_2}$ being associated with vehicles in which the front and rear responses were uncoupled. Olley was able to investigate the issue experimentally and these experiments led him to the belief that pitching motion was extremely important in the subjective assessment of vehicle ride comfort. He built the Cadillac k_2 rig in 1931 which was a 12 cylinder, 7 passenger Cadillac limousine of the period, fitted with front and rear outriggers each of which could carry up to 327 kg made up in 27 kg weights. To their surprise, under these supposedly ideal conditions, they still got an unsatisfactory ride. This arrangement gave no fixed oscillation centers and the ride had no pattern. However, by fitting all the weights they found that if the front spring static deflections are some 30% greater than the rear, then the revolutionary flat ride occurs. Olley's explanation

was that because the two ends of the car did not cross a given disturbance at the same instant it was important that the front wheels initiated the slower mode and that the rear wheels initiated the faster mode. This allowed the body movement at the rear to catch up the front and so produce the flat ride.

The condition of Flat Ride is expressed in various detailed forms; however, the main idea states that *the front suspension should have a 30% lower ride rate then the rear.* The physical explanation for why this is beneficial in reducing pitch motion is usually argued based on the time history of events following a vehicle hitting a bump. First, the front of the vehicle responds "approximately in the well-known damped oscillation manner." At some time later, controlled by the wheelbase and the vehicle speed, the rear responds in similar fashion. The net motion of the vehicle is then crudely some summation of these two motions which minimizes the vehicle pitch response [2].

Confirmation of the effectiveness in pitch reduction of the Olley design was given by Best [1] over a limited range of circumstances. Random road excitation was applied to a half-car computer model, with identical front and rear excitations, considering the time delay generated by the wheelbase and vehicle's speed. Pitch suppression was associated with the wheelbase filtering effect. Pitch suppression appeared to be necessarily associated with increases in bounce response, leaving in unclear whether or not it is a worthwhile goal [10].

Sharp and Pilbeam [11] attempted a more fundamental investigation of the phenomenon, primarily by calculating frequency response for the half-car over a wide range of speed and design conditions. At higher speeds, remarkable reductions in pitch response with only small costs in terms of bounce response were shown. At low speeds, the situation is reversed. These behavioral features were shown to be generic insofar as variations in mass center location, pitch inertia and damping level were concerned, and the implications from the frequency responses were confirmed by simulations with nonlinear asymmetric suspension damping.

Later on Sharp [10] discussed the rear to front stiffness tuning of the suspension system of a car, through reference to a half-car pitch plane mathematical model. He used new results relating to the frequency responses of the bouncing and pitching motions of the car body to show that the pitch minimization mechanism of Olley's flat ride tuning "involves interference between the responses to the front and rear axle inputs." He showed that interference with respect to the rotational motion implies reinforcement with respect to the translational motion, and vice versa. Sharp concludes almost the same facts mentioned by Best and other researchers before him, saying that at higher vehicle speeds, Olley tuning is shown to bring advantage in pitch suppression with a very little disadvantage in terms of body acceleration. At lower speeds, he continues, not only does the pitch tuning bring large vertical acceleration penalties but also suspension stiffness implied are impractical from an attitude control standpoint.

The flat ride problem was revisited by Crolla and King [2]. They generated vehicle vibration response spectra under random road excitations. Some results included the wheelbase filter effect, while others did not. Olley and reverse Olley designs were simulated at speeds of 10, 20, 30, and 40 m/s, with the result that

Olley design was good in pitch and bad in bounce in all cases. It was confidently concluded that the rear/front stiffness ratio has virtually no effect on overall levels of ride comfort.

In 2004, Odhams and Cebon investigated the tuning of a pitch-plane model of a passenger car with a coupled suspension system and compared it to that of a conventional suspension system, which followed the Rowell and Guest treatment [5]. They believed that there is a significant benefit from coupling front and rear suspensions; coupled suspensions with a "Hydrolastic" or "Hydragas" systems, in which the front and rear suspension struts are connected hydraulically, have proved very effective in some applications. The concluded that the Olley's flat ride tuning provides a near optimum stiffness choice for conventional suspensions for minimizing dynamic tire forces and is very close to optimal for minimizing horizontal acceleration at the chest (caused by pitching) but not the vertical acceleration.

Key Symbols

a_1	Distance from the front wheel to the C
a_2	Distance from the rear wheel to the C
c	Damping coefficient
C	Mass center
C_{DC}	Damping coefficient in compression
C_{DE}	Damping coefficient in extension
F_D	Damping force
I	$= mr^2$ mass moment
k	$= k_2/k_1$
k_1	Front spring rate
k_2	Rear spring rate
k_T	Tire stiffness
k_f	Front spring rate
k_r	Rear spring rate
k'_F	Front ride rate
k'_R	Rear ride rate
l	Wheelbase
m	Mass
m_1	Front mass portion
m_2	Rear mass portion
q_1	$= \left(k'_F + k'_R\right)/m$
q_2	$= \left(a_1 k'_F - a_2 k'_R\right)/m$
q_3	$= \left(a_1^2 k'_F + a_2^2 k'_R\right)/I$

r	Radius of gyration
τ	Time lag
t_{p_1}	Time of the third peak of the front
t_{p_2}	Time of the third peak of the rear
u_1	First mode shape of the system
u_2	Second mode shape of the system
v	Velocity of the vehicle
v_D	Vertical velocity of the damper
x_1	Vertical movement of the front wheel
x_2	Vertical movement of the rear wheel
y_1	Road input to the front wheel
y_2	Road input to the rear wheel

Greek

α	$= r^2/a_1a_2$ nondimensional parameter
β	$= l^2/a_1a_2$ nondimensional parameter
γ	Rate to front length ratio
θ	Pitch angle
ε	$= a_1/l$ nondimensional parameter
ξ_1	Front damping ratio
ξ_2	Rear damping ratio
ξ	$= \xi_2/\xi_1$ rear to front damping ratio
η_b	Distance from bounce center to the C
η_p	Distance from pitch center to the C
ω_1	First natural frequency of the system
ω_2	Second natural frequency of the system
Ω_1	$= \sqrt{k_1\beta/m}$ nondimensional parameter
Ω_2	$= \sqrt{k_2\beta/m}$ nondimensional parameter

References

1. Best A (2002) Vehicle ride-stages in comprehension. Phys Technol 15(4):205
2. Crolla D, King R (2000) Olley's "Flat Ride" [revisited]
3. Dixon J (2008) The shock absorber handbook. Wiley, New York
4. Milliken WF, Milliken DL, Olley M (2002) Chassis design. Professional Engineering Publishing, Bury
5. Odhams A, Cebon D (2006) An analysis of ride coupling in automobile suspensions. Proc Inst Mech Eng D J Automob Eng 220(8):1041–1061
6. Olley M (1934) Independent wheel suspension 'its whys and wherefores'. Soc Automot Eng J 34(3):73–81
7. Olley M (1938) National influences on American passenger car design. Proc Inst Automob Eng 32(2):509–572

8. Olley M (1946) Road manners of the modern car. Proc Inst Automob Eng 41(1):147–182
9. Rowell HS, Guest JJ (1923) Proc Inst Automob Eng 18:455
10. Sharp R (2002) Wheelbase filtering and automobile suspension tuning for minimizing motions in pitch. Proc Inst Mech Eng D J Automob Eng 216(12):933–946
11. Sharp R, Pilbeam C (1993) Achievability and value of passive suspension design for minimum pitch response. In: Vehicle Ride and Handling, vol 39, pp 243–259

Chapter 2
Light-Tracking Kinematics of Mobile Platform

Ahmad Salahuddin Mohd Harithuddin, Pavel M. Trivailo, and Reza N. Jazar

Abstract The formulation of tracking mechanism used for a light-tracking system is presented to maximize the collected energy. The solution considers the motion of the illumination sources and the translational and rotational motion of the light-receiver/collector. The tracker in consideration consists of two orthogonal rotary actuators to provide a hemispherical pointing capability. The tracker is assumed to be mounted on a mobile platform, such as a rover or a robot, which moves on a given path. The tracker's function is to change the orientation of the light-collector to face and receive the maximum incident radiation from multiple light sources. As the platform carrying the tracker is moving, the lights' positions and intensity may vary. This requires the tracker to actively point its payload towards the orientation that receives maximum light intensity while being in motion. An example of an indoor robot tracking radiant energy from fluorescent lights in a room is presented to demonstrate the concept. In addition, the coordinate transformation method using compound homogeneous transformation matrix is applied in the formula derivation.

2.1 Introduction

The function of a tracking system is to follow the motion of a relatively moving object, such as a light source, for purposes such as surveillance and energy reception. The current treatment of light tracking system usually deals with a single target of interest—tracking the Sun's motion for solar energy harvesting purposes.

A.S.M. Harithuddin • P.M. Trivailo • R.N. Jazar (✉)
School of Aerospace, Mechanical and Manufacturing Engineering, RMIT University, Melbourne, VIC, Australia
e-mail: s3305201@student.rmit.edu.au; pavel.jazar@rmit.edu.au; reza.jazar@rmit.edu.au

R.N. Jazar and L. Dai (eds.), *Nonlinear Approaches in Engineering Applications 2*,
DOI 10.1007/978-1-4614-6877-6_2,

The equation of motion of the Sun is usually given in ecliptic coordinates [1]. Hence, it is necessary to perform a set of coordinate transformations to program an Earth-based Sun-tracker to trace its motion. A more complicated example is a mobile robot exposed to multiple light sources.

An example of a setting with multiple light sources can be found in an indoor environment where radiance is provided by a combination of artificial and non-artificial lights (for example, radiance from fluorescent lamps and window lighting). The present photovoltaic panels are not optimized for extracting electrical power from indoor radiation into direct current electricity; however, works by Randall [10] and Sansoni et al. [12] show promises in the development of specialized photovoltaic cells to be used in Sunless settings. Another interesting multiply-lighted environment is a mobile robots in the polar regions. A solar-powered robot, aptly named Cool Robot [8], is used to conduct scientific experiments in the extreme climate of the South Pole. Exploiting the snowy environment, the solar panels are designed to generate photovoltaic energy from both the Sun and its snow-reflected component.

This article approaches the tracking system as a motion kinematics concept with a focus on the formula used by tracker to follow the target motion. The source can be from a single or multiple light sources. The tracker is assumed to be working without any help from a photosensor, i.e. the tracker follows a precalculated translation and orientation trajectory in order to receive maximum light intensity. In this article, the derivation of such formula is presented for the application of a ground-fixed solar tracker and a photovoltaic panels on a rover.

The existing methods for switching coordinates between reference frames use either spherical trigonometric technique or rotation matrix. In this article, the coordinate transformation includes both rotation and translation, using the 4×4 homogeneous transformation matrix.

To demonstrate the application of the analytical result, the problem of an illumination tracking photovoltaic panel on a moving platform, under multiple radiant energy sources is presented. The objective of the two-degree-of-freedom, dual-axis tracker is to assure that the maximum possible radiant energy intensity from multiple sources reaches the surface of the photovoltaic panels. To determine the angular trajectories, i.e. the azimuth and elevation angles of the panel, and the power usage of the system, the path of the vehicle and the illumination placements around the environment must be known a priori. The trajectories are determined such that the panel is oriented towards the direction which receives the most light intensity. The method for the maximization of electricity production for an indoor photovoltaic system in artificially lighted environment proposed in those paper is, at least to the knowledge of the authors, a novelty in the field of the light tracking system.

2.2 Previous Work

Formula-based, light-tracking method receives considerable attention especially in solar energy research as solar panels with tracking capabilities are more efficient than fixed-panels in harvesting energy from the radiant source. Traditionally, the equations for the apparent motion of the Sun and the intensity of the Sunray on an angled surface are described using spherical trigonometry which is mainly based on the work of astrodynamics [1]. Dealing with trigonometric calculation in technical computing tools, however, is not as straightforward as compared to working with matrix and vector operations. The vectorial approach, hence, has got more attention from researchers and practitioners in describing tracking formulas [9, 11, 13].

The next development to achieve a general Sun-tracking formula is done by Chen in conjunction with thermal solar energy [2]. They developed a tracking formula for a heliostat to direct and focus Sunlight onto a fixed target on the Earth. The formula is developed specifically for a rotation-elevation tracker. In 2006, Chen et al. derived a more versatile formula that also is applicable for heliostat with any type of orientation axes [3]. The formula can be used for an arbitrary located target.

Chong and Wong [4] derived a more general formula for the case of solar panels. Unlike the reflector, the solar panel is required to align its normal axis parallel to the Sun vector in order to receive maximum radiant energy. The formula is suitable for the application of azimuth-elevation and tip-tilt trackers.

These developments, however, only deal with tracker a single object, i.e. the Sun. The trackers in consideration of the authors also are assumed to be fixed on the Earth-surface frame. This work presents an improvement to the versatility of the existing formulas by generalizing the light tracking formula for any radiant energy-harvesting mechanism, including artificial lights in indoor settings. This includes the consideration of tracking multiple light sources and tracking on a moving platform for application in rovers and mobile robots. This work also focuses on the application of compound homogeneous transformation matrix in the problem of tracking radiant energy.

The type of radiance collector in this study can exist in the form of solar cells and indoor photovoltaic cells, which application requires the collector to be orientated towards a light source. For intermediate light receiver application, such as parabolic reflector or concentrator, the ray-tracing formula presented here can be further modified to include reflected light analysis.

2.3 Types of Tracker

Trackers can be grouped into classes by the number of the rotational degree-of-freedom: single axis trackers and dual axes trackers. Both types of trackers can be grouped in several subclasses by the orientation of the axes.

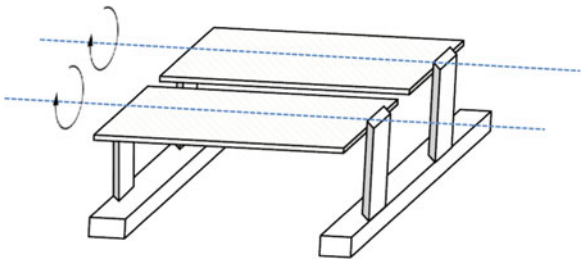

Fig. 2.1 Horizontal axis tracker

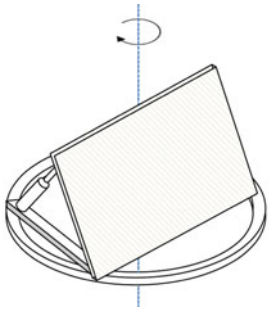

Fig. 2.2 Vertical axis tracker

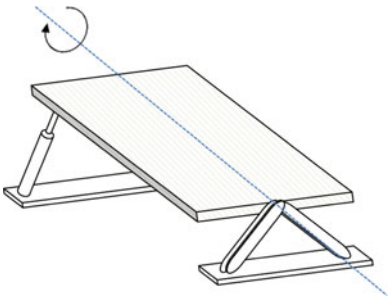

Fig. 2.3 Tilt axis tracker

2.3.1 Single Axis

Figure 2.1 shows a *horizontal axis tracker's* structure with a long, rotatable horizontal tube which is supported on bearing mounted on a frame structure. The photovoltaic module is installed on the horizontal tube facing upward to track the elevation of the Sun. A *vertical axis tracker* in Fig. 2.2 has an axis of rotation that is vertical to the ground with slanted photovoltaic modules that changes orientation from east to west to follow the azimuthal motion of the Sun. A *tilted axis tracker* shown in Fig. 2.3 has a similar setup to its horizontal counterpart with the tube slightly tilted several degrees from the ground.

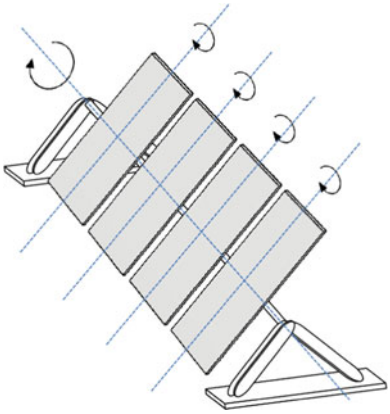

Fig. 2.4 Tilt-roll dual axis tracker

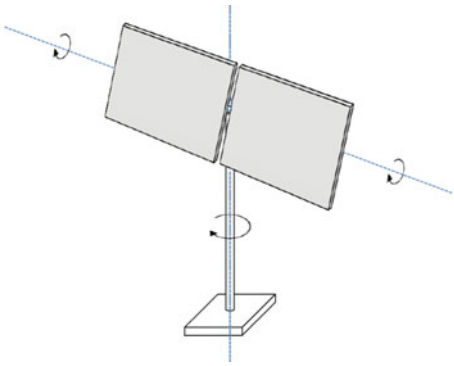

Fig. 2.5 Azimuth-elevation dual axis tracker

2.3.2 Dual Axes

Tilt-roll and *azimuth-elevation* are the two most commonly used dual axis configurations in solar tracking system. These trackers are free to rotate about two orthogonal axes, giving full orientation flexibility in tracking the Sun. The tilt-roll tracker has a configuration where its primary axis of rotation is parallel to the ground and its secondary axis is orthogonal to the primary axis as shown in Fig. 2.4. The azimuth-elevation tracker rotates about the azimuth axis, which is parallel to the zenith axis, as its primary axis and then rotates about the elevation axis, which is parallel to the ground as shown in Fig. 2.5. With two rotational degree-of-freedom, a dual axes tracker can track the Sun's azimuth and elevation angles throughout daytime.

2.4 Illuminance and Light Vectors

To assess the problem quantitatively, the illumination characteristics in the environment must be calculated before any information can be provided to the tracking control system. The direction of the brightest illumination with respect to vehicle's

position and orientation in the room must be predetermined. Radiant energy sources for photovoltaic cells can be obtained from the Sun (one single source), its reflected component (e.g., heliostats, snow), fluorescent tube lights, or window lighting.

2.4.1 Illuminance Computation

The illuminance received by a photovoltaic cells depends on the distance between the radiant energy source emitter and the receiver. Generally, the illuminance, E_s, is inversely proportional to the square of the distance of the source [10],

$$E_r = \frac{I}{r^2} \tag{2.1}$$

where I is the light intensity and r is the distance of the receiver from the light source. The illuminance E_r can also be measured as a function of the angle of incidence between the panel surface and the light direction [10],

$$E_\varphi = I \cos\varphi \tag{2.2}$$

where φ is the angle of incidence.

In the case of solar illuminance, the distance is not a factor; hence, Eq. (2.2) is sufficient. For a more general case, we will assume that the irradiance received from a light source is affected both by the distance between the emitter and the receiver and the angle of incidence of the incoming light ray:

$$E = \frac{I}{r^2} \cos\varphi. \tag{2.3}$$

In case of multiple light sources, we need to calculate the resultant of the amount of the illuminance of light rays from multiple emitters at the photovoltaic panel as shown in Fig. 2.6. Assuming that there are n emitters and the intensity of each source is I_i, we combine illuminance from multiple sources by a linear combination. The unit normal vector of the photovoltaic plane, $\hat{\mathbf{n}}$, is used to define the pointing direction of the panel and the unit vector, $\hat{\mathbf{r}}_i$, represents the light direction from the ith source as seen from the receiver:

$$E = \sum_i^n \frac{I_i}{r_i^2} \cos\varphi_i = \sum_i^n \frac{I_i}{r_i^2} \hat{\mathbf{n}} \cdot \hat{\mathbf{r}}_i \tag{2.4}$$

The objective of an automated tracker is to find the pointing direction such that the photovoltaic panel receives the maximum possible radiant energy from the multiple sources, that is, to find a vector $\hat{\mathbf{n}}$ such that E in Eq. (2.4) is maximum. Such vector $\hat{\mathbf{n}}$ is defined as *maximum illuminance vector*. Note that, in this work, Eq. (2.4) does not give the actual illuminance in photometry sense but is used to provide a method to quantify the illuminance based on the distances and the incident angles of multiple light sources with respect to the light tracking panel.

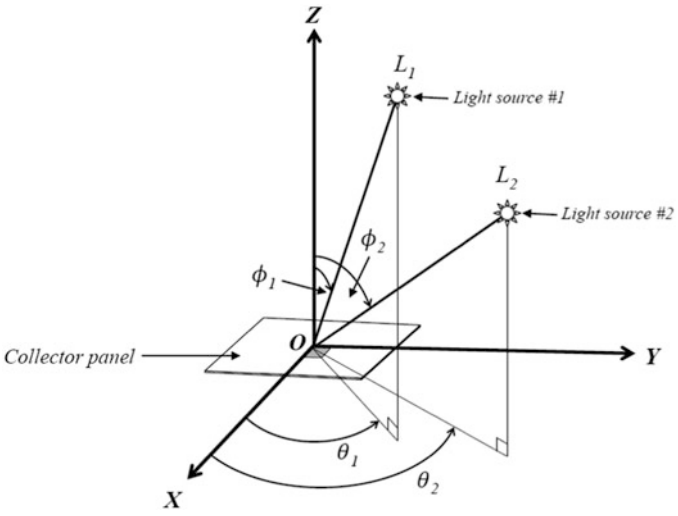

Fig. 2.6 Light vectors described in spherical coordinate system centered at the collector panel

2.4.2 Light Vectors in Spherical Coordinate System

Radiant energy from artificial lights such as fluorescent tubes can be similarly modeled as a point source or a line source. If the light emitter is modeled as a line source, the illuminance will vary with the reciprocal of the distance r for a bounded range $r_{i_1} < r_i < r_{i_2}$.

To express the analytical steps as a general rule, radiant energy from artificial source is modeled as a light ray coming from a point source.

Since the illuminance depends on the angle of incidence of the incoming light and the distance of the emitter from the receiver, it is more intuitive to model the artificial light ray vector using spherical coordinate system as shown in Fig. 2.6. In spherical coordinate system, a point is specified using the radial distance of that point from the origin, the polar angle φ measured from the zenith axis, and the azimuth angle θ which is orthogonal to the zenith axis.

2.5 Compound Homogeneous Transformation

In the derivation of tracking formula, it is important to describe the coordinate of the target (light sources) and the tracker. Both the target and the tracker can be static or moving. In the case of a Sun energy collector system, the target is moving while the tracker is usually fixed to the ground. In the case of an indoor robot feeding voltage or electric current from fluorescent lights, the targets are static while the tracker is moving. To describe the motion of both the target and the tracker, it is necessary to

define them in proper coordinate frames, the Earth-centered frame, the Earth-surface frame and the collector panel frame. The motion of the light ray that is described in one frame can be transformed to the collector panel frame for tracking purpose.

The previous Sun-tracking formulas [2,3] are only applicable for a ground-fixed tracker tracing the Sunlight. The formulas only involve rotation transformation since there is no translating motion of the tracker itself.

This section is dedicated to the description of the technique used in coordinate transformation. The technique described here takes into account the offset position of the tracker from the reference point on the ground which requires a translational transformation in addition to rotational transformation. This is useful for the application of photovoltaic-powered rovers and robots.

For single-source tracking purpose, the coordinate transformation of a position vector $\mathbf{r}$ between two frames, A and B, for a fixed tracker generally takes the form of:

$$^{A}\mathbf{r} = {}^{A}R_{B}\,{}^{B}\mathbf{r} \tag{2.5}$$

where R is the rotation matrix that transforms the vector $\mathbf{r}$ from B-frame to A-frame.

A tracking collector that is installed on a moving platform (e.g., rovers, robots), however, requires a coordinate transformation that involves translation of the platform as well. The coordinate transformation of a position vector $\mathbf{r}$ between two frames, A and B, for a *mobile* tracker takes the general form of

$$^{A}\mathbf{r} = {}^{A}R_{B}\,{}^{B}\mathbf{r} + {}^{A}\mathbf{d}_{B} \tag{2.6}$$

where $^{A}\mathbf{d}_{B}$ is the 3-by-1 Cartesian vector denoting the origin of frame B from the origin of frame A. It represents the distance of the tracker's center from a fixed reference point [5].

The rotation matrix and the translation vector in Eq. (2.6) can be combined into a single 4-by-4 matrix $^{A}T_{B}$ called the homogeneous transformation matrix:

$$^{A}T_{B} = \begin{pmatrix} r_{11} & r_{12} & r_{13} & d_1 \\ r_{21} & r_{22} & r_{23} & d_2 \\ r_{31} & r_{32} & r_{33} & d_3 \\ 0 & 0 & 0 & 1 \end{pmatrix} = \begin{pmatrix} {}^{A}R_{B} & {}^{A}\mathbf{d}_{B} \\ \mathbf{0} & 1 \end{pmatrix} \tag{2.7}$$

The upper left 3-by-3 submatrix $^{A}R_{B}$ denotes the orientation of a frame B with respect to the frame A. The upper right 3-by-1 submatrix $^{A}\mathbf{d}_{B}$ denotes the position of the origin of frame B relative to frame A. The lower left 1-by-3 zero matrix denotes a perspective transformation, and the lower right element is a scaling factor which in this case is one (no scaling).

Since the homogeneous transformation matrix is a 4-by-4 matrix, a vector needs to be represented as a 4-by-1 vector for compatibility. The homogeneous coordinate expression for such vector can be represented by adding the scaling factor 1 as the

fourth element. Therefore, a vector $\mathbf{r} = (x \quad y \quad z)^T$ can equally be expressed as a homogeneous vector as follows

$$\mathbf{r}_{4\times1} = \begin{pmatrix} \mathbf{r}_{3\times1} \\ 1 \end{pmatrix} = \begin{pmatrix} x \\ y \\ z \\ 1 \end{pmatrix} \tag{2.8}$$

Using the homogeneous transformation matrix and the homogeneous representation of a vector, Eq. (2.6) can now be rewritten more concisely as

$$\begin{aligned} {}^A\mathbf{r} &= {}^A R_B \, {}^B\mathbf{r} + {}^A\mathbf{d}_B \\ &= \begin{pmatrix} {}^A R_B & {}^A\mathbf{d}_B \\ \mathbf{0} & 1 \end{pmatrix} (\mathbf{r}_{4\times1}) = \begin{pmatrix} r_{11} & r_{12} & r_{13} & d_1 \\ r_{21} & r_{22} & r_{23} & d_2 \\ r_{31} & r_{32} & r_{33} & d_3 \\ 0 & 0 & 0 & 1 \end{pmatrix} \begin{pmatrix} x \\ y \\ z \\ 1 \end{pmatrix} \\ &= {}^A T_B \, {}^B\mathbf{r} \end{aligned} \tag{2.9}$$

More complete references on the properties of homogeneous transformation matrix can be found in Jazar [6] and Legnani [7]. Three of the important properties pertaining to the application in this work are reviewed here.

1. Decomposition of Homogeneous Transformation Matrix

The homogeneous transformation matrix ${}^A T_B$ can be decomposed to matrix product of a translation matrix ${}^A D_B$ and a rotation matrix ${}^A R_B$:

$$\begin{aligned} {}^A T_B &= {}^A D_B \, {}^A R_B \\ &= \begin{pmatrix} 1 & 0 & 0 & d_x \\ 0 & 1 & 0 & d_y \\ 0 & 0 & 1 & d_z \\ 0 & 0 & 0 & 1 \end{pmatrix} \begin{pmatrix} r_{11} & r_{12} & r_{13} & 0 \\ r_{21} & r_{22} & r_{23} & 0 \\ r_{31} & r_{32} & r_{33} & 0 \\ 0 & 0 & 0 & 1 \end{pmatrix} \end{aligned} \tag{2.10}$$

As Eq. (2.10) shows that the order of transformation is done by performing a pure rotation followed by a pure translation. The product of the matrices is not interchangeable

$${}^A T_B = {}^A D_B \, {}^A R_B \neq {}^A R_B \, {}^A D_B. \tag{2.11}$$

Corollary of the decomposition rule, the homogeneous transformation matrix can be modified to function as a pure translation matrix

$$ {}^{A}T_{B} = {}^{A}D_{B} = \begin{pmatrix} 1 & 0 & 0 & d_x \\ 0 & 1 & 0 & d_y \\ 0 & 0 & 1 & d_z \\ 0 & 0 & 0 & 1 \end{pmatrix} \tag{2.12} $$

or a pure rotation matrix

$$ {}^{A}T_{B} = {}^{A}R_{B} = \begin{pmatrix} r_{11} & r_{12} & r_{13} & 0 \\ r_{21} & r_{22} & r_{23} & 0 \\ r_{31} & r_{32} & r_{33} & 0 \\ 0 & 0 & 0 & 1 \end{pmatrix} \tag{2.13} $$

2. Inverse Homogeneous Transformation Matrix

Given the homogeneous transformation matrix from a frame B to a frame A

$$ {}^{A}T_{B} = \begin{pmatrix} {}^{A}R_{B} & {}^{A}\mathbf{d}_{B} \\ \mathbf{0} & 1 \end{pmatrix} \tag{2.14} $$

the homogeneous transformation matrix from the frame A to the frame B can be obtained by inversing the matrix ${}^{A}T_{B}$

$$ {}^{B}T_{A} = {}^{A}T_{B}^{-1} = \begin{pmatrix} {}^{A}R_{B} & {}^{A}\mathbf{d}_{B} \\ \mathbf{0} & 1 \end{pmatrix}^{-1} = \begin{pmatrix} {}^{A}R_{B}^{T} & -{}^{A}R_{B}^{T}{}^{A}\mathbf{d}_{B} \\ \mathbf{0} & 1 \end{pmatrix} \tag{2.15} $$

Unlike rotation matrix in orthogonal frames, the homogeneous transformation matrix is not orthogonal; hence, its inverse is not equal to its transpose

$$ {}^{A}T_{B}^{-1} \neq {}^{A}T_{B}^{T}. \tag{2.16} $$

3. Compound Homogeneous Transformation Matrix

Transforming body coordinates between more than two frames can be done with successive homogeneous transformation matrices. For example, if the homogeneous transformation matrix from frame A to frame B, and another transformation matrix to from frame B to frame C are

$$ {}^{B}T_{A} = \begin{pmatrix} {}^{B}R_{A} & {}^{B}\mathbf{d}_{A} \\ \mathbf{0} & 1 \end{pmatrix} \qquad {}^{C}T_{B} = \begin{pmatrix} {}^{C}R_{B} & {}^{C}\mathbf{d}_{B} \\ \mathbf{0} & 1 \end{pmatrix} \tag{2.17} $$

then transformation of body coordinates from frame A to frame C can be completed with a single homogeneous transformation matrix by multiplying ${}^{B}T_{A}$ and ${}^{C}T_{B}$ in order

$$ {}^{C}T_{A} = {}^{C}T_{B}\,{}^{B}T_{A} \tag{2.18} $$

2.6 Coordinate Frames and Transformation

The primary objective of tracking is to rotate the collector panel such that its normal vector $\hat{\mathbf{n}}$ is along the resultant light vector. The three main components in our tracking system—the light source(s), the tracking collector panel, and the body that is carrying the tracker—are more conveniently defined with each respective reference frame. For example, the Sun movement can be modeled in an Earth-centered frame, while the orientation of the collector panel is more appropriately defined with a reference frame that is centered on its rotation axes. The coordinate frames pertaining to these components need to be defined and transformation matrix is required to transfer geometrical and kinematical information between the frames.

2.6.1 Earth-Centered Frame E

The Sun vector for solar tracking purposes is most conveniently defined in the Earth-centered frame. Its position vector can be defined in the Earth-centered frame E as a 3-by-1 vector as

$$^{E}\mathbf{S} = \begin{pmatrix} \cos\delta\cos\omega \\ -\cos\delta\sin\omega \\ \sin\delta \end{pmatrix} \tag{2.19}$$

where δ is the declination angle and ω is the hour angle in the Earth-centered coordinate frame.

2.6.2 Earth-Surface Frame S

To make the $\mathbf{S}$-vector useful, a transformation from the Earth-centered frame E to the Earth-surface is required. To do this, a frame S is attached at a point O_S on the Earth surface with a distance R_0 from the center of the Earth. The x_S-axis is always oriented towards North, the y_S-axis points West, and the z_S is defined as the zenith axis. The origin of the frame O_S is located at a longitude ϕ and latitude λ. The distance vector $^{S}\mathbf{d}$ is then expressed as

$$^{S}\mathbf{d} = \begin{pmatrix} 0 \\ 0 \\ R_0 \end{pmatrix} \tag{2.20}$$

and the rotation matrix from the E-frame to the S-frame is

$$^{S}R_{E} = R_{z,\pi}R_{y,\pi/2-\lambda}R_{z,\phi} = \begin{pmatrix} -\cos\phi\sin\lambda & -\sin\phi\sin\lambda & \cos\lambda \\ \sin\phi & -\cos\phi & 0 \\ \cos\phi\cos\lambda & \sin\phi\cos\lambda & \sin\lambda \end{pmatrix} \tag{2.21}$$

Therefore, the transformation matrix from the Earth-centered E-frame and to the Earth-surface S-frame, therefore, is expressed as

$$^{S}T_{E} = \begin{pmatrix} ^{S}R_{E} & ^{S}\mathbf{d} \\ 0 & 1 \end{pmatrix} = \begin{pmatrix} -\cos\phi\sin\lambda & -\sin\phi\sin\lambda & \cos\lambda & 0 \\ \sin\phi & -\cos\phi & 0 & 0 \\ \cos\phi\cos\lambda & \sin\phi\cos\lambda & \sin\lambda & R_0 \\ 0 & 0 & 0 & 1 \end{pmatrix} \tag{2.22}$$

Now, the 4-by-1 Sun vector can be expressed in the Earth-surface frame S as

$$^{S}\mathbf{S} = {}^{S}T_{E}{}^{E}\mathbf{S} \tag{2.23}$$

The distance $^{S}\mathbf{d}$ can be assumed to be zero for Sun-tracking purpose. However, the formula here is treated generally to include satellite tracking where the relative distance of the satellite with the center of the Earth and the tracker's position are important. For solar tracking purpose, R_0 can be considered as zero.

2.6.3 Collector-Centered Frame C

The coordinate frame for the collector panel is shown in Fig. 2.7. The collector is assumed to have an arbitrary orientation with respect to the surface of the Earth. It is assumed also that the distance between the origin of the collector-centered C-frame O_C and the origin of the Earth-surface S-frame O_S is negligible; hence, their origins are coincident. The z_C-axis is defined along the direction of the normal of the collector plane, and the x_C–y_C plane is defined as the panel's surface plane. Initially, it is assumed that the orientation of the C-frame is parallel to the Earth-surface S-frame.

1. Tip-Roll Dual Axis Tracker

To point the normal of the collector panel to the light vector, the C-frame is turned from a coincident orientation with the S-frame about the y_C-axis (primary axis for the tip-tilt configuration) by $-\alpha$ degrees and then it is turned about the x_C-axis (secondary axis for the tip-roll configuration) by $-\beta$ degrees. Since both

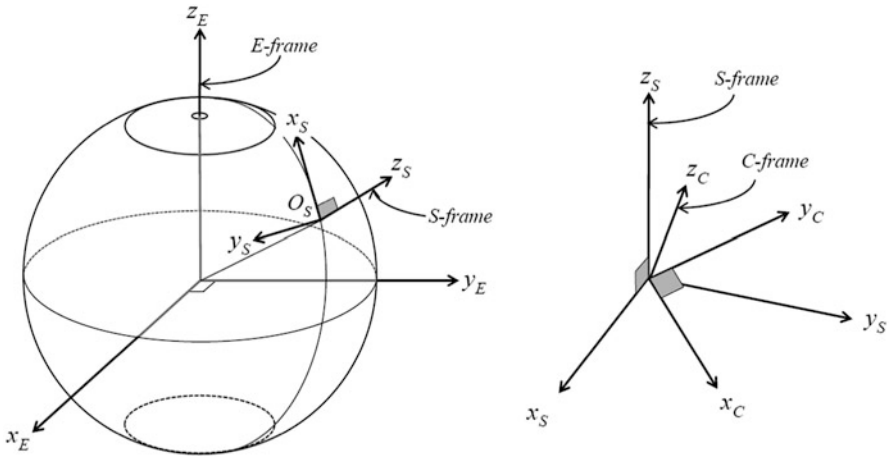

Fig. 2.7 Orientation of the panel-fixed C-frame with respect to the Earth-surface S-frame and the Earth-centered E-frame for a ground-fixed tracker

frames share the same origin, only rotation matrix is required to transform from the S-frame to the C-frame:

$$
\begin{aligned}
{}^{C}R_S = R_{x,-\beta}R_{y,-\alpha} &= \begin{pmatrix} 1 & 0 & 0 \\ 0 & \cos\beta & -\sin\beta \\ 0 & \sin\beta & \cos\beta \end{pmatrix} \begin{pmatrix} \cos\alpha & 0 & \sin\alpha \\ 0 & 1 & 0 \\ -\sin\alpha & 0 & \cos\alpha \end{pmatrix} \\
&= \begin{pmatrix} \cos\alpha & 0 & \sin\alpha \\ \sin\beta\sin\alpha & \cos\beta & -\sin\beta\cos\alpha \\ -\cos\beta\sin\alpha & \sin\beta & \cos\beta\cos\alpha \end{pmatrix}
\end{aligned} \tag{2.24}
$$

Therefore the transformation matrix for a ground-fixed, tip-roll dual axis tracker becomes

$$
{}^{C}T_S = \begin{pmatrix} \cos\alpha & 0 & \sin\alpha & 0 \\ \sin\beta\sin\alpha & \cos\beta & -\sin\beta\cos\alpha & 0 \\ -\cos\beta\sin\alpha & \sin\beta & \cos\beta\cos\alpha & 0 \\ 0 & 0 & 0 & 1 \end{pmatrix} \tag{2.25}
$$

2. Azimuth-Elevation Dual Axis Tracker

For azimuth-elevation configuration, the C-frame is turned from a coincident orientation with the S-frame about its primary z_C-axis by $-\alpha$ degrees, and then about its secondary x_C-axis by $-\beta$ degrees. The rotation matrix is required to transform from the S-frame to the C-frame in the azimuth-elevation configuration

$$
{}^{C}R_S = R_{x,-\beta}R_{z,-\alpha} = \begin{pmatrix} 1 & 0 & 0 \\ 0 & \cos\beta & -\sin\beta \\ 0 & \sin\beta & \cos\beta \end{pmatrix} \begin{pmatrix} \cos\alpha & -\sin\alpha & 0 \\ \sin\alpha & \cos\alpha & 0 \\ 0 & 0 & 1 \end{pmatrix}
$$

$$
= \begin{pmatrix} \cos\alpha & -\sin\alpha & 0 \\ \cos\beta\sin\alpha & \cos\beta\cos\alpha & -\sin\beta \\ \sin\beta\sin\alpha & \sin\beta\cos\alpha & \cos\beta \end{pmatrix} \tag{2.26}
$$

Therefore the transformation matrix for a ground-fixed, azimuth-elevation dual axis tracker becomes

$$
{}^{C}T_S = \begin{pmatrix} \cos\alpha & -\sin\alpha & 0 & 0 \\ \cos\beta\sin\alpha & \cos\beta\cos\alpha & -\sin\beta & 0 \\ \sin\beta\sin\alpha & \sin\beta\cos\alpha & \cos\beta & 0 \\ 0 & 0 & 0 & 1 \end{pmatrix} \tag{2.27}
$$

The rotation matrices for a tilt-roll and an azimuth-elevation configurations are presented here. For any other dual axis tracker configuration, Appendix provides the list of local frame rotation matrices to transform the coordinates from the Earth-surface frame S to the collector panel frame C.

2.6.4 Moving Platform Body Frame B

In case of mobile trackers where the tracker is installed on a moving platform such as a vehicle, or a robot, another body-fixed frame needs to be defined to take into account the translational and rotational motions of the platform. Its origin O_B is assumed to coincide with the origin of the collector-centered C-frame. The distance of the shared origin from the Earth-surface fixed reference point O_S is described by a vector ${}^{B}\mathbf{d}$

$$
{}^{S}\mathbf{d} = \begin{pmatrix} d_x \\ d_y \\ 0 \\ 1 \end{pmatrix} \tag{2.28}
$$

as it is moving on the x–y plane only. Figure 2.8 illustrates the coordinate frames. Assuming the movement of the platform is much less than the radius of the Earth, the platform can be considered as translationally static while tracking the Sun. For the case of artificial light tracking, the distance of the collector to the sources of light is important. For Sun-tracking purpose, the distance vector ${}^{B}\mathbf{d}$ can practically be considered zero.

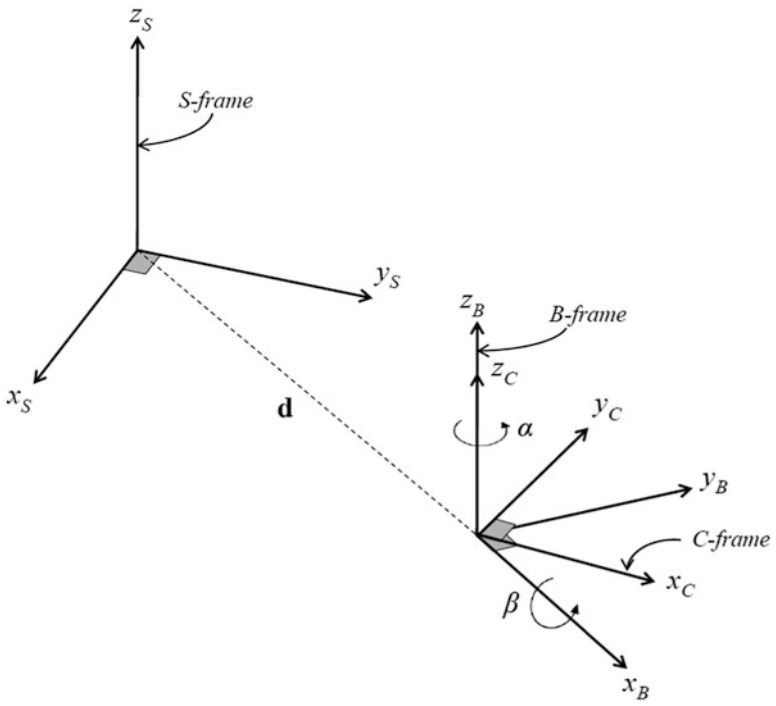

Fig. 2.8 Orientation of the platform-fixed B-frame and the panel-fixed C-frame with respect to the Earth-surface S-frame for a mobile tracker

The B-frame's orientation is assumed to be parallel to the orientation of the Earth-surface S-frame initially with its x_B-axis pointing North, the y_B-axis pointing West, and the z_B-axis in the zenith direction. The platform body frame B rotates about its z_B-axis by γ degrees. Thus, its transformation matrix is expressed as

$$
{}^{B}T_S = \begin{pmatrix} {}^{B}R_S & {}^{B}\mathbf{d} \\ 0 \quad 0 & 1 \end{pmatrix} = \begin{pmatrix} \cos\gamma & \sin\gamma & 0 & d_x \\ -\sin\gamma & \cos\gamma & 0 & d_y \\ 0 & 0 & 1 & 0 \\ 0 & 0 & 0 & 1 \end{pmatrix} \tag{2.29}
$$

Therefore, for a collector-frame C in B in tip-roll configuration, the transformation matrix from S-frame to C-frame becomes

$$
\begin{aligned}
{}^{C}T_S &= {}^{C}T_B\,{}^{B}T_S \\
&= \begin{pmatrix} c\alpha c\gamma & c\alpha s\gamma & s\alpha & d_x \\ s\beta\, s\alpha\, c\gamma - c\beta\, s\gamma & s\beta\, s\alpha\, s\gamma + c\beta\, c\gamma & -s\beta\, c\alpha & d_y \\ -s\alpha\, c\beta\, c\gamma - s\beta\, s\gamma & -s\alpha\, c\beta\, s\alpha + s\beta\, c\gamma & c\beta\, c\alpha & 0 \\ 0 & 0 & 0 & 1 \end{pmatrix}
\end{aligned} \tag{2.30}
$$

For azimuth-elevation configuration, the transformation matrix from S-frame to C-frame is

$$
\begin{aligned}
{}^{C}T_{S} &= {}^{C}T_{B}\,{}^{B}T_{S} \\
&= \begin{pmatrix} \cos\alpha + \gamma & -\sin\alpha + \gamma & 0 & d_x \\ \cos\beta\sin\alpha + \gamma & \cos\beta\cos\alpha + \gamma & -\sin\beta & d_y \\ \sin\beta\sin\alpha + \gamma & \sin\beta\cos\alpha + \gamma & \cos\beta & 0 \\ 0 & 0 & 0 & 1 \end{pmatrix}
\end{aligned} \tag{2.31}
$$

2.7 Example

A mobile robot carrying photovoltaic panels is moving across the floor of an indoor environment which is lit by several artificial lights attached on the ceiling. The panels orientation is controlled by a light-tracking that points the direction of the brightest illuminance. As the photovoltaic panel is translating across the room, the tracker has to actively find the brightest illuminance based on its relative position with respect to the light sources.

2.7.1 Trajectory Constraint

The indoor environment is assumed to be a room of 20 m in length and 10 m in width, with the height of a standard office room's ceiling which is approximately 2.5 m. Six light emitters modelled as point sources are positioned uniformly as shown in Fig. 2.9.

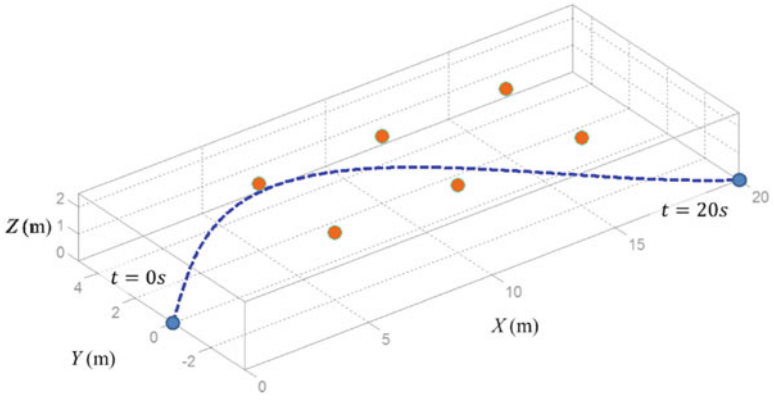

Fig. 2.9 An indoor environment with six ceiling-fixed light emitters and the path for the mobile tracker. The duration from the starting to the end point is 20 s

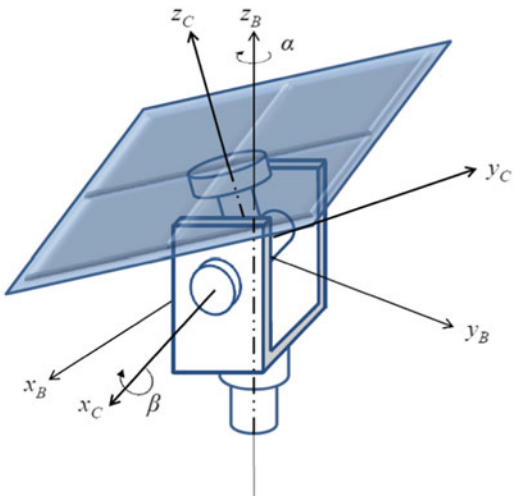

Fig. 2.10 Dual-axis light tracker configuration used in this example

To illustrate the light-tracking motion and the requirement for the directional control system, a path for the vehicle is defined a priori. The vehicle is to follow the path at a constant speed while maintaining its direction parallel to the tangent of the path line.

2.7.2 Dual-Axis Tracker

A conceptual illustration of the dual-axis tracking system is shown in Fig. 2.10. The mechanism is similar to an azimuth-altitude solar tracker which has its primary axis vertical to the local, body-frame of the vehicle which is called the azimuth or the yaw axis, and a secondary axis normal to the primary axis which is referred to as the elevation or the pitch axis. These two axes intersect at the wrist point. The orientation of the face of the panel is directed by two independent rotary actuators which control the yaw angle α and the pitch angle β. The amount of angular displacements and velocities depends on the panel's relative position with respect to the light emitters and the speed of the vehicle.

2.7.3 Reference Frames

We define a global reference frame G that is attached at a fixed reference point in the room with its X–Y plane describing the floor and the Z-axis pointing towards the ceiling. The positions of the light emitters and the mobile robot will be referred to this reference frame. A body-fixed frame, B, is attached to the vehicle which is moving in the G-frame. The light vectors are calculated in the B-frame in terms of

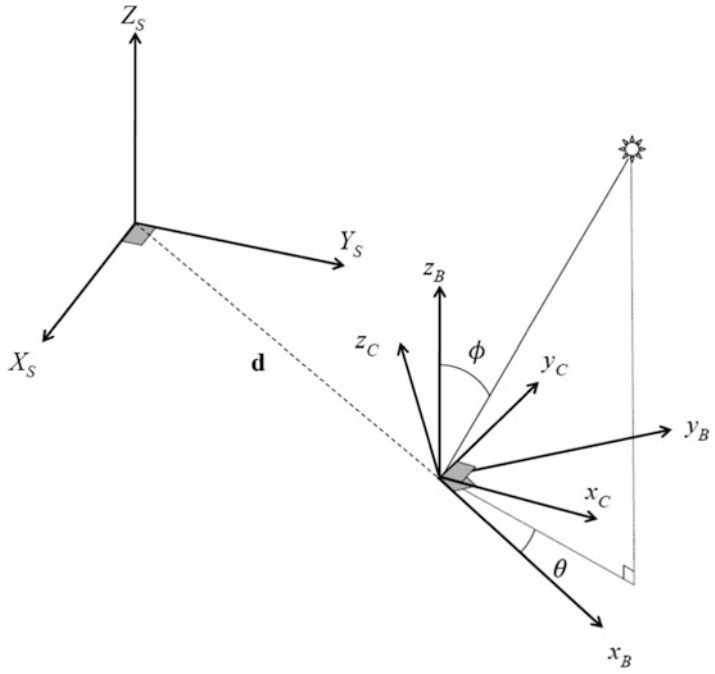

Fig. 2.11 Reference frames association for a mobile light-tracker. The vehicle body-fixed B-frame has a translation distance of d and a rotation angle of γ about the global Z-axis. The collector panel-fixed C-frame shares the same origin as the B-frame

azimuth angle θ and elevation angle ϕ, which would define their angles of incidence on the vehicle. Another body-frame C is attached to the mobile robot, sharing the same origin with B and follows the orientation of the vehicle, which is denoted by the angle γ about the z_B-axis. The input angles for both axes of the tracker are defined in this reference frame based on the azimuth and elevation angles expressed in B. These reference frames are depicted in Fig. 2.11.

The problem can be stated as the following: given the vehicle's position and its orientation with respect to a fixed, global reference frame, what are the angular displacements needed by the rotary actuators of the tracker to orient the photovoltaic panel to the direction of the brightest illuminance from an arbitrary panel orientation?

2.7.4 Computing the Illuminance Received by Collector Panel

Equation (2.4) is used as the basis in computing the illuminance received by the collector panel on the moving robot. The light intensity I_i of each source is assumed to be of a unit magnitude. Since the collector panel is moving, the illuminance received E is dependent on the position (distance) and the angle of incident of the

light sources with respect to the collector panel orientation. The position of the ith source at time t is recorded as $\mathbf{r}_i(t)$ and the pointing direction of the panel is recorded as $\mathbf{n}(t)$.

A step-by-step procedure for the algorithm is detailed as below:

1. Define the position vector of the light source in its natural frame (Earth-centered frame E for Sun tracking and the Earth-surface frame S for ground-fixed artificial light sources). For example, the position of an artificial light in an indoor environment is defined as a vector $\mathbf{r}$ in $G({}^{G}\mathbf{r})$

$$ {}^{G}\mathbf{r} = \text{position vector of light source as seen in } G \tag{2.32}$$

2. The body carrying the collector panel is assumed to be translating across the room on a prescribed path. To find the light position with respect to the body at a particular position in the G-frame, transform the vector $\mathbf{r}$ in the body-fixed frame B using the homogeneous transformation matrix ${}^{B}T_{G}$

$$ {}^{B}\mathbf{r} = {}^{B}T_{G}\,{}^{G}\mathbf{r} \tag{2.33}$$

3. Assuming the collector-centered frame C is different from the B-frame, another transformation is done to express the vector $\mathbf{r}$ in the C-frame

$$ {}^{C}\mathbf{r} = {}^{C}T_{B}\,{}^{B}\mathbf{r} = {}^{C}T_{B}\,{}^{B}T_{G}\,{}^{G}\mathbf{r} \tag{2.34}$$

4. The vector ${}^{C}\mathbf{r}$ is expressed in the Cartesian coordinates (x, y, z). The vector is transformed into spherical coordinates (r, θ, ϕ)

$$ {}^{C}\mathbf{r} = \begin{pmatrix} x \\ y \\ z \end{pmatrix} \rightarrow \begin{pmatrix} r \\ \theta \\ \phi \end{pmatrix} \tag{2.35}$$

5. Define the pointing direction of the collector panel n in terms of a unit vector in spherical coordinates to reduce the variables from the Cartesian coordinates x, y, and z to two angle variables as only the direction of the panel is concerned. As the distance is not of importance, the radial distance can be defined as 1

$$ \hat{\mathbf{n}} = \begin{pmatrix} 1 \\ \alpha \\ \beta \end{pmatrix} \tag{2.36}$$

6. To find the optimum orientation n that would receive the most illumination from the light source, Eq. (2.4) is used. Since the variables in this equation are α (yaw angle) and β (pitch angle) only, a $3D$ plot of illuminance E vs. α vs. β can be used to find the best $[\alpha^* \beta^*]$ pair that gives the largest E value:

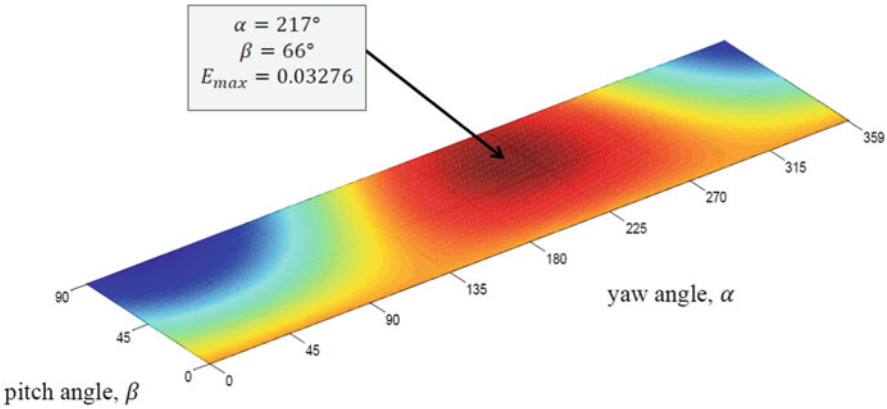

Fig. 2.12 A three-dimensional plot of illuminance, E vs. azimuth angle, α vs. pitch angle, β. For Example 1, the collector panel receives the brightest illuminance at the instance $t = 9$ s when its azimuth angle is 277° and its pitch angle is 66°

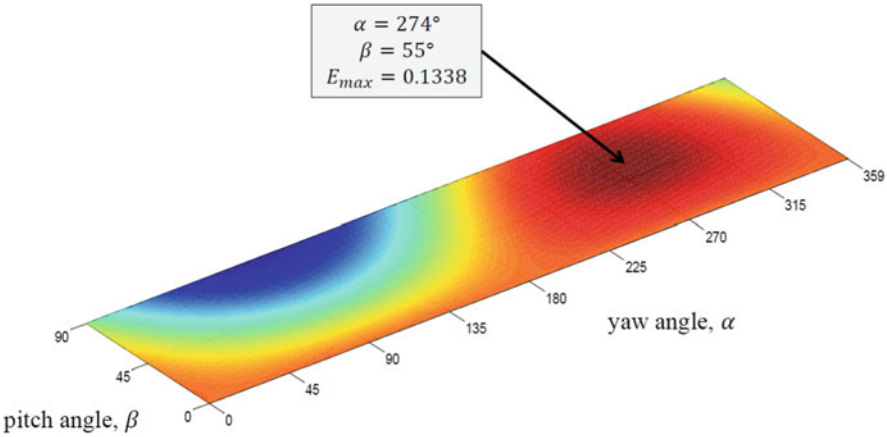

Fig. 2.13 A three-dimensional plot of illuminance, E vs. azimuth angle, α vs. pitch angle, β. For Example 2, the collector panel receives the brightest illuminance at the instance $t = 9$ s when its azimuth angle is 274° and its pitch angle is 55°

$$E = \sum_{i}^{n} \frac{1}{r_i^2} {}^{C}\hat{\mathbf{n}} \cdot {}^{C}\hat{\mathbf{r}}_i$$

Note that E is just a quantification of the intensity of the light received, not illumination in photometric. Examples of the 3D plot are shown in Figs. 2.12 and 2.13.

7. These steps are repeated for each new point in the prescribed path and the history of $[\alpha^* \beta^*]$ is recorded for every point.

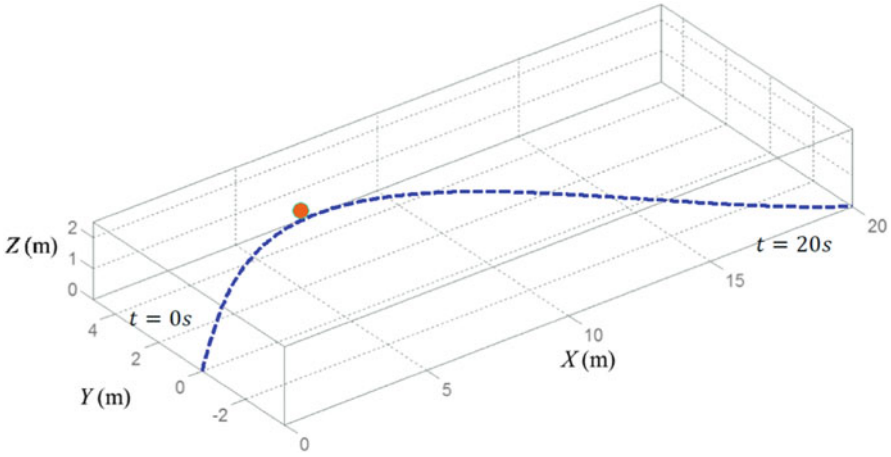

Fig. 2.14 An indoor environment with a ceiling-fixed light emitter and the path for the mobile tracker. The duration from the starting to the end point is 20 s

2.7.5 *Example 1*

Let us consider a simple problem where the room is lit by one artificial light at point ${}^{G}L = \begin{bmatrix} 5.0 & 2.0 & 2.5 \end{bmatrix}^{T}$ as shown in Fig. 2.14. To use this information and to transform the light vector ${}^{G}L$ to the collector panel frame, we need to perform three coordinate transformations: from the G-frame (${}^{G}L$) to the vehicle's B-frame (${}^{B}L$) to the collector panel's C-frame (${}^{C}L$). Following Eq. (2.31), the homogeneous transformation matrix can be expressed as

$$
\begin{aligned}
{}^{C}L &= {}^{C}T_{B}\,{}^{B}T_{G}\,{}^{G}T\,{}^{G}L \\
&= \begin{pmatrix} \cos\alpha + \gamma & -\sin\alpha + \gamma & 0 & X \\ \cos\beta\sin\alpha + \gamma & \cos\beta\cos\alpha + \gamma & -\sin\beta & Y \\ \sin\beta\sin\alpha + \gamma & \sin\beta\cos\alpha + \gamma & \cos\beta & 0 \\ 0 & 0 & 0 & 1 \end{pmatrix} \begin{pmatrix} 5.0 \\ 2.0 \\ 2.5 \\ 1 \end{pmatrix}
\end{aligned} \tag{2.37}
$$

where $d_x(t)$ and $d_y(t)$ are the positions of the vehicle in the G-frame, as shown in Fig. 2.15, and $\gamma(t)$ is the vehicle's orientation with respect to the G-frame, as shown in Fig. 2.16. These quantities are known as the vehicle's path is prescribed.

The time histories of the yaw angle $\alpha(t)$ and the pitch angle $\beta(t)$ for the tracker under a single artificial light are shown in Figs. 2.17 and 2.18. Figure 2.12 shows an example of illuminance received by the collector panel as a function of yaw angle and pitch angle at time $t = 9$ s. As shown in Fig. 2.19, the illuminance received by a dual-axis tracker is significantly higher compared to a non-tracking, zenith-fixed collector panel.

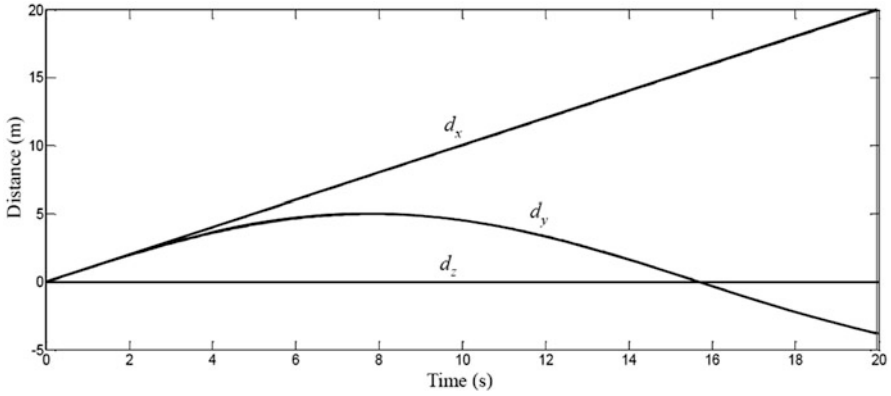

Fig. 2.15 Position of the mobile tracker with respect to the global frame in x, y, and z-direction over time

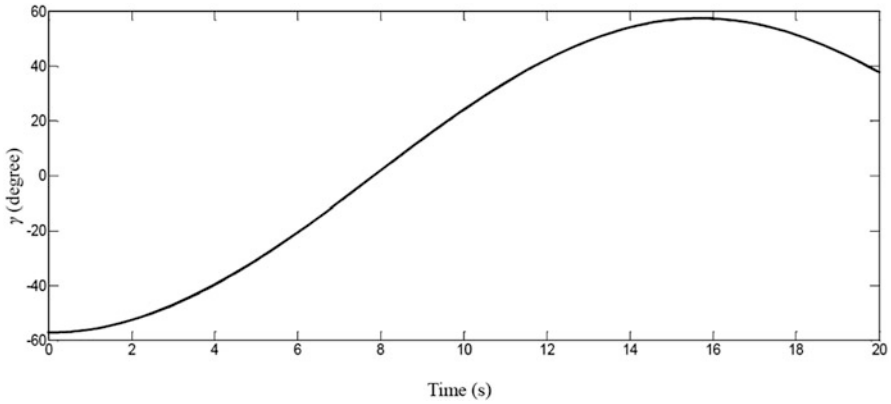

Fig. 2.16 Orientation of the mobile tracker with respect to the global frame γ (degree) vs. time (second)

2.7.6 Example 2

We assume the tracker is equipped on a moving vehicle under multiple lighting as shown in Fig. 2.9. The positions of the six lights are:

$$
\begin{aligned}
{}^{G}L_1 &= \begin{bmatrix} 5.0 & 2.0 & 2.5 \end{bmatrix}^T \\
{}^{G}L_2 &= \begin{bmatrix} [5.0 & 2.0 & 2.5 \end{bmatrix}^T \\
{}^{G}L_3 &= \begin{bmatrix} [10 & 2.0 & 2.5 \end{bmatrix}^T \\
{}^{G}L_4 &= \begin{bmatrix} 10 & -2 & 2.5 \end{bmatrix}^T
\end{aligned}
$$

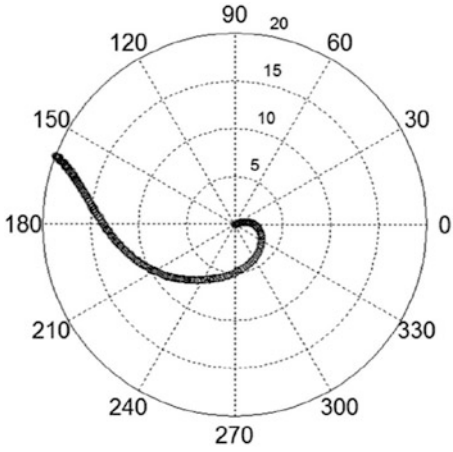

Fig. 2.17 Yaw angle α (degree) vs. time (second) for the single light emitter case

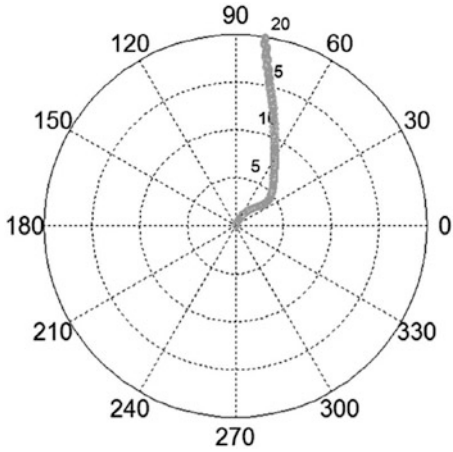

Fig. 2.18 Pitch angle β (degree) vs. time (second) for the single light emitter case

$$^{G}L_5 = \begin{bmatrix} 10 & 2 & 2.5 \end{bmatrix}^T$$

$$^{G}L_6 = \begin{bmatrix} 15 & -2 & 2.5 \end{bmatrix}^T$$

As the vehicle is moving across the room, the light intensity received by the collector panel is varying; therefore, the panel's orientation cannot be a function of the fixed positions of the lights. At each discrete point of the vehicle's path, **d**, each light position is calculated and the direction of the brightest illumination is denoted by $\hat{\mathbf{n}}(t)$ which maximizes Eq. (2.4)

$$max\ E_r(t) = \sum_{i}^{n} \frac{1}{r_i^2(t)} \hat{\mathbf{n}}(t) \cdot \hat{\mathbf{r}}_i(t) \tag{2.38}$$

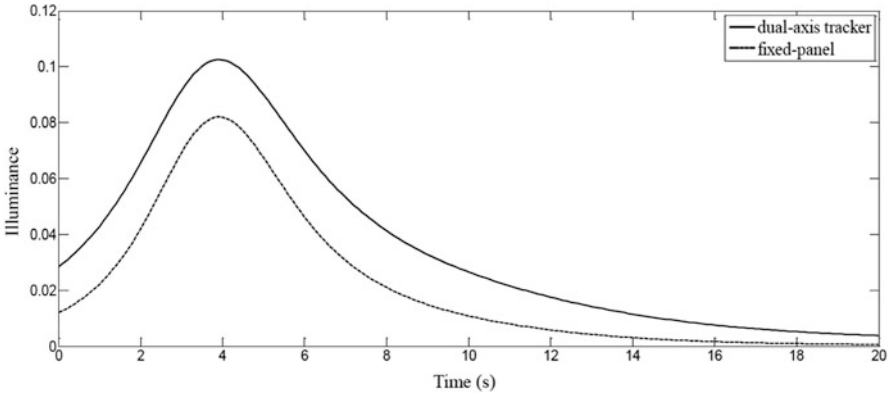

Fig. 2.19 Comparison of the brightness (illumination) received for a fixed panel and a tracking panel for the single light emitter case

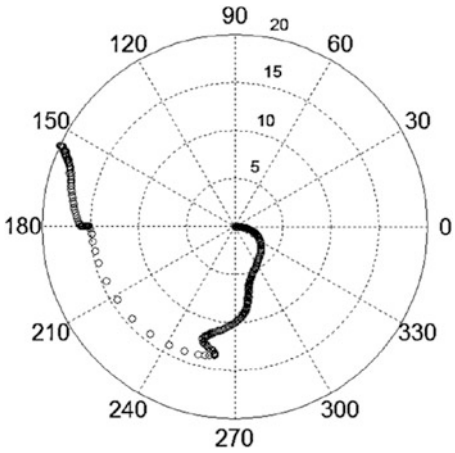

Fig. 2.20 Yaw angle α (degree) vs. time (second) for the multiple light emitters case

Prior to finding the vector $\hat{\mathbf{n}}(t)$ (Step 5), each light vector ${}^{G}\mathbf{r}_i$ needs to be rotated to the collector panel's frame C

$$
\begin{aligned}
{}^{C}\mathbf{r}_i &= {}^{C}T_B\,{}^{B}T_G\,{}^{G}T\,{}^{G}\mathbf{r}_i \\
&= \begin{pmatrix} \cos\alpha+\gamma & -\sin\alpha+\gamma & 0 & 0 \\ \cos\beta\sin\alpha+\gamma & \cos\beta\cos\alpha+\gamma & -\sin\beta & 0 \\ \sin\beta\sin\alpha+\gamma & \sin\beta\cos\alpha+\gamma & \cos\beta & 0 \\ 0 & 0 & 0 & 1 \end{pmatrix} {}^{G}\mathbf{r}_i
\end{aligned} \tag{2.39}
$$

where $d_x(t)$ and $d_y(t)$ are the known positions of the vehicle in the G-frame (Fig. 2.15), and $\gamma(t)$ is the vehicle's orientation with respect to the G-frame (Fig. 2.16).

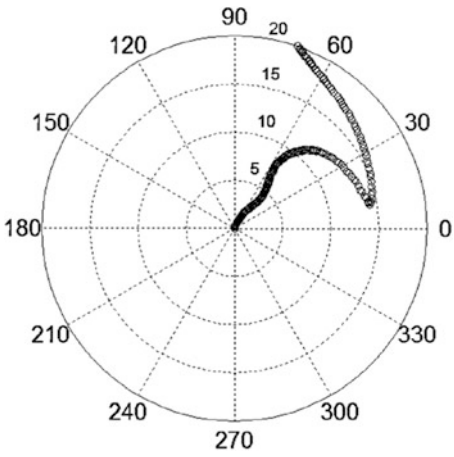

Fig. 2.21 Pitch angle β (degree) vs. time (second) for the multiple light emitters case

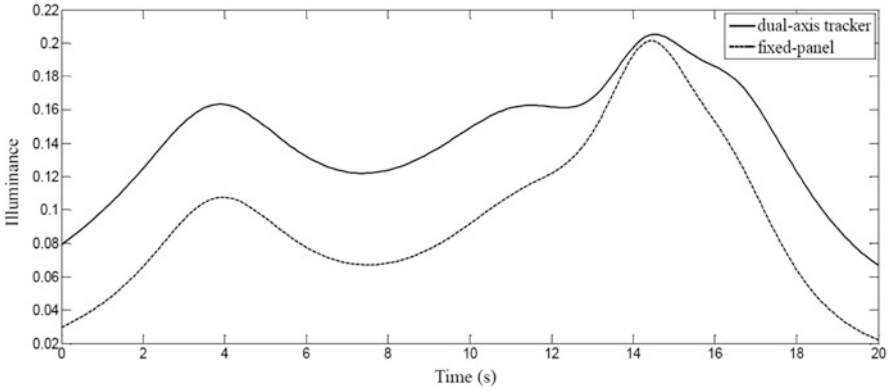

Fig. 2.22 Comparison of the brightness (illumination) received for a fixed panel and a tracking panel for the multiple light emitters case

The time histories of the yaw angle α and the pitch angle β for the tracker under multiple lights condition are shown in Figs. 2.20 and 2.21. Figure 2.13 shows an example of illuminance received by the collector panel as a function of yaw angle and pitch angle at time $t = 9$ s. Figure 2.22 shows that the dual-axis tracker collects significantly more illuminance in the multi-light environment compared to a fixed-panel.

2.8 Conclusions

The general light-tracking formula for generating power from radiation has been derived using compound homogeneous transformation method. The newly derived formula is more general mathematical solution for any dual-axis light tracker

as it can be applied to trackers on mobile platforms such as rovers and robots. The formula can also be employed on any conventional Sun-trackers and for indoor environment implementing orientatable photovoltaic modules. The formula, however, is limited for platforms moving on a smooth, two-dimensional plane.

The following suggestions may be included in the future studies of tracking system:

1. A three-dimensional translation motion for the mobile platform for the application of rovers in an uneven terrain. The derivation of the formula must take into account the pitching and rolling motion of the vehicle itself to orient its photovoltaic panels towards the radiance source.
2. Calculation of the light vector from extraterrestrial objects, such as Mars or Jupiter, for the application of a lunar rovers.
3. Sun-tracking formula as a function of Earth orbit elements for spacecraft application.

Appendix: Local Frame Double Rotation

The collector panel frame rotation matrices about local axes is presented in this appendix. The rotation matrix can be used for any six combination of primary and secondary axes to transform coordinates from the Earth-surface frame (global frame) to the collector panel frame (local frame). The angle about the primary axis is denoted by α and the angle about the secondary axis is denoted by β.

1. Primary: x-axis Secondary: y-axis

$$R_{y,-\beta} R_{x,-\alpha} = \begin{pmatrix} \cos\beta & \sin\alpha \sin\beta & \cos\alpha \sin\beta \\ 0 & \cos\alpha & -\sin\alpha \\ -\sin\beta & \cos\beta \sin\alpha & \cos\alpha \cos\beta \end{pmatrix} \tag{2.40}$$

2. Primary: x-axis Secondary: z-axis

$$R_{z,-\beta} R_{x,-\alpha} = \begin{pmatrix} \cos\beta & -\cos\alpha \sin\beta & \sin\alpha \sin\beta \\ \sin\beta & \cos\alpha \cos\beta & -\cos\beta \sin\alpha \\ 0 & \sin\alpha & \cos\alpha \end{pmatrix} \tag{2.41}$$

3. Primary: y-axis Secondary: x-axis (tip-tilt configuration)

$$R_{x,-\beta} R_{y,-\alpha} = \begin{pmatrix} \cos\alpha & 0 & \sin\alpha \\ \sin\alpha \sin\beta & \cos\beta & -\cos\alpha \sin\beta \\ -\cos\beta \sin\alpha & \sin\beta & \cos\alpha \cos\beta \end{pmatrix} \tag{2.42}$$

4. Primary: y-axis Secondary: z-axis

$$R_{z,-\beta}R_{y,-\alpha} = \begin{pmatrix} \cos\alpha\cos\beta & -\sin\beta & \sin\alpha\cos\beta \\ \cos\alpha\sin\beta & \cos\beta & \sin\alpha\sin\beta \\ -\sin\alpha & 0 & \cos\alpha \end{pmatrix} \tag{2.43}$$

5. Primary: z-axis Secondary: x-axis (azimuth-elevation configuration)

$$R_{x,-\beta}R_{z,-\alpha} = \begin{pmatrix} \cos\alpha & -\sin\alpha & 0 \\ \cos\beta\sin\alpha & \cos\alpha\cos\beta & -\sin\beta \\ \sin\alpha\sin\beta & \cos\alpha\sin\beta & \cos\beta \end{pmatrix} \tag{2.44}$$

6. Primary: z-axis Secondary: y-axis

$$R_{y,-\beta}R_{z,-\alpha} = \begin{pmatrix} \cos\alpha\cos\beta & -\cos\beta\sin\alpha & \sin\beta \\ \sin\alpha & \cos\alpha & 0 \\ -\cos\alpha\sin\beta & \sin\alpha\sin\beta & \cos\beta \end{pmatrix} \tag{2.45}$$

Key Symbols

d	Translation scalar
$\mathbf{d}$	Translation vector
d_i	Element i of $\mathbf{d}$
D	Homogeneous translation matrix
${}^{A}D_{B}$	Homogeneous translation matrix from B-frame to A-frame
E	Total illumination
E_r	Distance-dependant illuminance
E_φ	Incident angle-dependant illuminance
I, I_i	Light intensity
$\hat{\mathbf{n}}$	Normal unit vector to the collector
O	Origin point of a coordinate frame
r	Distance between target and source of light, position scalar
$\mathbf{r}$	Position vector
r_i	Element i of $\mathbf{r}$
r_{ij}	Element of row i and column j of matrix R
${}^{A}\mathbf{r}$	Vector $\mathbf{r}$ expressed in A-frame
$\hat{\mathbf{r}}$	Direction of light ray with respect to the collector
r, θ, ϕ	Local spherical coordinates
R	Rotation transformation matrix

${}^{A}R_{B}$	Rotation transformation matrix from B-frame to A-frame
$R_{x,\alpha}$	Rotation transformation about x-axis with α angle
$\mathbf{S}$	Sun vector
T	Homogeneous transformation matrix
${}^{A}T_{B}$	Homogeneous transformation matrix from B-frame to A-frame
x, y, z	Local coordinate axes
X, Y, Z	Global coordinate axes

α	Yaw angle
β	Pitch angle
γ	Orientation of the vehicle body-frame with respect to the global frame
θ	Azimuth angle
ϕ	Elevation angle
φ	Angle of incidence

References

1. Bretagnon P, Francou G (1988) Planetary theories in rectangular and spherical variables—vsop87 solutions. Astron Astrophys 202(1–2):309–315
2. Chen Y, Chong K, Bligh T, Chen L, Yunus J, Kannan K, Lim B, Lim C, Alias M, Bidin N, Aliman O, Salehan S, Shk. Abd. Rezan SAH, Tam C, Tan K (2001) Non-imaging, focusing heliostat. Sol Energy 71(3):155–164
3. Chen Y, Lim B, Lim C (2006) General sun tracking formula for heliostats with arbitrarily oriented axes. J Sol Energy Eng Trans ASME 128(2):245–250
4. Chong K, Wong C (2009) General formula for on-axis sun-tracking system and its application in improving tracking accuracy of solar collector. Sol Energy 83(3):298–305
5. Jazar RN (2010) Theory of applied robotics: kinematics, dynamics, and control. Springer, New York
6. Jazar RN (2011) Advanced dynamics: rigid body, multibody and aerospace applications. Wiley, Hoboken
7. Legnani G, Casolo F, Righettini P, Zappa B (1996) A homogeneous matrix approach to 3D kinematics and dynamics I. Mech Mach Theory 31(5):573–587
8. Lever J, Ray L (2008) Revised solar-power budget for cool robot polar science campaigns. Cold Regions Sci Technol 52(2):177–190
9. Parkin RE (2010) Solar angles revisited using a general vector approach. Sol Energy 84(6):912–916
10. Randall J (2005) Designing indoor solar products: photovoltaic technologies for AES. Wiley, Hoboken
11. Rapp-Arraras I, Domingo-Santos JM (2009) Algorithm for the calculation of the horizontal coordinates of the sun via spatial rotation matrices. Renew Energy 34(3):876–882
12. Sansoni P, Francini F, Fontani D, Mercatelli L, Jafrancesco D (2008) Indoor illumination by solar light collectors. Light Res Technol 40(4):323–332
13. Sproul AB (2007) Derivation of the solar geometric relationships using vector analysis. Renew Energy 32(7):1187–1205

Chapter 3
Diagnosis and Control of Nonlinear Oscillations of a Fluttering Plate

Liming Dai, Lu Han, Lin Sun, and Xiaojie Wang

Abstract This chapter focuses on both diagnosing and controlling the nonlinear dynamic responses of a fluttering plate excited by a high-velocity air flow. Six modes of the motion are considered for obtaining the numerical solutions of the system, and the modes are used to investigate the nonlinear dynamic responses of the fluttering. Due to the different characteristics of the diagnosing methods for nonlinear systems, Lyapunov Exponent method is employed to detect the system motion of each mode, while the Periodicity Ratio method is utilized to detect the behavior of entire system motion subjected to non-periodic excitations generated by the air flow. A newly developed control strategy, modified FSMC method, is applied to control the nonlinear oscillatory responses of the system. The approaches presented in this chapter have research and engineering application significances in the fields of aerodynamics, nonlinear dynamics, aircraft design, and design of space vehicles.

3.1 Introduction

Flutter behavior of plates exposed to air flow has been a subject of major interest and wide research attention because of its exceptional importance in the areas of aerodynamics, aircraft design, and design of space vehicles. The life expectancy and survivability of fluttering panels on high supersonic aircraft, for example, depend substantially on their resistance to the nonlinear fluttering oscillations of the panels subjected to excitations generated by high-speed air flow.

L. Dai (✉) • L. Han • L. Sun • X. Wang
Industrial Systems Engineering, University of Regina, Regina, SK, S4S 0A2 Canada
e-mail: liming.dai@uregina.ca; hanlu200@uregina.ca; sunli202@uregina.ca; wang249x@uregina.ca

R.N. Jazar and L. Dai (eds.), *Nonlinear Approaches in Engineering Applications 2*,
DOI 10.1007/978-1-4614-6877-6_3,

Von Karman's large deflection theory [1] has been employed by most researchers in the field. The Galerkin method [2, 3] was utilized by Dowell [4, 5] and the latter studies [6–8]. By the integration over the panel surface, these allow the numerical integration to a system of nonlinear ordinary differential equations. The dynamic behaviors, including deflection, stress, and frequency, under 2D and 3D, were analyzed with respect to various parameters. In a survey reported by Garrick and Reed [9], an overview of an aircraft flutter in historical retrospective is presented by the authors. The influence of maneuvering on the nonlinear response of a fluttering buckled plate on an aircraft has been studied by Sipcic [10], which suggests amplitude modulation as a possible new mode of transition to chaos. The flutter phenomenon in aeroelasticity and the mathematical analysis are given by Shubov [11]. Models of fluid–structure interaction with precise mathematical formulations available are selected and analytical results are obtained to explain flutter and its treatments. Due to the high velocity of fluid, thermal effects caused by friction have to be taken into consideration, which actually makes the problem more complicated. Enormous work could be found in this area such as [12–16]. Due to the existence of the effects of the aerodynamic, inertial, and elastic forces, the dynamic behaviors of the fluttering plate become extremely complicated especially when the speed of external fluid flow increases. One would expect that it would be of fundamental importance to know the role of the system parameters related to the different responses of the system.

Numerous research and great contributions have been made in investigating the characteristics of fluttering plates by researchers and engineers as mentioned above. The criteria for distinguishing the characteristics of the systems are crucial. Techniques providing high efficiency and accuracy in diagnosing and quantifying different characteristics such as chaos, periodicity, quasiperiodicity, and other nonlinear characteristics are always demanded. There are several methods available in the literature for determining the onset of chaotic oscillations and some predictive and diagnostic criteria for chaos are also reported [17–21]. Power spectral density is one of such methods that can be used to distinguish chaos from regular behavior of deterministic systems or generic stationary stochastic behavior [22]. Fractal Dimensions approach is able to identify the chaotic attractors' dimension [23–27]. Among all the diagnosing approaches, Lyapunov Exponent approach is probably the most popular approach [28, 29] due to its efficiency and simplicity. It measures the sensitivity of a system to initial conditions and therefore classifies the system's responses as either convergent or divergent and it is suitable for describing whether a response of the plate is convergent or divergent. However, Lyapunov Exponents cannot be used to distinguish quasiperiodicity and non-periodicity of a system. Periodicity Ratio method is developed Dai and Singh [30]. This approach and can be used to identify almost all the nonlinear characteristics and to be employed to plot the periodic–quasiperiodic–chaotic diagram efficiently for nonlinear dynamical systems.

In most applications of engineering, the nonlinear or irregular responses of the beams are desired to be controlled. Numerous control techniques and theories are available in the field. In 1992, a control theory, namely the theory of sliding modes control (SMC), was proposed and it has been pointed out that this control theory is of high efficiency in the control of multidimensional systems operating under conditions of uncertainties [31]. A decade later, an improved control strategy, which was developed on the basis of SMC, was developed with implementation of fuzzy logic theories and named as fuzzy sliding mode control (FSMC). Many researchers used the strategy and demonstrated the effectiveness of this control strategy in suppressing the nonlinear response of the system [32–34]. The FSMC strategy was also used in controlling the chaotic response of a micro mechanical resonator under electrostatic forces applied at both sides of the resonator, modeled as a beam [35]. In their study, the FSMC strategy demonstrated high efficiency in stabilizing the vibrations of the targeted system. It should be noticed the existing FSMC strategy is merely suitable to be applied in the system derived by first-order discretization. However, for the cases of second or higher order discretization and more reliable and accurate solutions, the existing FSMC strategy is not applicable. Therefore, a modified FSMC strategy [36] is developed.

This research is firstly to diagnose the characteristics of a plate subjected to non-periodic excitations of high-velocity flow with both Lyapunov Exponent (LE) and Periodicity Ratio (PR) methods. The responses of the fluttering plate are to be analyzed with considerations of various varying systems parameters. Furthermore, it would be interesting to apply the control theory to the nonlinear response of the system to reduce the harm. As figured out by Dowell [4] corresponding to the parameters selected in the study, 4–6 modes, rather than two modes, should be employed for quantitative accuracy. Hence, in this section the modified FSMC will be applied to control and stabilized the chaotic oscillation of the fluttering 2D plate, which has been described in terms of six modes as mentioned in the previous section. The main purpose of the present work focuses on the nonlinear influence of the system and applying control theory such as FSMC to reduce the system vibrations, where a chaotic case is used as the control example. The knowledge of detecting and controlling the flutter behavior of a vibrating plate is useful.

3.2 Governing Equation for the Motion of a 2D Plate

Same as Dowell's research, the fluttering plate considered in this research has simply supported boundaries, is a flat thin plate with infinite length in the y-direction and length L in the x-direction. The thickness is negligible in comparing with the other geometric dimensions of the plate. The panel is subjected to a supersonic flow over the outside surface with constant velocity U_∞. Gravity is perpendicular to the plate. The plate is induced to vibrate along the z-direction due to the loading generated by the interaction between the high-velocity flow and the plate, which is dominating and thus of great importance.

To obtain the governing equations of the motion of a 2D fluttering plate, some assumptions adopted are presented first as follows:

- The von Karman's large deflection plate theory is employed;
- The effects of in-plane load and static pressure differential are taken into consideration;
- The plate is undergoing cylindrical bending but no span-wise bending.

Based on the assumptions above, the governing equation reads [9]:

$$D\frac{\partial^4 w}{\partial x^4} - \left(N_x + N_x^{(a)}\right)\frac{\partial^2 w}{\partial x^2} + \rho_m h\frac{\partial^2 w}{\partial t^2} + (p - p_\infty) = \Delta p \tag{3.1}$$

where

$$\begin{aligned} N_x &= \alpha Eh/2L\int_0^L (\partial w/\partial x)^2 dx \\ \alpha &= KL/(KL + Eh) \end{aligned} \tag{3.2}$$

Following quasi-steady, supersonic theory, we have

$$p - p_\infty = \frac{2q}{\beta}\left[\frac{\partial w}{\partial x} + \left(\frac{M^2 - 2}{M^2 - 1}\right)\frac{1}{U}\frac{\partial w}{\partial t}\right] \tag{3.3}$$

Applying the nondimensionalization as follows:

$$\begin{aligned} \xi &= x/a \\ \tau &= t\left(D/\rho_m h a^4\right)^{1/2} \\ W &= w/h \\ \lambda &= 2qa^3/\beta D \\ \mu &= \rho a/\rho_m h \\ P &= \Delta p a^4/Dh \end{aligned} \tag{3.4}$$

Substituting Eqs. (3.2)–(3.4) into (3.1), the non-dimensionalized governing equation can be expressed as

$$\begin{aligned} &W'''' - \alpha 6(1-\nu^2)\left[\int_0^1 \left(W'\right)^2 d\xi\right] W'' - R_x W'' + \frac{\partial^2 W}{\partial \tau^2} \\ &+ \lambda\left\{W' + \left(\frac{M^2 - 2}{M^2 - 1}\right)\left(\frac{\mu}{\beta\lambda}\right)^{\frac{1}{2}}\frac{\partial W}{\partial \tau}\right\} = P \end{aligned} \tag{3.5}$$

For large Mach number, $M \gg 1$, the simplified relationship can be applied

$$\left[\frac{M^2-2}{M^2-1}\right]^2 \frac{\mu}{\beta} \rightarrow \frac{\mu}{M} \tag{3.6}$$

Following the Galerkin Method [37], for simply supported plate, the nondimensional displacement $W(\xi, \tau)$ can be expressed as:

$$W(\xi, \tau) = \sum_{m=1}^{\infty} a_m(\tau) \cdot \sin m\pi\xi \tag{3.7}$$

Substituting Eqs. (3.6) and (3.7) into Eq. (3.5), Eq. (3.5) can be rewritten as:

$$\begin{aligned}
&\sum a_m (m\pi)^4 \sin m\pi\xi + \alpha 6(1-\nu^2) \times \left[\sum_r a_r^2 \frac{(r\pi)^2}{2}\right] \sum_m a_m (m\pi)^2 \sin m\pi\xi \\
&\quad + R_x \sum_m a_m (m\pi)^2 \sin m\pi\xi + \sum_m \frac{d^2 a_m}{d\tau^2} \sin m\pi\xi \\
&\quad + \lambda \left[\sum_m a_m (m\pi) \cos m\pi\xi + \left(\frac{\mu}{M\lambda}\right)^{\frac{1}{2}} \sum_m \frac{da_m}{d\tau} \sin m\pi\xi\right] = P
\end{aligned} \tag{3.8}$$

By multiplying Eq. (3.8) by $\sin m\pi\xi$ and integrating over the length of the panel, Eq. (3.8) can be reduced into a set of ordinary differential equations.

$$\begin{aligned}
&a_s \frac{(s\pi)^4}{2} + \alpha 6\left(1-\nu^2\right)\left[\sum_r a_r^2 \frac{(r\pi)^2}{2}\right] a_s \frac{(s\pi)^2}{2} + R_x a_s \frac{(s\pi)^2}{2} + \frac{d^2 a_m}{d\tau^2}\frac{1}{2} \\
&\quad + \lambda \left\{\sum_m \frac{sm}{s^2-m^2} \times \left[1-(-1)^{s+m}\right] a_m + \frac{1}{2}\left(\frac{\mu}{M\lambda}\right)^{\frac{1}{2}} \frac{da_s}{d\tau}\right\} \\
&\quad = P\frac{\left[1-(-1)^2\right]}{s\pi}, s = 1, \cdots, \infty
\end{aligned} \tag{3.9}$$

Equation (3.9) is comprised of a coupled set of ordinary, nonlinear differential equations with respect to time. The equations will be numerically solved. It has been reported by Garrick and Reed [9] that to obtain accurate solutions, at least four modes must be used. When the in-plane or static pressure loading produces larger tension in the plate, more modes would be taken into consideration. In this chapter, under the range of parameters applied, all the calculations are performed using six modes.

3.3 Periodicity Ratio Method

It is widely acknowledged that the corresponding Poincare map for a steady state periodic motion of a dynamic system consists of a finite number of visible points [30, 38]. The visible points in the Poincare map are then the points overlapping many points periodically appeared. On the other hand, the points in the Poincare map of a chaotic case must distribute in an unpredictable manner. This implies that the overlapping points in the Poincare map of a chaotic response are extremely minimal. Quasiperiodic response is another type of phenomenon in nonlinear dynamic systems. A quasiperiodic case may also contain negligibly small number of overlapping points, though some regularity of the system responses can be identified. Based on these findings, Dai and Singh [30, 39, 40] proposed an index named Periodicity Ratio (PR) which counts the ratio of periodic points among all the points in the Poincare map. The methodology of Periodicity Ratio approach is based on the measure of periodicity of a response of a nonlinear system. The more periodic a dynamic system is, the closer the corresponding PR value is to a unit. When the PR approaches zero, the corresponding system has no periodicity at all and therefore represents either chaotic or quasiperiodic response of the system. The most significant advantage of the Periodicity Ratio method is that the PR value can be used as a single value index in diagnosing the periodicity therefore the behavior of a dynamic system. Moreover, Periodicity Ratio method reveals the fact that there are infinite number of fashions of motion in between chaos and periodic responses for a nonlinear dynamic system.

The Periodicity Ratio is defined as [30]:

$$\gamma = \lim_{n\to\infty} \frac{NPP}{n} \tag{3.10}$$

where *NPP* is the number of periodically overlapping points and n is designated as the total number of all the points in the Poincare map. *NPP* in Eq. (3.10) can be calculated by

$$NPP = \phi(1) + \sum_{m=2}^{n} (\phi(m).P(\prod_{j=1}^{m-1} Q(\phi(j)))) \tag{3.11}$$

where

$$\phi(l) = \sum_{i=m+q+1}^{n} P(\prod_{h=0}^{q-l} Q(X_{i+h} - X_{m+l+h}))(\prod_{k=1}^{l} Q(X_{i-k} - X_{m+l-k})) \tag{3.12}$$

which represents the number of points periodically overlapping the *l*th point in the Poincare map. In the above two equations, *q, m, i,* and *l* are all positive integers. Note that *q* value in the above equation can be different from one group of points to another group of points.

In the above equations, two step functions $Q(y)$, $P(z)$ are introduced. The two step functions are expressible in the form

$$Q(y) = \begin{cases} 1, \text{ if } y = 0 \\ 0, \text{ if } y \neq 0 \end{cases}, P(z) = \begin{cases} 0, \text{ if } z = 0 \\ 1, \text{ if } z \neq 0 \end{cases} \tag{3.13}$$

In order to describe the visible and overlapping points in a Poincare map, introduce $X_i = \begin{Bmatrix} x_i \\ \dot{x}_i \end{Bmatrix}$ and denote it as a vector of both displacement and velocity. With this designation, the determination of whether or not a point in the Poincare map is an overlapping point is based on the judgment described by the following equations.

$$\begin{aligned} X_{ki} &= x_k - x_i \\ \dot{X}_{ki} &= \dot{x}_k - \dot{x}_i \end{aligned} \tag{3.14}$$

where k is an integer in the range of $1 \leq k \leq j$ and j represents the finite number of points (known as visible points) appearing in the Poincare map corresponding to a dynamic system, and $\dot{X}$ is the time derivative of X. Points under consideration are overlapping points if and only if the following conditions are satisfied.

$$\begin{aligned} X_{ki} &= 0 \\ \dot{X}_{ki} &= 0 \end{aligned} \tag{3.15}$$

In this case, the way to obtain the points in the Poincare map is to get several points with same displacements since the fixed time step of the irregular excitation system is hardly to be captured [20]. Specifically, the peak and bottom value in every period of the wave form will be collected. If the system finally leads to a periodic solution, after a long enough period of time, all the points of the Poincare map will converge to a finite number of individual points which must have the form $\{X_m, X_{m+1}, \ldots, X_{m+q}\}$.

Thus, any overlapping point X_p in a Poincare map would be a periodic point, if and only if the following condition is satisfied:

$$P(\sum_{i=0}^{q} \{P(\prod_{h=0}^{q-l} Q(X_{i+h} - X_{m+l+h}))(\prod_{k=1}^{l} Q(X_{i-k} - X_{m+l-k}))\}) = 1 \tag{3.16}$$

Once the periodic points are determined completely, the Periodicity Ratio can be determined accurately.

If the behavior of a system in a steady state is periodic, the points in the corresponding Poincare map must all be overlapping points. Accordingly, the value of the Periodicity Ratio, γ, should simply be unity. For a chaotic response of a system, on the other hand, the number of periodic points overlapped should be zero or insignificant in comparing with n. This is to say, γ approaches zero for chaos.

With the definition of the Periodicity Ratio, γ is clearly a quantified description of periodicity for a dynamic system. This is to state that γ indicates quantitatively how close the response of a dynamic system is to a perfect periodic motion. For example, a motion with γ equals to 0.9 is more close to a periodic motion in comparing with a motion to which γ equals to 0.8. Contrastively, a motion with γ approaching zero will show no periodic behavior, and therefore is a perfectly nonperiodic motion. When γ takes a value such that $0 < \gamma < 1$, it implies that some points in the Poincare map are periodically overlapping points while the others are not. Nonperiodic cases in between chaos and periodic motions may include the intermittent chaos in which chaotic motions occur between periods of regular motion.

It should be noted, however, the expression shown in Eq. (3.10) is theoretical, as it requires an infinitely large number of n for a perfect measurement of γ and the time range considered must be $t \in [0, \infty)$ such that t will be sufficient for a perfect γ. This implies that the Periodicity Ratio γ can be precisely calculated only in the cases for which the analytical solutions corresponding to the dynamical systems are available. For most nonlinear dynamic systems, however, the calculation for the Periodicity Ratio has been done on a numerical basis with the aid of a computer, as analytical solutions for these systems are not available. As $Q(y)$, $P(z)$ in the equations are step functions, the numerical calculation for γ can be conveniently carried out. In numerically determining for γ, therefore, a sufficiently large n should be used in performing the actual numerical calculation for γ in the practice of numerical calculation. In computing the Periodicity Ratio, errors caused by numerical calculation and by the mathematical models of numerical purpose should also be considered. Furthermore, in numerically calculating for γ, all of the n points must be compared to see whether they are overlapping points or not. Once a point is counted as an overlapping point, it should not be counted again in the numerical calculations.

For nonlinear dynamic systems, a motion with Periodicity Ratio equals to zero may not necessarily be a chaotic motion. By the definition of Periodicity Ratio, a perfect quasiperiodic motion also has a Periodicity Ratio of zero. In this case, another technique, Lyapunov Exponent approach can be employed.

3.4 Lyapunov Exponent Spectrum

The definition of Lyapunov Exponent is associated with a measure of the average rates of expansion and contraction of trajectories surrounding a given trajectory. They are asymptotic quantities, defined locally in state space, and describe the exponential rate at which a perturbation to a trajectory of a system grows or decays with time at a certain location in the state space. They are useful in characterizing the asymptotic state of an evolution. The spectrum of Lyapunov Exponent has proven to be one of the practically sound techniques for diagnosing chaotic systems. It is probably the most widely used index in characterizing the behaviors of nonlinear

dynamic systems. The approach is based on the important characteristic that chaos of a nonlinear dynamic system is sensitivity to initial conditions, which counts the average exponential rates of divergence or convergence of close orbits of a vibrating object in the phase space of a dynamic system. Wolf et al. [29] gave a powerful and efficient method for determining Lyapunov Exponents from time series. Rong et al. [41] investigated the principal resonance of a stochastic Mathieu oscillator to random parametric excitation and gave the conclusion that the instability of the stochastic Mathieu system depends on the sign of the maximum Lyapunov Exponent. Lyapunov Exponent was also used to analyze the numerical characteristic [42]. It is usually determined by experiments or computer simulations. Nayfeh has clearly described the definition of Lyapunov Exponent as followings [20].

Let $X(t)$ such that $X(t=0) = X_0$ represent a trajectory of the system governed by the following n-dimensional autonomous system:

$$\dot{\mathbf{x}} = \mathrm{F}(\mathbf{x}; \mathrm{M}) \tag{3.17}$$

where the vector $\mathbf{x}$ is made up of n state variables, the vector function F describes the nonlinear evolution of the system, and M represents a vector of control parameters. Denoting the perturbation provided to $X(t)$ by $y(t)$ and assuming it to be small, an equation after linearization in the disturbance terms can be obtained. The perturbation is governed by

$$\frac{dy(t)}{dt} = Jy(t) \tag{3.18}$$

where, in general, $J = D_x\mathrm{F}(\mathbf{x}(t); \mathrm{M})$ is a $n \times n$ matrix with time dependent coefficients. If we consider an initial deviation $y(0)$, its evolution is described by

$$y(t) = \Phi(t)y(0) \tag{3.19}$$

where $\Phi(t)$ is the fundamental (transition) matrix solution of Eq. (3.18) associated with the trajectory $X(t)$.

For an appropriately chosen $y(0)$ in Eq. (3.19), the rate of the exponential expansion or contraction in the direction of $y(0)$ on the trajectory passing through X_0 is given by

$$\bar{\lambda}_i = \lim_{t\to\infty} \frac{1}{t} \ln\left(\frac{\|y(t)\|}{\|y(0)\|}\right) \tag{3.20}$$

where the symbol $\|\|$ denotes a vector norm. The asymptotic quantity $\bar{\lambda}_i$ is then defined as the Lyapunov Exponent. There are several different methods to calculate the Lyapunov Exponent, such as the whole Lyapunov Exponent, global and local Lyapunov Exponent, and Lyapunov Spectrum. The method of whole Lyapunov Exponent also known as the Maximum Lyapunov Exponent is suitable for the discrete differential system, whereas the Lyapunov Spectrum is more suitable for

continuous differential systems [20]. The global Lyapunov exponent, on the other hand, gives a measure for the total predictability of a system; whereas the Local Lyapunov Exponent estimates the local predictability around a given point X_0 in phase space.

Specifically, to obtain the Lyapunov spectrum for a continuous dynamical system, a set of n linearly independent vectors $y_1, y_2, \ldots, y_n$ may form the basis for the n-dimensional state space. Choosing an initial deviation along each of these n factors, n Lyapunov Exponent $\bar{\lambda}_i(y_i)$ can be determined. The set of n numbers $\bar{\lambda}_i(y_i)$ is defined as the Lyapunov spectrum. For system (3.17), n orthonormal initial vectors y_i such that $y_1 = (1, 0, 0, \ldots)$, $y_2 = (0, 1, 0, \ldots), \ldots, y_n = (0, 0, 0, \ldots, 1)$ can be assigned. For each of these initial vectors, Eqs. (3.17) and (3.18) can be integrated for a finite time T_f and a set of vectors $y_1(T_f), y_2(T_f), \ldots, y_n(T_f)$ can then be obtained. The new set of vectors is orthonormalized using the Gram-Schmidt procedure to produce

$$\hat{y}_1 = \frac{y_1(T_f)}{\|y_1(T_f)\|}$$

$$\hat{y}_n = \frac{y_n(T_f) - \sum_{i=1}^{n-1} [y_n(T_f).\hat{y}_i]\hat{y}_i}{\left\| y_n(T_f) - \sum_{i=1}^{n-1} [y_n(T_f).\hat{y}_i]\hat{y}_i \right\|} \tag{3.21}$$

Subsequently, using $X(t = T_f)$ as an initial condition for Eq. (3.18) and using each of the $\hat{y}_i$ as an initial condition for Eq. (3.19), Eqs. (3.18) and (3.19) can be integrated again for a finite time and carry out the Gram-Schmidt procedure to obtain a new set of orthonormal vectors. The norm in the denominator can be denoted by N_j^k. Thus, after repeating the integrations and the processes of Gram-Schmidt orthonormalization r times, the Lyapunov Exponent can be obtained from

$$\hat{\lambda}_i = \frac{1}{rT_f} \sum_{k=1}^{r} \ln N_j^k \tag{3.22}$$

The Lyapunov spectrum can thus be determined.

3.5 Utilizing Lyapunov Exponent and Periodicity Ratio Methods to Detect the System Motions

From the above description about Lyapunov Exponents, the Jacobi matrix which is directly related to the expressions of the system equations is required for calculation in every step. However, the system displacement in Eq. (3.7) cannot be obtained by this way because the Jacobi matrix would vary with different mode whose governing equation is stated in Eq. (3.9). And the Jacobi matrix for the whole

system displacement cannot be combined by the individual matrix under each mode. Therefore, Lyapunov Exponents could only measure the system behavior at each mode other than the whole trend, which can disclose certain system properties while still not enough to diagnose the real system behavior, since the involved modes are only introduced by the mathematical transformation that in the real model the behavior under single mode cannot be distinguished from each other. So it is not that typical to use the behavior under each mode to represent the whole system. In the meantime, the Periodicity Ratio Method does not have the difficulty to determine the varied Jacobi matrix since it merely depends on the system solutions, which is forward straight to be obtained once the system solutions are numerically solved in this case.

Based on Eq. (3.9), the Jacobi matrix for calculating the Lyapunov Exponents at each mode (s = 1, 2, 3, 4, 5, 6) is specifically formulized as

$$J = \begin{bmatrix} 0 & 0 & 0 \\ 0 & 0 & 1 \\ 0 & -(s\pi)^4 - \alpha 6\left(1-\nu^2\right)\left[\sum_r a_r^2 \frac{(r\pi)^2}{2}\right](s\pi)^2 - R_x(s\pi)^2 & -\frac{1}{2}\left(\frac{\mu\lambda}{M}\right)^{\frac{1}{2}} \end{bmatrix} \tag{3.23}$$

Several typical motions and their corresponding PR values and LE values are demonstrated as the following, with figures and descriptions. It should be notice that the wave form and phase diagram figures for Lyapunov Exponent approach are corresponding to each and every modes of the six modes of oscillatory responses of the panel, as needed in determining for all the Lyapunov Exponents. Moreover, the Lyapunov Exponents of each of the modes are different, i.e., can be positive representing divergent responses of the panel or negative representing convergent response of the panel. The PR approach considers the behavior of the plate system as a whole. In the calculations of the PR approach, the motion in the first 15 s is discarded to waive the initial effect.

A buckled motion is exhibited in the series figures of Figs. 3.1, 3.2, 3.3, and 3.4. In this case the plate is a stabilized at a position other than at the equilibrium. Figure 3.1 illustrates the whole system motion in wave form and phase diagram. The wave forms and phase diagrams for the first three modes are shown in the Figs. 3.2, 3.3, and 3.4. These three modes contribute most to the whole system responses including displacements and velocities.

The series of figures in Figs. 3.5, 3.6, and 3.7 are showing the sectioning points for calculating the PR index. The diamonds in Fig. 3.5 are the peak displacements and the stars in Fig. 3.5 are the bottom displacements. They are both used to calculate the PR values. Figure 3.6 shows the velocities of corresponding points, from which it can be seen the velocities of all the collected peak and bottom points are close to zero. The deviation from the theoretical zero value is due to the numerical calculation errors. It seems a bit suspicious in Fig. 3.5 that the peak points and bottom points are always a cluster without clear distinguishment. To test the way to collect the peak and bottom points of the whole displacement, the displacements

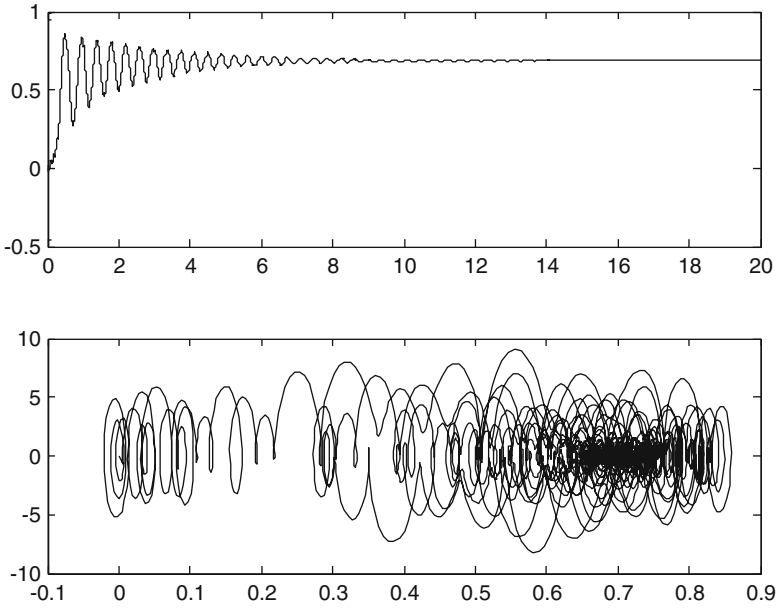

Fig. 3.1 Wave form and phase diagram of a buckled motion. $Rx = -3\pi^2, \lambda = 60$

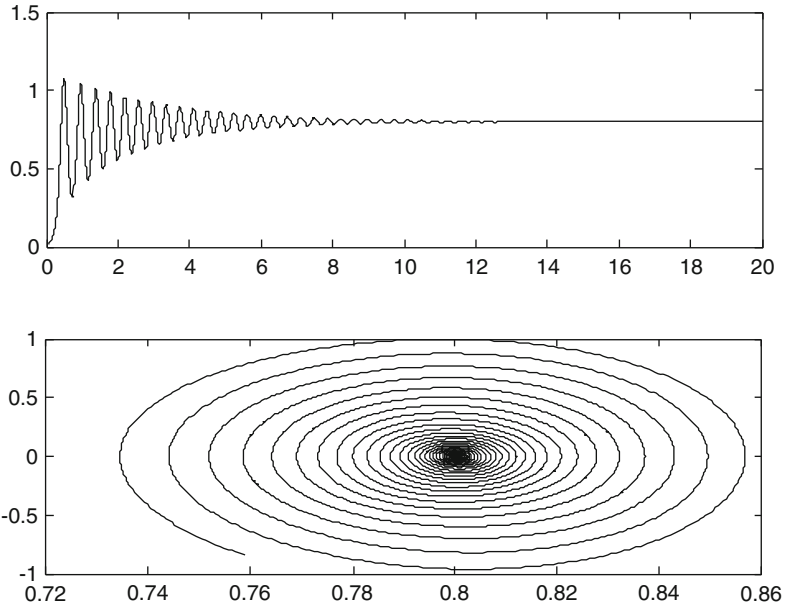

Fig. 3.2 Wave form and phase diagram of a buckled motion at mode 1. $Rx = -3\pi^2, \lambda = 60, LE = (-0.0803, -0.1510, -2.8592)$

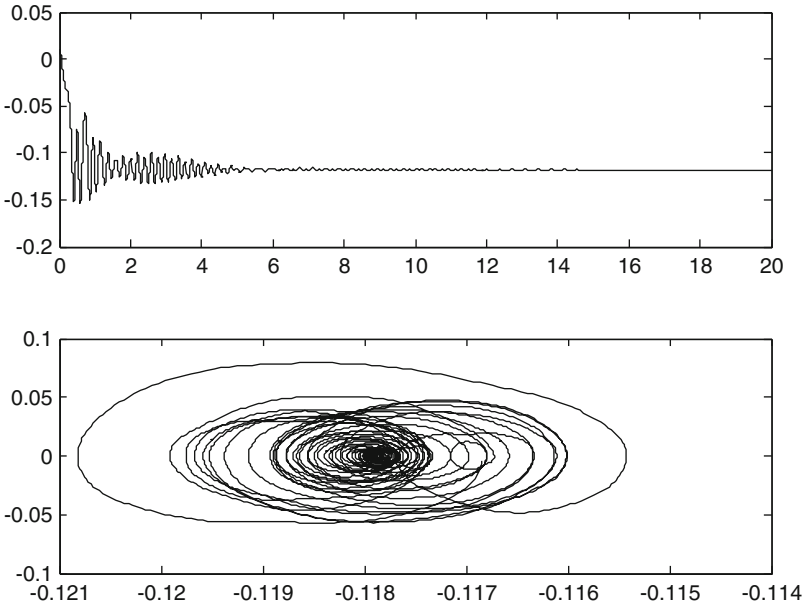

Fig. 3.3 Wave form and phase diagram of a buckled motion at mode 2. $Rx = -3\pi^2, \lambda = 60$, $LE = (-0.0301, -0.0472, -0.0473)$

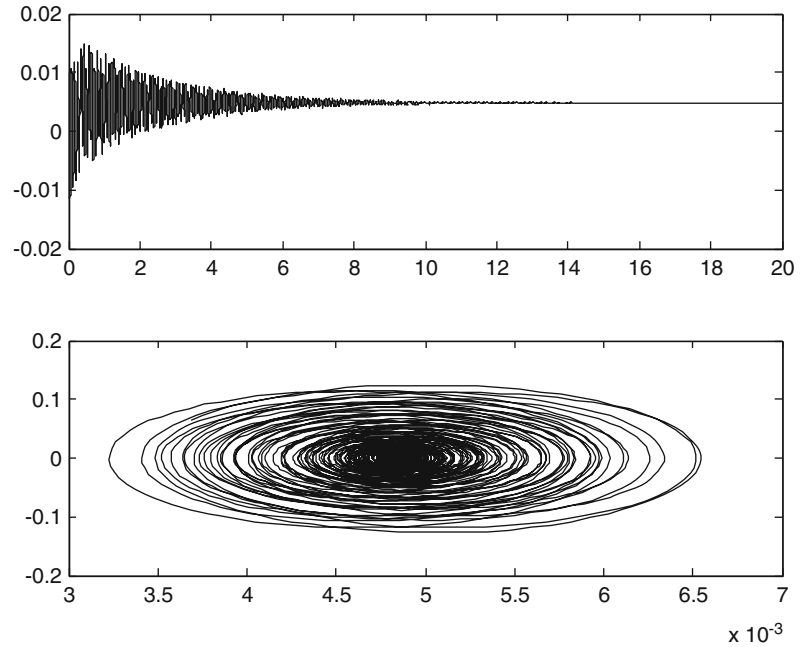

Fig. 3.4 Wave form and phase diagram of a buckled motion at mode 3. $Rx = -3\pi^2$, $\lambda = 60, LE = (-0.0023, -0.0256 - 0.0677)$

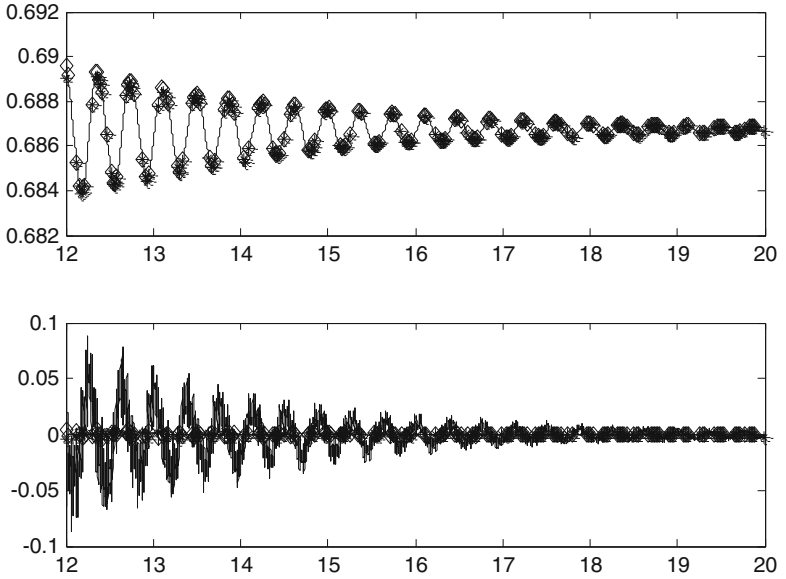

Fig. 3.5 Maximum and minimum points sectioning of a buckled motion. $Rx = -3\pi^2$, $\lambda = 60, PR = 0.9798$

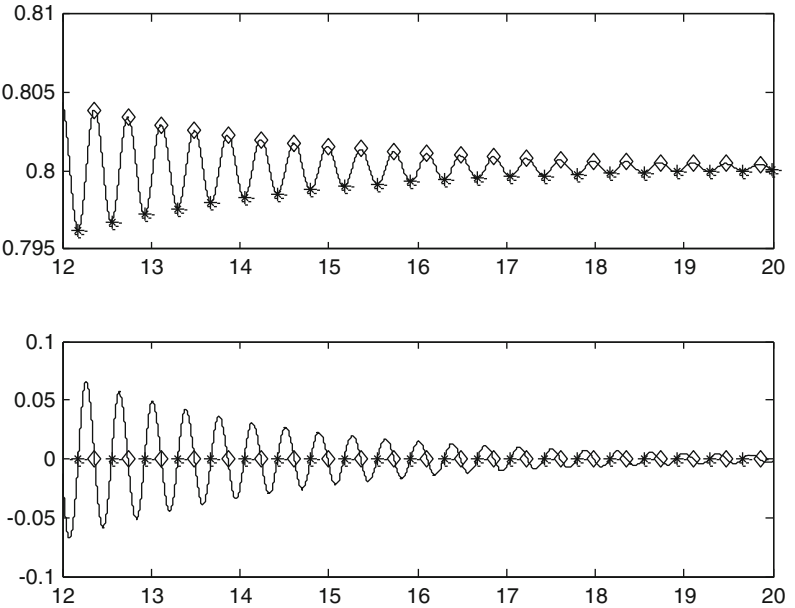

Fig. 3.6 Maximum and minimum points sectioning of a buckled motion at mode 1. $Rx = -3\pi^2, \lambda = 60$

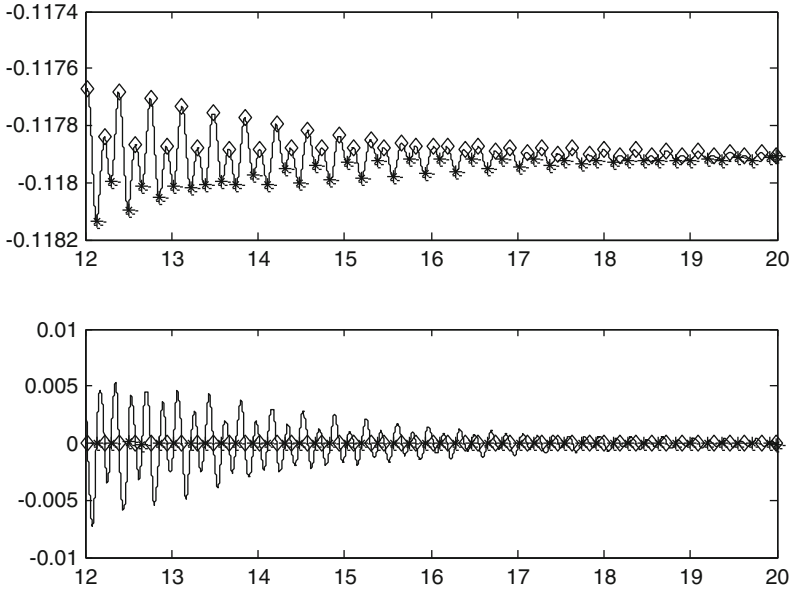

Fig. 3.7 Maximum and minimum points sectioning of a buckled motion at mode 2. $Rx = -3\pi^2, \lambda = 60$

of peak and bottom are collected within mode 1 and mode 2 in Figs. 3.6 and 3.7 and verification explains the cluster of peak and bottom points is caused by the supposition of the motion at different modes.

Figures 3.8, 3.9, 3.10, and 3.11 is about a chaotic case. Figure 3.8 is the whole system motion in wave form and phase diagram. Figures 3.9, 3.10, and 3.11 are respectively the wave forms and phase diagrams for the first three modes which contribute most to the whole system displacement. The corresponding Lyapunov Exponents are calculated under each mode other than the system whole motion.

Similar as before, in Fig. 3.12, peak points and bottom points are collected for each period to calculate the PR index of the system whole motion. The diamonds are the peak displacements and the stars are the bottom displacements.

Figure 3.13 is the whole system motion of a periodic case in wave form and phase diagram. Different from the buckled and chaotic case which just include the motion of first three modes, Figs. 3.14, 3.15, 3.16, 3.17, 3.18, and 3.19 are the wave forms and phase diagrams of each mode of all the six modes. This is because none of six modes can be neglected for considering the system motion since all of the displacement is not small. Another reason is to show some incompatible cases of the results diagnosed by Lyaponov Exponents and Periodicity Ratio. Again, sectioning points are collected in Fig. 3.20 which includes the diamonds and the stars representing the peak displacements and the bottom displacements respectively.

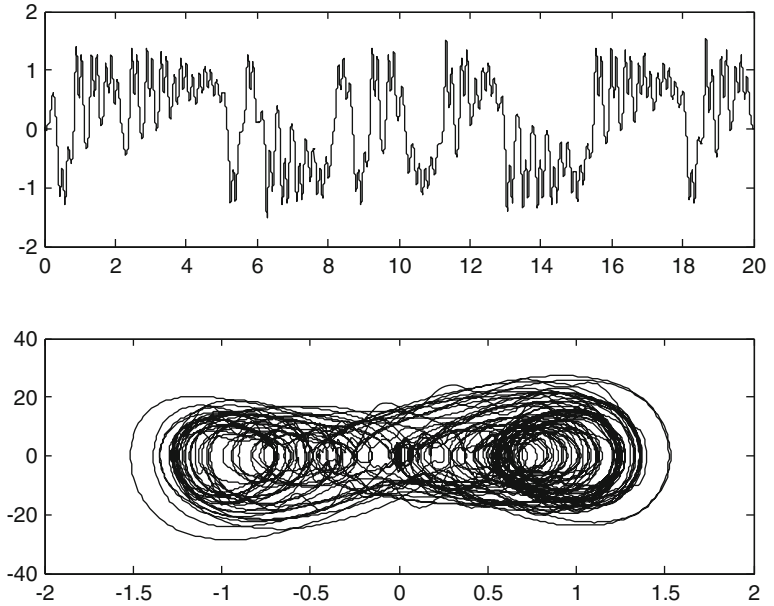

Fig. 3.8 Wave form and phase diagram of a chaotic motion. $Rx = -4.5\pi^2, \lambda = 117$

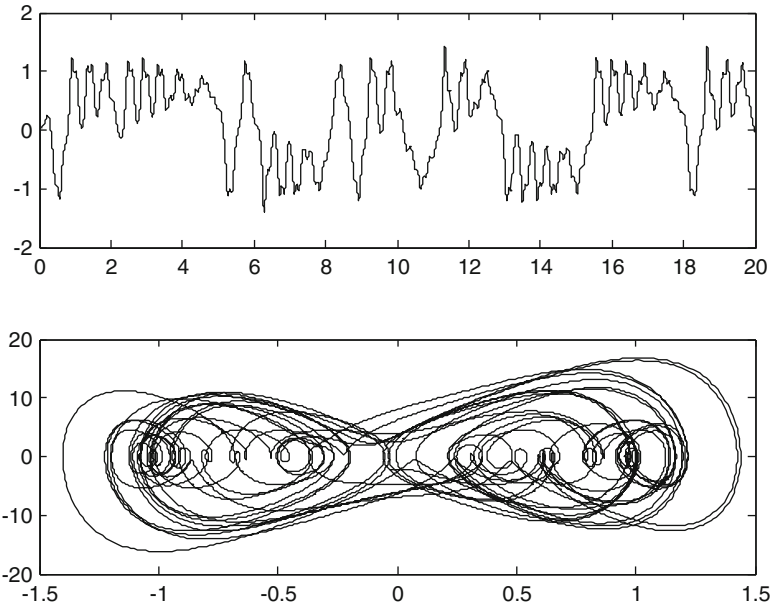

Fig. 3.9 Wave form and phase diagram of a chaotic motion at mode 1 $Rx = -4.5\pi^2, \lambda = 117, LE = (0.1366, -0.0172, -0.2994)$

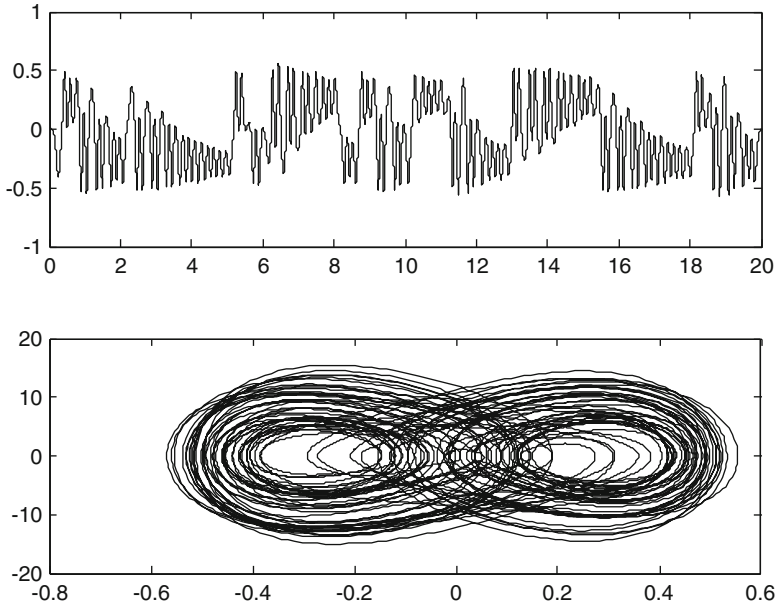

Fig. 3.10 Wave form and phase diagram of a chaotic motion at mode 2. $Rx = -4.5\pi^2, \lambda = 117, LE = (0.1317, -0.0172, -0.2994)$

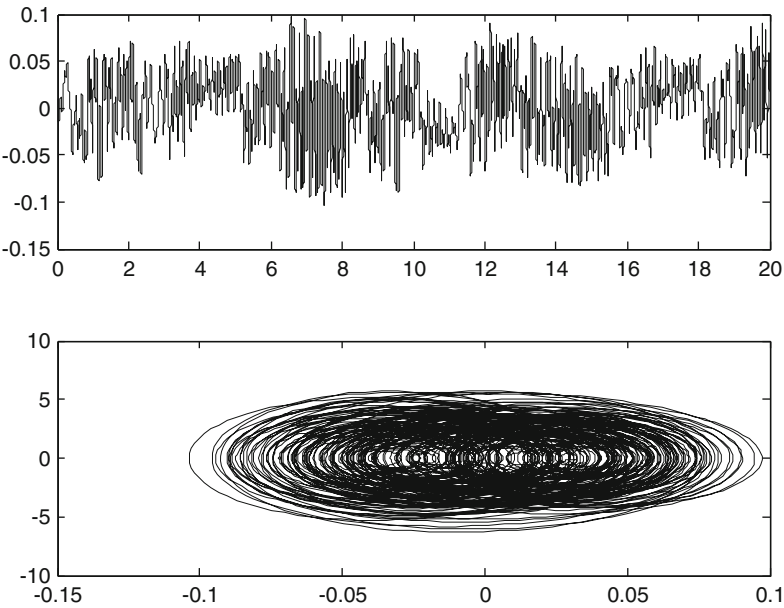

Fig. 3.11 Wave form and phase diagram of a chaotic motion at mode 3. $Rx = -4.5\pi^2, \lambda = 117, LE = (0.0812, -0.0848, -0.4265)$

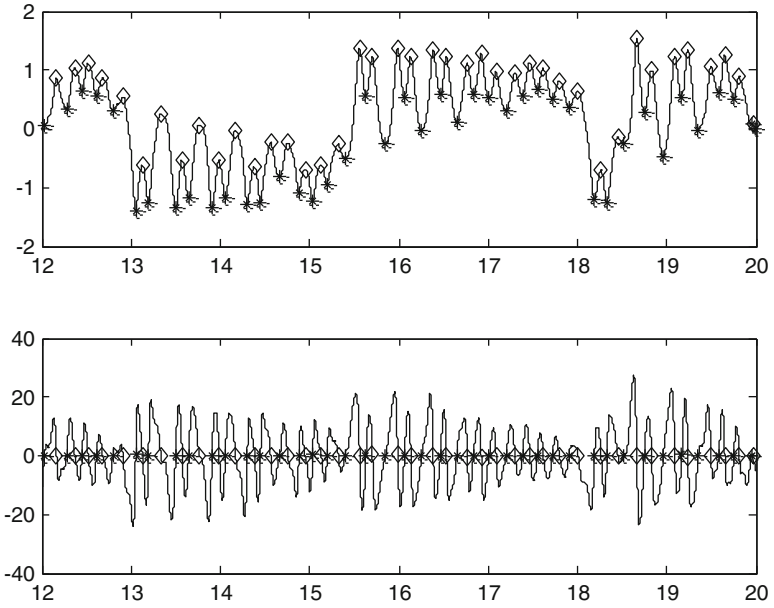

Fig. 3.12 Maximum and minimum points sectioning of a chaotic motion. $Rx = -4.5\pi^2, \lambda = 117, PR = 0$

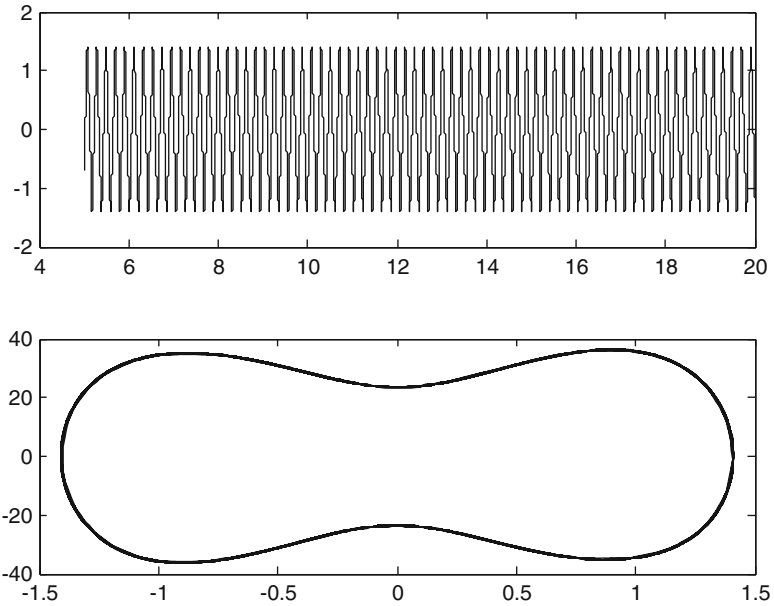

Fig. 3.13 Wave form and phase diagram of a periodic motion. $Rx = -4\pi^2, \lambda = 375$

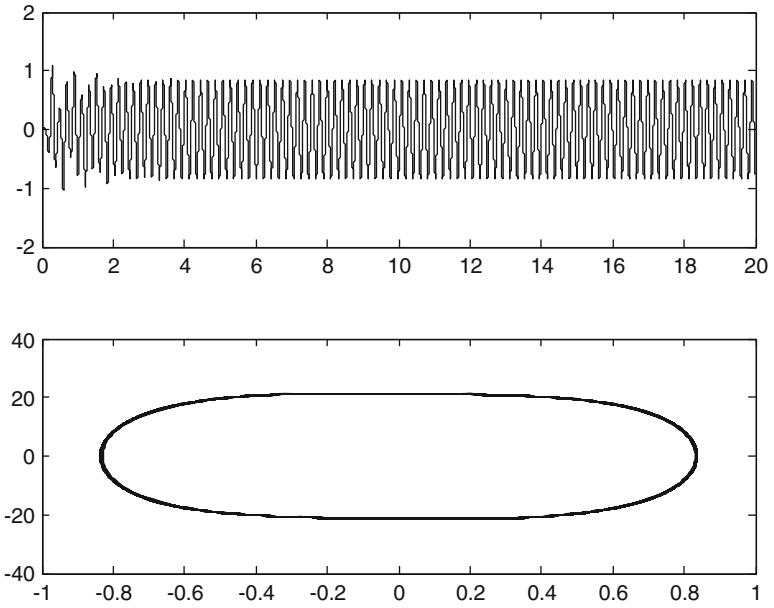

Fig. 3.14 Wave form and phase diagram of a chaotic motion at mode 1. $Rx = -4\pi^2, \lambda = 375, LE = (-0.094, -0.1617, -0.8203)$

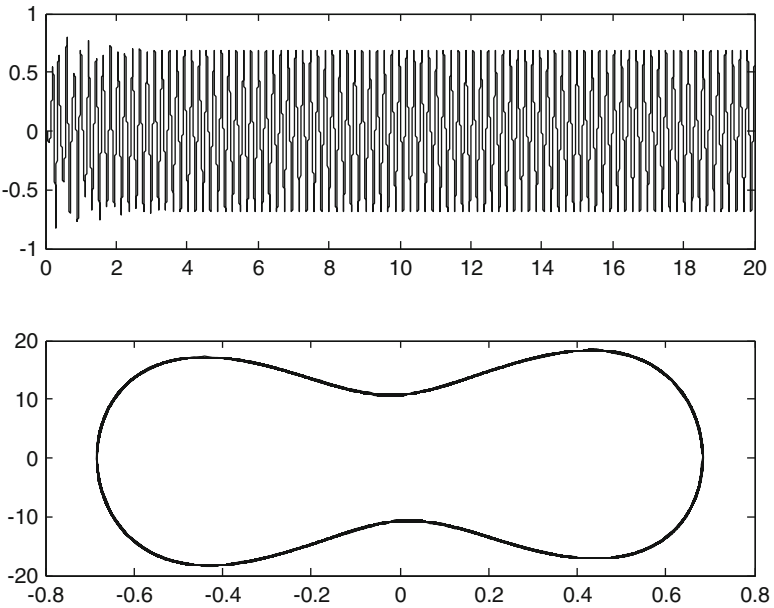

Fig. 3.15 Wave form and phase diagram of a chaotic motion at mode 2. $Rx = -4\pi^2, \lambda = 375, LE = (-0.0044, -0.2296, -0.2647)$

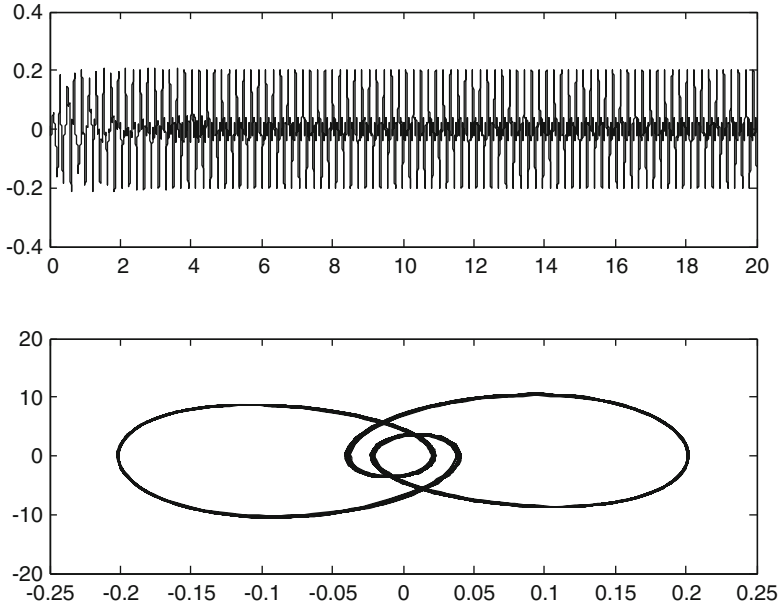

Fig. 3.16 Wave form and phase diagram of a chaotic motion at mode 3. $Rx = -4\pi^2, \lambda = 375, LE = (0.0022, -0.3437, -0.3726)$

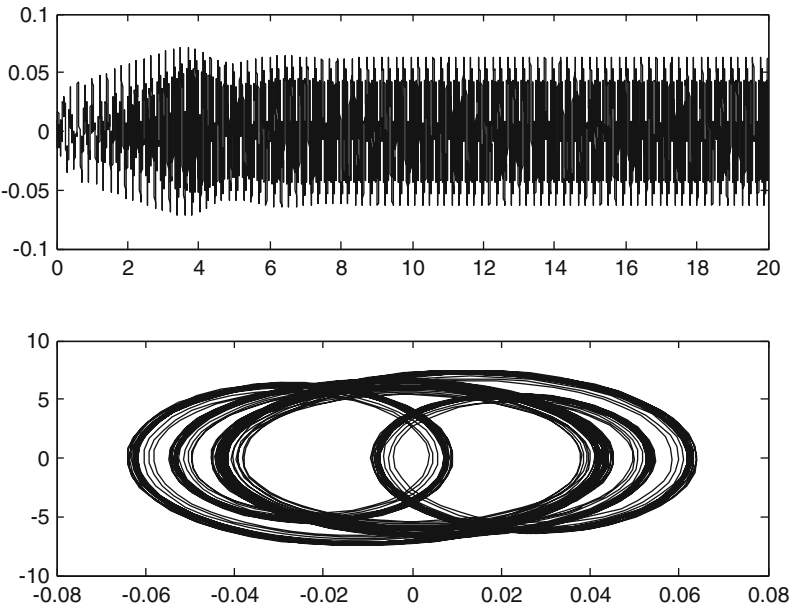

Fig. 3.17 Wave form and phase diagram of a chaotic motion at mode 4. $Rx = -4\pi^2, \lambda = 375, LE = (0.0033, -0.2817, -0.3414)$

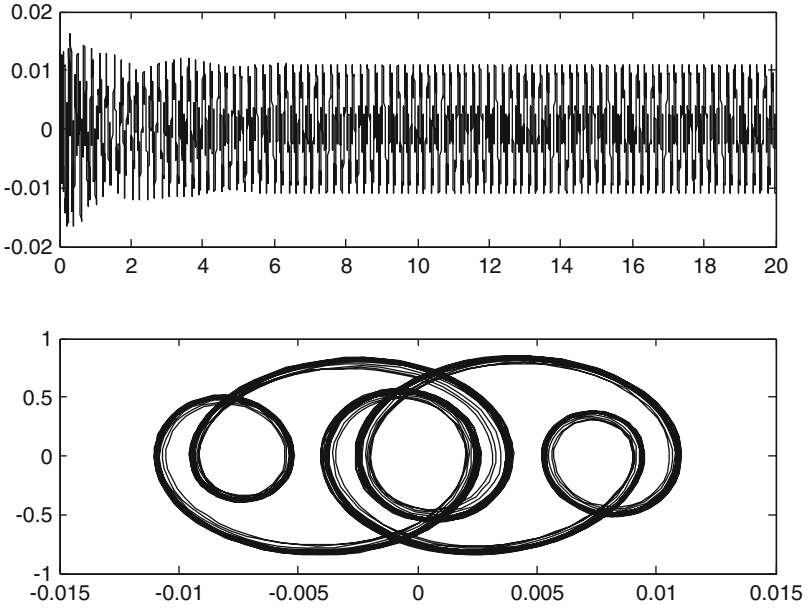

Fig. 3.18 Wave form and phase diagram of a chaotic motion at mode 5. $Rx = -4\pi^2, \lambda = 375, LE = (0.0038, -0.0689, -0.7586)$

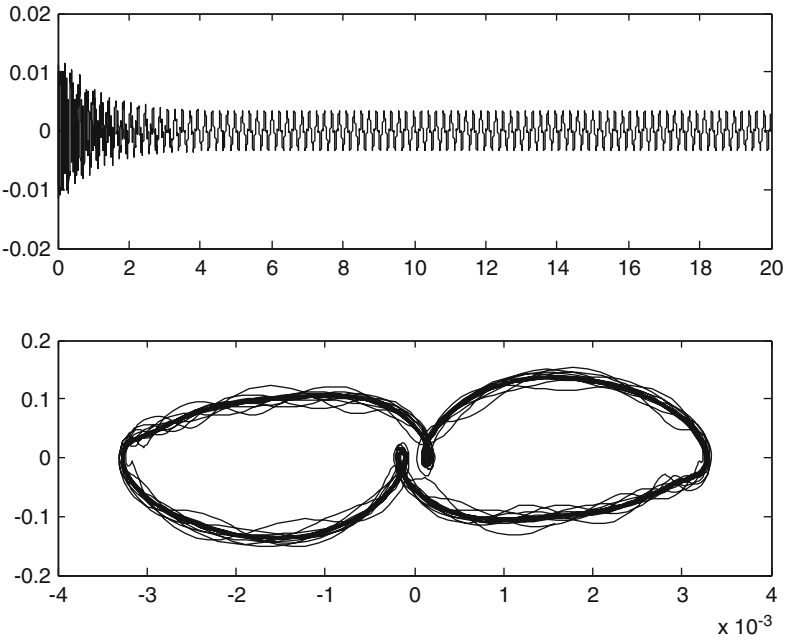

Fig. 3.19 Wave form and phase diagram of a chaotic motion at mode 6. $Rx = -4\pi^2, \lambda = 375, LE = (0.0024, -0.3903, -0.4275)$

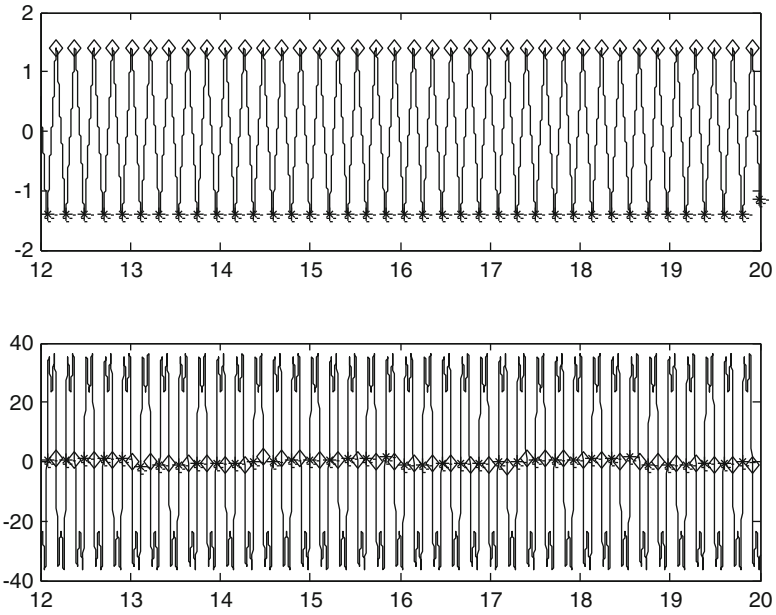

Fig. 3.20 Maximum and minimum points sectioning of a periodic motion. $Rx = -4\pi^2, \lambda = 375, PR = 0.9775$

The last case is a stabilized motion case. Figure 3.21 is the whole system motion in wave form and phase diagram. Same as the buckled and chaotic case which just includes the motion of first three modes, Figs. 3.22, 3.23, and 3.24 are the wave forms and phase diagrams of each mode of first three modes of the system motion. And Fig. 3.25 is about the peak and bottom points in a 2 s time span, the reason for considering such a small time span is to show the fluctuation of the curve in a very limited displacement variation range.

From the above illustration of the different motions, several characters of the behavior of the fluttering plate can be categorized

The diagnosed behavior of the system by LE and PR method most time reach the compatible conclusions. By PR method, the buckled and flat motions all have the PR value of 1. Their motions at most separated modes have negative or zero Lyapunov Exponent which indicates convergence. And chaotic motion has the expected zero values for the whole system displacement and positive Lyapunov Exponent which indicates divergence. Both methods are powerful to distinguish the system behavior, while PR method is much easier to calculate since the calculation procedure is not affected by the forms of the system.

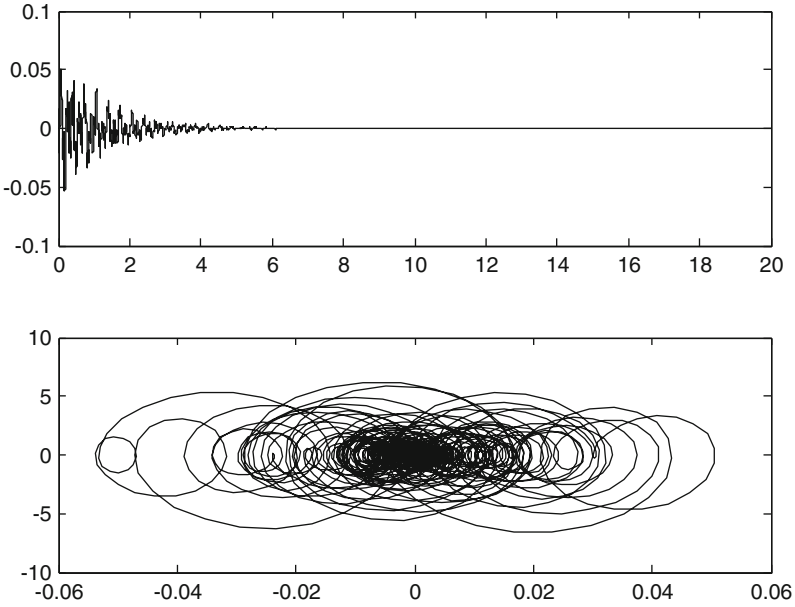

Fig. 3.21 Wave form and phase diagram of a flat motion at $Rx = -0.8, \lambda = 210$

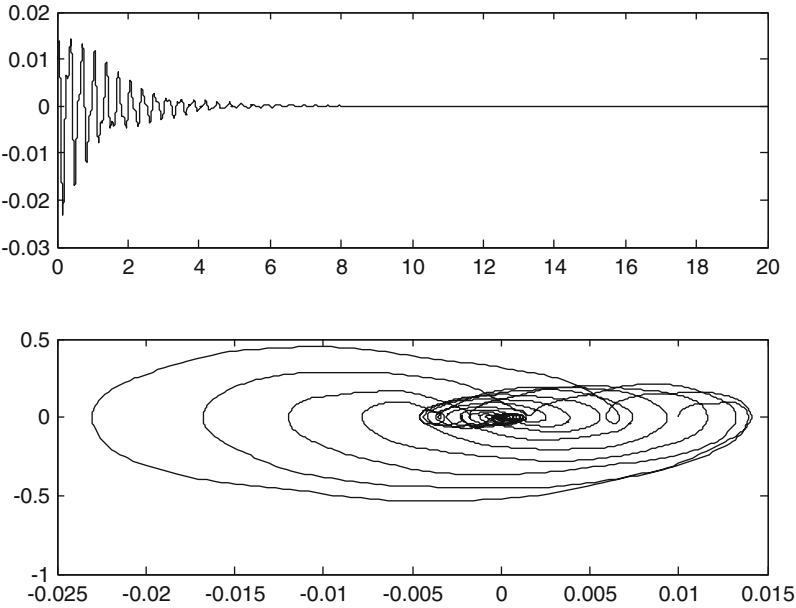

Fig. 3.22 Wave form and phase diagram of a flat motion at mode 1. $Rx = -0.8, \lambda = 210, LE = (-0.0501, -0.9997, -1.0003)$

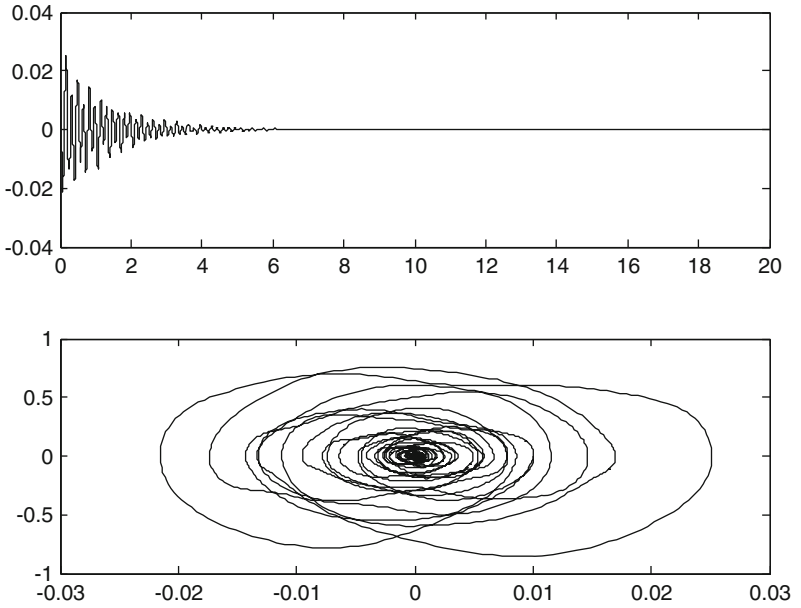

Fig. 3.23 Wave form and phase diagram of a flat motion at mode 2. $Rx = -0.8, \lambda = 210, LE = (-0.0533, -0.2574, -0.2286)$

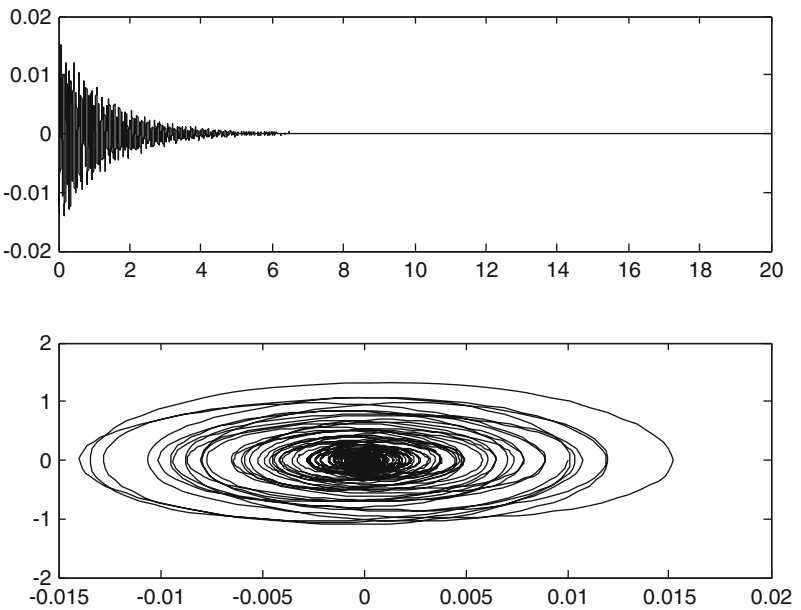

Fig. 3.24 Wave form and phase diagram of a flat motion at mode 3. $Rx = -0.8, \lambda = 210, LE = (-0.0624, -0.4869, -0.5131)$

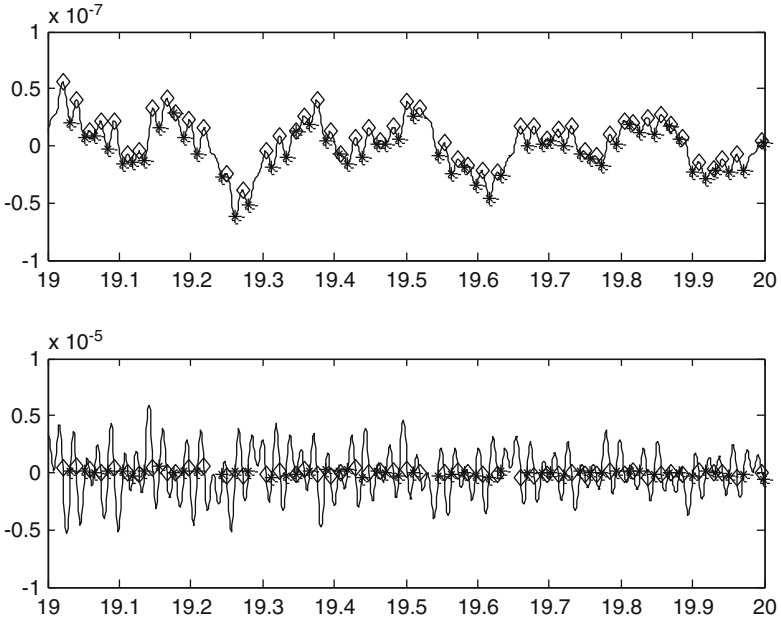

Fig. 3.25 Wave form and phase diagram of a flat motion. $Rx = -0.8, \lambda = 210, PR = 0.9997$

For the most stabilized static case like buckled and flat case, the displacement at first three modes are much larger than the other modes that they are the main contributors to the whole system displacement. Comparing Figs. 3.5, 3.6, and 3.7 with 3.21, 3.22, 3.23 and 3.24, though both stabilized at last, the flat motion convergences more quickly than the buckled motion to the equilibrium position. Therefore, the last three modes can be neglected. For the dynamic system like periodic and chaotic case, all the six modes need to be included to consider the system motion.

For the periodic case in Figs. 3.13, 3.14, 3.15, 3.16, 3.17, 3.18, and 3.19, although each motion at mode 3 to mode 5 is more like divergent as the maximum Lyapunov Exponent is a little bit larger than zero; the whole system motion is diagnosed as periodicity. This is because the supposition effect of the system motion at several modes may have canceling effect with others. This case exhibits the advantage of PR method to LE method when the individual diagnosis of the motion of each mode is not consistent with each other.

3.6 Control of Nonlinear Oscillations with Modified Fuzzy Sliding Mode Control Strategy

Equation (3.9) can be expressed as

$$\frac{d^2a_s}{d\tau^2} = -a_s(s\pi)^4 - \alpha 12\left(1-\upsilon^2\right)\left[\sum_r a_r^2\frac{(r\pi)^2}{2}\right]a_s\frac{(s\pi)^2}{2} - R_x a_s(s\pi)^2$$
$$-\lambda 2\left\{\sum_m \frac{sm}{s^2-m^2}\times\left[1-(-1)^{s+m}\right]a_m + \frac{1}{2}\left(\frac{\mu}{M\lambda}\right)^{\frac{1}{2}}\frac{da_s}{d\tau}\right\} + P2\frac{[1-(-1)^s]}{s\pi} \tag{3.24}$$

where $s = 1, \ldots, \infty$.

Thus, based on the modified FSMC [36], the control strategy of the 2D fluttering plate can be derived as

$$\begin{cases} \dfrac{da_{s1}}{d\tau} = a_{s2} \\ \dfrac{da_{s2}}{d\tau} = f_s(\mathrm{a},\tau) + d_s(\mathrm{a},\tau) + u_s \end{cases}$$
$$\begin{cases} \dfrac{dx_{s1}}{d\tau} = x_{s2} \\ \dfrac{dx_{s2}}{d\tau} = g_s(\mathrm{x},\tau) \end{cases} \tag{3.25}$$

where $s = 1, \ldots, \infty$, $d_s(\mathrm{a},\tau)$ denotes the uncertain external disturbance corresponding to the sth mode, $u_s \in R$ denotes the control input corresponding to the sth mode, a is the column vector of the velocity and acceleration of the s modes and is given as $\mathrm{a} = [a_{11}\ a_{12}\ a_{21}\ a_{22}\cdot s\ a_{s1}\ a_{s2}]^T$, x_{s1} denotes the reference signal corresponding to the sth mode, $g_s(\mathrm{x},\tau)$ denotes the specific expression of $\frac{dx_{s2}}{d\tau}$, x is the column vector of the velocity and acceleration of the control input corresponding to the s modes and is given as $\mathrm{x} = [x_{11}\ x_{12}\ x_{21}\ x_{22}\cdot s\ x_{s1}\ x_{s2}]^T$, and $f_s(\mathrm{a},\tau)$ denotes the specific expression of $\frac{d^2a_s}{d\tau^2}$ and is given below:

$$f_s(\mathrm{a},\tau) = -a_s(s\pi)^4 - \alpha 12\left(1-\upsilon^2\right)\left[\sum_r a_r^2\frac{(r\pi)^2}{2}\right]a_s\frac{(s\pi)^2}{2} - R_x a_s(s\pi)^2$$
$$-\lambda 2\left\{\sum_m \frac{sm}{s^2-m^2}\times\left[1-(-1)^{s+m}\right]a_m + \frac{1}{2}\left(\frac{\mu}{M\lambda}\right)^{\frac{1}{2}}\frac{da_s}{d\tau}\right\} + P2\frac{[1-(-1)^s]}{s\pi} \tag{3.26}$$

Based on the FSMC ([32, 33]), the control input u_s is given as

$$u_s = ueq_s - k\,f_s * uf_s \tag{3.27}$$

Table 3.1 The fuzzy rule of uf_s

		ueq_s						
uf_s		1	2/3	1/3	0	−1/3	−2/3	−1
$\frac{dueq_s}{d\tau}$	1	−1	−1	−1	−1	−2/3	−1	0
	2/3	−1	−1	−1	−2/3	−1	0	1/3
	1/3	−1	−1	−2/3	−1	0	1/3	2/3
	0	−1	−2/3	−1	0	1/3	2/3	1
	−1/3	−2/3	−1	0	1/3	2/3	1	1
	−2/3	−1	0	1/3	2/3	1	1	1
	−1	0	1/3	2/3	1	1	1	1

where ueq_s is the equivalent control input corresponding to the sth mode and is given as

$$ueq_s = -\left[(a_{s2} - x_{s2}) + \eta_s * (a_{s1} - x_{s1})\right] \tag{3.28}$$

and $\eta_s \in R^+; kf_s > |a_{s1}|$ is the normalization factor of a corresponding to the sth mode, and uf_s is determined by the fuzzy control rule shown in the Table 3.1.

In this section, the modified FSMC will be applied in controlling and stabilizing the chaotic motion of the 2D fluttering plate, which has been identified with LE and PR methods and shown in Figs. 3.8, 3.9, 3.10, and 3.11.

The initial condition is given below:

$$a_{11} = 0.01,\ a_{21} = 0.01,\ a_{31} = 0.01,\ a_{41} = 0.01,\ a_{51} = 0.01,\ a_{61} = 0.01$$
$$a_{12} = 0,\ a_{22} = 0,\ a_{32} = 0,\ a_{42} = 0.,\ a_{52} = 0,\ a_{62} = 0$$

The uncertain external disturbance is given below:

$$d_1(\mathrm{a}, \tau) = -0.01 \sin(a_{11}),$$
$$d_2(\mathrm{a}, \tau) = -0.005 \sin(a_{21}),$$
$$d_3(\mathrm{a}, \tau) = -0.001 \sin(a_{31}),$$
$$d_4(\mathrm{a}, \tau) = -0.0001 \sin(a_{41}),$$
$$d_5(\mathrm{a}, \tau) = -0.00002 \sin(a_{51}),$$
$$d_6(\mathrm{a}, \tau) = -0.00001 \sin(a_{61})$$

The reference signals are given below:

$$x_{11} = 0.8 \sin(\pi\tau),\ x_{21} = 0.3 \sin(\pi\tau),\ x_{31} = 0.03 \sin(\pi\tau)$$
$$x_{41} = 0.005 \sin(\pi\tau),\ x_{51} = 0.001 \sin(\pi\tau),\ x_{61} = 0.0005 \sin(\pi\tau)$$

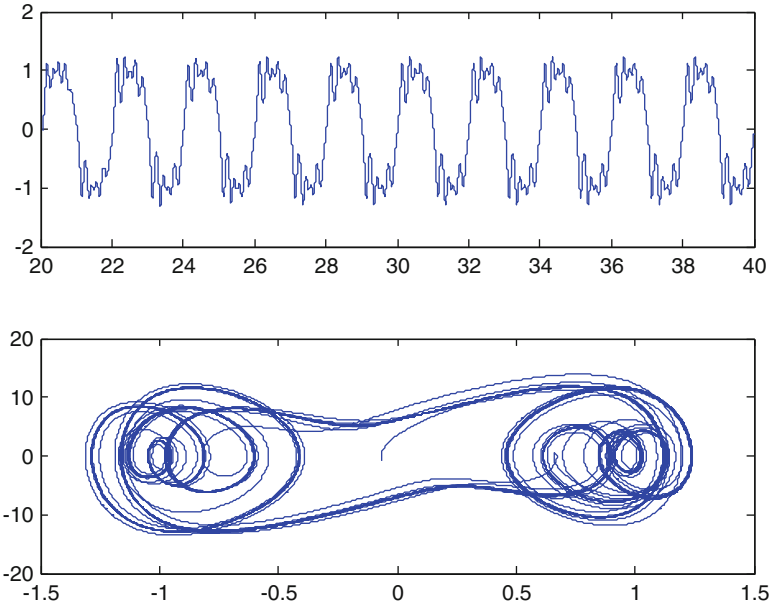

Fig. 3.26 Wave form and phase diagram of the motion at mode 1 after the modified FSMC applied. $R_x = -4\pi^2$, $\lambda = 117$

η_s and $k\,f_s$ are given below:

$$\eta_1 = \eta_2 = \eta_3 = \eta_4 = \eta_5 = \eta_6 = 1500$$
$$k\,f_1 = k\,f_2 = k\,f_3 = k\,f_4 = k\,f_5 = k\,f_6 = 50$$

The responses corresponding to the six modes are presented in Figs. 3.32, 3.33, 3.34, 3.35, 3.36, and 3.37. It can be discovered: once the modified FSMC is applied, the motion of the six modes will be synchronized to the corresponding reference signals and gradually stabilized.

The control inputs corresponding to the six modes are presented in Figs. 3.32, 3.33, 3.34, 3.35, 3.36, and 3.37 from which it can be learned the control inputs corresponding to the six modes would vary periodically. Besides, from Figs. 3.26, 3.27, 3.28, 3.29, 3.30, 3.31 and Figs. 3.32, 3.33, 3.34, 3.35, 3.36, 3.37, it can be found the higher the number of the mode is, the lower the amplitude of the vibration of the mode will be, and the smaller the control input corresponding to the mode will be required.

The response of the specific point, which is located at 75% length of the beam, is presented in Fig. 3.38. It can be discovered once the modified FSMC is applied, the motion of the six modes will be synchronized and gradually stabilized, and thus the response of the selected point of the fluttering 2D plate will be stabilized from the chaotic motion into a periodic motion, amplitude of which will be reduced as well.

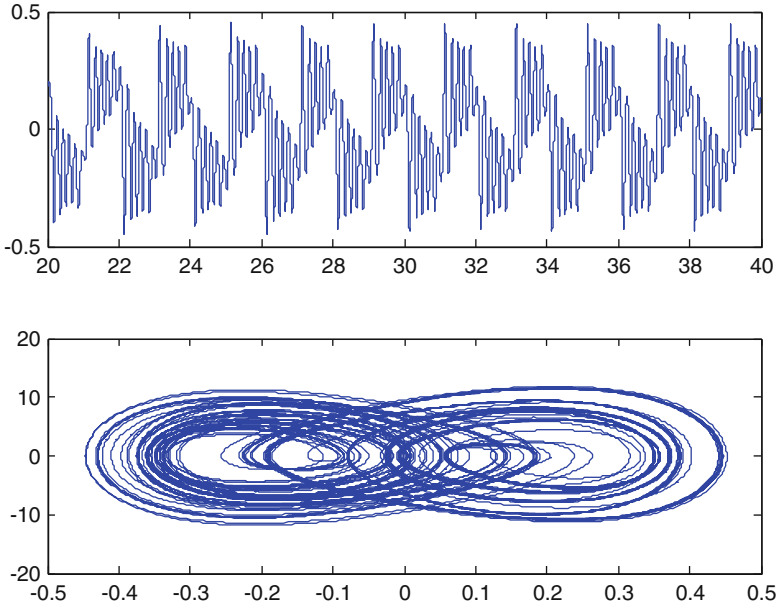

Fig. 3.27 Wave form and phase diagram of the motion at mode 2 after the modified FSMC applied. $R_x = -4\pi^2$, $\lambda = 117$

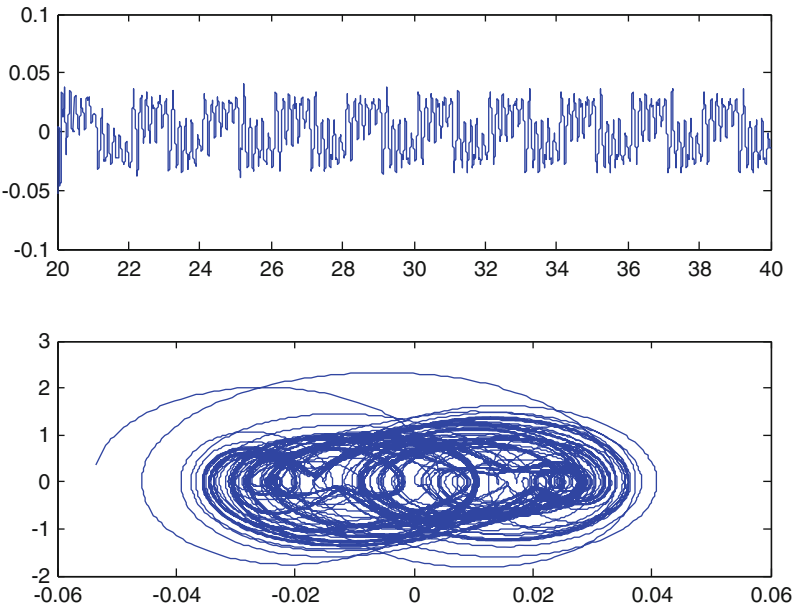

Fig. 3.28 Wave form and phase diagram of the motion at mode 3 after the modified FSMC applied. $R_x = -4\pi^2$, $\lambda = 117$

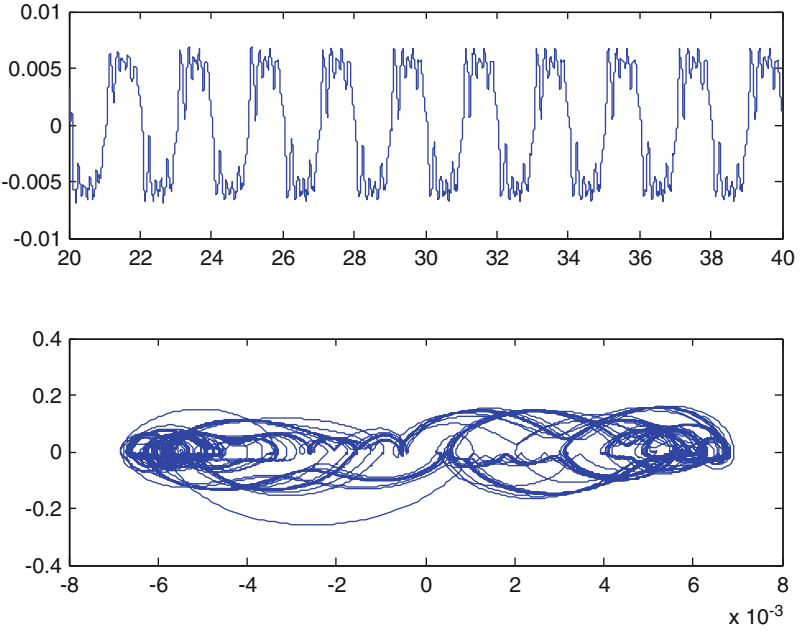

Fig. 3.29 Wave form and phase diagram of the motion at mode 4 after the modified FSMC applied. $R_x = -4\pi^2$, $\lambda = 117$

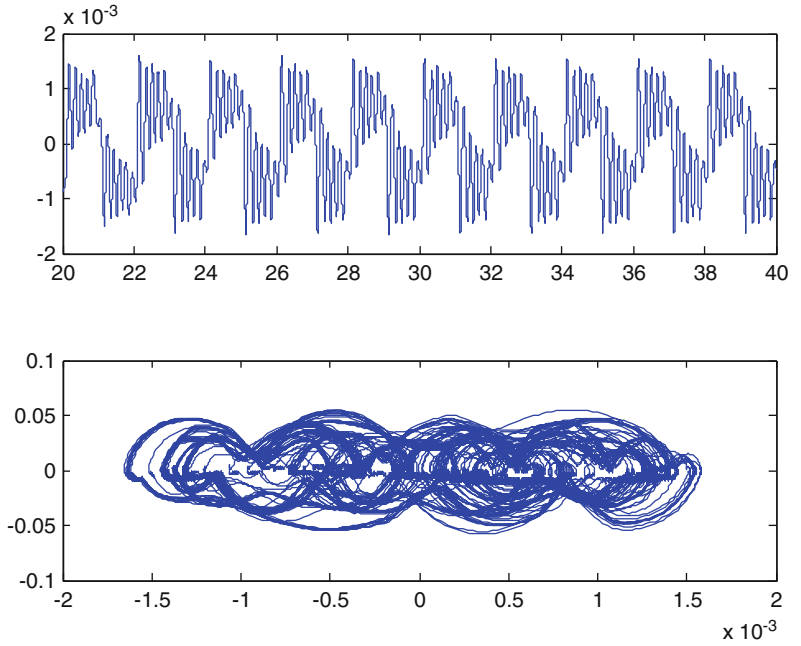

Fig. 3.30 Wave form and phase diagram of the motion at mode 5 after the modified FSMC applied. $R_x = -4\pi^2$, $\lambda = 117$

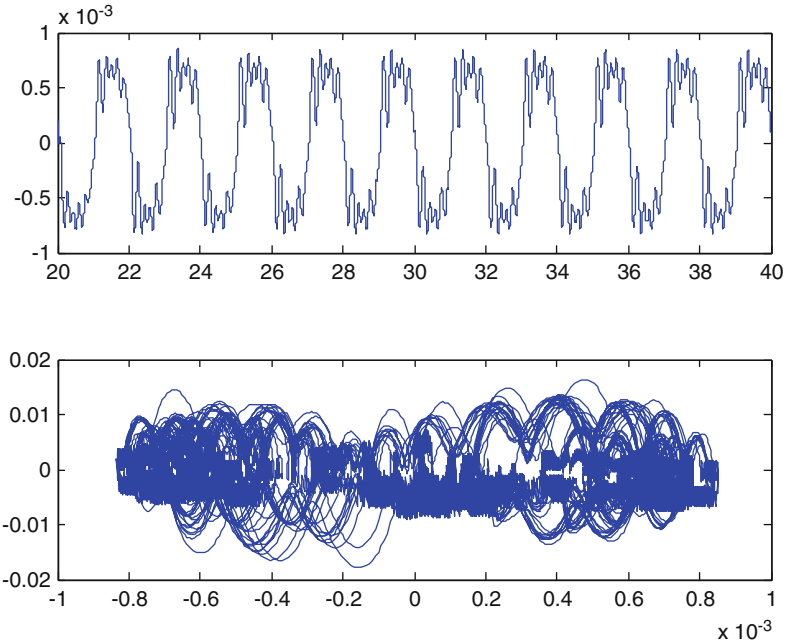

Fig. 3.31 Wave form and phase diagram of the motion at mode 6 after the modified FSMC applied. $R_x = -4\pi^2$, $\lambda = 117$

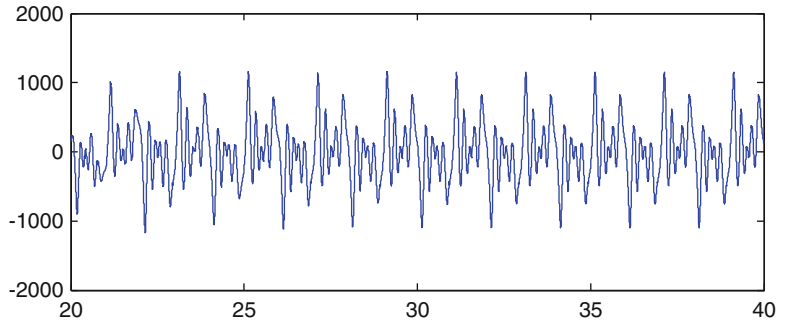

Fig. 3.32 Control input at mode 1

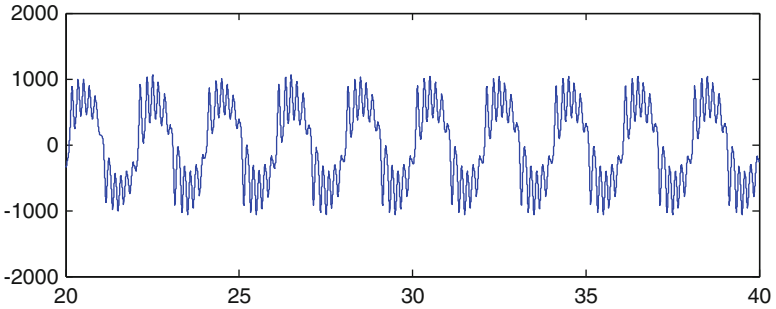

Fig. 3.33 Control input at mode 2

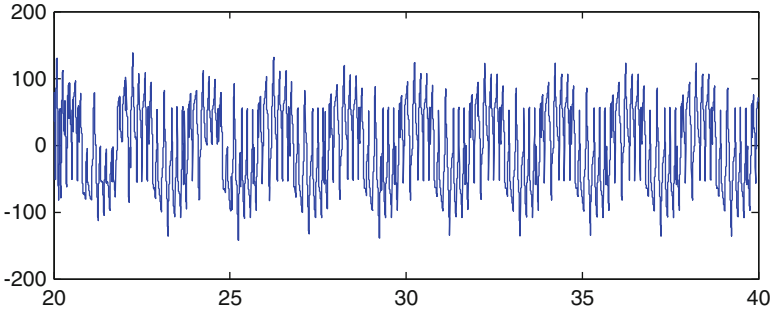

Fig. 3.34 Control input at mode 3

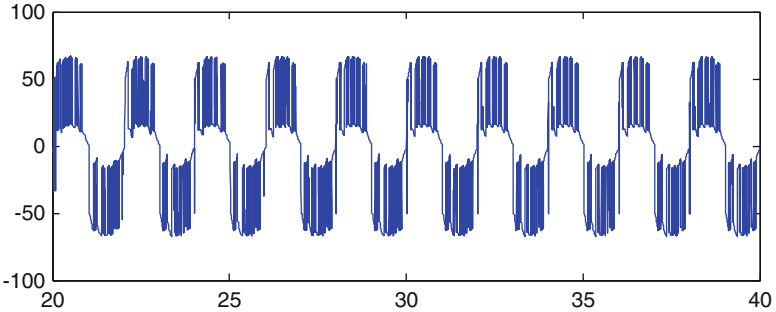

Fig. 3.35 Control input at mode 4

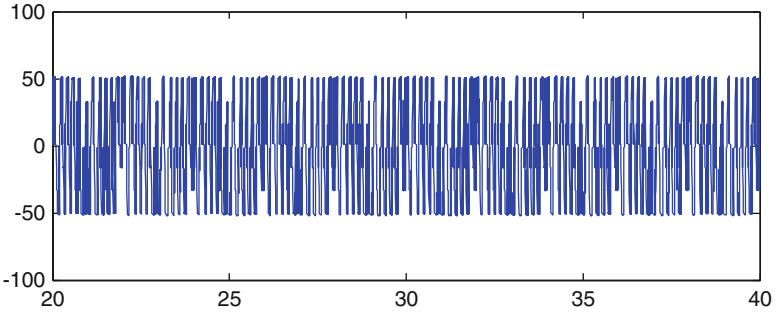

Fig. 3.36 Control input at mode 5

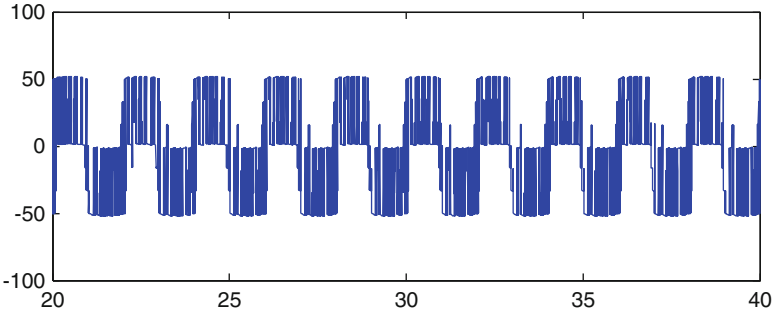

Fig. 3.37 Control input at mode 6

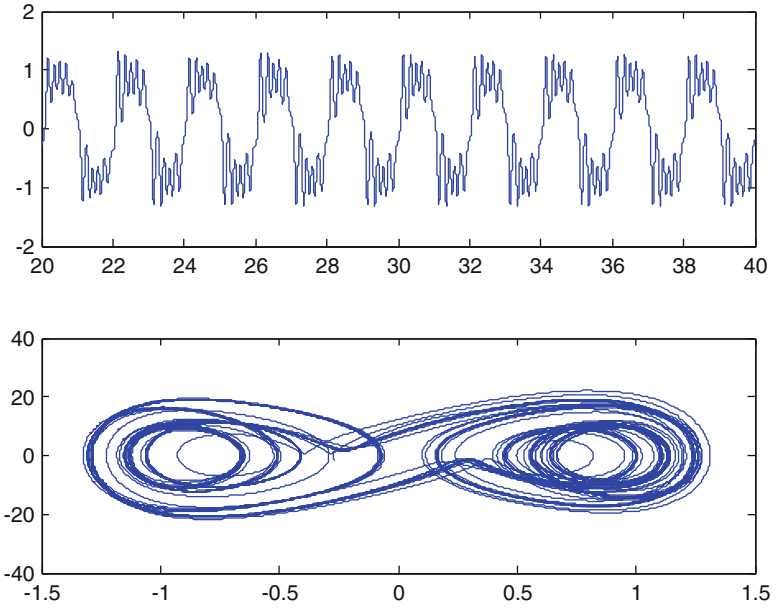

Fig. 3.38 Wave form and phase diagram of the selected point located at the 75% length of the beam after the application of the modified FSMC

Key Symbols

D	Plate stiffness
E	Modulus of elasticity
h	Plate thickness
K	Spring constant
L	Panel length
M	Mach number
m	Mode number
N_x	In-plane force
$N_x^{(a)}$	Applied in-plane force
$p - p_\infty$	Aerodynamic pressure
Δp	Static pressure differential across the panel
P	$\Delta p l^4 / Dh$
R_x	$N_x^{(a)} L^2 / D$
r	Mode number
s	Mode number
t	Time
U_∞	Flow velocity
W	w/h
w	Plate deflection
α	Spring stiffness parameter
β	$(M^2 - 1)^{1/2}$
λ	$2qa^3 / \beta D$
μ	$\rho L / \rho_m h$
ν	Poisson's ratio
ρ	Air density
ρ_m	Plate density
τ	$t(D/\rho_m h l^4)^{1/2}$
a_{s1}	The displacement corresponding to the sth mode
a_{s2}	The velocity corresponding to the sth mode
x_{s1}	The displacement of the reference signal of the sth mode
x_{s2}	The velocity of the reference signal corresponding to the sth mode
a	The column vector of the velocity and acceleration of the s modes
f_s (a, τ)	The expression of the acceleration corresponding to the sth modes
g_s (a, τ)	The expression of the reference signal acceleration of the sth mode
d_s (a, τ)	The uncertain external disturbance corresponding to the sth mode
u_s	The control input corresponding to the sth mode
R	Real number
ueq_s	The equivalent control input corresponding to the sth mode
η_s	A positive real number
$k f_s$	The normalization factor of a corresponding to the sth mode
n	The number of points in Poincare map
NPP	The number of periodically overlapped points in Poincare map

$Q(.), P(.)$	The step functions
γ	The periodicity ratio
$f_s(\mathrm{a}, \tau)$	The expression of the acceleration corresponding to the sth modes
J	The Jacobian matrix
$LE(\hat{\lambda})$	Lyapunov Exponents

References

1. Bolotin VV (1963) Nonconservative problems of the theory of elastic stability. Pergamon Press, New York
2. Kantorowich LV, Krylov VI (1964) Approximate methods of higher analysis. Interscience, New York
3. Mikhlin, SG (1964) Variational methods in mathematical physics. MacMillan, New York
4. Dowell EH (1966) Nonlinear oscillations of a fluttering plate. AIAA J 4(7):1267–1275
5. Dowell EH (1967) Nonlinear oscillations of a fluttering plate II. AIAA J 5(10):1856–1862
6. Shiau LC, Lu LT (1992) Nonlinear flutter of two-dimensional simply supported symmetric composite laminated plates. J Aircraft 29(1):140–145
7. Reddy JN (1986) Applied functional analysis and variational methods in engineering. McGraw-Hill, New York
8. Ketter DJ (1967) Flutter of flat, rectangular, orthotropic panels. AIAA J 5(1):116–124
9. Garrick EI, Reed WH (1981) Historical development of aircraft flutter. J Aircraft 18(11):897–912
10. Sipcic SR (1990) The chaotic response of a fluttering panel: the influence of maneuvering. Nonlinear Dyn 1(3):243–264
11. Shubov MA (2006) Flutter phenomenon in aeroelasticity and its mathematical analysis. J Aerospace Eng 19(1):1–12
12. Dowell EH, Ventres CS (1970) Comparison of theory and experiment for nonlinear flutter of loaded plates. AIAA J 8(11):2022–2030
13. Li KL, Zhang JZ, Lei PF (2010) Simulation and nonlinear analysis of panel flutter with thermal effects in supersonic flow. In: Luo ACJ (ed) Dynamical systems. Springer, New York, pp 61–76
14. Librescu L, Marzocca P, Silva WA (2004) Linear/nonlinear supersonic panel flutter in a high-temperature field. J Aircraft 41(4):918–924
15. Schaeffer HG, Heard WL (1965) Flutter of a flat panel subjected to a nonlinear temperature distribution. AIAA J 3(10):1918–1923
16. Xue DY, Mei C (1993) Finite element nonlinear panel flutter with arbitrary temperatures in supersonic flow. AIAA J 31(1):154–162
17. Alligood KT, Sauer T, Yorke JA (1997) Chaos: an introduction to dynamical systems. Springer, New York, LLC
18. Devaney RL (2003) An introduction to chaotic dynamical systems. Westview Press
19. Gollub JP, Baker GL (1996) Chaotic dynamics. Cambridge University Press
20. Nayfeh AH, Mook DT (1989) Non-linear oscillation. Wiley, New York
21. Strogatz S (2000) Nonlinear dynamics and chaos. Perseus Publishing
22. Valsakumar MC, Satyanarayana SV, Sridhar V (1997) Signature of chaos in power spectrum. Pramana J Phys 48:69–85
23. Peitgen HO, Richter PH (1986) The beauty of fractals: images of complex dynamical systems. Springer
24. Peitgen HO, Saupe D (1988) The science of fractal images. Springer
25. Lauwerier H (1991) Fractals. Princeton University Press
26. Kumar A (2003) Chaos, fractals and self-organisation, new perspectives on complexity in nature. National Book Trust

27. Zaslavsky GM (2005) Hamiltonian chaos and fractional dynamics. Oxford University Press
28. Parks PC (1992) Lyapunov's stability theory – 100 years on. IMA J Math Control Inf 9:275–303
29. Wolf A, Swift JB, Swinney HL, Vastano JA (1985) Determining Lyapunov Exponents from a time series. Phys D Nonlinear Phenom 16(3):285–317
30. Dai L, Singh MC (1997) Diagnosis of periodic and chaotic responses in vibratory systems. J Acoust Soc Am 102(6):3361–3371
31. Utkin VI (1992) Sliding modes in control and optimization. Springer, Berlin
32. Kuo CL, Shieh CS, Lin CH, Shih SP (2007) Design of fuzzy sliding-mode controllerfor chaos synchronization. Commun Comput Inf Sci 5:36–45
33. Yau HT, Kuo CL (2006) Fuzzy sliding mode control for a class of chaos synchronization with uncertainties. Int J Nonlinear Sci Numer Simul 7(3):333–338
34. Yau HT, Wang CC, Hsieh CT, Cho CC (2011) Nonlinear analysis and control of the uncertain micro-electromechanical system by using a fuzzy sliding mode control design. Comput Math Appl 61(8):1912–1916
35. Haghighi HH, Markazi AH (2010) Chaos prediction and control in MEMS resonators. Commun Nonlinear 15(10):3091–3099
36. Dai L, Sun L (2012) On the fuzzy sliding mode control of nonlinear motion in a laminated beam. JAND 1(13):287–307
37. Donea JA (1984) Taylor–Galerkin method for convective transport problems. Int J Numer Meth Eng 20(1):101–119
38. Dai L, Han L (2011) Analysing periodicity, nonlinearity and transitional characteristics of nonlinear dynamic systems with Periodicity Ratio (PR). Commun Nonlinear Sci Numer Simul 16(12):4731–4744
39. Dai L, Singh MC (1995) Periodicity ratio in diagnosing chaotic vibrations. In: 15th Canadian congress of applied mechanics, vol 1, pp 390–391
40. Dai L, Singh MC (1998) Periodic, Quasiperiodic and chaotic behavior of a driven froude pendulum. Nonlinear Mech 33(6):947–965
41. Rong H, Meng G, Wang X, Xu W, Fang T (2002) Invariant measures and Lyapunov-exponents for stochastic Mathieu system. Nonlinear Dyn 30:313–321
42. Shahverdian AY, Apkarian AV (2007) A difference characteristic for one-dimensional deterministic systems. Commun Nonlinear 12(3):233–242

Chapter 4
A New Approach to the Tracking Control of Uncertain Nonlinear Multi-body Mechanical Systems

Firdaus E. Udwadia and Thanapat Wanichanon

Abstract This chapter presents a new approach for the tracking control of uncertain mechanical systems. Real-life multi-body systems are in general highly nonlinear and modeling them is intrinsically error prone due to uncertainties related to both their description and the description of the various forces that they may be subjected to. As such, in the modeling of such systems one only has in hand the so-called nominal system—a model based upon our best assessment of the system and our best assessment of the generalized forces acting on it. Uncertainties that are time-varying, unknown but bounded, are assumed in this chapter, and a new approach to the development of a closed-form controller is developed. The approach uses the concept of a generalized sliding surface. Its closed-form approach can guarantee, regardless of the uncertainty, that the uncertain system can track a desired reference trajectory that the nominal system is required to follow. An example of a simple multi-body system whose description is known only imprecisely is illustrated showing the simplicity of the approach and its efficacy in tracking the trajectory of the nominal system. The approach is easily implemented for a wide range of complex multi-body mechanical systems.

4.1 Introduction

Most real-life complex mechanical systems are only known imprecisely. Uncertainties in the description of such physical systems and in the description of the generalized forces acting on them are often inescapable. A tracking controller that

F.E. Udwadia (✉)
University of Southern California, 430K Olin Hall, Los Angeles, CA 90089-1453, USA
e-mail: fudwadia@usc.edu

T. Wanichanon
Department of Mechanical Engineering, Mahidol University, 25/25 Puttamonthon, Nakorn Pathom 73170, Thailand
e-mail: thanapat.wan@mahidol.ac.th

R.N. Jazar and L. Dai (eds.), *Nonlinear Approaches in Engineering Applications 2*,
DOI 10.1007/978-1-4614-6877-6_4,

can deal with such uncertainties in the modeling of uncertain nonlinear multi-body mechanical systems is thus needed. The problem of tracking controls for such uncertain systems has been actively studied by numerous researchers. [1–7] give a brief sampling of some of the researchers who have made substantial contributions in this area.

In this chapter, a new approach is developed to obtaining a closed-form controller for uncertain multi-body systems. The general procedure used in obtaining this controller is made up of two steps. We first obtain a controller for a nominal system, which is the system that refers to our best assessment of a given real-life uncertain system. This nominal controller can be analytically obtained with the aid of a recent finding in analytical dynamics, the so-called *fundamental equation* (Udwadia and Kalaba [8–10]), to guarantee exact constraint-following for the assumed nominal system. However, this analytical result is correct only under the assumption that the modeling of the physical system has no errors and uncertainties. In the second step, using the trajectory obtained from the nominal system as the tracking signal, we modify the nominal controller to account for uncertainties in our nominal model. These uncertainties stem from two main sources—uncertainties in the knowledge of the physical system and/or uncertainties in the 'given' forces applied to the system. These uncertainties could be time-varying; no further information is assumed in this work about them, except that they are bounded. The aim is to develop a closed-form controller that allows the real-life uncertain system to track a prespecified trajectory for the corresponding nominal system. The generalized concept based on a sliding surface control is used to design an additional additive controller to compensate for the uncertainty in the mechanical system. An example of a mechanical system is provided to demonstrate the efficacy and ease of implementation of the tracking control methodology.

The general approach that we follow is to view the tracking control problem in the framework of constrained motion. We view the control requirements as constraints on the nonlinear dynamical system and obtain closed-form generalized control forces to satisfy these requirements. In what follows we shall therefore use the terms 'requirements' and 'constraints,' interchangeably, as well as the terms 'control forces' and 'constraint forces,' and the terms 'controlled system' and 'constrained system.'

4.2 On the Dynamics of the Nominal Multi-body Systems

4.2.1 System Description of the Nominal System

We begin by introducing the description of the nominal system, by which we mean our best assessment of the actual real-life system (whose description is known only imprecisely). It is useful to conceptualize the description of such a nominal multi-body system in a three-step procedure [11–15]. We do this in the following way:

First, we describe the uncontrolled (unconstrained) system in which the coordinates are all assumed independent of each other. The equation of motion of this system is given, using Lagrange's equation, by

$$M(q,t)\ddot{q} = Q(q,\dot{q},t), \tag{4.1}$$

with the initial conditions

$$q(t=0) = q_0,\ \dot{q}(t=0) = \dot{q}_0, \tag{4.2}$$

where q is the generalized coordinate n-vector; $M > 0$ is the n by n mass matrix which is a function of q and t; and Q is an n-vector, called the 'given' force, which is a known function of q, $\dot{q}$, and t.

From Eq. (4.1) we find the acceleration of the uncontrolled system given by

$$a := M^{-1}(q,t)\ Q(q,\dot{q},t). \tag{4.3}$$

Second, we impose a set of control requirements as constraints on this uncontrolled system. We suppose that the uncontrolled system is now subjected to the m sufficiently smooth control requirements given by [13]

$$\varphi_i(q,\dot{q},t) = 0,\ \ i = 1,2,\ldots,m, \tag{4.4}$$

where $r \leq m$ equations in the equation set (4.4) are functionally independent. The control constraints described by Eq. (4.4) include all the usual varieties of holonomic and/or nonholonomic constraints, and then some. The presence of the control requirements does not permit all the components of the n-vectors q_0 and $\dot{q}_0$ to be independently assigned. We shall assume that the initial conditions (4.2) satisfy the m control requirements. (If not, the control constraints can be expressed in an alternative form so that they are asymptotically satisfied [16]; see Sect. 4.2.2).

Differentiating the control requirements (4.4) with respect to time t we obtain the relation [17]

$$A(q,\dot{q},t)\,\ddot{q} = b(q,\dot{q},t), \tag{4.5}$$

where A is an m by n matrix whose rank is r and b is an m-vector. We note that each row of A arises by appropriately differentiating one of the m control requirements in the set given in relation (4.4).

In the third step, the equation of motion of the '*controlled nominal system*' or the '*nominal system*' is given by

$$M(q,t)\,\ddot{q} = Q(q,\dot{q},t) + Q^c(q,\dot{q},t), \tag{4.6}$$

where Q^c is the control force n-vector that arises to ensure that the control requirements (4.5) are satisfied. The explicit equation of motion of the nominal system is given by the *fundamental equation* [10, 16]

$$M\ddot{q} = Q + A^T(AM^{-1}A^T)^{+}(b - Aa), \tag{4.7}$$

wherein the various quantities have been defined in the previous two steps and the superscript "+" denotes the Moore–Penrose (MP) inverse of a matrix. In the above equation, and in what follows, we shall suppress the arguments of the various quantities unless required for clarity.

We note that Eq. (4.7) is valid: (1) whether or not the control requirements are holonomic or nonholonomic, (2) whether or not they are nonlinear functions of their arguments, and (3) whether or not they are functionally dependent.

We also note that from Eq. (4.7) the control force that the uncontrolled system is subjected to, because of the presence of the control requirements (4.4), can be explicitly expressed as

$$Q^c(t) := Q^c(q(t), \dot{q}(t), t) = A^T(AM^{-1}A^T)^+(b - Aa). \tag{4.8}$$

The control force given in Eq. (4.8) is optimal in the sense that it minimizes the control cost $Q^{cT}M^{-1}Q^c$ at *each* instant of time [16, 17].

We refer to the system described by Eq. (4.7) as the '*nominal system*,' implying that (1) it includes our best assessment of the information we have regarding the system's parameters, its structure, and the nature of the 'given' force n-vector Q that the system is subjected to, and (2) it exactly satisfies the control requirements placed on it. Pre-multiplying both sides of Eq. (4.7) with M^{-1}, the acceleration of the nominal system that satisfies the constraint (4.4) can be expressed as

$$\ddot{q} = a + M^{-1}A^T(AM^{-1}A^T)^+(b - Aa) := a + M^{-1}Q^c(t), \tag{4.9}$$

a relation which we shall require later on.

While the methodology presented in this chapter is applicable to general nonlinear, dynamical systems, throughout this chapter we shall illustrate the methodology by applying it to the simple example of a triple pendulum.

4.2.2 An Example

To demonstrate the applicability of the control methodology, we introduce an example of a simple multi-body system. We will continue this example all the way through this chapter. It is straightforward to extend this example to more general situations.

Consider a planar pendulum consisting of three masses m_1, m_2, and m_3 suspended from massless rods of lengths L_1, L_2, and L_3 moving in the XY-plane (see Fig. 4.1). The inertial frame of reference is fixed at the point of suspension, O, of the triple pendulum and the X-axis is taken as the datum for computing the potential energy of the system. Though simple, the system can exhibit highly complex dynamics.

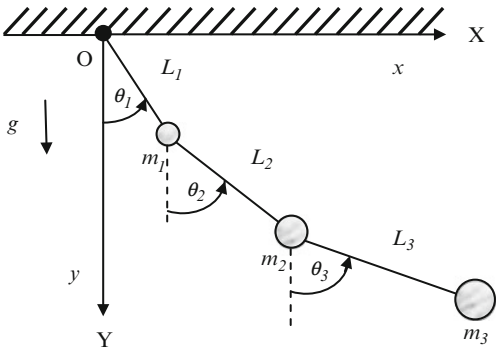

Fig. 4.1 Triple pendulum with the datum at the origin O

The masses are constrained to move so that the total energy, $E(t)$, of the system is required to equal the sum of the energies (kinetic and potential) of only the two masses m_2 and m_3, i.e., $E(t) = E_2(t) + E_3(t)$ where we have denoted $E_i(t)$ as the total energy of mass m_i. We now develop the closed-form controller for this nominal system, in which the properties of the system, its structure, and the forces acting on it are considered to be known.

The three-step approach described in the last subsection is now illustrated. We begin by writing the equation of the uncontrolled system [corresponding to Eq. (4.1)] using the generalized coordinate 3-vector $q = [\theta_1, \theta_2, \theta_3]^T$ whose components, in the absence of the above-mentioned energy control requirement, are independent of one another. Lagrange's equations then yield the relation

$$M(q;\, m_1, m_2, m_3)\ddot{q} = Q(q;\, m_1, m_2, m_3) \tag{4.10}$$

where the elements of the 3 by 3 symmetric matrix M are given by

$$\begin{aligned} &M_{11} = (m_1 + m_2 + m_3)L_1^2;\; M_{12} = (m_2 + m_3)L_1 L_2 \cos(\theta_{12});\; M_{13} = m_3 L_1 L_3 \cos(\theta_{13}) \\ &M_{22} = (m_2 + m_3)L_2^2;\; M_{23} = m_3 L_2 L_3 \cos(\theta_{23});\; M_{33} = m_3 L_3^2, \end{aligned} \tag{4.11}$$

and the elements of the 3-vector Q are given by

$$\begin{aligned} Q_1 &= -(m_2 + m_3)L_1 L_2 \dot{\theta}_2^2 \sin(\theta_{12}) - m_3 L_1 L_3 \dot{\theta}_3^2 \sin(\theta_{13}) \\ &\quad - (m_1 + m_2 + m_3) g L_1 \sin\theta_1 \\ Q_2 &= (m_2 + m_3)L_1 L_2 \dot{\theta}_1^2 \sin(\theta_{12}) - 2(m_2 + m_3)L_1 L_2 \dot{\theta}_1 \dot{\theta}_2 \sin(\theta_{12}) \\ &\quad - m_3 L_2 L_3 \dot{\theta}_3^2 \sin(\theta_{23}) - (m_2 + m_3) g L_2 \sin\theta_2 \\ Q_3 &= m_3 L_1 L_3 (\dot{\theta}_1^2 - 2\dot{\theta}_1 \dot{\theta}_3) \sin(\theta_{13}) + m_3 L_2 L_3 (\dot{\theta}_2^2 - 2\dot{\theta}_2 \dot{\theta}_3) \sin(\theta_{23}) \\ &\quad - m_3 g L_3 \sin\theta_3. \end{aligned} \tag{4.12}$$

In the above, we have denoted $\theta_{ij} = \theta_i - \theta_j$, and we explicitly show in Eq. (4.10) the parameters m_1, m_2, and m_3 which we will later consider to be known only imprecisely.

Using the X-axis as the datum (see Fig. 4.1), in the second step we describe the energy control requirement $E(t) = E_2(t) + E_3(t)$ which is equivalent to the relation

$$E_1(t) = 0, \tag{4.13}$$

where the energy E_1 of mass m_1 is given by

$$E_1 = \frac{1}{2} m_1 L_1^2 \dot{\theta}_1^2 - m_1 g L_1 \cos\theta_1. \tag{4.14}$$

Since the system may not initially (at time $t = 0$) satisfy this control requirement we modify the control requirement (4.13) using the trajectory stabilization relation [16],

$$\dot{E}_1 + \alpha E_1 = 0, \tag{4.15}$$

where $\alpha(t) > 0$ is a positive function. By Eqs. (4.14) and (4.15) we obtain the control requirement

$$A\ddot{q} := \begin{bmatrix} L_1^2\dot{\theta}_1 & 0 & 0 \end{bmatrix} \ddot{q} = -gL_1 \sin\theta_1 \dot{\theta}_1 - \alpha\left(\frac{1}{2} L_1^2 \dot{\theta}_1^2 - gL_1 \cos\theta_1\right) := b. \tag{4.16}$$

We note that the masses m_i do not enter this control requirement. For the final step we use the information from Eqs. (4.10)–(4.12) and (4.16) to obtain the description of the motion of the controlled nominal system as [see Eq. (4.6)]

$$M\ddot{q} = Q + Q^c, \tag{4.17}$$

where Q^c represents the generalized control forces that will be exerted on the bobs, causing them to move so that at every instant of time the control requirement (4.16) is satisfied. The determination of these control forces is given by using the fundamental equation as in [10] [see Eq. (4.8)]

$$Q^c(t) := Q^c(q, \dot{q}, t) = A^T (AM^{-1}A^T)^+ (b - Aa). \tag{4.18}$$

Using Eq. (4.18) in Eq. (4.17) and pre-multiplying both sides of the equation by M^{-1}, we obtain the constrained acceleration of the nominal system as [see Eq. (4.9)],

$$\ddot{q} = a + M^{-1}A^T (AM^{-1}A^T)^+ (b - Aa). \tag{4.19}$$

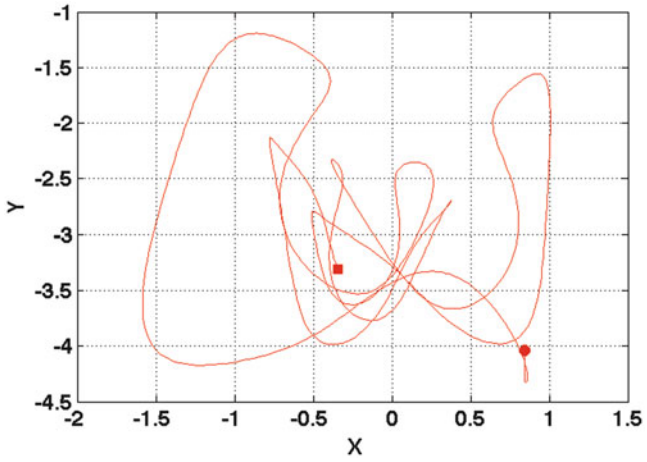

Fig. 4.2 Trajectory of mass m_3 in the XY-plane (meter) of the triple pendulum shown for a duration of 10 s. The trajectory starts at the *circle* and ends at the *square*

4.2.3 Numerical Results and Simulations of the Control Problem

In what follows we shall assume that the real-life planar triple pendulum described above has masses whose values are only imprecisely known and that our best assessment of their values is: $m_1 = 1$ kg, $m_2 = 2$ kg, and $m_3 = 3$ kg. Thus, these are the values of the three masses of our nominal system.

The lengths of the massless rods are $L_1 = 1$ m, $L_2 = 1.5$ m, and $L_3 = 2$ m. At $t = 0$, the masses are located with the angles of $\theta_1(0) = 1$ rad, $\theta_2(0) = 0$ rad, and $\theta_3(0) = 0$ rad with respect to the vertical Y-axis (see Fig. 4.1). The initial velocities of the three bobs are taken to be $\dot{\theta}_1(0) = 0.001$ rad/s, $\dot{\theta}_2(0) = 0$ rad/s, and $\dot{\theta}_3(0) = 0$ rad/s. We note that these initial conditions do not satisfy the constraint, $E_1 = 0$. Thus the parameter α in Eq. (4.15) is chosen to be $0.02\,\|A\|_2^4$ where $\|A\|_2$ is the L^2 norm of the matrix A in Eq. (4.16). The acceleration due to gravity is downwards and of magnitude $g = 9.81\ m/s^2$. Numerical integration throughout this chapter is done in the *Matlab* environment, using a variable time step integrator with a relative error tolerance of 10^{-8} and an absolute error tolerance of 10^{-12}.

Figure 4.2 plots the trajectory of mass m_3 of the triple pendulum in the XY-plane for a period of 10 s. The start of the trajectory is marked by a circle and its end is marked by a square, as shown in the figure. From here on throughout this chapter, the start and the end of all trajectories are indicated likewise. Figure 4.3 shows the angular responses, in numbers of revolutions (of 360°), of each of the masses as a function of time. The energies of the three masses are shown in Fig. 4.4. We see that

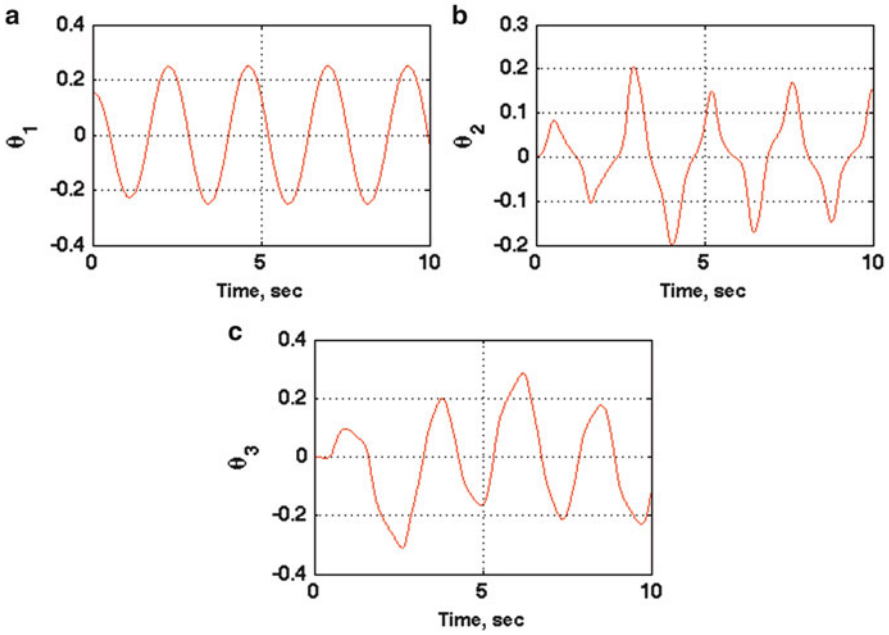

Fig. 4.3 Angular responses of the masses (**a**) m_1, (**b**) m_2, and (**c**) m_3 [no. of revolutions (360°)]

the total energy (E) is the sum of the energies of mass m_2 (E_2) and mass m_3 (E_3), i.e., $E = E_2 + E_3$. Figure 4.4a also shows the extent of error in satisfying this control requirement $E_1 = 0$. The magnitude of this error is seen to be commensurate with the relative error tolerance used in the numerical integration. In Fig. 4.5, we show the control force Q^c on the nominal system in order to follow the desired control requirement $E(t) = E_2(t) + E_3(t)$.

4.3 Description of the Control Approach

Our nominal system, for which we have found an exact controller so far, is our best assessment of our real-life system. As mentioned before, there are always uncertainties in the description of any real-life dynamical systems. These uncertainties arise due to our lack of precise knowledge of the system, and/or of the given forces acting on it. With the conceptualization of the nominal system given in the previous section, these uncertainties are now assumed to be encapsulated in the elements of the n by n matrix M and/or the n-vector Q [see Eq. (4.1)].

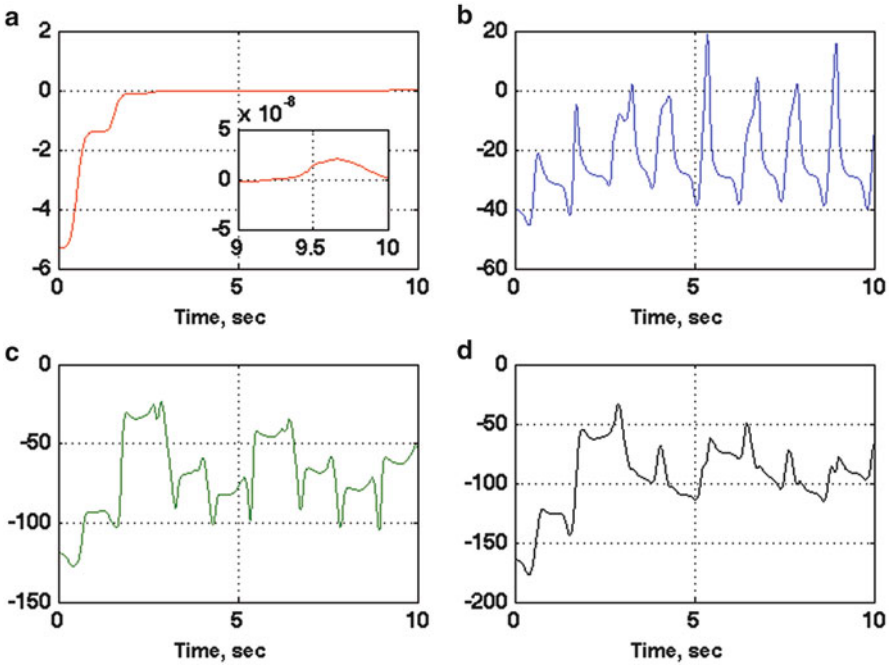

Fig. 4.4 Energies in Newtons (**a**) E_1, (**b**) E_2, (**c**) E_3, and (**d**) $E = E_2 + E_3$

4.3.1 Description of the Actual System

We assume that the mass matrix of the uncertain real-life system, which we do not know exactly, is $M_a := M + \delta M > 0$, where $M > 0$ is the n by n nominal mass matrix, our best estimate of the mass matrix of the actual system, and δM is the n by n matrix that characterizes our uncertainty in the mass matrix of the actual system. The subscript 'a' denotes the *actual*, real-life system whose parameters are uncertain. Similarly, the 'given' force n-vector acting on the real-life system is taken to be $Q_a := Q + \delta Q$, where the n-vector Q denotes the 'given' force on the nominal system and δQ denotes the n-vector of uncertainty in Q.

The equation of motion of the actual unconstrained (uncontrolled) system, whose description is known only imprecisely, is then given by

$$M_a(\tilde{q}, t)\ddot{\tilde{q}} = Q_a(\tilde{q}, \dot{\tilde{q}}, t), \tag{4.20}$$

where $\tilde{q}$ is the generalized coordinate n-vector of the actual system, the n by n matrix $M_a > 0$ is the mass matrix of the actual system which is a function of $\tilde{q}$ and t, and the n-vector Q_a is the given force acting on the actual system, which is a function of $\tilde{q}$, $\dot{\tilde{q}}$, and t. Equation (4.20) is then the description of the '*actual system*' which is known only imprecisely, since $\delta M(\tilde{q}, t)$ and $\delta Q(\tilde{q}, \dot{\tilde{q}}, t)$ are, in general, unknown.

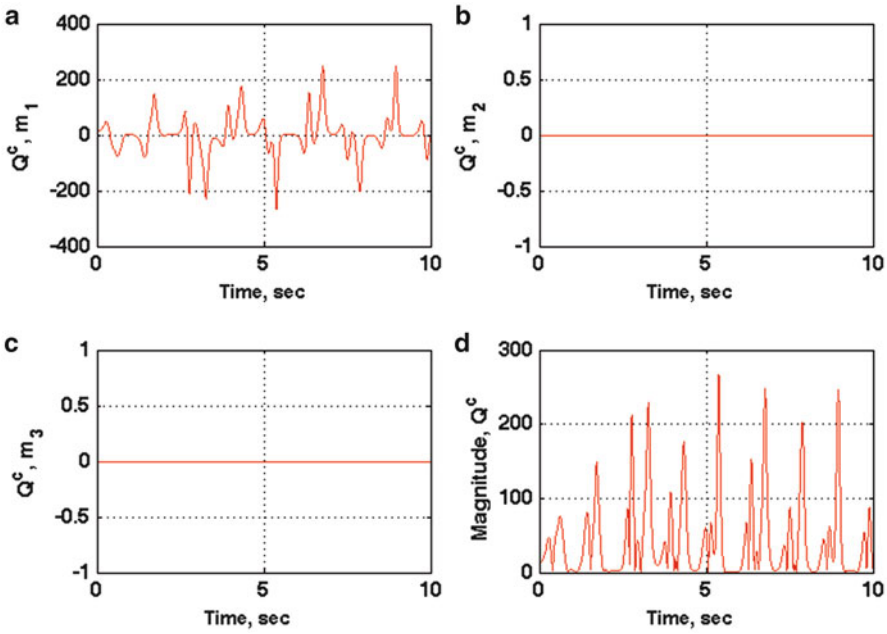

Fig. 4.5 Control forces applied to nominal system to satisfy $E = E_2 + E_3$ (Newtons) (**a**) on mass m_1, (**b**) on mass m_2, (**c**) on mass m_3, and (**d**) magnitude of control force

Our aim is to control this 'actual system' so that it mimics the motion of the nominal system and thereby satisfies the control requirements (4.4) imposed on the nominal system. With no exact knowledge of δM and δQ, the only control force that we have at hand to satisfy the control requirement (4.4) is the one we have obtained for the nominal system—our best estimate of the actual system. We then attempt to control the actual system so that it satisfies the trajectory requirements given by the set (4.4), by using this control force Q^c, which is explicitly obtained in Eq. (4.8). Thus, the equation of motion of the actual system, so controlled, becomes

$$M_a \ddot{\tilde{q}} := Q_a(\tilde{q}, \dot{\tilde{q}}, t) + Q^c(t). \tag{4.21}$$

Pre-multiplying both sides of Eq. (4.21) by M_a^{-1}, the acceleration of the actual system is given by

$$\ddot{\tilde{q}} := M_a^{-1} Q_a(\tilde{q}, \dot{\tilde{q}}, t) + M_a^{-1} Q^c(t). \tag{4.22}$$

We note that Eq. (4.21) involves (1) the description of the actual system given by Eq. (4.20) whose parameters are only known imperfectly and (2) the control force $Q^c(t)$ given by Eq. (4.8) which is obtained on the basis of our best estimate of this actual system, namely, on the basis of the corresponding nominal system.

By applying this control force to the actual system described by Eq. (4.20), one obtains a different state $(\tilde{q}, \dot{\tilde{q}})$ from that obtained for the controlled nominal system $(q, \dot{q})$. This causes an error in satisfying our desired control requirements (4.4), and a corresponding difference between the trajectories of the actual system and the nominal system.

We note that even if we apply the correct control force to the actual system by assuming that we have somehow gained precise knowledge of our uncertain system, so that

$$M_a \ddot{q}_a = Q_a(q_a, \dot{q}_a, t) + A_a^T (A_a M_a^{-1} A_a^T)^+ (b_a - A_a a_a), \tag{4.23}$$

the actual system's response $(q_a, \dot{q}_a)$ will not track the trajectory of the nominal system $(q, \dot{q})$, which is our goal.

We note that in Eq. (4.23), q_a denotes the generalized coordinate n-vector of the actual system, which is obtained by using the correct control force that the actual system is required to be subjected to, so that it satisfies the control requirements (4.5), namely, $A_a(q_a, \dot{q}_a, t)\, \ddot{q} = b_a(q_a, \dot{q}_a, t)$. In Eq. (4.23), since M_a and Q_a are assumed to be known, $a_a := M_a^{-1} Q_a$.

Pre-multiplying both sides of Eq. (4.23) by M_a^{-1}, the acceleration of the actual system can be expressed as

$$\ddot{q}_a = a_a + M_a^{-1} A_a^T (A_a M_a^{-1} A_a^T)^+ (b_a - A_a a_a). \tag{4.24}$$

We illustrate this by continuing our example of the triple pendulum system considered in Sect. 4.2, with uncertainties in the masses m_1, m_2, and m_3. We assume that each mass has a random uncertainty of $\pm 10\%$ with respect to our best estimate of it, i.e., of its nominal value.

For illustrative purposes, we pick a specific system with $\delta m_1 = 0.1$, $\delta m_2 = -0.2$, $\delta m_3 = 0.3$ and perform a simulation using Eq. (4.24), with all other parameter values the same as those prescribed in Sect. 4.2.3. We note that the elements of the 3 by 3 symmetric matrix M_a and of the 3-vector Q_a are given in a manner similar to Eqs. (4.11) and (4.12), respectively. In this case, we have replaced m_i in Eqs. (4.11) and (4.12) with $m_i = m_i + \delta m_i$, $i = 1, 2, 3$. We note that $A_a = A$ and $b_a = b$, since our constraint (4.16) does not involve any of the masses m_i. The response of mass m_3 over a duration of 10 s is shown in Fig. 4.6b for illustration. We observe that it is vastly different from that of the corresponding nominal system shown in Fig. 4.6a over the same duration of time, though both systems satisfy the energy constraint (4.15).

4.3.2 Description of the Controlled Actual Systems

To compensate for the uncertainty, the control force given by the second member on the right-hand side of Eq. (4.21), $Q^c(t)$, needs to be modified to compensate for the

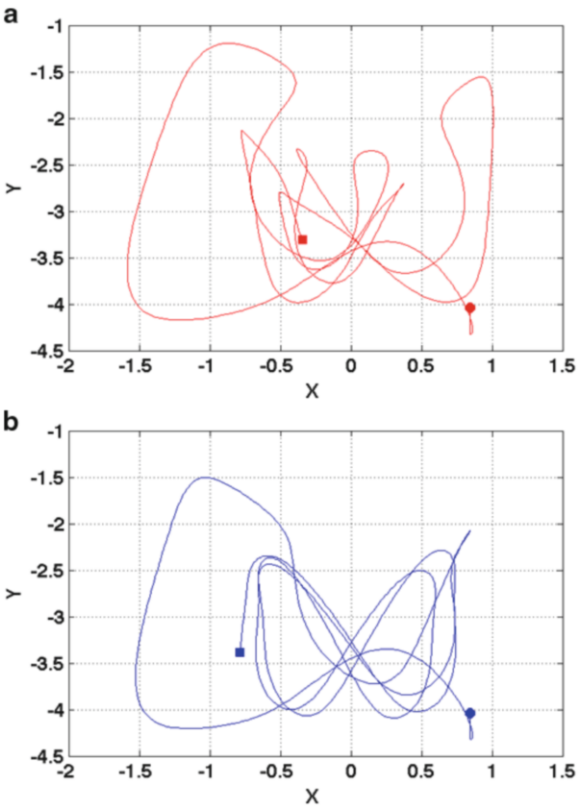

Fig. 4.6 The difference in the trajectory of mass m_3 in the XY-plane over a period of 10 s for (**a**) the nominal system and (**b**) the actual system, when the uncertainties in masses are prescribed as $\delta m_1 = 0.1$ kg, $\delta m_2 = -0.2$ kg, and $\delta m_3 = 0.3$ kg. Both systems satisfy the energy constraint (4.15)

fact that it has been calculated on the basis of the nominal system and is now instead being applied to the actual unknown system. We do this by adding another control force Q^u from a compensating controller, resulting in a new state $(q_c, \dot{q}_c)$ (see Fig. 4.7). We define the difference between $q_c(t)$ and $q(t)$ as a tracking error signal $e(t)$ (see Fig. 4.7). We note that the additional force Q^u from the compensating controller depends on both the state $(q, \dot{q})$ and the tracking error e. In this chapter, we develop this additive controller based on a generalization of the notion of sliding surface control, which is discussed in Sect. 4.5.

The equation of motion of the controlled actual system thus becomes

$$M_a(q_c, t)\ddot{q}_c = Q_a(q_c, \dot{q}_c, t) + Q^c(t) + Q^u \tag{4.25}$$

where q_c is the generalized coordinate n-vector of the controlled actual system, $Q^c(t)$ is the control force given by Eq. (4.8) that is obtained from the corresponding nominal system and which causes the nominal system to satisfy the constraint (4.5),

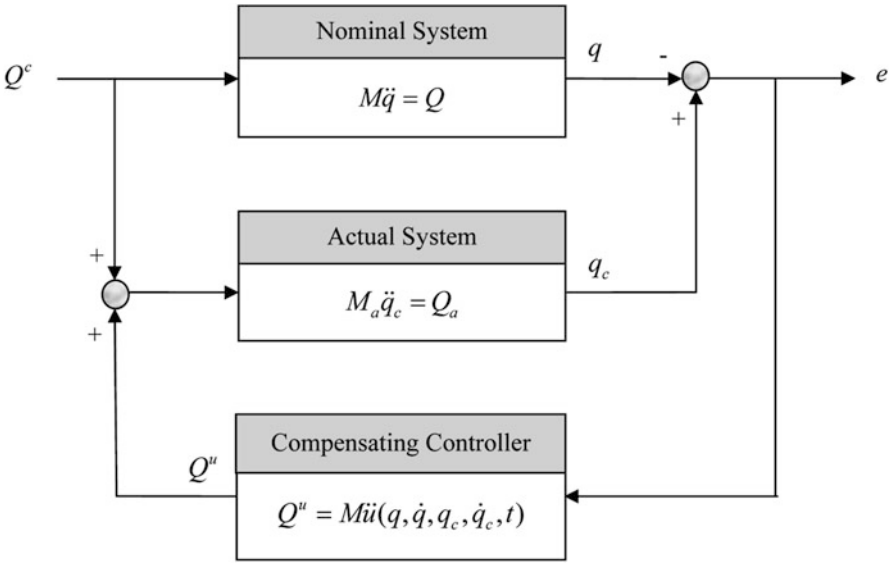

Fig. 4.7 The block diagram of the controlled actual system. Note that the compensating controller uses the mass matrix of the nominal system

and Q^u is the additional control force n-vector which we shall develop in closed form. We now refer to Eq. (4.25) as the description of the '*controlled actual system*,' or '*controlled system*,' for short, implying that in addition to the control force $Q^c(t)$ given by Eq. (4.8) and obtained on the basis of the corresponding nominal system, the system is also subjected to the additional control force Q^u. Pre-multiplying both sides of Eq. (4.25) by M_a^{-1}, the acceleration of this controlled system can then be expressed as

$$\ddot{q}_c = a_a + M_a^{-1} Q^c(t) + M_a^{-1} M \ddot{u}. \tag{4.26}$$

Here $a_a := M_a^{-1} Q_a$ and $Q^u := M\ddot{u}$, where $\ddot{u}$ is the additional generalized acceleration provided by the additional control forces Q^u to compensate for uncertainties in our knowledge of the actual system.

It is important to note that the mass matrix M in Eq. (4.26) is that of the nominal system—the only mass matrix we have in hand, since the mass matrix M_a of the actual real-life system is unknown. Hence, after we obtain a compensating control acceleration $\ddot{u}$, in order to obtain the control force we need to multiply it with this mass matrix M, so that $Q^u = M\ddot{u}$. However, the generalized acceleration of the controlled actual system due to the compensating control acceleration $\ddot{u}$ is $M_a^{-1}Q^u := M_a^{-1}M\ddot{u}$ which is shown in the last term of Eq. (4.26). And so we observe that this term $M_a^{-1}Q^u$ still contains the mass matrix M_a of the actual

system, which is uncertain! However, as shown later in the proof of Lyapunov stability in Sect. 4.5, our control approach will take care of this uncertainty as well. Furthermore, we note that the n by n mass matrix of the actual system $M_a := M + \delta M > 0$ is, in general, a function of q_c and t, and the actual 'given' force vector of the controlled actual system $Q_a := Q + \delta Q$ is, in general, a function of q_c, $\dot{q}_c$, and t. Before embarking on the determination of Q^u, we consider the uncertainties in the dynamics of the mechanical system next.

4.4 Uncertainties in the Dynamics of Mechanical Systems

Defining the tracking error as

$$e(t) = q_c(t) - q(t) \tag{4.27}$$

and differentiating Eq. (4.27) twice with respect to time, we get

$$\ddot{e} = \ddot{q}_c - \ddot{q}, \tag{4.28}$$

which upon use of Eqs. (4.9) and (4.26) yields

$$\begin{aligned}\ddot{e} &= \left[a_a(q_c, \dot{q}_c, t) + {M_a}^{-1}(q_c, t)Q^c(t) + M_a^{-1}M\ddot{u}\right] - \left[a(q, \dot{q}, t) + M^{-1}(q, t)Q^c(t)\right] \\ &= [a_a(q_c, \dot{q}_c, t) - a(q, \dot{q}, t)] + \left[{M_a}^{-1}(q_c, t) - M^{-1}(q, t)\right] Q^c(t) + M_a^{-1}M\ddot{u} \\ &:= \delta\ddot{q} + M_a^{-1}M\ddot{u} = \delta\ddot{q} + [I - (I - M_a^{-1}M)]\ddot{u} := \delta\ddot{q} + \ddot{u} - \bar{M}\ddot{u}.\end{aligned} \tag{4.29}$$

In the above equation, we have defined

$$\begin{aligned}\bar{M} &= I - M_a^{-1}(q_c, t)\, M(q, t) = I - \left(M(q_c, t) + \delta M(q_c, t)\right)^{-1} M(q, t) \\ &= I - \left(M^{-1}(q, t)\, M(q_c, t) + M^{-1}(q, t)\, \delta M(q_c, t)\right)^{-1},\end{aligned} \tag{4.30}$$

and denoted the acceleration $\delta\ddot{q}$ as

$$\delta\ddot{q}(q, \dot{q}, q_c, \dot{q}_c, t) = [a_a(q_c, \dot{q}_c, t) - a(q, \dot{q}, t)] + \left[{M_a}^{-1}(q_c, t) - M^{-1}(q, t)\right] Q^c(t), \tag{4.31}$$

where $a_a := M_a^{-1}Q_a$, with $M_a := M(q_c, t) + \delta M(q_c, t)$ and $Q_a := Q(q_c, \dot{q}_c, t) + \delta Q(q_c, \dot{q}_c, t)$.

The aim in this section is to find a suitable bound on $\delta\ddot{q}$ which we shall use in the following section to develop a set of additive controllers to compensate for the uncertainties involved in our knowledge of the actual multi-body system.

Using Taylor's expansion, Eq. (4.31) can be expanded as

$$\begin{aligned}
\delta\ddot{q}(q,\dot{q},q_c,\dot{q}_c,t) &= M_a{}^{-1}(q,t)Q_a(q,\dot{q},t) - M^{-1}(q,t)Q(q,\dot{q},t) \\
&+ M_a{}^{-1}(q,t)\left[\sum_{j=1}^{n}\frac{\partial Q_{a,i}}{\partial q_{c,j}}\Big|_{q,\dot{q},t}(q_{c,j}-q_j) + \sum_{j=1}^{n}\frac{\partial Q_{a,i}}{\partial \dot{q}_{c,j}}\Big|_{q,\dot{q},t}(\dot{q}_{c,j}-\dot{q}_j)\right] \\
&+ \left[\sum_{j=1}^{n}\frac{\partial M^{-1}_{a,ik}}{\partial q_{c,j}}\Big|_{q,t}(q_{c,j}-q_j)\right]\left[Q_a(q,\dot{q},t) + \sum_{j=1}^{n}\frac{\partial Q_{a,i}}{\partial q_{c,j}}\Big|_{q,\dot{q},t}(q_{c,j}-q_j)\right. \\
&\left.+ \sum_{j=1}^{n}\frac{\partial Q_{a,i}}{\partial \dot{q}_{c,j}}\Big|_{q,\dot{q},t}(\dot{q}_{c,j}-\dot{q}_j)\right] \\
&+ \left\{M_a{}^{-1}(q,t) + \left[\sum_{j=1}^{n}\frac{\partial M^{-1}_{a,ik}}{\partial q_{c,j}}\Big|_{q,t}(q_{c,j}-q_j)\right] - M^{-1}(q,t)\right\}Q^c(t) \\
&+ H.O.T., \text{ for } i = 1,\ldots,n \text{ and } k = 1,\ldots,n,
\end{aligned} \tag{4.32}$$

where *H.O.T.* denotes higher order terms in $(q_c - q)$ and $(\dot{q}_c - \dot{q})$.

We note that in Eq. (4.32), $Q_{a,i}$, $q_{c,j}$, and q_j denote the corresponding ith and jth components of the n-vectors Q_a, q_c, and q, respectively. Also $M^{-1}_{a,ik}$ represents the (i,k) element of the n by n matrix M_a^{-1}.

The aim is to develop a controller $\ddot{u}$ such that the motion of the controlled actual system closely tracks the motion of the nominal system and thereby satisfies the control requirements (4.4). We assume for the moment that the compensating control acceleration $\ddot{u}$ is capable of this and causes the trajectory of the controlled actual system $(q_c, \dot{q}_c)$ to sufficiently approximate that of the nominal system so that $(q_c, \dot{q}_c) \approx (q, \dot{q})$. Under this assumption, we take the lowest order terms in Eq. (4.32) and approximate $\delta\ddot{q}$ as

$$\begin{aligned}
\delta\ddot{q}(q,\dot{q},t) \approx &\left[M_a^{-1}(q,t)Q_a(q,\dot{q},t) - M^{-1}(q,t)Q(q,\dot{q},t)\right] \\
&+ \left[M_a{}^{-1}(q,t) - M^{-1}(q,t)\right]Q^c(t),
\end{aligned} \tag{4.33}$$

and similarly approximate $\bar{M}$ as [see Eq. (4.30)]

$$\bar{M} \approx I - \left(I + M^{-1}(q,t)\,\delta M(q,t)\right)^{-1}. \tag{4.34}$$

Since [18]

$$M_a^{-1}(q,t) = [M(q,t) + \delta M(q,t)]^{-1} = M^{-1} - M^{-1}(I + \delta M\ M^{-1})^{-1}\delta M\ M^{-1}, \tag{4.35}$$

expanding Eq. (4.33) and utilizing Eq. (4.35), we obtain

$$\delta\ddot{q}(t) \approx -(M+\delta M)^{-1}\delta M\ M^{-1}(Q+Q^c) + (M+\delta M)^{-1}\delta Q, \tag{4.36}$$

which includes the combined effect of the uncertainties δM and δQ. By taking the norm of relation (4.36), one can obtain an estimate of the bound, $\Gamma(t)$, on $\|\delta\ddot{q}\|$ as

$$\|\delta\ddot{q}(t)\| \approx \left\|-(M+\delta M)^{-1}\delta M\ M^{-1}(Q+Q^c) + (M+\delta M)^{-1}\delta Q\right\| \leq \Gamma(t), \tag{4.37}$$

where $\Gamma(t)$ is a positive function of time.

Remark 1. With the knowledge on the bounds on the uncertainties in the mass matrix, $\|\delta M\|$, and the given force, $\|\delta Q\|$, and the assumption that $\left\|M^{-1}\delta M\right\| \ll 1$, we can also obtain an estimate of a suitable bound on $\delta\ddot{q}$ as

$$\begin{aligned}\|\delta\ddot{q}(t)\| \leq \left(1+\left\|M^{-1}\right\|\ \|\delta M\|\right)\ \left\|M^{-1}\right\|\ \left(\left\|M^{-1}\right\|\ \|Q+Q^c\|\ \|\delta M\|\right.\\ \left.+\|\delta Q\|\right) \leq \Gamma(t),\end{aligned} \tag{4.38}$$

where $\Gamma(t)$ is a positive function of time.

The bounds $\Gamma(t)$ both in Eqs. (4.37) and (4.38) depend on our bounds on δM and δQ, which in turn depend on the state of our knowledge (or ignorance) about the actual system. Both Eqs. (4.37) and (4.38) can be used to get the general form of $\|\delta\ddot{q}\|$ and are also applicable to those special situations in which either δM or δQ may be judged to be so negligibly small as to be approximated by zero.

In the simulations that follow in Sect. 4.6, we obtain estimates on the bound on $\|\delta\ddot{q}\|$ by using relation (4.37), which appears to provide a close enough approximation to the norm of $\delta\ddot{q}$ given in Eq. (4.31).

4.5 Control Designs

Having obtained an estimate of the bound $\|\delta\ddot{q}\| \leq \Gamma(t)$, we now develop a methodology for obtaining a compensating controllers, $\ddot{u}$ [see Eq. (4.26)], which is the generalized sliding surface controller (G_{SS}).

The aim is to develop a compensating controller that can guarantee the tracking of the nominal system's trajectory (to within desired error bounds) despite our uncertain knowledge of the actual system. The formulation of this controller permits the use of a large class of control laws that can be adapted to the practical limitations of the specific compensating controller being used and to the desired measure of compensation for the uncertainties. The controller can guarantee tracking of the nominal system's trajectories in the presence of uncertainties within desired error bounds. Its tracking responses are shown later in Sect. 4.6.

Noting Eq. (4.29), the tracking error signal in acceleration can be expressed as

$$\ddot{e} = \delta\ddot{q} + M_a^{-1} M\ddot{u} := \delta\ddot{q} + \ddot{u} - \bar{M}\ddot{u}. \tag{4.39}$$

Since the compensating control causes the trajectory of the controlled actual system $(q_c, \dot{q}_c)$ to sufficiently approximate that of the nominal system so that $(q_c, \dot{q}_c) \approx (q, \dot{q})$, taking the lowest order terms as before, $\bar{M}$ in Eq. (4.30) can be approximated as $\bar{M} \approx I - \left(I + M^{-1}(q,t)\ \delta M(q,t)\right)^{-1}$.We again note that $\bar{M}$ is unknown, since δM is unknown, and it is embedded in our controller $\ddot{u}$. We shall show that the uncertain term $\bar{M}$ will be taken care of by the proof of Lyapunov stability.

We now define a sliding surface

$$s(t) = k_1 e(t) + \dot{e}(t), \tag{4.40}$$

where $k_1 > 0$ is an arbitrary small positive number and s is an n-vector. Our aim is to maneuver the system to the sliding surface $s \in \Omega_\varepsilon$, whereupon by Eq. (4.40), ideally speaking when the size of the surface Ω_ε is zero, we obtain the relation $\dot{e} = -k_1 e$, whose solution $e(t) = e_0 \exp(-k_1 t)$ shows that the tracking error $e(t)$ exponentially reduces to zero along this lower dimensional surface in phase space.

Differentiating Eq. (4.40) with respect to time and using Eq. (4.39), we get

$$\dot{s} = k_1\dot{e} + \ddot{e} = k_1\dot{e} + \delta\ddot{q} + \ddot{u} - \bar{M}\ddot{u}. \tag{4.41}$$

Since $(\dot{q}_c - \dot{q})$ can be measured, to cancel the known term $k_1\dot{e} = k_1(\dot{q}_c - \dot{q})$ in Eq. (4.41), we choose the controller $\ddot{u}$ to be of the form

$$\ddot{u} = -k_1\dot{e}(t) + G_{SS}(t), \tag{4.42}$$

so that

$$\dot{s} = G_{SS}(t) + \delta\ddot{q}(t) - \bar{M}(t)\left[-k_1\dot{e}(t) + G_{SS}(t)\right]. \tag{4.43}$$

We note that $\|\delta\ddot{q}\| \leq \Gamma(t)$. Here, we have used the bound $\Gamma(t)$ that is related to the uncertainties involved in the actual system and that is obtained from relation (4.37) [or (4.38)]. In what follows we shall denote $\|\cdot\|$ to mean the infinity norm.

We shall now show that the system can indeed be maneuvered to the sliding surface $s \in \Omega_\varepsilon$ when Ω_ε is defined as any appropriately small surface around $s = 0$ whose exact description will be shortly discussed.

We start by considering a function $\beta(t)$ such that

$$\beta(t) \geq \frac{n\left(\Gamma(t) + \beta_0\right)}{\alpha_0} > 0, \tag{4.44}$$

where

$$\beta_0 > k_1 \left\| \bar{M}(t) \right\| \|\dot{e}(t)\| \quad \text{and} \quad 0 < \alpha_0 < 1 - n\sigma \left\| \bar{M}(t) \right\| \tag{4.45}$$

are any arbitrary positive constants over the time duration over which the control is applied.

The positive constant σ is chosen such that

$$\gamma \leq \sigma \leq 1, \tag{4.46}$$

where

$$\gamma := \frac{\|s\| \ \|f(s)\|}{s^T f(s)} \leq 1. \tag{4.47}$$

We note that since $\gamma \leq 1$, the choice $\sigma = 1$ would suffice in Eq. (4.44) when choosing α_0. The function $f(s)$ will be defined shortly.

We now define a control n-vector $G_{SS}(t)$ so that

$$G_{SS}(t) := -\sigma\beta(t) f(s). \tag{4.48}$$

The ith component, $f_i(s)$, of the n-vector $f(s)$ is defined as

$$f_i(s) = g\left(s_i/\varepsilon\right), \ i = 1, \ldots, n \tag{4.49}$$

where s_i is the ith component of the n-vector s, ε is defined as any (small) positive number, and the function $g\left(s_i/\varepsilon\right)$ is *any* arbitrary monotonic increasing odd continuous function of s_i on the interval $(-\infty, +\infty)$ that satisfies

$$\|f_i(s)\| = \|g(s_i/\varepsilon)\| \geq \frac{\Gamma(t) + k_1 \left\| \bar{M}(t) \right\| \|\dot{e}(t)\|}{\Gamma(t) + \beta_0}, \quad \text{if } s_i \text{ is outside the surface } \Omega_\varepsilon(t), \tag{4.50}$$

where $\Omega_\varepsilon(t)$ is defined as the surface of the n-dimensional cube around the point $s = 0$, each of whose sides has a computable length (as show below). We note that the right-hand side of relation (4.50) is always less than unity since $\beta_0 > k_1 \left\| \bar{M}(t) \right\| \|\dot{e}(t)\|$, and hence relation (4.50) will always be satisfied when $\|f(s)\| \geq 1$.

Result 1. The control law

$$\ddot{u} = -k_1 \dot{e}(t) + G_{SS}(t) = -[k_1 \dot{e}(t) + \sigma\beta(t) f(s)] \tag{4.51}$$

with $k_1 > 0$ and $G_{SS}(t)$ defined in Eq. (4.48) to Eq. (4.50) will cause $s(t) \to \Omega_\varepsilon$.

Proof. Consider the Lyapunov function

$$V = \frac{1}{2} s^T s. \tag{4.52}$$

Differentiating Eq. (4.52) once with respect to time, we get

$$\dot{V} = s^T \dot{s}. \tag{4.53}$$

Substituting Eq. (4.43) in Eq. (4.53), we have

$$\dot{V} = s^T(t) G_{SS}(t) + s^T(t) \delta\ddot{q}(t) + k_1 s^T(t) \bar{M}(t) \dot{e}(t) - s^T \bar{M}(t) G_{SS}(t). \tag{4.54}$$

Then using Eq. (4.48) in Eq. (4.54), we obtain

$$\dot{V} = -\sigma\beta s^T f(s) + s^T \delta\ddot{q} + k_1 s^T \bar{M}\ \dot{e} + \sigma\beta s^T \bar{M}\ f(s), \tag{4.55}$$

so that

$$\dot{V} \leq -\sigma\beta s^T f(s) + \left\| s^T \right\| \ \|\delta\ddot{q}\| + k_1 \left\| s^T \right\| \ \left\| \bar{M} \right\| \ \|\dot{e}\| + \sigma\beta \left\| s^T \right\| \ \left\| \bar{M} \right\| \ \|f(s)\| \ . \tag{4.56}$$

Then using the relation $\|\delta\ddot{q}\| \leq \Gamma(t)$, we obtain

$$\dot{V} \leq -\sigma\beta s^T f(s) + \left\| s^T \right\| \Gamma(t) + k_1 \left\| s^T \right\| \ \left\| \bar{M} \right\| \ \|\dot{e}\| + \sigma\beta \left\| s^T \right\| \ \left\| \bar{M} \right\| \ \|f(s)\| \ . \tag{4.57}$$

Since [see Eqs. (4.46) and (4.47)]

$$\sigma\ s^T f(s) \geq \|s\| \, \|f(s)\| \, , \tag{4.58}$$

relation (4.57) becomes

$$\begin{aligned} \dot{V} &\leq -\left\| s^T \right\| \left(\beta \frac{\|s\|}{\left\| s^T \right\|} \|f(s)\| - \sigma\beta \left\| \bar{M} \right\| \ \|f(s)\| - \Gamma(t) - k_1 \left\| \bar{M} \right\| \ \|\dot{e}\| \right) \\ &\leq -\left\| s^T \right\| \left[\beta \left(\frac{1}{n} - \sigma \left\| \bar{M} \right\| \right) \|f(s)\| - \Gamma(t) - k_1 \left\| \bar{M} \right\| \ \|\dot{e}\| \right] \\ &= -\left\| s^T \right\| \left[\frac{\beta}{n} \left(1 - n\sigma \left\| \bar{M} \right\| \right) \|f(s)\| - \Gamma(t) - k_1 \left\| \bar{M} \right\| \ \|\dot{e}\| \right], \end{aligned} \tag{4.59}$$

where the second inequality follows because $\frac{\|s\|}{\left\| s^T \right\|} \geq \frac{1}{n}$.

Using Eq. (4.44) in Eq. (4.59), we then have

$$\begin{aligned}\dot{V} &\leq -\left\|s^T\right\| \left[\frac{(\Gamma(t)+\beta_0)}{\alpha_0}\left(1-n\sigma\left\|\bar{M}\right\|\right)\|f(s)\| - \Gamma(t) - k_1\left\|\bar{M}\right\| \|\dot{e}\|\right] \\ &\leq -\left\|s^T\right\| \left[(\Gamma(t)+\beta_0)\|f(s)\| - \Gamma(t) - k_1\left\|\bar{M}\right\| \|\dot{e}\|\right], \end{aligned} \tag{4.60}$$

where the last inequality follows because $\frac{(1-n\sigma\|\bar{M}\|)}{\alpha_0} \geq 1$.

Since by Eq. (4.50), $(\Gamma(t)+\beta_0)\|f(s)\| - \Gamma(t) - k_1\left\|\bar{M}(t)\right\| \|\dot{e}(t)\| := \Delta(t) \geq 0$ outside the surface $\Omega_\varepsilon(t)$, we have

$$\dot{V} \leq -\left\|s^T\right\| \Delta(t), \text{ outside the surface } \Omega_\varepsilon(t), \tag{4.61}$$

so that the derivative $\dot{V}$ is negative, and we have convergence to the closed set interior to the region enclosed by the surface Ω_ε. □

Thus for the right-hand side of relation (4.60) to be negative, we require relation (4.50), namely,

$$\|f(s)\| = \|g(s/\varepsilon)\| \geq \frac{\Gamma(t) + k_1\left\|\bar{M}(t)\right\| \|\dot{e}(t)\|}{\Gamma(t)+\beta_0} := \Xi(t), \tag{4.62}$$

where, as noted before, $\Xi(t) < 1$. Relation (4.62) then yields

$$\|s\| \geq \varepsilon g^{-1}[\Xi(t)]. \tag{4.63}$$

In the region in which $\|s\|$ satisfies Eq. (4.63), the Lyapunov derivative $\dot{V}$ is negative. This shows us that the controller (4.51) will cause $s(t)$ to decrease until it reaches the boundary $s \in \Omega_\varepsilon(t)$. Further, since $\Xi(t) < 1$, and the function g(*) is a monotonically increasing function, $\Omega_\varepsilon(t)$ is enclosed in an n-dimensional cube of constant size around the point $s = 0$, each of whose sides has length

$$L_\varepsilon(t) = 2\varepsilon g^{-1}[\Xi(t)] < 2\varepsilon g^{-1}(1) := \Sigma. \tag{4.64}$$

This gives an estimate of the n-dimensional cubical region Ω_ε (each of whose sides is estimated to be of *constant* length Σ) to which trajectories of the controlled actual system will be attracted to.

Noting the fact that $\|s(t)\|$ is bounded by $L_\varepsilon/2$ inside the surface Ω_ε, we now have an estimate of the error bounds given by

$$\|e(t)\| \leq \frac{\Sigma}{2k_1} \text{ and } \|\dot{e}(t)\| \leq \Sigma, \text{ as } t \to \infty. \tag{4.65}$$

Remark 2. Under the proviso $\left\|\bar{M}(t)\right\| \|\dot{e}(t)\| < 1$ for $t \in [0, T]$ where $[0, T]$ is the interval over which the control is applied, which is something that we expect, we then have

$$L_\varepsilon(t) <\approx 2\varepsilon g^{-1}\left[\left(\Gamma(t) + k_1\right)/\left(\Gamma(t) + \beta_0\right)\right]. \tag{4.66}$$

For ease of implementation, one could *choose* the function $\Gamma(t)$ to be a constant by taking it to be the upper bound, Γ_m, so that $\|\delta\ddot{q}(t)\| \leq \Gamma_m$ for $t \in [0, T]$, where $[0, T]$ is the interval over which the control is applied. Then relation (4.66) becomes

$$L_\varepsilon <\approx 2\varepsilon g^{-1}\left[\left(\Gamma_m + k_1\right)/\left(\Gamma_m + \beta_0\right)\right]. \tag{4.67}$$

One can then, accordingly, obtain an estimate of the error bounds by replacing Σ in the expressions in Eq. (4.65) by the expression on the right-hand side of Eq. (4.67).

Main Result (G_{SS}). The closed-from generalized sliding surface controller for the uncertain system,

$$M_a\ddot{q}_c = Q_a + Q^c(t) + M\ddot{u} = Q_a + Q^c(t) - M\left[k_1\dot{e} + n\sigma\left(\frac{\Gamma(t) + \beta_0}{\alpha_0}\right) f(s)\right], \tag{4.68}$$

where:

(1) the control force $Q^c(t)$ is given by Eq. (4.8) and is obtained on the basis of the nominal system;
(2) $k_1 > 0$ is an arbitrary small positive number;
(3) σ can be chosen to be unity, and for the function $f(s)$ *any* arbitrary monotonically increasing odd continuous function of s on the interval $(-\infty, +\infty)$ as described in Eq. (4.49) with $\|f(s)\| \geq 1$ in Ω_ε would be sufficient;
(4) $\|\delta\ddot{q}(t)\| < \Gamma(t)$ where $\Gamma(t)$ is chosen based on the estimate of $\delta\ddot{q}$ from Eq. (4.37) [or (4.38)];
(5) α_0 is a small positive number that satisfies

$$0 < \alpha_0 < 1 - n\sigma\left\|\bar{M}(t)\right\|, \tag{4.69}$$

over the time duration over which the control is done; and

(6) under the proviso, and the expectation, that $\left\|\bar{M}\right\| \|\dot{e}\| << 1$, β_0 is chosen such that

$$\beta_0 = k_1, \tag{4.70}$$

will cause the actual system to track the trajectory of the nominal system within the estimated error bounds given by Eq. (4.65).

Proof Using Eq. (4.28) in Eq. (4.39), we have

$$\ddot{e} = \ddot{q}_c - \ddot{q} = \delta\ddot{q} + M_a^{-1} M \ddot{u}, \tag{4.71}$$

so that

$$\ddot{q}_c = \ddot{q} + \delta\ddot{q} + M_a^{-1} M \ddot{u}. \tag{4.72}$$

Consider Eq. (4.31),

$$\begin{aligned} \delta\ddot{q} &= (a_a - a) + \left(M_a{}^{-1} - M^{-1}\right) Q^c(t) \\ &= \left(a_a + M_a{}^{-1} Q^c(t)\right) - \left(a + M^{-1} Q^c(t)\right) \\ &= a_a + M_a{}^{-1} Q^c(t) - \ddot{q}. \end{aligned} \tag{4.73}$$

In the last equality above, we have used Eq. (4.9).
Substituting Eq. (4.73) in Eq. (4.72), we then get

$$\ddot{q}_c = a_a + M_a{}^{-1} Q^c(t) + M_a^{-1} M \ddot{u}. \tag{4.74}$$

Pre-multiplying both sides of Eq. (4.74) by M_a, we obtain

$$M_a \ddot{q}_c = Q_a + Q^c(t) + M \ddot{u}. \tag{4.75}$$

Finally, using Result 1 [Eq. (4.51)] and Eq. (4.65), the main result (G_{SS}) follows. □

4.6 Numerical Results and Simulations

In this section we continue to illustrate the control methodology in the presence of uncertainties by considering the same example of the triple pendulum. The approach is straightforward to apply to other systems. While our nominal system has $m_1 = 1$, $m_2 = 2$, and $m_3 = 3$, there is an uncertainty of $\pm 10\%$ in each of these values when describing the actual system.

With imperfect knowledge of the parameters in the system, in order to control the actual system's motion so that it tracks the motion of the controlled nominal system and thereby satisfies the control requirements imposed on the nominal system, we would have to use the controlled actual system [see Eq. (4.25)]

$$M_a \ddot{q}_c = Q_a + Q^c(t) + Q^u := Q_a + Q^c(t) + M\,\ddot{u}, \tag{4.76}$$

which contains the additional control force Q^u to compensate for our uncertainty in the knowledge of the actual system. The additional additive controller $\ddot{u}$ can be defined explicitly, using the control law as discussed in Sect. 4.5.

We next select the structure and parameters for the generalized sliding surface controller given by Eq. (4.68). We choose

$$f_i(s) = \alpha_c (s_i/\varepsilon)^3, \tag{4.77}$$

where $\alpha_c, \varepsilon > 0$ and ε is a suitable small number. We then obtain in closed form the generalized sliding surface controller that guarantees to compensate for uncertainties in the actual system as

$$M_a \ddot{q}_c = Q_a + Q^c(t) - M \left[k_1 \dot{e} + n\sigma \left(\frac{\Gamma(t) + \beta_0}{\alpha_0} \right) \alpha_c (s/\varepsilon)^3 \right]. \tag{4.78}$$

We note that with this choice of $f_i(s) = \alpha_c (s_i/\varepsilon)^3$, the region outside the surface Ω_ε is the region outside of the n-dimensional cube around $s = 0$, each of whose sides has length $L_\varepsilon <\approx 2\varepsilon((\Gamma_m + k_1)/\alpha_c(\Gamma_m + \beta_0))^{1/3}$ [see Eq. (4.67)]. In this region Eq. (4.61) assures us that the controlled actual system (4.78) will cause $s(t)$ to strictly decrease, until it reaches the boundary $s \in \Omega_\varepsilon$ and remains inside this n-box thereafter.

Pre-multiplying both sides of Eq. (4.78) by M_a^{-1}, we obtain the closed-form equation of motion of the controlled actual system as

$$\ddot{q}_c = a_a + M_a^{-1} Q^c(t) - M_a^{-1} M \left[k_1 \dot{e} + n\sigma \left(\frac{\Gamma(t) + \beta_0}{\alpha_0} \right) \alpha_c (s/\varepsilon)^3 \right], \tag{4.79}$$

which will cause the actual system to track the trajectory of the nominal system, thereby compensating for the uncertainty in our knowledge of the actual system.

However, while we have no knowledge of the actual parameters, in order to affect a compensating controller, a suitable bound on the uncertainty in $\delta\ddot{q}$ is required. We next estimate Γ_m and $\Gamma(t)$. We note that $\Gamma_m \geq \Gamma(t)$, where $\Gamma(t)$ is the bound on $\delta\ddot{q}$ [see Eq. (4.37)] in the presence of the ± 10 percent uncertainties in each of the masses m_1, m_2, and m_3 as described in Sect. 4.3.1. In order to estimate Γ_m and $\Gamma(t)$, we use Eq. (4.37) and perform a Monte Carlo simulation using 1,014 uniformly distributed, independent samples of the uncertain masses δm_1, δm_2, and δm_3. The location of the actual masses for each sample is shown in Fig. 4.8 and the probability density function of $\|\delta\ddot{q}\|$ (at each instant of time t) that is obtained is shown in Fig. 4.9.

The mass properties of our actual system, though unknown, lie somewhere inside the box shown in Fig. 4.8. In order to check the efficacy of our controller in compensating for our lack of exact knowledge of the actual system, we pick the set $\delta m_1 = 0.1$, $\delta m_2 = -0.2$, and $\delta m_3 = 0.3$, which is assumed to represent our actual system. To check the performance of our controller, we perform a simulation using Eq. (4.79) by choosing $\Gamma(t) = \Gamma_m = 100$ for $t \in [0, 10]$ as shown in Fig. 4.9 (red line) and using the parameters $k_1 = 10$, $\beta_0 = k_1$, $\alpha_c = 2$, $\alpha_0 = 0.01$, $\sigma = 1$, and $\varepsilon = 10^{-2}$ to specify our controller. All other parameter values are the same as those prescribed in Sect. 4.2.3. We note that the chosen set of deviations from the nominal

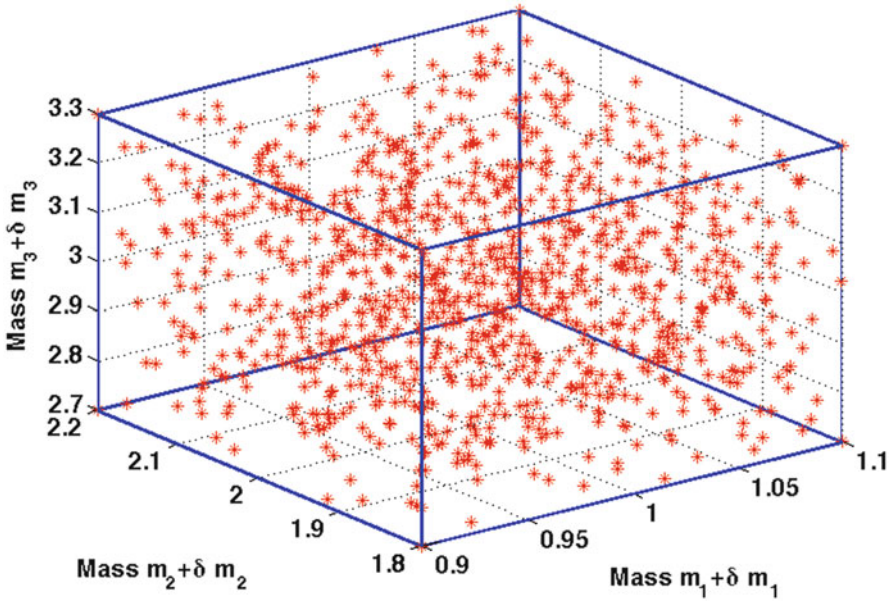

Fig. 4.8 The three masses $m_i \pm \delta m_i$, $i = 1,2,3$ of the actual system lie somewhere in the box shown. The figure shows the 1,014 uniformly distributed random points generated from a Monte Carlo simulation

values ($m_1 + \delta m_1 = 1.1$, $m_2 + \delta m_2 = 1.8$, and $m_3 + \delta m_3 = 3.3$) represents simply one out of the random triples shown in Fig. 4.8. Also the estimate of $\Gamma(t)$ is not sensitive to the magnitude of additional control forces Q^u in our control approach.

The constrained trajectories of mass m_3 in the XY-plane of the nominal, the controlled, and the actual systems are illustrated in Fig. 4.10. We see that the controlled system (given by Eq. (4.79) and shown in Fig. 4.10b) tracks the nominal system (given by Eq. (4.19) and shown in Fig. 4.10a), while the actual system (given by Eq. (4.24) and shown in Fig. 4.10c) deviates from the desired nominal system. We note that all three systems satisfy the energy control requirement (4.15). Figure 4.11 gives an alternative view of the trajectory responses. In this figure, the trajectories in θ_1, θ_2, and θ_3 of the nominal (solid red line), the actual (solid blue line), and the controlled (dotted line) systems are shown. As time increases, the actual system's response differs from those of the nominal and controlled systems, while the controlled system tracks the nominal system very well. This illustrates the performance of the closed-form Eq. (4.79) showing that the controlled actual system tracks the trajectories prespecified by the nominal system in the presence of the $\pm 10\%$ uncertainties in masses of the triple pendulum and the control requirement imposed on it given by Eq. (4.15). Figures 4.12 and 4.13 correspondingly show the displacement errors ($\theta - \theta_c$) and velocity errors ($\dot{\theta} - \dot{\theta}_c$) between the nominal system (4.19) and the controlled actual system (4.79). Both figures show that the tracking errors are small. The errors are seen to be of $O(10^{-5})$ for the displacement

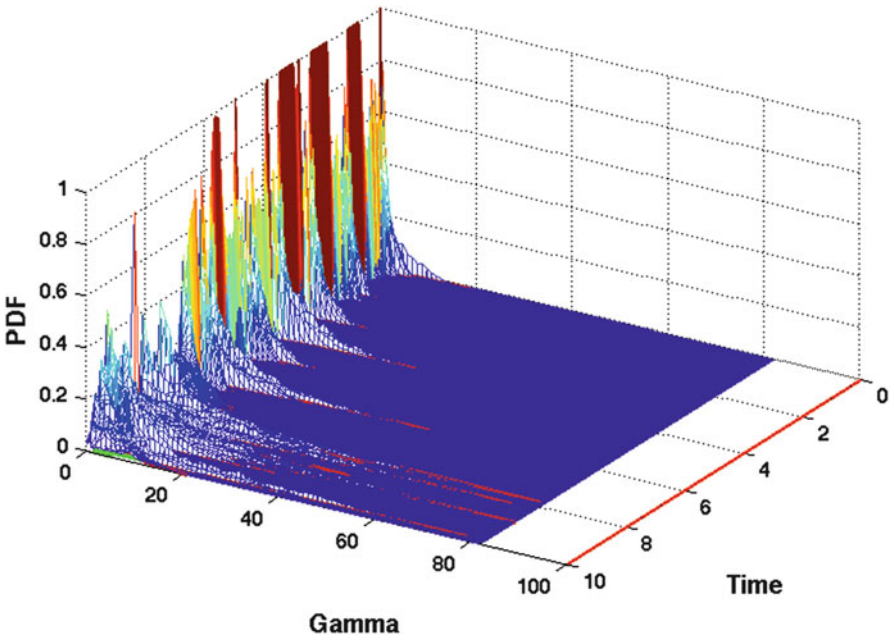

Fig. 4.9 Probability density function of $\|\delta\ddot{q}\|$ at each time t using Eq. (4.37) for the 1,014 simulation points in which the mass have ± 10 % uncertainties

and of $O(10^{-4})$ for the velocity. We see that these errors are within the estimated error norms $\|e(t)\| <\approx L_\varepsilon/2k_1 \approx 8 \times 10^{-4}$ and $\|\dot{e}(t)\| <\approx L_\varepsilon \approx 1.6 \times 10^{-2}$ as prescribed by Eqs. (4.65) and (4.67), where

$$L_\varepsilon <\approx 2\varepsilon((\Gamma_m + k_1)/\alpha_c(\Gamma_m + \beta_0))^{1/3} \approx 1.6 \times 10^{-2}. \tag{4.80}$$

We note that the use of the specified smooth cubic function eliminates chattering. We also note from the numerical simulation of this example that our assumptions $\beta_0 > k_1 \left\|\bar{M}(t)\right\| \|\dot{e}(t)\|$, $0 < \alpha_0 < 1 - n\sigma \left\|\bar{M}(t)\right\|$, and $\sigma\, s^T f(s) \geq \|s\|\, \|f(s)\|$ always hold.

Pre-multiplying Eq. (4.79) by M_a, we obtain [see Eq. (4.68)]

$$\begin{aligned} M_a\ddot{q}_c &= Q_a + Q^c - M\left(k_1\dot{e} + n\sigma\left(\frac{\Gamma(t) + \beta_0}{\alpha_0}\right)\alpha_c(s/\varepsilon)^3\right) \\ &:= Q_a + Q^c + M\ddot{u} := Q_a + Q^c + Q^u. \end{aligned} \tag{4.81}$$

The total control force applied to the actual system is given by $Q^T = Q^c + Q^u$. Here Q^c is the control force obtained from the nominal system, and Q^u is the force applied by the additional compensating controller to compensate for our inexact

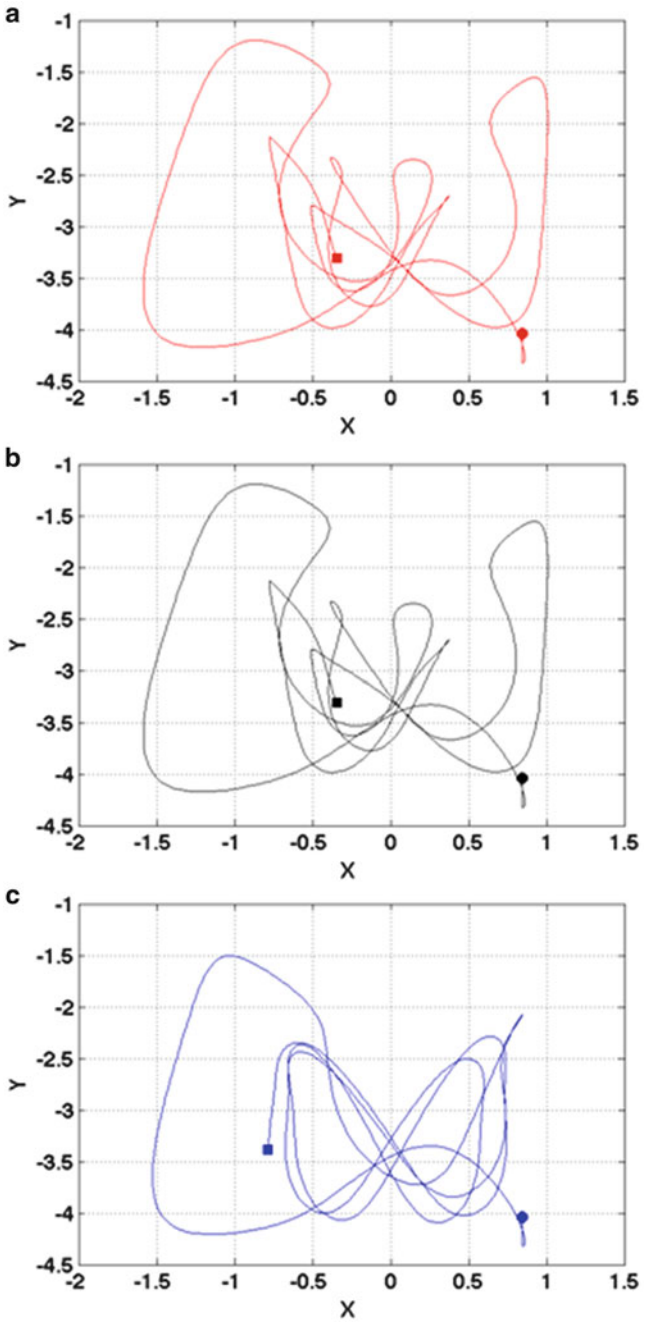

Fig. 4.10 G_{SS}—Trajectory responses (meter) of the mass m_3 over a period of 10 s of (**a**) the nominal system and (**b**) the controlled actual system are approximately the same, while (**c**) the actual system yields a totally different trajectory when the uncertainties in masses are prescribed as $\delta m_1 = 0.1$ kg, $\delta m_2 = -0.2$ kg, and $\delta m_3 = 0.3$ kg and the uncertainty's bound in Eq. (4.79) is chosen to be $\Gamma = 100$

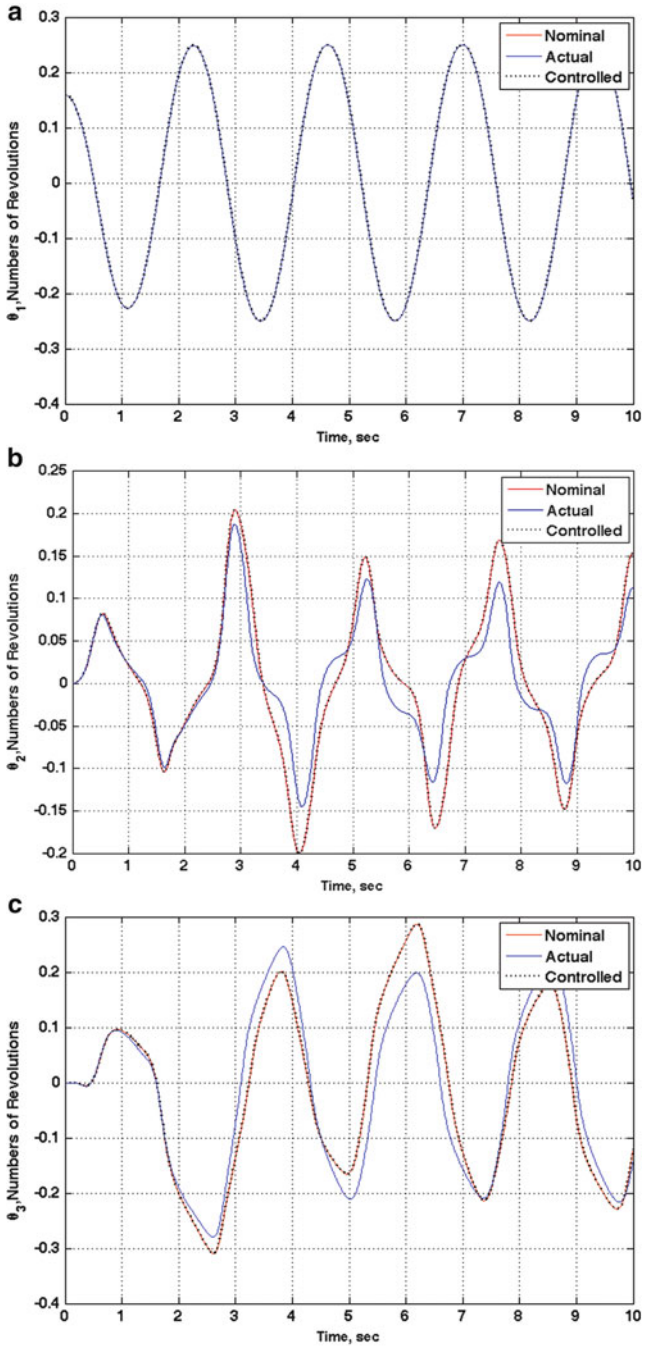

Fig. 4.11 G_{SS}—Angular responses [no. of revolutions (360°)] of the masses (**a**) m_1, (**b**) m_2, and (**c**) m_3. The angular responses of the masses m_2 and m_3 of the actual system move away from those of the nominal system as time increases while those of the controlled system track the nominal system very well

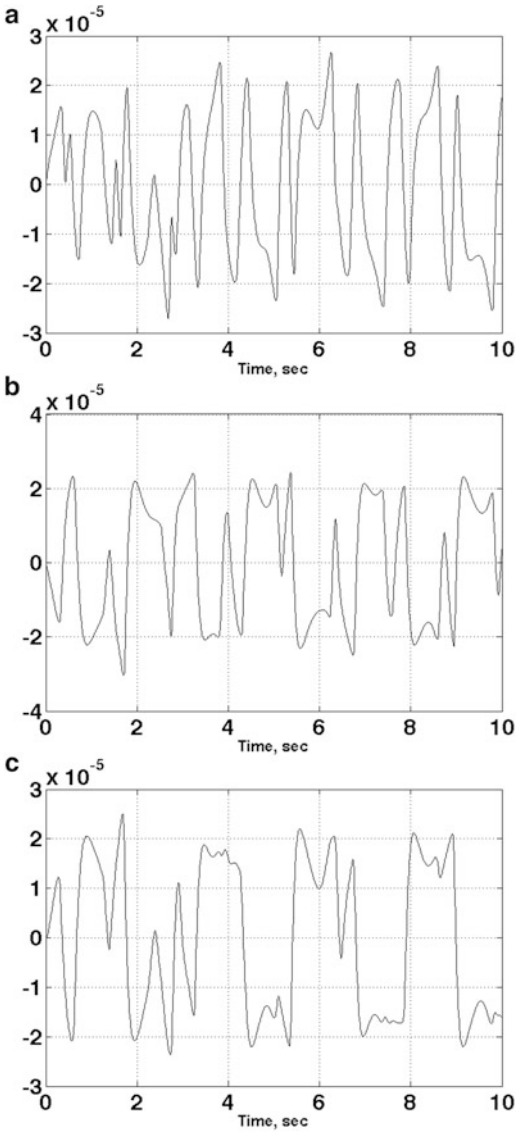

Fig. 4.12 G_{SS}—Tracking errors (radians) between the controlled nominal system and the controlled actual system ($\theta - \theta_c$) in displacement of the masses (**a**) m_1, (**b**) m_2, and (**c**) m_3

knowledge of the actual system. The control forces Q^T and Q^u on the masses m_1, m_2, and m_3 of the actual pendulum are shown in Fig. 4.14. The magnitude of the additional control forces, Q^u, applied by the compensating controller G_{SS} is seen to be small relative to the magnitude of the total control forces, Q^T.

As mentioned earlier that the estimate of $\Gamma(t)$ is not sensitive to the magnitude of additional control forces Q^u in our control approach, we next consider the previous example to show that even if we miss-estimate the bound $\Gamma(t)$, for example, five

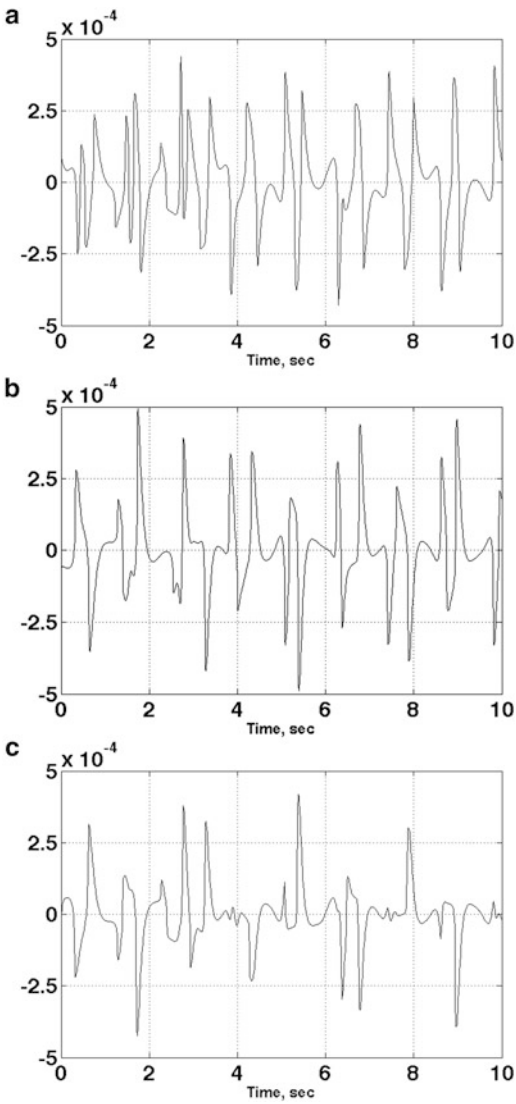

Fig. 4.13 G_{SS}—Tracking errors (rad/s) between the controlled nominal system and the controlled actual system ($\dot{\theta} - \dot{\theta}_c$) in velocity of the masses (**a**) m_1, (**b**) m_2, and (**c**) m_3

times its original value of a 100, i.e., $\Gamma(t) = 500$ for $t \in [0, 10]$, the magnitude of the additional control forces Q^u that is obtained by using the generalized sliding surface controller (4.79) with $\Gamma(t) = 500$ (see Fig. 4.15d) is still approximately the same amount as that obtained by using $\Gamma(t) = 100$ (see Fig. 4.14d). Also the displacement errors ($\theta - \theta_c$) and velocity errors ($\dot{\theta} - \dot{\theta}_c$) between the nominal system (4.19) and the controlled actual system (4.79) are approximately in the same order of magnitudes as can be seen from the comparisons between Figs. 4.12 and 4.16 and between Figs. 4.13 and 4.17, respectively. These show that the equation of the

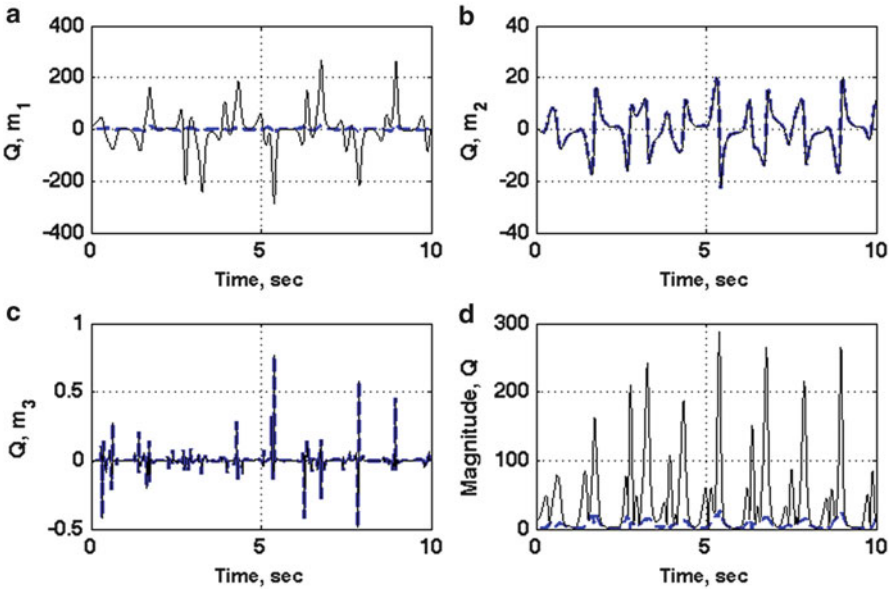

Fig. 4.14 G_{SS}—Control forces (Newtons) on the controlled actual system. The *solid line* shows the total control force, Q^T, and the *dashed line* shows the additional force, Q^u, needed to compensate for uncertainties in the actual system

approximation of the uncertainty's bound (4.37) is valid to use instead of Eq. (4.31) in our control design.

The guaranteed errors in tracking in both displacement and velocity from Figs. 4.12 and 4.13 and the small additional control forces to compensate for uncertainties from Fig. 4.14 guarantee that the proposed control design is robust with respect to the uncertainties in modeling systems.

4.7 Conclusion

In this chapter, the set of closed-form controllers for nonlinear uncertain multi-body systems is developed. This controller is able to guarantee tracking of a desired reference trajectory, which the nominal system—the best estimate of the actual real-life situation—is required to follow. Thus, theoretically speaking, the control requirements placed on the nominal system are thereby followed. The main contributions of this chapter are as follows:

(1) We obtain the exact closed-form solution to the energy control problem of a multi-body system. The control force that must be applied to the system because of the presence of the energy control requirement imposed on the system is

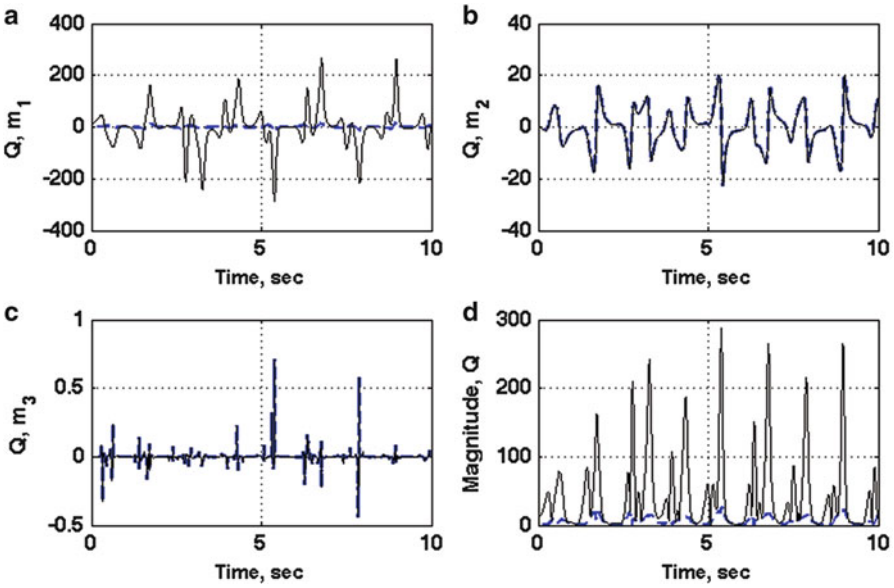

Fig. 4.15 G_{SS}—Control forces (Newtons) on the controlled actual system when using $\Gamma = 500$. The *solid line* shows the total control force, Q^T, and the *dashed line* shows the additional force, Q^u, needed to compensate for uncertainties in the actual system

easily obtained. Also, when starting with initial states that do not satisfy this energy requirement, the error in satisfying it converges to zero exponentially.

(2) The general closed-form equation of motion for uncertain nonlinear multi-body systems—the so-called *controlled actual system*—has been developed. The novelty in the approach developed here is that we first use the *fundamental equation* to obtain exact control of the nominal, nonlinear, non-autonomous, mechanical system. This control, Q^c, ensures that the trajectory constraints are exactly satisfied by the nominal system and that it optimizes the control cost given by $Q^{c^T} M^{-1} Q^c$ at *each* instant of time. Control of the *actual system*, in which both the mass matrix and the 'given' forces may be imprecisely known, is then carried out using the concept of the generalized sliding surface control.

(3) The proposed controlled actual system can simultaneously control the states of the actual system to follow the trajectory that is prespecified by the control requirements imposed on the nominal system and compensate for the uncertainty from the imperfect knowledge of the parameters in the actual system. Thus the proposed control approach is superior to that proposed in many previous studies.

(4) Based on the concept of a generalization of the sliding surface control, the compensating controller is developed to work with the proposed controlled actual system. This leads to the set of closed-form controllers—the generalized sliding surface controller G_{SS}—which can guarantee tracking of the nominal

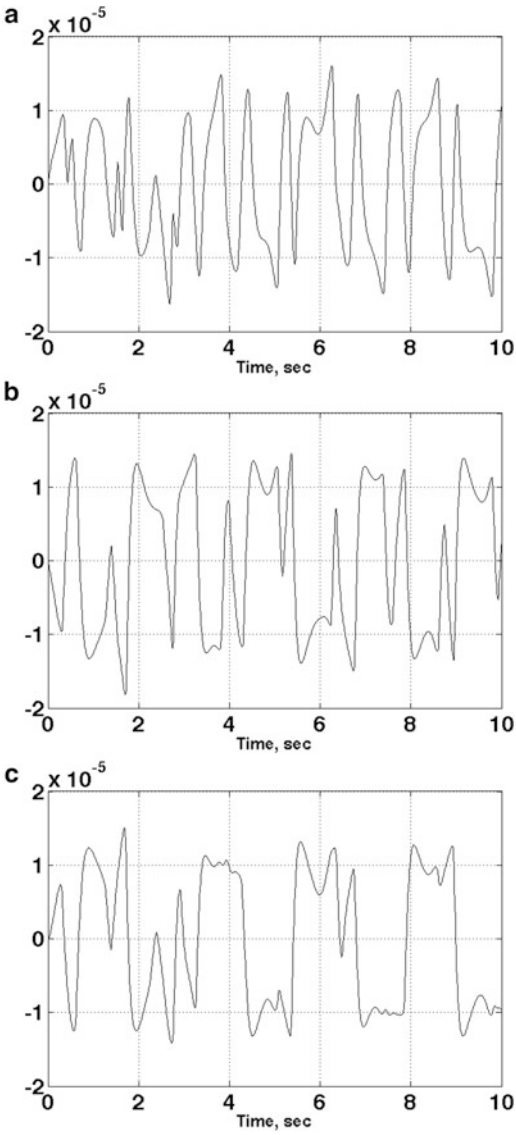

Fig. 4.16 G_{SS}—Tracking errors (radians) between the controlled nominal system and the controlled actual system ($\theta - \theta_c$) in displacement of the masses (**a**) m_1, (**b**) m_2, and (**c**) m_3

system's trajectory within prescribed error bounds. The descriptions of the closed-form controllers involve (i) the description of the actual system given by $M_a\ddot{q}_c = Q_a$, whose parameters are known only imperfectly; (2) the control force $Q^c(t)$ given by Eq. (4.8), which is obtained on the basis of our best estimate of this actual system, namely, on the basis of the corresponding nominal system; and (3) the additional control forces $Q^u := M\ddot{u}$ to compensate for uncertainties, which depend on the estimate of the uncertainties in $\delta\ddot{q}$.

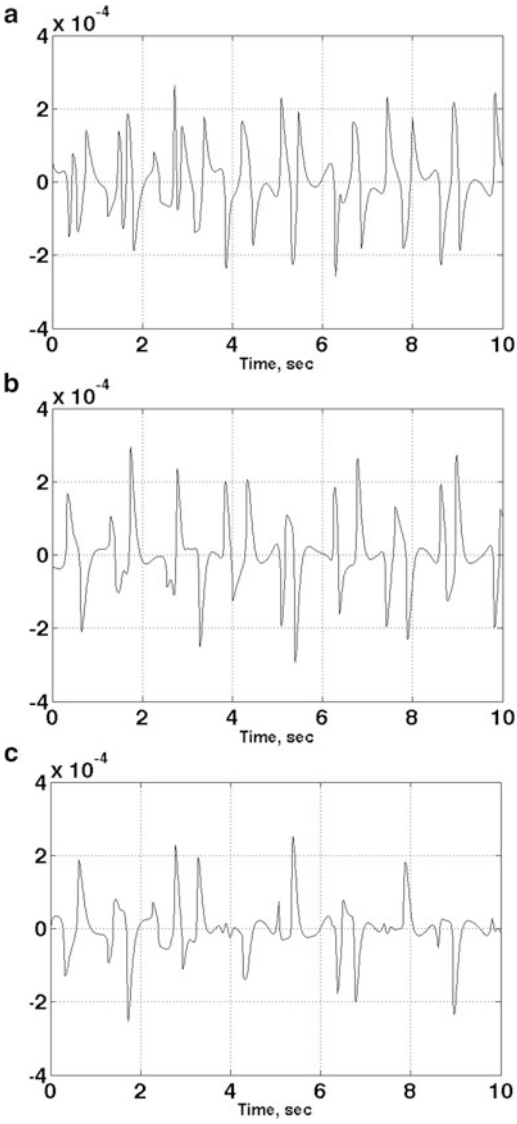

Fig. 4.17 G_{SS}—Tracking errors (rad/s) between the controlled nominal system and the controlled actual system ($\dot{\theta} - \dot{\theta}_c$) in velocity of the masses (**a**) m_1, (**b**) m_2, and (**c**) m_3

(5) The quantity $\delta\ddot{q}$ is not known, but we have an estimate of the uncertainty involved: $\|\delta\ddot{q}\| \leq \Gamma(t)$. The bound $\Gamma(t)$ depends on our bounds on δM and δQ, which in turn depend on the state of our knowledge about the actual system.

(6) Configuration variables subjected to both holonomic and nonholonomic control requirements, or to a combination of such requirements, are handled in a uniform manner in the proposed control methodologies.

(7) We have generalized the concept of the sliding surface control by including control functions $f_i(s)$ that are not necessarily signum or saturation functions

[19–22]. These control functions and the parameters that define the additive controller can therefore be chosen depending on a practical consideration of the control environment, and the extent to which the compensation of the uncertainties is desired. These parameters can be adjusted so that desired error bounds can be guaranteed when the uncertain system is required to track the nominal system. Thus when dealing with large, complex multi-body systems greater flexibility is afforded. The flexibility in choosing the control functions becomes more important when practical limitations of the control are specified. For example, the use of the cubic function in the example considered may obviate the need for a high-gain controller and would also allow the continuous control, thereby preventing chattering.

(8) For brevity, we have illustrated through numerical examples uncertainties that are related to the properties of a simple physical system. However, the formulation of the proposed control methodology encompasses both general sources of uncertainties—uncertainties in the description of the physical system and uncertainties in knowledge of the 'given' force applied to the system. The closed-form controllers developed herein is therefore general enough to be applicable to complex dynamical system in which both types of uncertainties may be important.

(9) The control design is evaluated using numerical solution comparisons of the tracking errors between the nominal and the controlled actual systems. The results demonstrate that the controller has good transient behaviors and is robust with respect to the uncertainties in the modeling process. Furthermore, with the simplicity and accuracy obtained, the control scheme proposed in this chapter can be implemented for various cases and for even more complex dynamical problems.

Key Symbols

M	The n by n nominal mass matrix
Q	The n-vector nominal given force
q	The n-vector generalized coordinate of the nominal mechanical system
$\dot{q}$	The n-vector generalized velocity of the nominal mechanical system
a	The n-vector unconstrained generalized acceleration of the nominal mechanical system ($a = M^{-1}Q$)
φ	The m-vector constraints (holonomic and/or nonholonomic)
A	The left-handed side, m by n matrix of constraint equations, see Eq. (4.5)
b	The right-handed side, m-vector of constraint equations, see Eq. (4.5)
r	The rank of matrix A
Q^c	The n-vector generalized constraint force
$+$	The Moore–Penrose (MP) inverse of a matrix
g	The gravitational acceleration
m_i	The ith mass of the system

L_i The length of the ith massless rod of the pendulum, see Fig. 4.1

θ_i The angle between the ith massless rod of the pendulum and the vertical axis, see Fig. 4.1

E_i The total energy of the mass m_i

α The arbitrary, nowhere-zero, sufficiently smooth real function of time

M_a The n by n actual mass matrix ($M_a = M + \delta M$)

δM The n by n matrix that characterizes uncertainties in the actual mass matrix

Q_a The n-vector given force of the actual system ($Q_a = Q + \delta Q$)

δQ The n-vector of uncertainties in given force of the actual system

$\tilde{q}$ The n-vector generalized coordinate of the actual mechanical system

$\dot{\tilde{q}}$ The n-vector generalized velocity of the actual mechanical system

q_a The n-vector generalized coordinate of the actual mechanical system, which is obtained by using the correct control force that the actual system is required to be subjected to, because of the control requirements

$\dot{q}_a$ The n-vector generalized velocity of the actual mechanical system, which is obtained by using the correct control force that the actual system is required to be subjected to, because of the control requirements

a_a The n-vector unconstrained generalized acceleration of the actual mechanical system ($a_a = M_a^{-1} Q_a$)

Q^u The n-vector additional generalized control force that compensates for uncertainties ($Q^u = M\ddot{u}$)

$\ddot{u}$ The n-vector additional generalized acceleration to compensate for uncertainties

q_c The n-vector generalized coordinate of the controlled actual mechanical system

$\dot{q}_c$ The n-vector generalized velocity of the controlled actual mechanical system

e The tracking error between the controlled actual system's response and the nominal system's response ($e = q_c - q$)

$\delta\ddot{q}$ The n-vector of uncertainties in acceleration of the actual system

$\bar{M}$ The n by n matrix of uncertainties in the compensating controller ($\bar{M} \approx I - \left(I + M^{-1}\delta M\right)^{-1}$)

Γ The arbitrary positive function of time that characterizes the bound on $\delta\ddot{q}$ ($\|\delta\ddot{q}\| \leq \Gamma(t)$)

Γ_m The constant upper bound on the function $\Gamma(t)$

s The n-vector sliding surface

k_1 The arbitrary small positive number

Ω_ε The surface of the n-dimensional cube around the point $s = 0$

β_0 The arbitrary positive constant ($\beta_0 > k_1 \left\|\bar{M}\right\| \|\dot{e}\|$)

γ The small positive constant ($\gamma = \frac{\|s\|\|f(s)\|}{s^T f(s)}$)

σ The arbitrary small positive constant ($\gamma \leq \sigma \leq 1$)

α_0 The arbitrary small positive constant ($0 < \alpha_0 < 1 - n\sigma \left\|\bar{M}\right\|$)

β The positive function of time ($\beta(t) > \frac{n(\Gamma+\beta_0)}{\alpha_0}$)

ε The arbitrary small positive constant

α_c The arbitrary positive constant

$f(s)$ The arbitrary monotonic increasing odd continuous function of s

G_{ss} The generalized sliding surface controller
V The Lyapunov function
L_ε The length of each side of the cubical surface Ω_ε
Q^T The n-vector total control force of the mechanical system ($Q^T = Q^c + Q^u$)

References

1. Su CY, Stepanenko Y (1994) Robust motion/force control of mechanical systems with classical nonholonomic constraints. IEEE Trans Autom Control 39:609–614
2. Oya M, Su CY, Katoh R (2003) Robust adaptive motion/force tracking control of uncertain nonholonomic mechanical systems. IEEE Trans Robot Automat 19:175–181
3. Tseng CS, Chen BS (2003) A mixed H_2/H_∞ adaptive tracking control for constrained nonholonomic systems. Automatica 39:1011–1018
4. Chang YC, Chen BS (2000) Robust tracking designs for both holonomic and nonholonomic constrained mechanical systems: adaptive fuzzy approach. IEEE Trans Fuzzy Syst 8:46–66
5. Wang J, Zhu X, Oya M, Su CY (2006) Robust motion tracking control of partially nonholonomic mechanical systems. Automatica 54:332–341
6. Wang ZP, Ge SS, Lee TH (2004) Robust motion/force control of uncertain holonomic/nonholonomic mechanical systems. IEEE/ASME Trans Mech 9:118–123
7. Song Z, Zhao D, Yi J, Li X (2005) Robust motion control for nonholonomic constrained mechanical systems: sliding mode approach. In: American control conference, pp 2883–2888
8. Udwadia FE, Kalaba RE (1992) A new perspective on constrained motion. Proc R Soc London A 439:407–410
9. Udwadia FE, Kalaba RE (1996) Analytical dynamics: a new approach. Cambridge University Press, New York, pp 82–103
10. Udwadia FE, Kalaba RE (2002) On the foundations of analytical dynamics. Int J Nonlin Mech 37:1079–1090
11. Kalaba RE, Udwadia FE (1993) Equations of motion for nonholonomic, constrained dynamical systems via Gauss's principle. J Appl Mech 60(3):662–668
12. Udwadia FE (1996) Equations of motion for mechanical systems: a unified approach. Int J Nonlin Mech 31(6):951–958
13. Udwadia FE (2000) Nonideal constraints and Lagrangian dynamics. J Aerosp Eng 13(1):17–22
14. Udwadia FE, Phohomsiri P (2006) Explicit equations of motion for constrained mechanical systems with singular mass matrices and applications to multi-body dynamics. Proc R Soc London A 462:2097–2117
15. Udwadia FE, Kalaba RE (2002) What is the general form of the explicit equations of motion for constrained mechanical systems. J Appl Mech 69(3):335–339
16. Udwadia FE (2003) A new perspective on the tracking control of nonlinear structural and mechanical systems. Proc R Soc London A 459:1783–1800
17. Udwadia FE (2005) Equations of motion for constrained multibody systems and their control. J Optim Theory Appl 127(3):627–638
18. Henderson HV, Searle SR (1981) On deriving the inverse of a sum of matrices. SIAM Rev 23(1):53–60
19. Utkin VI (1977) Variable structure with sliding mode-A survey. IEEE Trans Autom Control 22(2):212–222
20. Tsypkin YZ (1995) Teoriya Releinykh System Avtomati Cheskogo Regulirovaniya (Theory of switching control systems). Gostekhizdat, Moscow
21. Edwards C, Spurgeon S (1999) Sliding mode control: theory and applications. Taylor and Francis, London
22. Khalil HK (2002) Nonlinear systems. Prentice-Hall, Upper Saddle River, NJ, pp 551–589

Chapter 5
Robustness of Orthogonal Eigenstructure Control to Actuators Failure

Mohammad Rastgaar and Nina Mahmoudian

Abstract Orthogonal eigenstructure control (OEC) is a feedback control method applicable to multi-input multi-output linear systems. While the available control design methodologies offer a large and complex design space of options that can often overwhelm a designer, this control method offers a significant simplification of the design task while still allowing some experience-based design freedom. In this chapter, the robustness of the method to the failure of the actuators was investigated. It was shown the control gain was capable of controlling the systems during an actuator failure, as OEC generates the control gain by maintaining the closed-loop eigenvectors within the achievable eigenvectors set. A system of lumped masses was used to explain the method; then, the problem of failed actuators in the vibration control of a plate was investigated. Finite element analysis was used for modeling the plate to simulate the dynamic behavior of the system. Five cases were considered and the suppression of the vibration in a plate with three working actuators was compared to the performance of a similar control system with a failed actuator. Also, the behaviors of the system with failed actuators were compared to the systems that were designed to operate with lesser control actuators. It was shown that the number of closed-loop eigenvalue pairs that moved from the cluster of the open-loop poles was equal to the number of working actuators. The closed-loop poles in all the systems were moved to the vicinity of one specific area, generating a break frequency with sufficient damping for robust active vibration control.

M. Rastgaar (✉) • N. Mahmoudian
Mechanical Engineering–Engineering Mechanics Department, Michigan Technological University, Houghton, MI 49931, USA
e-mail: rastgaar@mtu.edu

R.N. Jazar and L. Dai (eds.), *Nonlinear Approaches in Engineering Applications 2*,
DOI 10.1007/978-1-4614-6877-6_5,

5.1 Introduction

OEC was developed to address the need for more robust control method that is relatively easy to design and implement and allows control engineers to achieve good performing designs even with little design experience. In this chapter, the problem of robustness of the vibration control to the failure of actuators was investigated using OEC, a feedback control method applicable to multi-input multi-output linear systems. While the available control design methodologies offer a large and complex design space of options that can often overwhelm a designer, this control method offers a significant simplification of the design task while still allowing some experience-based design freedom. This control method needs neither predefining the locations for the closed-loop poles nor shaping the closed-loop eigenvectors. The orthogonal eigenstructure control regenerates the open-loop system and simultaneously finds the vectors that are orthogonal to its eigenvectors. The determined orthogonal vectors are within the achievable eigenvectors set, so the error due to the difference between achievable eigenvectors and the desirable eigenvectors, as is common in eigenstructure assignment methods, is eliminated. It has been shown that eigenstructure assignment methods are effective for active vibration cancelation in structures. The methods currently available, however, depend on the experience of the controller designer, based on the geometry and dynamics of the structures. In general, there are no unified methods for the application of eigenstructure assignment with the purpose of vibration cancelation in structures. Existing methods require *apriori* definition of the desired eigenstructure [1]. Identifying the desirable locations for the closed-loop eigenvalues and defining the desirable closed-loop eigenvectors are not a straightforward task [2]. For large scale systems it becomes impractical to define a desired closed-loop eigenstructure. Therefore, the existing methods are not able to be applied to such systems or many other similar practical engineering structures. Considering that there are no one-to-one relationship between the elements of closed-loop eigenvectors and the states of the system, one may define a desirable eigenvector, but not achievable, that does not satisfy a given design criterion. This may lead to excessive actuation forces because of improper closed-loop poles. Additionally, the desirable eigenvectors do not necessarily lie within the space of achievable eigenvectors. The missing piece of this puzzle is a control method that can systematically lead to a set of desirable, and obviously achievable, closed-loop eigenvectors that result in a decoupled control and less sensitive to actuator failure.

Critical issues may arise when the actuator fails in a system. The application of robustness of control methods to actuator failure by absorbing some of the impacts on the performance of the control system may prevent a complete failure of the system and allow for delayed maintenance. Many researchers have investigated different methods to accommodate actuator failure in a variety of applications. A method for actuator failure was proposed by Tao et al. as a direct adaptive state feedback control scheme for linear time-invariant systems [3–5]. Their method was model based and the failure pattern was simulated such that some of the control

inputs were stuck at unknown values at unknown time instants. They investigated the conditions and controller structures for matching system and model states during actuator failure. Tang et al. proposed a method with a similar concept for multi-input multi-output nonlinear systems [6]. Fei et al. developed an output feedback control for output tracking in discrete linear time-invariant systems, with uncertain failures [7]. Some methods address the failure of actuators by multiple model design, for example, Chen et al. studied the problem of actuator failure for linear and nonlinear systems [8]. In this method, all the possible scenarios of the actuator failure were accumulated and used for both state and output feedback control by combining the observer design with the adaptation method. Also, a design technique to prevent stuck actuators was proposed by Chen et al. based on an iterative learning observer and designing a reconfigurable controller using estimated states to compensate for the effect of the failed actuators [9]. The optimal control approach was also used for compensating the effect of failed actuators. Yang et al. studied a low-cost LQ regulator for discrete-time systems with actuator failure [10]. Seo et al. considered the actuator failures as disturbance signals of arbitrary values to the system, and designed a robust and reliable H_∞ state feedback control for linear uncertain systems with time-varying norm-bounded parameter uncertainty [11]. Wang et al. proposed a H_∞ control for a class of switched nonlinear systems with actuator failures among a prespecified subset of the situations of the actuators' failure [12]. They used a multiple-Lyapunov function method to derive a sufficient condition for the switched nonlinear system to be asymptotically stable with H_∞ norm bound. Zhao et al. used a linear Matrix Inequality Approach (LMI) for state feedback control design applied to a class of systems with model uncertainties and actuators' failures [13].

The eigenstructure assignment methods have been used to address the problem of actuator failure and reconfiguring the systems. Liu et al. combined the time-domain performance specifications provided by eigenstructure assignment and robust performance specifications in the frequency domain considered by H_∞ control to develop a joint optimal robust control design [14]. A method for designing the reconfiguring class of second-order systems has been proposed by Wang et al. based on the parametric eigenstructure assignment by PD feedback developed earlier by Duan [15]. This method finds the parametric forms of all the re-synthesized gain matrices. Zhang et al. proposed an integrated fault detection, diagnosis, and reconfigurable control scheme based on the interacting multiple model approach and used an eigenstructure assignment technique for reconfigurable feedback control law design [16]. Another method based on the eigenstructure assignment method for reconfiguring the control system to recover the eigenvalues and eigenvectors of the original closed-loop system has been presented by Jiang et al. [17]. This method leads to a stable system when full state feedback is available and, for the output feedback problems, recovers the subsequent dominant eigenvalues and eigenvectors of the original system. Apkarian et al. used the eigenstructure assignment with Lyapunov-type constraints to develop a control method with enhanced LMI characterizations [18].

OEC was introduced by the authors [19] and was developed further for systems with non-collocated actuators and sensors [20]. Application of OEC in high degrees of freedom systems was presented in [21]. The experimental application of this method for active vibration cancelation using piezoelectric actuators was shown in [22]. A comparison of OEC with eigenstructure assignment techniques was discussed in [23].

In this chapter we evaluated the robustness of OEC when used for vibration cancelation in a plate. First, we defined the orthogonal eigenstructure control. Then, using a simple lumped mass model, we described how the method provided the control gain matrix such that both the closed-loop system with working actuators and the one with the failed actuator have eigenvectors within achievable eigenvectors set. Finally, we applied the control method to a finite element model of a plate and investigated the vibration cancelation in the presence of the failed actuator. Comparisons were made between systems with three working actuators and systems with two working and one failed actuators. Moreover, a comparison between the systems with two working and one failed actuators were compared to the systems that were designed specifically with two actuators.

5.2 Orthogonal Eigenstructure Control

Let's consider the first order realization of a closed-loop multi-input multi-output linear system;

$$\dot{x} = Ax + Bu + Ef \tag{5.1}$$

$$y = Cx \tag{5.2}$$

$$u = Ky \tag{5.3}$$

where x and $\dot{x}$ are the $2n \times 1$ state vector and its time derivative, A is the $2n \times 2n$ state matrix, B is a $2n \times m$ input matrix, where $m \geq 2$ is the number of the actuators, E is the disturbance input matrix, f is the disturbance vector with appropriate dimensions, and u is the input vector of dimension m. Assume the actuators and sensors are colocated; therefore, the output vector y is $m \times 1$ and the output matrix C is $m \times 2n$. K is $m \times m$ feedback gain matrix. The closed-loop equation of motion is

$$\dot{x} = (A + BKC)x + Ef \tag{5.4}$$

For the closed loop system of Eq. (5.4), the eigenvalue problem is defined as

$$(A + BKC)\phi_i = \lambda_i \phi_i \quad i = 1, \ldots, 2n \tag{5.5}$$

where ϕ_i and λ_i are the closed-loop eigenvectors and eigenvalues of the system, respectively. Equation (5.5) may be written in matrix form as follows:

$$[A - \lambda_i I \ |B] \begin{Bmatrix} \phi_i \\ KC\phi_i \end{Bmatrix} = 0 \ i = 1, \ldots, 2n \tag{5.6}$$

where I is the $2n \times 2n$ identity matrix. Equation (5.6) implies that the vector $\begin{Bmatrix} \phi_i \\ KC\phi_i \end{Bmatrix}$ spans the null space of the matrix $S_{\lambda i} = [A - \lambda_i I \ |B]_{2n\times(2n+m)}$. Calculating the singular value decomposition of $S_{\lambda i}$, we may write

$$S_{\lambda i} = [U_i]_{2n\times 2n}[\Sigma_i | 0_{2n\times m}]_{2n\times(2n+m)}[V_i^*]_{(2n+m)\times(2n+m)} \tag{5.7}$$

U_i and V_i are the left and right orthonormal matrices, respectively, and V_i^* is the conjugate transpose of the complex matrix V_i. The index i specifies the equations for the ith operating eigenvalue. In OEC, operating eigenvalue λ_i are chosen from the open-loop eigenvalues set. Substituting operating eigenvalue λ_i in Eq. (5.6) allows for regenerating the open-loop system and systems with eigenvectors almost orthogonal to the eigenvectors of the regenerated open-loop system simultaneously. The number of operating eigenvalues is the same as the number of the required pairs of actuators and sensors m. It has been shown that the m farthest open-loop eigenvalues from the origin are proper options for the operating eigenvalues [21]. After partitioning V_i, the second column block of V_i spans the null space of $S_{\lambda i}$ [24, 25].

$$[V_i]_{(2n+m)\times(2n+m)} = \begin{bmatrix} [V_{11}^i]_{2n\times 2n} & [V_{12}^i]_{2n\times m} \\ [V_{21}^i]_{m\times 2n} & [V_{22}^i]_{m\times m} \end{bmatrix} \tag{5.8}$$

An achievable eigenvector ϕ_i^a of the closed-loop system is any linear combination of m columns of V_{12}^i using a coefficient vector r^i.

$$\phi_i^a = V_{12}^i r^i \tag{5.9}$$

The control gain matrix K is defined as

$$KC\phi_i^a = V_{22}^i r^i \tag{5.10}$$

which requires finding the appropriate r^i. We define the modal energy corresponding to the ith achievable eigenvector of the closed-loop system:

$$E_i = r^{i*} V^* V_{12}^i r^i \tag{5.11}$$

Since V_{12}^i is complex, then ${V_{12}^i}^* V_{12}^i$ is a Hermitian matrix and its eigenvalue decomposition is

$$V_{12}^{i}{}^{*}V_{12}^{i} = \bar{U}^{i}\Lambda^{i}\bar{U}^{i*} \tag{5.12}$$

where $\bar{\Lambda}_i$ and $\bar{U}^i$ are the eigenvalues and eigenvectors matrices of $V_{12}^{i}{}^{*}V_{12}^{i}$. Similarly, V_{22}^{i} is a complex matrix and the eigenvalue decomposition of the Hermitian matrix $V_{22}^{i}{}^{*}V_{22}^{i}$ is

$$V_{22}^{i}{}^{*}V_{22}^{i} = \bar{U}_{w}^{i}\bar{\Lambda}_{w}^{i}\bar{U}_{w}^{i*} \tag{5.13}$$

where $\bar{\Lambda}_{w}^{i}$ and $\bar{U}_{w}^{i}$ are the eigenvalue and eigenvector matrices of $V_{22}^{i}{}^{*}V_{22}^{i}$. It has been shown by the authors [24, 26] that the eigenvalues of the Hermitian products $V_{12}^{i}{}^{*}V_{12}^{i}$ and $V_{22}^{i}{}^{*}V_{22}^{i}$ belong to the [0 1] interval. Moreover, it has been shown that the eigenvectors of $V_{22}^{i}{}^{*}V_{22}^{i}$ and $V_{12}^{i}{}^{*}V_{12}^{i}$ are identical and the summation of the eigenvalues of $V_{12}^{i}{}^{*}V_{12}^{i}$ and $V_{22}^{i}{}^{*}V_{22}^{i}$ associated with similar eigenvectors are in unity [24, 26].

$$\bar{\Lambda}_{w}^{i} + \bar{\Lambda}^{i} = I \tag{5.14}$$

$$\bar{U}^{i} = \bar{U}_{w}^{i} \tag{5.15}$$

Rearranging the Eq. (5.12) implies

$$\bar{U}^{i*}V_{12}^{i}{}^{*}V_{12}^{i}\bar{U}^{i} = \bar{\Lambda}^{i} \tag{5.16}$$

If the eigenvector $\bar{U}_J^i$ associated with a unity eigenvalue of $V_{12}^{i}{}^{*}V_{12}^{i}$ in Eq. (5.11) is considered as r^i, its modal energy $E^i = 1$.

$$\bar{U}_J^{i*}V_{12}^{i}{}^{*}V_{12}^{i}\bar{U}_J^{i} = 1 \tag{5.17}$$

That results in

$$\bar{U}_J^{i*}(V_{22}^{i}{}^{*}V_{22}^{i})\bar{U}_J^{i} = 0 \tag{5.18}$$

Equations (5.17) and (5.18) yield

$$V_{22}^{i}\bar{U}_J^{i} = 0 \tag{5.19}$$

which results in the zero gain matrix

$$KC\phi_i^a = V_{22}^{i}r^i = V_{22}^{i}\bar{U}_J^{i} = 0 \tag{5.20}$$

which implies that the open-loop system has been regenerated. Therefore, if the eigenvector $\bar{U}_J^i$ associated with a unity eigenvalue of $V_{12}^{i}{}^{*}V_{12}^{i}$ is selected as r^i, one can generate the open-loop eigenvectors within the null space of the closed-loop eigenvectors associated with the operating eigenvalue λ_i. In other words, $V_{12}^{i}\bar{U}_J^{i}$

is parallel to the eigenvector corresponding to the open-loop eigenvalue or the operating eigenvalue. Any other eigenvectors associated with non-unity eigenvalues of ${V_{12}^i}^* V_{12}^i$ are orthogonal to the eigenvector associated with the unity eigenvalue of ${V_{12}^i}^* V_{12}^i$. Therefore, a set of closed-loop eigenvectors can be found that are orthogonal to the open-loop ones. The modal energies associated with the closed-loop eigenvectors are equal to non-unity eigenvalues of ${V_{12}^i}^* V_{12}^i$. Since all the non-unity eigenvalues of ${V_{12}^i}^* V_{12}^i$ are small, the modal energies of the modes associated with the operating eigenvalues become zero or negligible.

V and W are determined by appending the calculated closed-loop eigenvectors for all the operating eigenvalues

$$V = \left[V_{12}^1 r^1 \cdots V_{12}^m r^m\right] \tag{5.21}$$

$$W = \left[V_{22}^1 r^1 \cdots V_{22}^m r^m\right] \tag{5.22}$$

The control gain matrix K is

$$K = W(CV)^{-1} \tag{5.23}$$

The state matrix of the closed-loop system is

$$A_c = A + BKC \tag{5.24}$$

There are m eigenvectors belong to ${V_{12}^i}^* V_{12}^i$ that can be chosen as r^i. Therefore, there are m^m possible closed-loop systems. ${V_{12}^i}^* V_{12}^i$ has one unity eigenvalue and $m-1$ zero or negligible ones. Excluding the regenerated open-loop system, there are $m^m - 1$ possible closed-loop systems.

Most of the eigenstructure assignment methods use a different approach such as eigenvector shaping to define a desired eigenvector for the system [ϕ_i^a in Eq. (5.10)]. In general, methods that use the pseudo inverse of V_{12}^i to find the required r^i have limitations because there is always a distance between the desired and controlled eigenvectors and the controlled eigenvectors will not be identical to the desired ones. This is not an issue in OEC.

Figure 5.1 shows the open-loop eigenvectors and achievable closed-loop eigenvectors of a system with three collocated actuators and sensors. For each open-loop eigenvector associated with one operating eigenvalue, two orthogonal eigenvectors can be found within the achievable eigenvectors set. To have a closed-loop system, it is sufficient to alter just one open-loop eigenvector and replace it with an orthogonal vector. It results in $3^3 - 1 = 26$ closed-loop systems from which the most desirable one must be chosen. It has been shown, however, that for a high dimensional system like a plate, if the operating eigenvalues are chosen as the farthest open-loop eigenvalues from the origin, all the possible closed-loop system converge [21].

In the next sections, we used the OEC to isolate the vibrations due to the disturbance in the system with lumped masses. We explained how the failure of one actuator does not change the behavior of the system, since the reduced gain matrix still was able to generate a closed-loop system with eigenvalues close those of the

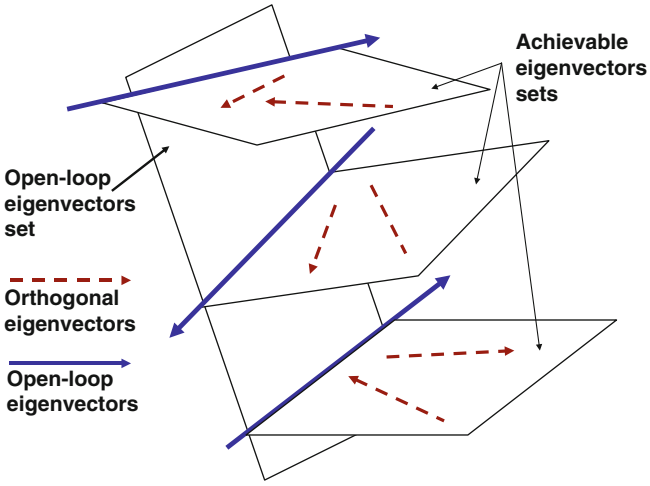

Fig. 5.1 Schematics of the process of orthogonal eigenstructure control. Open-loop eigenvectors are the intersections of the open-loop eigenvectors set and the achievable eigenvectors set. The orthogonal eigenvectors within the achievable eigenvectors set are being substituted as the open-loop ones

system with working actuators. Also, it was shown that the closed-loop eigenvectors were within the achievable eigenvectors set. Then, the OEC was applied to a plate for vibration suppression, and the robustness of the control to the failure of the actuators was investigated.

5.3 Explanatory Example: System of Lumped Masses

To investigate the effects of failure of one of the actuators during the control of a system, a simple system of longitudinally vibrating masses was considered. First, we applied OEC to isolate the left side of the system from vibrating. As shown on Fig. 5.2, the system consisted of 10 masses which were consecutively connected by springs and dampers. The force disturbance was considered to be a chirp input applied to m_{10}. It reached from 0 Hz to 30 Hz in 1 s with magnitude of 500 N. All masses were 100 kg, and damping coefficients were assumed to be 10 N s m^{-1}. The stiffnesses of the springs were 2,000 N m^{-1}.

We assumed there were three pairs of collocated actuators and sensors on masses m_6, m_7, and m_8. For simplicity, all the elements of the B and C matrices were assumed to be zero except for

$$B(16,1) = B(17,2) = B(18,3) = -1/100$$
$$C(1,6) = C(2,7) = C(3,8) = 1$$

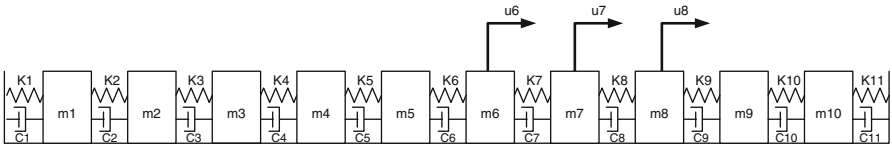

Fig. 5.2 Actuation forces for the system with failed actuator

As stated earlier, since there were three actuators and sensors, the operating eigenvalues were the three greatest open-loop eigenvalues [21]. Knowing that the complex conjugates of the operating eigenvalues lead to similar results, the operating eigenvalues were $\lambda_1 = -0.4919 + 8.8396i$, $\lambda_2 = -0.4683 + 8.5692i$, and $\lambda_3 = -0.4310 + 8.1246i$.

Following the procedure of the OEC, for the first operating eigenvalue λ_1, the product of the complex conjugate of the basis of the null space to the matrix itself could be written as follows:

$$V_{12}^{1*}V_{12}^{1} = \begin{bmatrix} 0.4128 & -0.3789 & 0.3143 \\ -0.3789 & 0.3479 & -0.2886 \\ 0.3143 & -0.2886 & 0.2394 \end{bmatrix} = \bar{U}^1\bar{\Lambda}^1\bar{U}^{1*}$$

$$= \underbrace{\begin{bmatrix} -0.6425 & -0.6699 & 0.3722 \\ 0.5898 & -0.1222 & 0.7982 \\ -0.4892 & 0.7324 & 0.4736 \end{bmatrix}}_{\bar{U}_1^1 \quad \bar{U}_2^1 \quad \bar{U}_3^1} \begin{bmatrix} 1 \cdots 0 \\ \vdots \quad 0 \quad \vdots \\ 0 \cdots 0 \end{bmatrix} \begin{bmatrix} -0.6425 & 0.5898 & -0.4892 \\ -0.6699 & -0.1222 & 0.7324 \\ 0.3722 & 0.7982 & 0.4736 \end{bmatrix}$$

$$V_{22}^{1*}V_{22}^{1} = \begin{bmatrix} 0.5872 & 0.3789 & -0.3143 \\ 0.3789 & 0.6521 & 0.2886 \\ -0.3143 & 0.2886 & 0.7606 \end{bmatrix} = \bar{U}^1\bar{\Lambda}_w^1\bar{U}^{1*}$$

$$= \underbrace{\begin{bmatrix} -0.6425 & -0.6699 & 0.3722 \\ 0.5898 & -0.1222 & 0.7982 \\ -0.4892 & 0.7324 & 0.4736 \end{bmatrix}}_{\bar{U}_1^1 \quad \bar{U}_2^1 \quad \bar{U}_3^1} \begin{bmatrix} 0 \cdots 0 \\ \vdots \quad 1 \quad \vdots \\ 0 \cdots 1 \end{bmatrix} \begin{bmatrix} -0.6425 & 0.5898 & -0.4892 \\ -0.6699 & -0.1222 & 0.7324 \\ 0.3722 & 0.7982 & 0.4736 \end{bmatrix}$$

Similarly, the second operating eigenvalue λ_2 yielded

$$V_{12}^{2*}V_{12}^{2} = \begin{bmatrix} 0.0464 & -0.1275 & 0.1673 \\ -0.1275 & 0.3502 & -0.4597 \\ 0.1673 & -0.4597 & 0.6035 \end{bmatrix} = \bar{U}^2\bar{\Lambda}^2\bar{U}^{2*}$$

$$= \underbrace{\begin{bmatrix} -0.2154 & -0.8861 & 0.4104 \\ 0.5918 & 0.2159 & 0.7767 \\ -0.7768 & 0.4101 & 0.4779 \end{bmatrix}}_{\bar{U}_1^2 \quad \bar{U}_2^2 \quad \bar{U}_3^2} \begin{bmatrix} 1 & \cdots & 0 \\ \vdots & 0.0001 & \vdots \\ 0 & \cdots & 0 \end{bmatrix} \begin{bmatrix} -0.2154 & 0.5918 & -0.7768 \\ -0.8861 & 0.2159 & 0.4101 \\ 0.4104 & 0.7767 & 0.4779 \end{bmatrix}$$

$$V_{22}^{2*}V_{22}^{2} = \begin{bmatrix} 0.9536 & 0.1275 & -0.1673 \\ 0.1275 & 0.6498 & 0.4597 \\ -0.1673 & 0.4597 & 0.3965 \end{bmatrix} = \bar{U}^2\bar{\Lambda}_w^2\bar{U}^{2*}$$

$$= \underbrace{\begin{bmatrix} -0.2154 & -0.8861 & 0.4104 \\ 0.5918 & 0.2159 & 0.7767 \\ -0.7768 & 0.4101 & 0.4779 \end{bmatrix}}_{\bar{U}_1^2 \quad \bar{U}_2^2 \quad \bar{U}_3^2} \begin{bmatrix} 0 & \cdots & 0 \\ \vdots & 0.9999 & \vdots \\ 0 & \cdots & 1 \end{bmatrix} \begin{bmatrix} -0.2154 & 0.5918 & -0.7768 \\ -0.8861 & 0.2159 & 0.4101 \\ 0.4104 & 0.7767 & 0.4779 \end{bmatrix}$$

Finally, the third operating eigenvalue λ_3 resulted in

$$V_{12}^{3*}V_{12}^{3} = \begin{bmatrix} 0.6929 & -0.2160 & -0.4076 \\ -0.2160 & 0.0673 & 0.1270 \\ -0.4076 & 0.1270 & 0.2399 \end{bmatrix} = \bar{U}^3\bar{\Lambda}^3\bar{U}^{3*}$$

$$= \underbrace{\begin{bmatrix} -0.8324 & 0.2253 & 0.5063 \\ 0.2594 & -0.6489 & 0.7153 \\ 0.4897 & 0.7268 & 0.4816 \end{bmatrix}}_{\bar{U}_1^3 \quad \bar{U}_2^3 \quad \bar{U}_3^3} \begin{bmatrix} 1 & \cdots & 0 \\ \vdots & 0.0001 & \vdots \\ 0 & \cdots & 0 \end{bmatrix} \begin{bmatrix} -0.8324 & 0.2594 & 0.4897 \\ 0.2253 & -0.6489 & 0.7268 \\ 0.5063 & 0.7153 & 0.4816 \end{bmatrix}$$

$$V_{22}^{3*}V_{22}^{3} = \begin{bmatrix} 0.3071 & 0.2160 & 0.4076 \\ 0.2160 & 0.9327 & -0.1270 \\ 0.4076 & -0.1270 & 0.7601 \end{bmatrix} = \bar{U}^{3}\bar{\Lambda}_{w}^{3}\bar{U}^{3*}$$

$$= \underbrace{\begin{bmatrix} -0.8324 & 0.2253 & 0.5063 \\ 0.2594 & -0.6489 & 0.7153 \\ 0.4897 & 0.7268 & 0.4816 \end{bmatrix}}_{\bar{U}_1^3 \quad \bar{U}_2^3 \quad \bar{U}_3^3} \begin{bmatrix} 0 & \cdots & 0 \\ \vdots & 0.9999 & \vdots \\ 0 & \cdots & 1 \end{bmatrix} \begin{bmatrix} -0.8324 & 0.2594 & 0.4897 \\ 0.2253 & -0.6489 & 0.7268 \\ 0.5063 & 0.7153 & 0.4816 \end{bmatrix}$$

The coefficient vectors $r^1 = \bar{U}_2^1$, $r^2 = \bar{U}_3^2$, and $r^3 = \bar{U}_3^3$ provided the most desirable vibration suppression that shows a short settling time and very small overshoot. It implied that

$$V_{22}^{1}r^{1} = V_{22}^{1}\bar{U}_2^{1} = \begin{bmatrix} 0.5876 & 0.3789 & -0.3148 \\ 0.3786 & 0.6521 & 0.2890 \\ -0.3140 & 0.2886 & 0.7602 \end{bmatrix} \underbrace{\begin{bmatrix} -0.6699 \\ -0.1222 \\ 0.7324 \end{bmatrix}}_{\bar{U}_2^1} = \begin{bmatrix} -0.6705 \\ -0.1216 \\ 0.7318 \end{bmatrix}$$

$$V_{22}^{2}r^{2} = V_{22}^{2}\bar{U}_1^{2} = \begin{bmatrix} 0.9524 & 0.1275 & -0.1669 \\ 0.1306 & 0.6497 & 0.4587 \\ -0.1714 & 0.4598 & 0.3978 \end{bmatrix} \underbrace{\begin{bmatrix} 0.4104 \\ 0.7767 \\ 0.4779 \end{bmatrix}}_{\bar{U}_3^2} = \begin{bmatrix} -0.4101 \\ -0.7774 \\ -0.4769 \end{bmatrix}$$

$$V_{22}^{3}r^{3} = V_{22}^{3}\bar{U}_1^{3} = \begin{bmatrix} 0.3085 & 0.2142 & 0.4110 \\ 0.2155 & 0.9332 & -0.1281 \\ 0.4068 & -0.1260 & 0.7582 \end{bmatrix} \underbrace{\begin{bmatrix} 0.5063 \\ 0.7153 \\ 0.4816 \end{bmatrix}}_{\bar{U}_3^3} = \begin{bmatrix} -0.5073 \\ -0.7150 \\ -0.4810 \end{bmatrix}$$

W in Eq. (5.22) was determined by combining $V_{22}^{1}r^{1}$, $V_{22}^{2}r^{2}$ and $V_{22}^{3}r^{3}$;

$$W = \begin{bmatrix} -0.6705 & -0.4101 & -0.5073 \\ -0.1216 & -0.7774 & -0.7150 \\ 0.7318 & -0.4769 & -0.4810 \end{bmatrix}$$

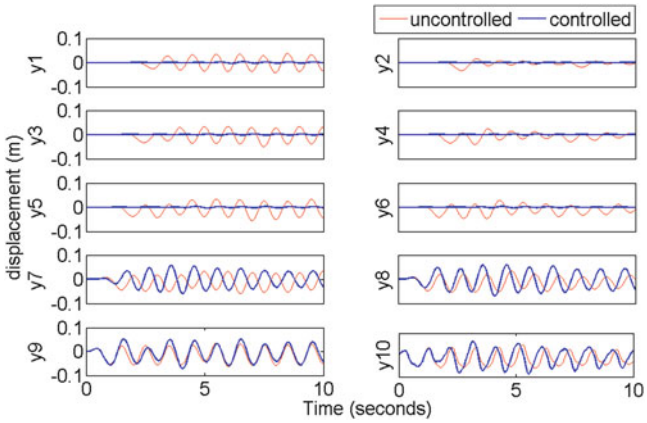

Fig. 5.3 Displacement of masses due to a chirp input at m_{10}

The real gain matrix was obtained as

$$K = W(CV)^{-1} = 1.0 \times 10^3 \begin{bmatrix} -2.6766 & -1.7254 & -0.2792 \\ 3.3596 & -3.0603 & 0.4400 \\ 1.5346 & -2.0474 & -1.7616 \end{bmatrix}$$

Figure 5.3 showed the displacement y_{1-10} of masses m_{1-10} due to the short duration chirp disturbance at m_{10}. It shows that the vibration in the isolated region that includes m_{1-6} was significantly reduced. The transient region that consists of m_{5-7} was located between the isolated and confined region and the masses that were connected to the control actuators. Both isolation and confinement of the vibration could be seen on those masses.

The vibration of m_6 was reduced while the vibrations of m_{7-8} were increased slightly. The vibrational energy was confined to m_{9-10}; therefore, masses in the confined region had higher amplitudes of vibration.

Figure 5.4 shows the actuation force for the three actuators. The maximum force at the outer actuator was greater than the other actuators and was 243.64 N. The maximum actuation forces at the inner and middle actuators were 126.54 and 148.18 N, respectively.

Based on Eq. (5.23), failure of any of the actuators was similar to setting rows of the gain matrix to zero. For example, if we assumed the outer actuator had failed, we might set the third row of the control gain matrix to zero. It implied that the third row of W was all zero, since $(CV)^{-1}$ could not have zero rows in general. The intention was to show how setting rows of W to zero after defining the control gain matrix makes a closed-loop system where its eigenvectors still belonged to the achievable eigenvectors set.

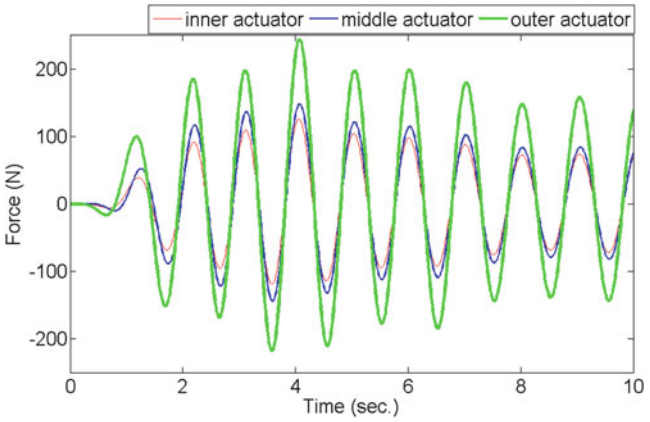

Fig. 5.4 Actuation forces due to a chirp input at m_{10}

OEC regenerated the open-loop system using the eigenvectors associated with zero eigenvalues of ${V_{22}^i}^* V_{22}^i$. For example, for the first operating eigenvalue, we had

$$[V_{22}^1]\bar{U}_1^1 = \bar{\lambda}^1 \bar{U}_1^1$$

$$= \begin{bmatrix} 0.5876 & 0.3789 & -0.3148 \\ 0.3786 & 0.6521 & 0.2890 \\ -0.3140 & 0.2886 & 0.7602 \end{bmatrix} \begin{bmatrix} -0.6425 \\ 0.5898 \\ -0.4892 \end{bmatrix} = (0) \begin{bmatrix} -0.6425 \\ 0.5898 \\ -0.4892 \end{bmatrix} = \begin{bmatrix} 0 \\ 0 \\ 0 \end{bmatrix}$$

If the outer actuator was assumed to have failed, the third row of the $[V_{22}^1]$ was set to zero and the new matrix was called $[\tilde{V}_{22}^1]$.

$$[\tilde{V}_{22}^1]^*[\tilde{V}_{22}^1] = \tilde{U}^1 \tilde{\Lambda}^1 \tilde{U}^{1*}$$

$$= \begin{bmatrix} 0.5876 & 0.3786 & 0 \\ 0.3789 & 0.6521 & 0 \\ -0.3148 & 0.2890 & 0 \end{bmatrix} \begin{bmatrix} 0.5876 & 0.3789 & -0.3148 \\ 0.3786 & 0.6521 & 0.2890 \\ 0 & 0 & 0 \end{bmatrix}$$

$$= \begin{bmatrix} 0.4886 & 0.4695 & -0.0756 \\ 0.4695 & 0.5688 & 0.0692 \\ -0.0756 & 0.0692 & 0.1827 \end{bmatrix}$$

$$= \begin{bmatrix} -0.6764 & 0.3602 & 0.6425 \\ -0.7366 & -0.3310 & -0.5898 \\ 0.0002 & -0.8721 & 0.4892 \end{bmatrix} \begin{bmatrix} 1 & 0 & 0 \\ 0 & 0.24 & 0 \\ 0 & 0 & 0 \end{bmatrix} \begin{bmatrix} -0.6764 & -0.7366 & 0.0002 \\ 0.3602 & -0.3310 & -0.8721 \\ 0.6425 & -0.5898 & 0.4892 \end{bmatrix}$$

The open-loop system could be regenerated again, since the eigenvectors associated with zero eigenvalue of ${V_{22}^i}^* V_{22}^i$ and ${\tilde{V}_{22}^i}^* \tilde{V}_{22}^i$ were identical.

$$
\begin{aligned}
&[\widehat{V}_{22}^{1}]\widehat{U}^{1} = \widehat{\lambda}^{1}\widehat{U}^{1} \\
&= \begin{bmatrix} 0.5876 & 0.3789 & -0.3148 \\ 0.3786 & 0.6521 & 0.2890 \\ 0 & 0 & 0 \end{bmatrix} \begin{bmatrix} -0.6425 \\ 0.5898 \\ -0.4892 \end{bmatrix} = (0) \begin{bmatrix} -0.6425 \\ 0.5898 \\ -0.4892 \end{bmatrix} = \begin{bmatrix} 0 \\ 0 \\ 0 \end{bmatrix}
\end{aligned}
$$

Previously, we had

$$
[V_{22}^{1}]\widehat{U}^{1} = \begin{bmatrix} 0.5876 & 0.3789 & -0.3148 \\ 0.3786 & 0.6521 & 0.2890 \\ -0.3140 & 0.2886 & 0.7602 \end{bmatrix} \begin{bmatrix} -0.6425 \\ 0.5898 \\ -0.4892 \end{bmatrix} = \begin{bmatrix} 0 \\ 0 \\ 0 \end{bmatrix}
$$

It was seen that both V_{22}^{1} and $\widehat{V}_{22}^{1}$ could regenerate the open-loop eigenvector using the eigenvector associated with zero eigenvalue of ${V_{22}^i}^* V_{22}^i$ and ${\widehat{V}_{22}^i}^* \widehat{V}_{22}^i$, respectively. Similar results for the second and the third operating eigenvalues could be found. It implied that the system with the failed actuator was still using the coefficient vectors that generated the closed-loop eigenvectors orthogonal to the open-loop eigenvectors.

The control gain matrix for the system with the failed actuator was

$$
K = 1.0 \times 10^3 \begin{bmatrix} -1.3211 & -0.8670 & -0.1340 \\ 1.5735 & -1.5267 & 0.1759 \\ 0 & 0 & 0 \end{bmatrix}
$$

Figure 5.5 shows the displacements of masses of the system due to the chirp disturbance to m_{10}. Similar to the system with working actuators stated earlier, a good isolation could be seen at m_{1-6}. Behaviors of the masses in transient and confined regions were similar to the system with working actuators. Figure 5.6 compares the displacements of m_1 in the complete system and the system with the failed actuator. The time histories of the displacements were slightly different. A slightly slower decay could be seen in the system with the failed actuator. Actuation forces of the actuators were shown on Fig. 5.7. Maximum actuation forces of the inner and middle actuators were 132.18 N and 150.94 N, respectively. The amount of increase in the actuation forces of the inner and middle actuators were 5.62 N and 2.76 N, respectively.

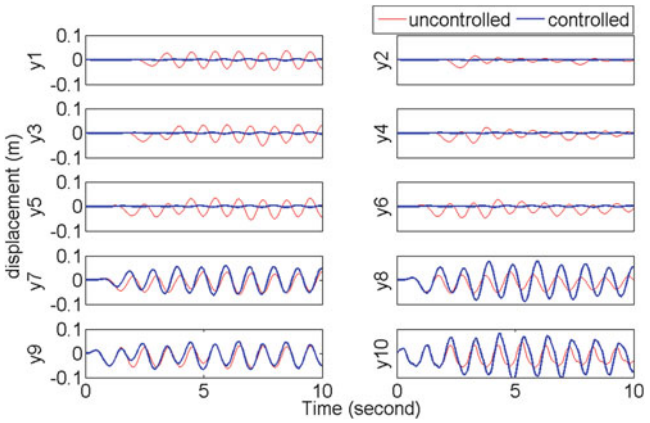

Fig. 5.5 Comparison of displacement of masses due to a unit impulse at m_{10}, using reduced gain matrix for the case with three sensors and two actuators

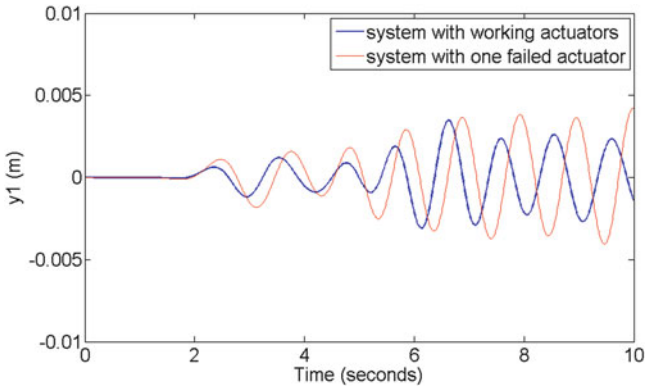

Fig. 5.6 Comparison of displacement of m_1 in the system of lumped masses with working actuators to the system with one failed actuator due to a chirp disturbance at m_{10}

5.4 Case Study: Isolation of Vibration in a Plate

Figure 5.8 shows the nodes of a finite element model of a plate that is simply supported at four edges with Young's modulus of 2.09×10^9 N m^{-2} and the Poisson's ratio is 0.33. It is a square plate, with length of 40 cm, and thickness of 1 mm. A code was written in Matlab for modeling the plate and solving its equation of motion. Mindlin plate theory was used to define the displacement field of the plate; therefore, there were 3 degrees of freedom for each node. Two of the degrees of freedom were in-plane displacements (u and v directions) and the third one was the transverse displacement y. Using linear quadrilateral elements, we used the procedure reported in [27] for calculating the mass and stiffness matrices of each

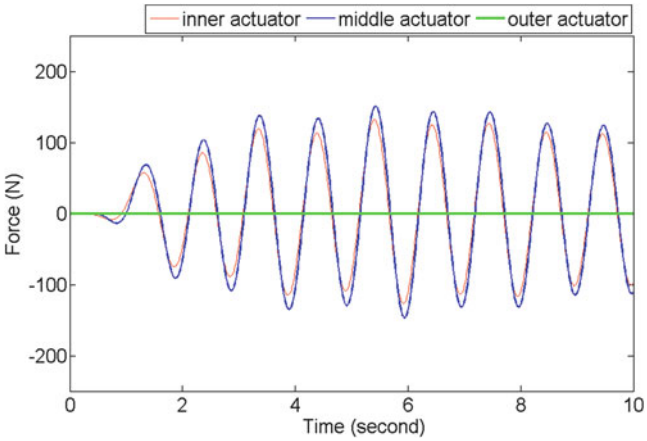

Fig. 5.7 Actuation forces for the system with failed actuator

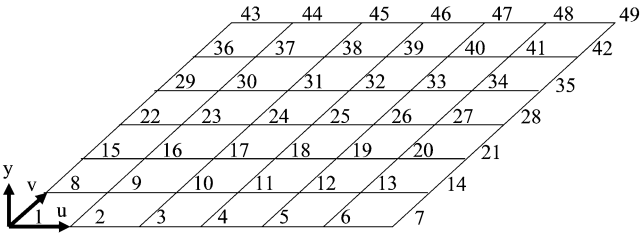

Fig. 5.8 Simply supported plate with 49 nodes and 36 elements

element. The dimensions of global mass and stiffness matrices, were 149×149, since the model had 49 nodes and each had 3 degrees of freedom. Damping matrix D_d, was assumed to be a linear damping defined as $D_d = 0.2M + 0.002K_s$ after scaling the mass and stiffness matrices. As a result, the dimension of the state matrix A for the state space realization of system in Eq. (5.1) was 298×298.

The disturbance force applied to the plate was a sine wave with a frequency of 2 kHz and amplitude of 10 N. The disturbance force was applied to the plate at node 27 and was normal to the plate that results in the plate bending.

We consider five cases with different scenarios for the actuators. Case 1 was a plate with three working actuators, case 2 was similar to case 1 with the middle actuator failed. Case 3 was similar to case 1 with a failed outer actuator. The control gains for cases 4 and 5 were designed specifically for two actuators. Case 4 was a plate with two control actuator at the nodes where working actuators of case 2 are located. Case 5 also had two actuators at the location of the working actuators of case 3.

As stated earlier, the operating eigenvalues were the greatest open-loop eigenvalues of the system, for all the cases the operating eigenvalues were $-24.9799 + 155.743\text{i}$, $-24.9799 + 155.743\text{i}$, and $-24.8108 + 155.2264\text{i}$. Since

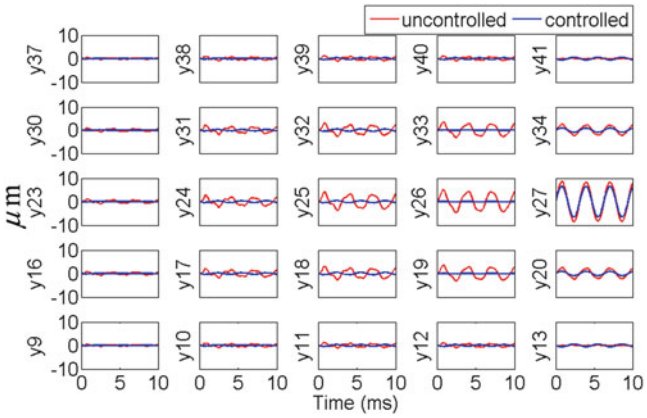

Fig. 5.9 Case 1, displacements of the nodes of plate due to a 2 kHz sine wave disturbance at node 27. Actuators are on nodes 19, 26, and 33

using complex conjugates of the operating eigenvalues results in similar closed-loop systems, we only used the operating eigenvalues with positive imaginary parts.

We assumed that there were sensors collocated with the actuators and the signals from those sensors were used for position feedback. As explained earlier, there were 26 possible closed-loop systems for the systems in cases 1, 2, and 3 with three actuators and there were three possible closed-loop systems for systems of cases 4 and 5 where two actuators were used.

5.4.1 Case 1: Plate with Three Working Actuators

As shown in earlier studies [21], when the greatest open-loop eigenvalues were chosen as the operating eigenvalues, all the closed-loop systems would be identical. Also, all the off-diagonal elements were small in comparison to diagonal elements, and the control becomes decoupled. In this case the control gain matrices were converged to the following matrix.

$$K = 1.0 \times 10^4 \begin{bmatrix} -2.1656 & 0.0420 & 0.0267 \\ 0.0034 & -2.1985 & 0.0030 \\ -0.0319 & -0.0444 & -2.2220 \end{bmatrix}$$

In fact, setting the off-diagonal elements did not change the results noticeably. Figure 5.9 shows that the suppression of vibrations on different nodes of the plate. Actuation forces also can be seen on Fig. 5.10. The maximum actuation forces were 0.86 N on nodes 19, 6.60 N on node 26, and 0.86 N on node 33. Because of the symmetry, the actuation forces of the actuators on nodes 19 and 33 were coincident.

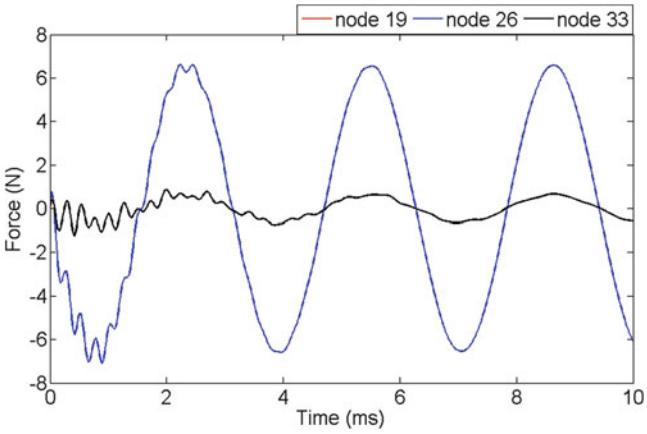

Fig. 5.10 Case 1, actuation forces at nodes 19 and 33 are identical. The amplitude of the disturbance is 10 N

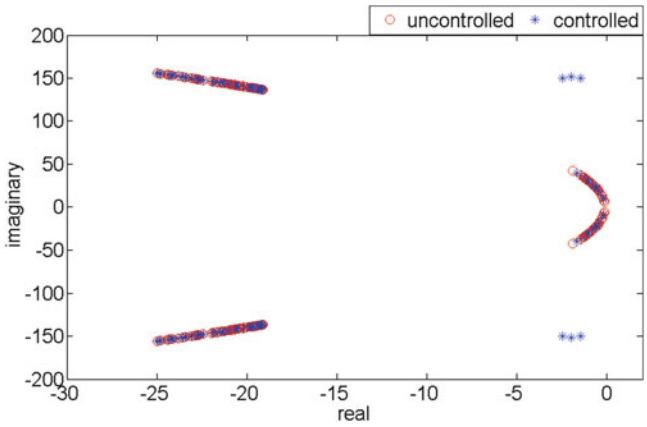

Fig. 5.11 Case 1, eigenvalues of the open-loop and closed-loop systems

Figure 5.11 illustrates the distributions of the open-loop and closed-loop poles. It was seen that three pairs of the closed-loop poles were moved away from the locus of the open-loop poles.

5.4.2 Case 2: Plate with Two Working Actuators and Failed Middle Actuator

We assumed that the middle actuator located on node 33 had failed. This resulted in setting the middle row of the control gain matrix to zero. Figure 5.12 shows

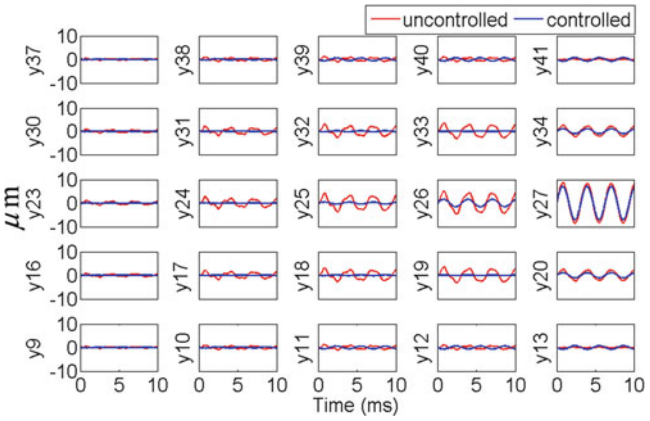

Fig. 5.12 Case 2, displacements of the nodes of plate due to a 2 kHz sine wave disturbance at node 27. Working actuators on nodes 19, 26, and failed actuator on node 33

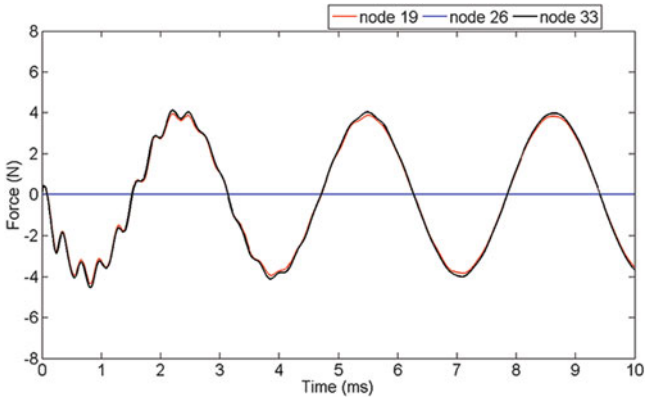

Fig. 5.13 Case 2, actuation forces. The amplitude of the disturbance is 10 N

the displacement of the nodes of the plate. The noticeable difference was the displacement of node 26, which has a failed actuator. Maximum actuation forces were shown on Fig. 5.13. The middle actuator had not applied any force to the system. The maximum actuation force on the actuator on node 19 was 3.94 N and on the node 33 was 4.12 N. The actuation forces are increased in comparison to case 1. The slight difference was because the control gain matrix is not symmetric. The control gain matrix was

$$K = 1.0 \times 10^4 \begin{bmatrix} -2.1656 & 0.0420 & 0.0267 \\ 0 & 0 & 0 \\ -0.0319 & -0.0444 & -2.2220 \end{bmatrix}$$

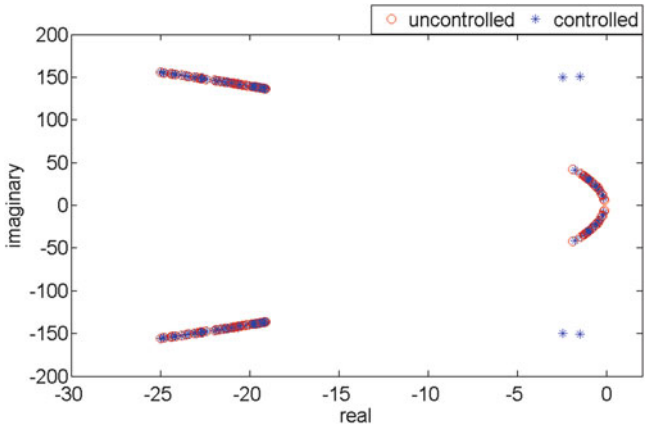

Fig. 5.14 Case 2, eigenvalues of the open-loop and closed-loop systems

Figure 5.14 shows the closed-loop and open-loop poles of the system. It was seen that two closed-loop poles were moved away from the open-loop poles cluster, as was expected since there were two working actuators. Comparing Figs. 5.14 and 5.11, one finds that the moved closed-loop poles were placed in a similar region.

5.4.3 Case 3: Plate with Two Working Actuators and Failed Outer Actuator

In this case, we assume that the faulty actuator was located on node 33. Therefore the control gain matrix was

$$K = 1.0 \times 10^4 \begin{bmatrix} -2.1656 & 0.0420 & 0.0267 \\ 0.0034 & -2.1985 & 0.0030 \\ 0 & 0 & 0 \end{bmatrix}$$

The displacement shown on Fig. 5.15 shows a good isolation on different nodes of the plate. The displacement of the node 25; however, was different form case 1, because of the failed actuator. Time history of the actuation forces was shown in Fig. 5.16. The maximum actuation force of the actuator on node 19 is 0.72 N and on node 26 is 7.2 N which was very close to the actuation forces in case 1.

Figure 5.17 shows the displacement of the middle node of the plate for cases 1, 2, and 3. The amplitudes of vibration for all the cases were very close. Vibration in Case 3 was in phase with the displacement in case 1. In case 2, however, there was a $\pi/2$ phase shift with respect to the response of case 1. This showed a great

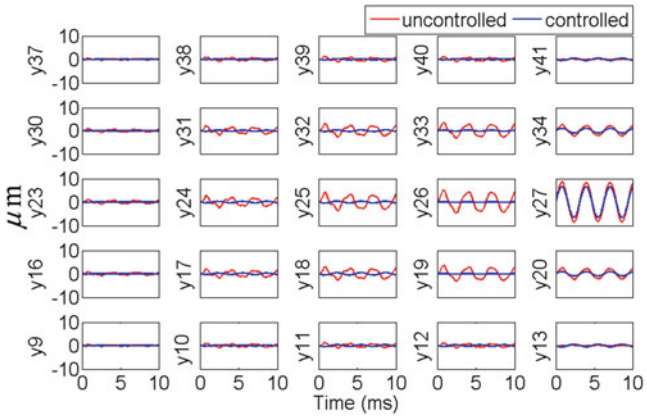

Fig. 5.15 Case 3, displacements of the nodes of plate due to a 2 kHz sine wave disturbance at node 27. Working actuators on nodes 19, 33, and failed actuator on node 26

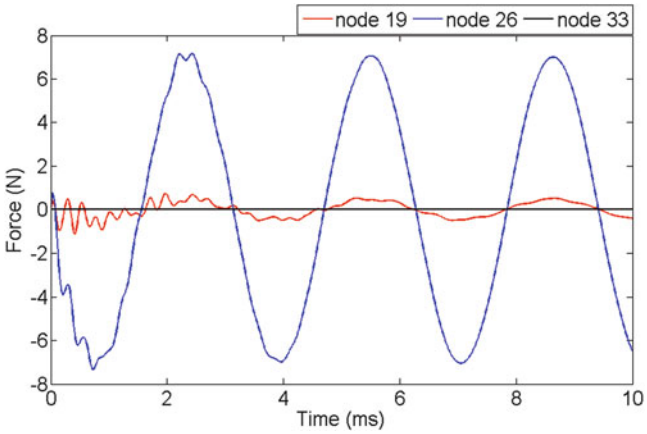

Fig. 5.16 Case 3, actuation forces. The amplitude of the disturbance is 10 N

robustness for the OEC to the actuator failure since that failure of each of the actuators had a local effect in the vicinity of the failed actuator, but the overall vibration cancelation in the plate had remained significantly intact. Figure 5.18 shows the closed-loop and open-loop poles of the system that indicates two of the closed-loop poles were moved away from the open-loop poles cluster similar to cases 1 and 2.

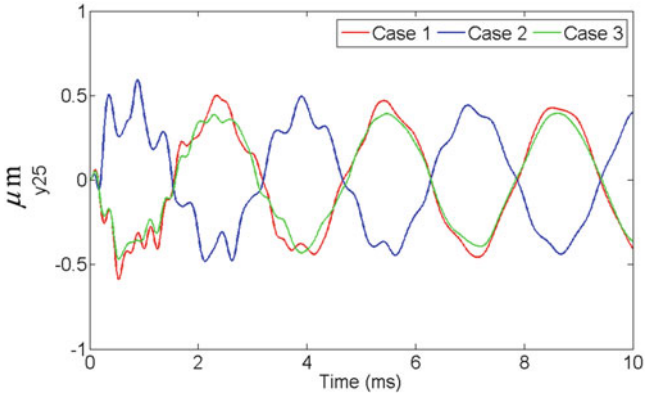

Fig. 5.17 Displacement of plate's middle node for cases 1, 2, and 3

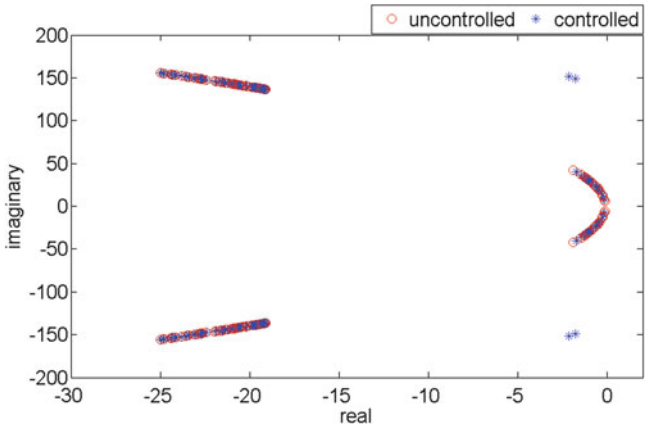

Fig. 5.18 Case 3, eigenvalues of the open-loop and closed-loop systems

5.4.4 Case 4: Plate with Two Working Actuators Similar to Case 2

Case 4 was the control of the vibration in a plate with two working actuators on nodes 19 and 33. It was similar to case 2 unless there was no failed actuator and the control gain matrix was

$$K = 1.0 \times 10^4 \begin{bmatrix} -2.2027 & 0.0028 \\ 0.0028 & -2.2027 \end{bmatrix}$$

that was symmetric due to the symmetry of the geometrical symmetry of plate and the location of the actuators and disturbance. The same property in the gain

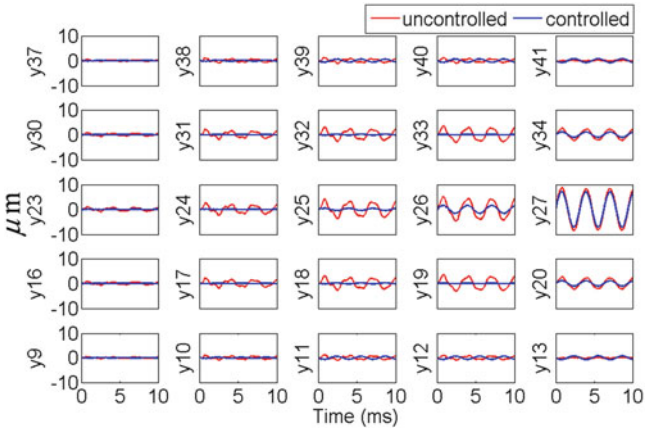

Fig. 5.19 Case 4, displacements of the nodes of plate due to a 2 kHz sine wave disturbance on node 27, actuators are on nodes 19 and 26

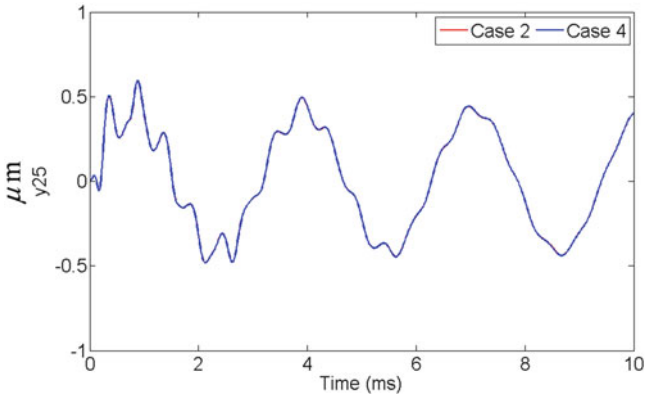

Fig. 5.20 Identical displacements of plate's middle node for cases 2 and 4

matrix of the case 1 could be seen here. The off-diagonal elements were three orders of magnitudes smaller than the diagonal elements; therefore, a decoupled control could be expected. Figure 5.19 shows the displacements of different nodes on the plate depicting a good isolation throughout the plate similar to earlier cases. A comparison between the displacements of node 25, the middle point in the plate, is shown in Fig. 5.20. It was seen that the displacements are identical. The time history of the actuation forces was shown in Fig. 5.21. The maximum force at the actuators on nodes 19 and 33 were identically 4.03 N, which was close to the actuation forces in case 2. The distribution of the eigenvalues of the open-loop and closed-loop systems was shown in Fig. 5.22. Two of the closed-loop system eigenvalues, similar to those in case 2, were moved away from the cluster of the open-loop eigenvalues.

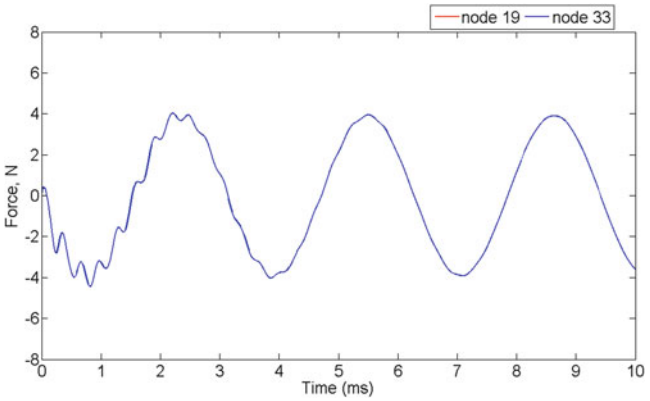

Fig. 5.21 Case 4, actuation forces in actuators on nodes 19 and 33 are identical. The amplitude of the disturbance is 10 N

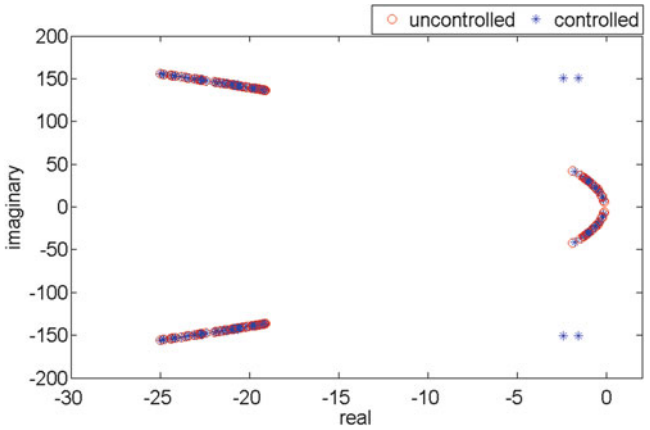

Fig. 5.22 Case 4, eigenvalues of the open-loop and closed-loop systems

5.4.5 Case 5: Plate with Two Working Actuators Similar to Case 3

Case 5 investigated the vibration isolation of the plate using two actuators, which were placed on nodes 19 and 26, the same locations as the working actuators of the case 3. The control gain matrix was

$$K = 1.0 \times 10^4 \begin{bmatrix} -2.2027 & -0.0032 \\ -0.0026 & -2.2064 \end{bmatrix}$$

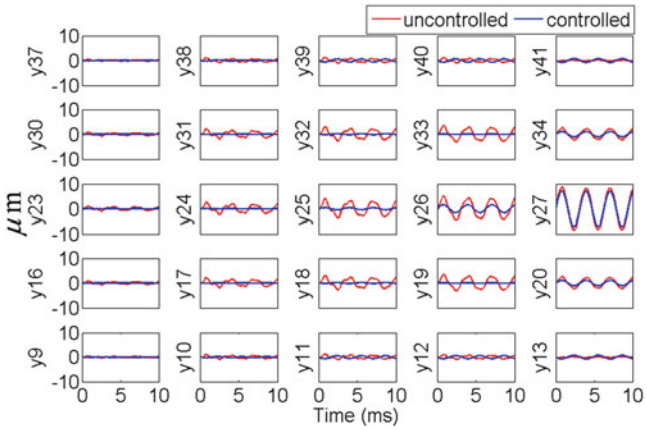

Fig. 5.23 Case 5, displacements of the nodes of plate due to a 2 kHz sine wave disturbance on node 27, actuators are on nodes 19 and 26

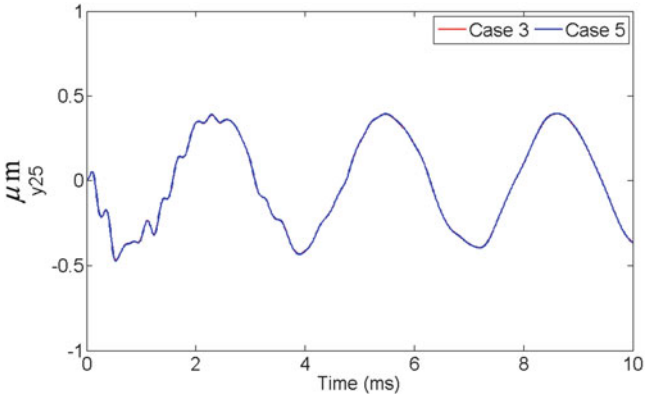

Fig. 5.24 Identical displacement of the plate's middle node for cases 3 and 5

similar to case 4. Figure 5.23 shows vibration similar to the earlier cases. The identical behavior of the middle point of the plate in case 3 and 5 was depicted in Fig. 5.24. Also, the time histories of the actuation forces were shown in Fig. 5.25. The Maximum actuation forces of the actuators on nodes 19 and 26 were 0.73 N and 7.16 N, respectively, which was very close to case 3. Similar to earlier cases, two of the closed-loop eigenvalues were moved away from the open-loop cluster, as shown in Fig. 5.26.

Comparing the results of the case 2 and 3 to case 1, one could see a reliable control design when OEC was used. The actuation forces in working actuators in cases 2 and 3 that contain failed actuators were very close to the forces of the system with three working actuators. Similar displacement time history could be seen

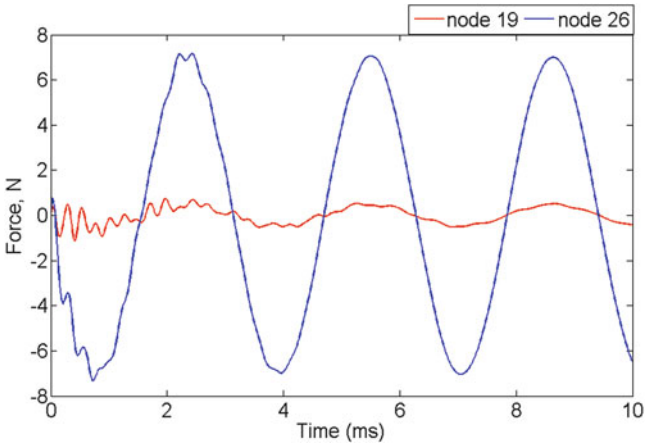

Fig. 5.25 Case 5, actuation forces. The amplitude of the disturbance is 10 N

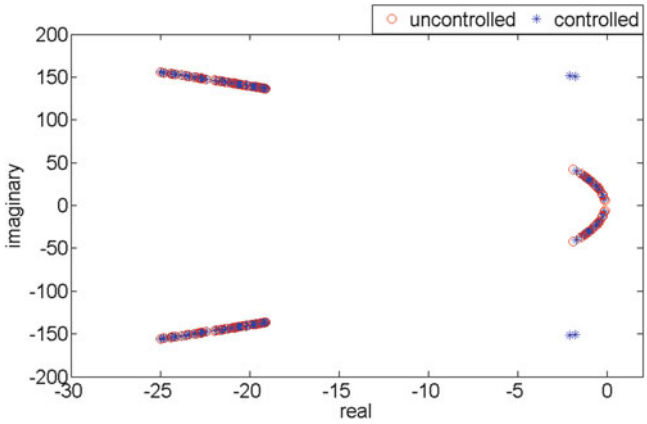

Fig. 5.26 Case 5, eigenvalues of the open-loop and closed-loop systems

throughout the plate except nodes with failed actuators. Moreover, comparing case 4 to 2 and 5 to 3, respectively, shows that there was slight difference between the system with one failed actuator and the system that was designed for two actuators. Orthogonal eigenstructure control with three actuators proved to be robust in such a way that the behavior of the system with one failed and two working actuators were identical to the behavior of the system that was designed primarily for two actuators. Table 5.1 shows the closed-loop eigenvalues that were moved away from the locus of the open-loop eigenvalues. It shows that for all the cases, the poles were placed in a small region. The rest of the closed-loop eigenvalues were moved slightly on the locus of the open-loop poles, without noticeable deviation away from the cluster.

Table 5.1 Moved closed-loop poles in cases 1–5

	Pair 1	Pair 2	Pair 3
Case 1	$-1.99 \pm 151.35i$	$-1.43 \pm 150.17i$	$-2.47 \pm 150.08i$
Case 2	$-1.50 \pm 150.79i$	$-2.46 \pm 150.13i$	
Case 3	$-1.78 \pm 148.91i$	$-2.11 \pm 151.25i$	
Case 4	$-1.56 \pm 150.95i$	$-2.40 \pm 150.60i$	
Case 5	$-1.78 \pm 150.54i$	$-2.11 \pm 151.19i$	

5.5 Applicability of OEC

Proper use of design freedom is depended on the experience of the controller designer. The improper use of the design freedom may cause excessive actuation forces. OEC reduces those design freedoms that are depended on the designer experience. It limits the design freedom to vectors orthogonal to the eigenvectors of the system and allows the controller designer to substitute the eigenvectors with vectors that are almost orthogonal to them. OEC can systematically determine the feedback control law with minimal input from a controller designer and is capable of performing robustly in the presence of a wide variety of disturbances.

OEC eliminates the need for defining the desirable eigenvectors and eigenvalues of the closed-loop system, which are usually needed by other eigenstructure assignment methods. This significantly reduces the amount of time needed for developing a new controller for structural control. Orthogonal eigenstructure control is able to suggest a set of closed-loop systems. OEC reduces the controller development cycle significantly through a mathematically sound approach that can easily be implemented to a broad range of systems in practice.

For the cases studies presented in this chapter, the control gains determined by OEC were almost diagonal that suggests a decoupled control. Therefore the effects of the failure of an actuator on the performance of the system will be limited. This makes OEC more readily applicable to real-life applications, by better dealing with limitations that happen in case of components failure.

5.6 Conclusion

The robustness of the OEC to the actuator failure in vibration cancelation in a plate was studied in this chapter. First, a simple system of lumped masses was considered and the effect of failure of an actuator was explained. Then, the same method was used to describe the effect of the failed actuator in a plate. Finite element analysis was used to model the plate and the plate response to force perturbations was simulated. Five cases were considered for the different scenarios with the actuators of the plate and the results were compared. It was shown that when the operating eigenvalues were the farthest open-loop eigenvalues from

the origin, a reliable and almost decoupled control could be achieved. Behaviors of the systems with failed actuators followed closely the behavior of the system with no faulty actuators. Moreover, the cancelations of vibration in the systems with failed actuators were almost identical to the systems that were primarily designed for two actuators. While there was no need to define the required locations for the closed-loop poles, few pairs of the closed-loop eigenvalues were moved away from the locus of the open-loop eigenvalues. The number of pairs of the moved eigenvalues was equal to the number of the actuators in each case. Since in all the cases the closed-loop eigenvalues were moved to one specific area, the behaviors of all the systems were similar and the control was robust to the actuator failure.

Key Symbols

A	Open-loop state matrix
A_c	Closed-loop state matrix
B	Input matrix
C	Output matrix
E	Disturbance input matrix
E_i	Modal energy of ith mode
f	Disturbance
I	Identity matrix
K	Gain matrix
m	Number of inputs (actuators/sensors)
N^i	Matrix that spans the null space of ith mode
n	Dimension of second order system
r^i	Vector of coefficients
$S_{\lambda i}$	Augmented matrix associated with λ_i
u	Input vector
U_i	Left unitary matrix of $S_{\lambda i}$
$\bar{U}^i$	Eigenvalue matrix of $V_{12}^{i*}V_{12}^i$ and $V_{22}^{i*}V_{22}^i$
$\bar{U}_w^i$	Eigenvalue matrix of $V_{22}^{i*}V_{22}^i$, equals to $\bar{U}^i$
$\bar{U}_j^i$	Eigenvalue of $V_{12}^{i*}V_{12}^i$ associated with non-unity eigenvalues
$\bar{U}_J^i$	Eigenvalue of $V_{12}^{i*}V_{12}^i$ associated with unity eigenvalue
V_i	Right unitary matrix of $S_{\lambda i}$
V_{12}^i	Upper part of N^i
V_{22}^i	Lower part of N^i
V	Appended matrix of $[V_{12}^i]r^i$
W	Appended matrix of $[V_{22}^i]r^i$
x	State vector
$\dot{x}$	Time derivative of state vector
y	Output vector
ϕ_i	ith closed-loop eigenvalue

ϕ_i^a Achievable eigenvector of ith mode
λ_i ith operating eigenvalue
$\bar{\lambda}_j^i$ Eigenvalues of $V_{12}^{i*} V_{12}^i$
$\bar{\Lambda}_i$ Eigenvalue matrix of $V_{12}^{i*} V_{12}^i$
$\bar{\Lambda}_w^i$ Eigenvalue matrix of $V_{22}^{i*} V_{22}^i$
Σ_i Matrix of singular values of $S_{\lambda i}$
$*$ Conjugate transpose symbol

References

1. D'Azzo JJ, Houpis CH (1995) Linear control system analysis and design: conventional and modern, 4th edn. McGraw-Hill
2. Moore BC (1976) On the flexibility offered by state feedback in multivariable systems beyond closed loop eigenvalue assignment. IEEE Trans Autom Control 21:689–692
3. Tao G, Ma X, Joshi SM (2000) Adaptive state feedback control of systems with actuator failures. In: American control conference, Chicago, IL
4. Tao G, Joshi SM, Ma X (2001) Adaptive state feedback and tracking control of systems with actuator failures. IEEE Trans Autom Control 46(1):78–95
5. Tao G, Chen S, Joshi SM (2002) An adaptive control scheme for systems with unknown actuator failures. Automatica 38:1027–1034
6. Tang X, Tao G, Joshi SM (2007) Adaptive actuator failure compensation for nonlinear mimo systems with an aircraft control application. Automatica 43:1869–1883
7. Fei J et al (2005) Robust adaptive control scheme for discrete-time system with actuator failures. J Dyn Syst Meas Control 127:520–526
8. Chen W, Saif M (2005) An actuator fault isolation strategy for linear and nonlinear systems. In: American control conference, Portland, OR
9. Chen W, Jiang J (2005) Fault-tolerant control against stuck actuator faults. IEE Proc Control Theory Appl 152(2):138–146
10. Yang Y, Yang GH, Soh YC (2000) Reliable control of discrete-time systems with actuator failure. IEE Proc Control Theory Appl 147(4):428–432
11. Seo CJ, Kim BK (1996) Robust and reliable Hoo control for linear systems parameter uncertainty and actuator failure. Automatica 32(3):465–467
12. Wang R, Liu M, Zhao J (2007) Reliable H_{oo} control for a class of switched nonlinear systems with actuator failures. Nonlinear Anal Hybrid Syst 1:317–325
13. Zhao Q, Cheng C (2003) Robust state feedback for actuator failure accommodation. In: The American control conference, Denver, CO
14. Liu GP, Patton RJ (1998) Robust eigenstructure assignment combining time- and frequency-domain performance specifications. Int J Robust Nonlinear Control 8:61–78
15. Wang G, Liang B, Duan G (2005) Reconfiguring second-order dynamic systems via P-D feedback eigenstructure assignment: a parametric method. Int J Control Autom Syst 3(1):109–116
16. Zhang Y, Jiang J (2001) Integrated active fault-tolerant control using IMM approach. IEEE Trans Aerosp Electron Syst 37(4):1221–1235
17. Jiang J (1994) Design of reconfigurable control systems using eigenstructure assignments. Int J Control 59(2):395–410
18. Apkarian P, Tuan HD, Bernussou J (2000) Analysis, eigenstructure assignment and H2 multi-channel synthesis with enhanced LMI characterizations. In: Proceedings of the 39th IEEE conference on decision and control Sydney, Sydney, Australia
19. Rastgaar M, Ahmadian M, Southward SC (2010) Orthogonal eigenstructure control for vibration suppression. J Vib Acoust 132(1):1–10

20. Rastgaar MA, Ahmadian M, Southward SC (2009) Orthogonal eigenstructure control with non-collocated actuators and sensors. J Vib Control 15(7):1019–1047
21. Rastgaar M, Ahmadian M, Southward SC (2010) Vibration cancellation in a plate using orthogonal eigenstructure control. ASME J Appl Mech 77:061007
22. Rastgaar M, Ahmadian M, Southward SC (2010) Experimental application of orthogonal eigenstructure control for structural vibration cancellation. J Sound Vib 329(19):3873–3887
23. Rastgaar MA, Ahmadian M, Southward SC (2009) A review on eigenstructure assignment methods and orthogonal eigenstructure control of structural vibrations. Shock Vib 16(5):555–564
24. Rastgaar M, Ahmadian M, Southward SC (2007) Vibration confinement by minimum modal energy eigenstructure assignment. In: ASME international design engineering technical conferences, IDETC/CIE 2007, Las Vegas, NV
25. Shelley FJ, Clark WW (2000) Experimental application of feedback control to localize vibration. J Vib Acoust 122:143–150
26. Rastgaar M, Ahmadian M, Southward SC (2007) Effect of the actuators' location on vibration confinement using minimum modal energy eigenstructure assignment. In: ASME international design engineering technical conferences, IDETC/CIE 2007, Las Vegas, NV
27. Weaver W, Johnston PR (1987) Structural dynamics by finite element. Prentice-Hall

Part II
Practical Nonlinearity

Chapter 6
Energy Harvesting from Flows Using Piezoelectric Patches

J.M. McCarthy, A. Deivasigamani, S. Watkins, S.J. John, and F. Coman

Abstract The highly nonlinear phenomenon of fluid–structure interaction is discussed, including examples drawn from nature and early work on aircraft flutter. Recent work on extracting the energy in a fluid stream by piezoelectric elements is reviewed, including some of the underlying physics. Whilst the energy extracted from fluttering elements is low, it is a subject of interest for powering Ultra-Low Power (ULP) devices and systems since this method of energy extraction is thought to offer a quiet alternative to conventional wind turbines. Researchers have investigated the use of thin piezoelectric patches coupled to a geometrically shaped, polymeric membrane (via a revolute hinge) which can amplify the bending, strain and hence power. Such systems respond via flutter induced by resonant bending instability of the system, or by the utilisation of time-varying external pressure gradients formed around the system. Key factors that influence performance are examined, such as critical flutter speed, mass ratio, position of revolute hinge, aspect ratio and type of piezoelectric material. The chapter concludes with a discussion of the practical implications of such systems in the future.

J.M. McCarthy • A. Deivasigamani • S. Watkins (✉) • S.J. John
School of Aerospace, Mechanical and Manufacturing Engineering, RMIT University,
PO Box 71, Bundoora, VIC 3083, Australia
e-mail: jesse.mccarthy@rmit.edu.au; arvind.deivasigamani@rmit.edu.au;
simon.watkins@rmit.edu.au; sabu.john@rmit.edu.au

F. Coman
Fabrics & Composites Science & Technologies Pty. Ltd., PO Box 613,
South Carlton, VIC 3053, Australia
e-mail: floreana.coman@fcst.com.au

R.N. Jazar and L. Dai (eds.), *Nonlinear Approaches in Engineering Applications 2*,
DOI 10.1007/978-1-4614-6877-6_6,

6.1 A Prologue

Fluid–structure interaction (FSI) is all around us, in our everyday lives. Perhaps you have looked at a flag fluttering in the wind and wondered what is causing the interesting "rippling" shapes as the wind blows past the flag. Maybe you have noticed the antenna on your vehicle vibrating rapidly side-to-side when you drive at a certain speed. You may have even become annoyed when the venetian blinds in your house rattle when they are closed across an open window! All of these seemingly trivial events give way to a rich plethora of problems in the scientific and engineering communities, known as FSIs.

Definition 1. Fluid–structure interactions are physical interactions that take place whenever a fluid in motion impinges on a solid body, whether rigid or deformable. The interactions may be one-way, meaning that the resulting deformations of the solid body (however minuscule) do not significantly affect the fluid flow; or the interactions may be two-way, meaning that the solid-body deformations are such that the flow field is affected significantly enough to instigate a continuing cycle of fluid–structure energy transfer, the manifestation usually being solid-body vibration.

Let us take the case of the flag flapping in the wind, as an example; though the motion of the flag seems almost elegant in nature, the underlying physics that govern that motion are far from simple. Classical observations often attributed the flag flutter[1] to a combination of two events [4]: (1) the Bernárd–von-Kármán vortex shedding (Fig. 6.1) at the trailing edge of the flag and (2) the Kelvin–Helmholtz instability problem (Fig. 6.2) of the growth of perturbations along an infinite extent at the interface of two fluids, moving at different velocities [30].

Upon consideration of the solid boundary, it became clear that Kelvin–Helmholtz instabilities were not instigating flutter of the flag, since the boundary separates the shear layers of the working fluid. In flow visualisation work by Jun et al. [26], it was clearly seen that the vortex shedding from the trailing edge of the filament was occurring at a much higher frequency than that of the flutter frequency (Fig. 6.3), obviating the influence of the von-Kármán vortices over the filament flutter.

Flutter investigated in the laboratory (such as the case of flag flutter above) environment posed new challenges and questions to researchers and stimulated curiosity: what then, was causing a thin body immersed in a flow to flap, if the classical observations hypothesised[2] were to be rejected? In fact, it is now generally understood that flutter can be a self-excited phenomenon [42].

[1] Flutter is a type of FSI, where the solid-body oscillates in the fluid flow, usually with large deformation amplitudes.

[2] Namely, the Bernárd–von-Kármán vortex shedding and the Kelvin–Helmholtz instability.

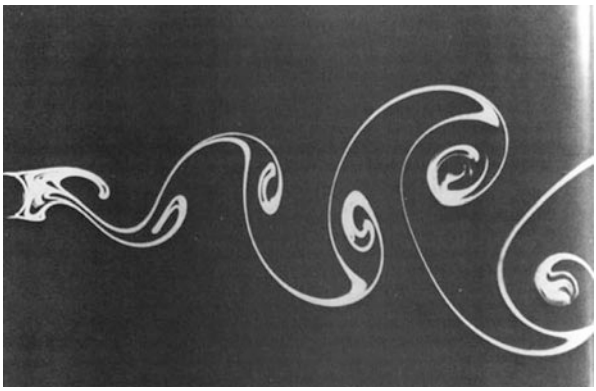

Fig. 6.1 von-Kármán vortex shedding behind a cylinder at a Reynolds number of 140 (photo by Sadatoshi Taneda [17])

Fig. 6.2 A depiction of the Kelvin–Helmholtz instability between two fluids of different densities. The shear layer perturbations can be seen between the dark and light fluids [45]

Fig. 6.3 A filament flapping in a two-dimensional, parallel flow. The von-Kármán vortex wake can be seen to be at a higher frequency than the flapping of the filament [26]

Flutter has existed in nature since the beginning of time, but only recently did engineers and scientists discover that flutter of structures could bring about negative results. From the time of the advent of flight for example, wing flutter was an issue—and a deadly one,[3] with many cases of pilots and passengers losing their lives in aircraft that failed structurally due to primary-structure flutter (i.e. wings and horizontal and vertical stabilisers). The wing flutter issue was formally addressed by Theodorsen back in 1935 [44] using analytical potential flow methods to determine the general mechanism of flutter; specifically, how it started and sustained itself. Theodorsen mathematically considered ideal flow conditions (i.e. incompressible, inviscid and irrotational) over a conformally mapped aerofoil. He identified two major components of the potential flow: (1) the non-circulatory velocity potential, which described the flow and pressure distribution over the aerofoil and (2) the circulatory velocity potential, arising from the need to describe the vortex shedding at the trailing edge of the aerofoil.

Another example of flutter bringing about devastating results is the well-known Tacoma Bridge disaster in 1940. The bridge oscillated with such a large torsional amplitude that it collapsed. Initially, it was thought that vortex shedding, occurring at a frequency according to the Strouhal number,[4] over the bridge excited a torsional natural frequency, but the collapse was later found to have occurred because of *aeroelastic* flutter [5]. Perhaps a more interesting discovery: in 1995, Huang [24] investigated palatal flutter as the most probable cause for snoring in humans.

Not all flutter is bad, however. The sound that comes from a wind instrument, such as a saxophone or clarinet, ensues because the reed in the instrument flutters in the airflow provided by the person playing the instrument. Fluttering components in some types of industrial mixing systems actually enhance the mixing process. Païdoussis [34] noted that even in ancient artefacts, flutter was used—one example being the Aeolian harp, a harp that would be "played" by the wind.

Only recently, has it been suggested that flutter be exploited for energy harvesting purposes. Until now, flutter (for the most part) had been considered a nuisance because of its detrimental effect on structures; whether causing catastrophic failure as in the case of wing flutter, long-term fatigue damage in the case of vibrating mixing components, or even causing noise levels that are undesirable, as in the case of a "singing" hydrofoil on a submarine.

In 2008, Dickson [14] conceptualised a piezoelectric "tree", shown in Fig. 6.4. The inherent ability of the piezoelectric patch to generate electrical energy when placed under mechanical strain was a major driving force in the development of this concept.

Could a tree-like construct, with hundreds of these piezoelectric "leaf-stalks" possibly be implemented in urban areas in the near future? With all the safety

[3]One particular catastrophic case of aircraft wing flutter was the Braniff Airlines Flight 542 Lockheed Electra, in 1959. Everyone onboard perished when the airframe failed due to a flutter mode excited by engine propeller whirl. The crash investigation report was released in 1961 [9].

[4]The Strouhal number is discussed in more detail in Sect. 6.2.2.

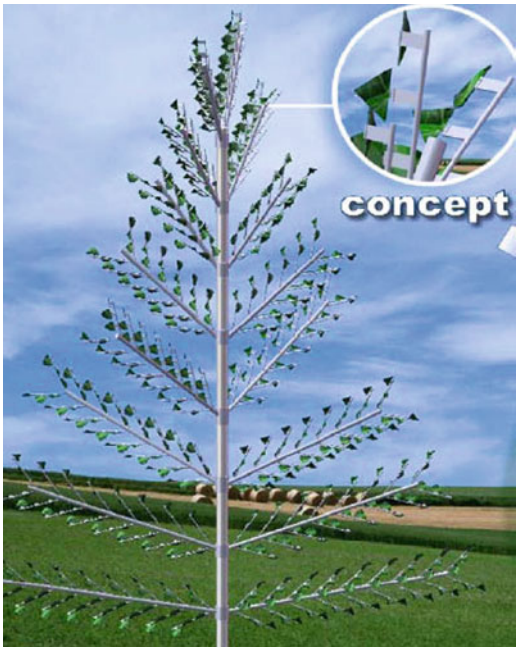

Fig. 6.4 The piezoelectric tree concept introduced by Dickson [14], as an aesthetically pleasing, safe alternative to urban-based wind turbines

concerns, noise and vibration issues [19], and poor cost effectiveness issues [49, 50] surrounding urban-based wind turbines, there is certainly room for this technology to flourish. Furthermore, with the current shift to Ultra-Low Power (ULP) technologies[5] in buildings and structures [37], coupled with the global desire to discover new means of extracting renewable energy, this piezoelectric flutter system shows promising potential. In the next section, we'll examine this type of system, and how it works.

6.2 Piezoelectric Energy Harvesters

Piezoelectric materials have a special property: they are electro-mechanical, which means that when mechanically strained they are capable of generating an electric charge. The opposite is true as well—when an electrical current is passed through a piezoelectric material, it will distort accordingly. This electro-mechanical property arises from the alignment of the material's atomic structure. The transduction direction of energy defines the usage of the piezoelectric material.

[5]ULP here denotes both ULP consumption devices and ULP generation technologies. Two examples of ULP consumption devices would be wireless sensor nodes and LED lighting.

Fig. 6.5 The three-way physics interaction that occurs with a piezoelectric patch fluttering in a fluid flow

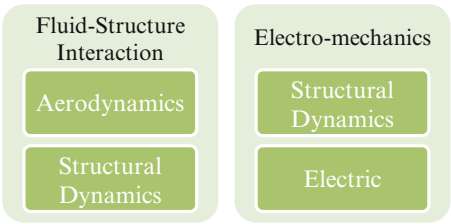

Fig. 6.6 The coupled physics fields within the aero-mechanical–electrical interaction

6.2.1 Overview of Physics Interactions

In the case of flutter energy harvesters, the input forcing function comes from the unsteady aerodynamic forces (being imparted by the flowing fluid), causing mechanical strains of the piezoelectric patch, which translates to an electrical charge output. The schematic in Fig. 6.5 perhaps more clearly illustrates this three-way, *aero-mechanical–electrical* interaction.

Definition 2. Aero-mechanical–electrical interaction is energy transduction within a system, involving flow kinetic energy, structural strain energy and electrical energy.

This three-way interaction may be further broken down into *coupled* fields (Fig. 6.6), both of which are considered to be nonlinear couplings.

6.2.2 Fluid–Structure Coupling

The FSI interactions are what were discussed generally in Sect. 6.1; in this section, we look more in-depth at flutter itself, and the different types and classes of flutter.

Movement-Induced Excitation Flutter

The highly nonlinear nature of the fluid–structure coupling makes it so that analytical treatments become very complex, especially two-way interactions (see

Definition 1 on p. 170). Naudascher and Rockwell [32, 33] in their work classified different types of flutter, based on the excitation mechanisms at work. One class of flutter that was briefly touched on before (Sect. 6.1) was Movement-Induced Excitation (MIE) type. Herein, the immersed structure will be denoted as a *beam*.

Definition 3. Movement-Induced Excitation flutter is where flutter of a beam immersed in a fluid flow is started by the fluid exciting a resonant instability in the beam, whether bending or torsional.

MIE-type flutter is a self-excited phenomena, meaning that no externally imposed forces are required to initiate flutter of the beam. Rather, at a certain flow speed past the beam, flutter spontaneously occurs. The flow speed at which flutter is seen to occur is known as the *critical flutter speed*, or *cut-in* speed of the flow. There have been many analytical studies conducted, on understanding the fundamental principles of this critical flutter speed.

Critical Flutter Speed

Kornecki et al. [27] examined the critical flutter speed and flutter frequency of a beam for both clamped–clamped, and clamped-free end conditions. Three different types of theoretical analyses were carried out and compared to experimental results:

1. Non-circulatory aerodynamic theory
2. Quasi-steady lifting line theory
3. Full unsteady aerodynamic theory

All three theoretical models were found to correlate well with experimental findings for the flutter frequency of the clamped-free beam. The non-circulatory and full-unsteady theory compared well against the experimental results for the critical flutter speed; however, the quasi-steady theory proved inadequate for comparison. It was concluded that beams clamped at the leading edge and free at the trailing edge lose their stability by flutter. This analysis was only applicable for parallel flow over the beam; also, because the theory was for ideal conditions, and only one experiment was conducted, the authors concluded [27, p. 176]:

> The theory of non-circulatory flow is unacceptable on physical grounds. No final conclusions can be drawn on the basis of a single experiment. Further work is necessary to ascertain the effectiveness of the calculation method.

As mentioned before in Sect. 6.1, Huang [24] addressed the issue of flutter in a similar manner to Kornecki et al. [27], but for the purpose of understanding and preventing snoring in humans. Linear theory was utilised for characterising the onset of steady-state fluttering of a beam in a two-dimensional flow, and via

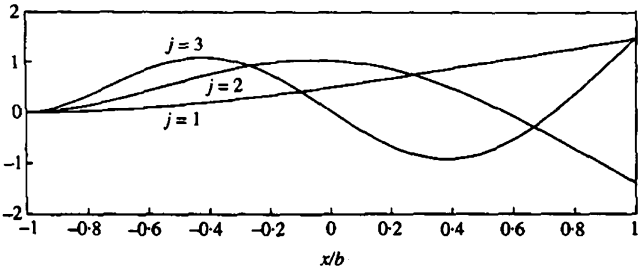

Fig. 6.7 In vacuo normalised mode shapes plotted for a cantilever beam, where j is the mode number [24]

experimental corroboration, Huang [24] showed that cantilevered beams lose their stability via flutter and that the critical flutter speed is strongly dependent on the length and stiffness of the beam. It was also suggested that the fluttering motion is a combination of *in vacuo* mode shapes, mainly the first and second modes. This suggestion is in part substantiated by simple observation of the fluttering filament in the work by Jun et al. [26] (Fig. 6.3, p. 171), and comparison with the well-known mode shapes of a clamped cantilever beam, shown below in Fig. 6.7.

It was also suggested by Hariri et al. [22] that flutter is a combination of modes. Argentina and Mahadevan [4] extended this idea and showed that either the fundamental mode or the second mode of vibration may be excited in a uniform parallel flow, depending on the value of the added mass parameter, more generally known as the fluid-to-structure *mass ratio*.

Effect of the Mass Ratio

Definition 4. The mass ratio is a dimensionless parameter, relating the mass properties of the beam to the mass of the fluid in which it is immersed.

Quantitatively, the mass ratio, μ, is calculated as

$$\mu = \frac{\rho_s h}{\rho_f L}, \tag{6.1}$$

where ρ_s is the beam density, h is the beam thickness, ρ_f is the fluid density, and L is the beam length. The mass ratio is an important parameter to consider, when analysing flutter of immersed beams. Yamaguchi et al. [52] analytically treated the onset of flutter for both a high- and low-mass ratio beam. The governing assumptions were such that the disturbances of motion were infinitesimally small, and the contributions of the second- and higher-order modes were neglected.

The beam geometry was discretised via a mesh and the resulting linear homogenous system of equations was size $6 \times N$, where N is the number of discretisation points. The analysis was cumbersome to assemble, since they chose not to represent the flutter motion of the beam as a superposition of modes (as done previously by Huang [24]), but rather directly solving for the forces and displacements over time. Yamaguchi et al. [52] argued that for sufficiently small mass ratios, the deviation of observed flutter modes from predicted in vacuo mode shapes was significant and mode superposition gave erroneous results. This agreed with observations by Watanabe et al. [47] for low mass ratios. Furthermore, the predominance of traveling waves at relatively low mass ratios was evinced by time-varying pressure forces in the results, shown in Fig. 6.8.

There was good agreement between these results, and experimental results published later [51]. They concluded that [51, Conclusion]:

1. For high mass ratios ($\mu > 0.7$), the beams yielded motions similar to in vacuo second mode shapes, and frictional effects were not significant.
2. For medium mass ratios ($0.7 > \mu > 0.05$), the beam oscillations were much different than those of in vacuo mode shapes, the spatial pressure distribution had more peaks than the mode shapes, and the frictional effects became much more pronounced. The frequency of oscillations was also increased.
3. For low mass ratios ($\mu < 0.05$), the frequency of oscillations nearly became independent of the mass ratio, and beam motion was chiefly governed by frictional effects, and [perhaps] fluid added mass effects.

Connell and Yue [11] conducted both a preliminary linear stability analysis and a thorough numerical analysis of a pinned-free, low-bending stiffness beam in an inviscid, incompressible, uniform flow. They utilised a Fluid–Structure Direct Simulation (FSDS), which consisted of a Fluid-Dynamics Simulation (FDS) solver (used the finite difference approach to directly solve the Navier–Stokes equations; i.e. a Direct Numerical Simulation [DNS]) and a Structural-Dynamics Simulation (SDS) solver (employed a nonlinear, arbitrary configuration, second-order finite difference scheme). Each of the solvers was separately validated against benchmarking problems and found to perform adequately. Subsequently, the coupled solver was benchmarked and found to perform satisfactorily. Three distinct regions of flutter response were identified by Connell and Yue [11]:

1. Fixed point stability.
2. Limit-cycle flapping (LCO).
3. Chaotic flapping.

The differences between each regime may be seen in Fig. 6.9. This result substantiated the work in Yamaguchi et al. [51], as it was found that the flutter regime of the beam was directly related to the mass ratio.

As the mass ratio increased, it can be seen from Fig. 6.9 that the time-varying displacement amplitude transitions from an underdamped behaviour in the fixed point stability regime, to LCO in the second regime, to stochastic, randomly varying

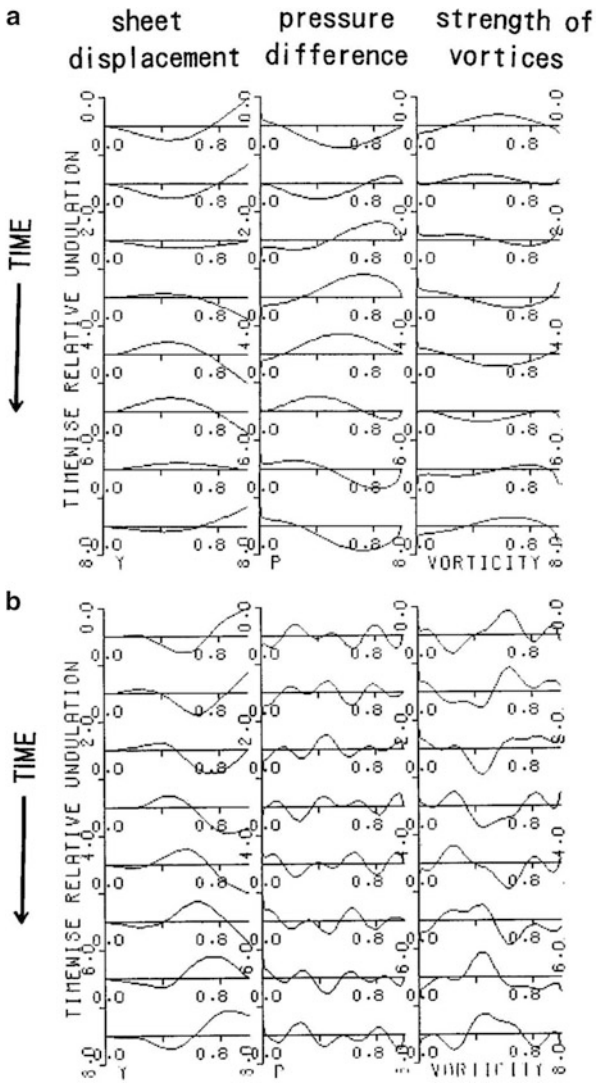

Fig. 6.8 Time-varying beam deformation, pressure and vorticity results for a mass ratio of (**a**) 2.92 and (**b**) 0.04 [52, Fig. 6]

in the chaotic regime. It is also interesting to note the difference in normalised cross-stream displacement and velocity power spectrum for each of the plotted mass ratios, as shown in Fig. 6.10.

Although the mass ratio was varied and bending stiffness kept constant in Fig. 6.10, there appears to be correlation between these results and the outcomes presented by Alben and Shelley [1], where the mass ratio was kept constant and

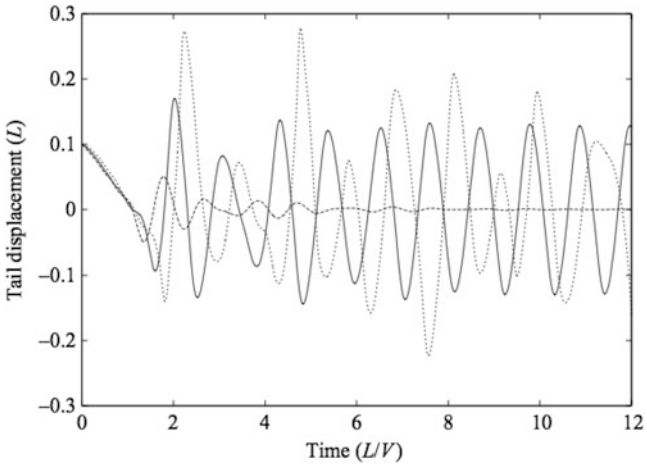

Fig. 6.9 The normalised trailing edge displacement plotted against the non-dimensional time for (a) fixed point stability regime with $\mu = 0.025$ (- - -), (b) limit-cycle flapping regime with $\mu = 0.1$ (—-), and (c) chaotic flapping regime with $\mu = 0.2$ ($\cdots$) [11, Fig. 8]

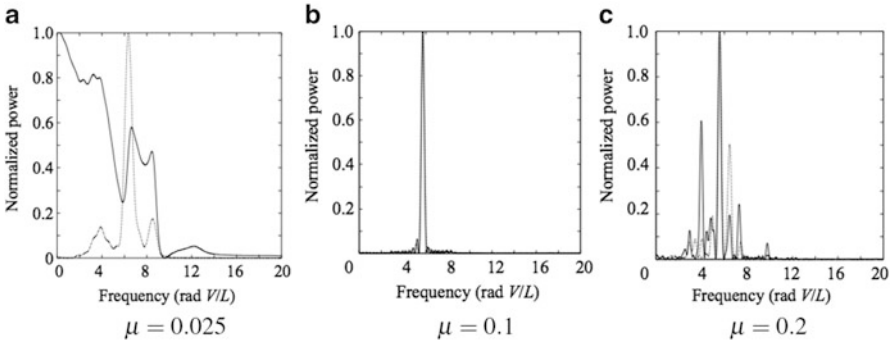

Fig. 6.10 The normalised power spectrum of the trailing-edge cross-stream displacement (—-) and velocity ($\cdots$) for the three different mass ratios [11]. (**a**) $\mu = 0.025$, (**b**) $\mu = 0.1$ and (**c**) $\mu = 0.2$

the bending stiffness varied. In general, for lower mass ratios and lower bending rigidities there appears a more broadband response of the normalised power of the system.

Subcritical Bifurcation and Hysteresis

Connell and Yue [11] observed *subcritical bifurcation* in their FSDS simulations; that is, based on the initial displacement conditions of the beam, either the stable or unstable regimes of flutter could be realised. Jun et al. [26] and Watanabe et al. [48] also detected subcritical bifurcation in their experimental work. This is characteristic

of hysteresis in the system, and Watanabe et al. [48] indeed found that the critical flutter speed u_c for the beam did not equal the "quenching" speed—the wind speed at which the beam ceased to flutter (u_q). Instead, they found after 30 test specimens that the quenching speed was related to the critical flutter speed by the approximate function,

$$u_q = 0.75u_c \pm 0.2. \tag{6.2}$$

For instance, if at $t = 0$ the beam is fluttering, then when the flow speed is reduced, $u_q \neq u_c$ because of the initial state of the beam. Similarly, if at $t = 0$ the trailing-edge displacement $y(x,t) \approx 0$, then Connell and Yue [11] found that the fixed point stable regime was realised; for $y(x,t) > 0$ at $t = 0$, they found that the limit-cycle regime was induced.

Extraneously-Induced Excitation

Another type of flutter that Naudascher and Rockwell [32, 33] classified is Extraneously-Induced Excitation. This class of flutter has seen greater utilisation in the area of flutter energy harvesting, despite the requirement for a more complex and detailed setup.

Definition 5. Extraneously-Induced Excitation flutter is where flutter of the immersed beam is caused by external, time-varying pressure gradients, such as those generated by vortex shedding off of a bluff body.

Overview of Vortex Shedding

Unlike MIE-type flutter discussed in Sect. 6.2.2, EIE-type flutter requires a preliminary understanding of the vortex shedding from bluff bodies, as a primary excitation mechanism of the beam flutter. The vortex shedding behind bluff bodies has been studied extensively elsewhere and will not be examined in detail here. Generally, the objective is to maximise the amplitude of vibrations of the beam via fluid-forced resonance of the beam. The upstream bluff body sheds vortices at a certain frequency as governed by the Strouhal number, defined as

$$\mathrm{St} = \frac{fD}{u}, \tag{6.3}$$

where f is the vortex shedding frequency, D is the characteristic dimension of the bluff body (usually a diameter), and u is the fluid flow velocity. These vortices are advected past and impinge on the beam and, when the shedding frequency matches

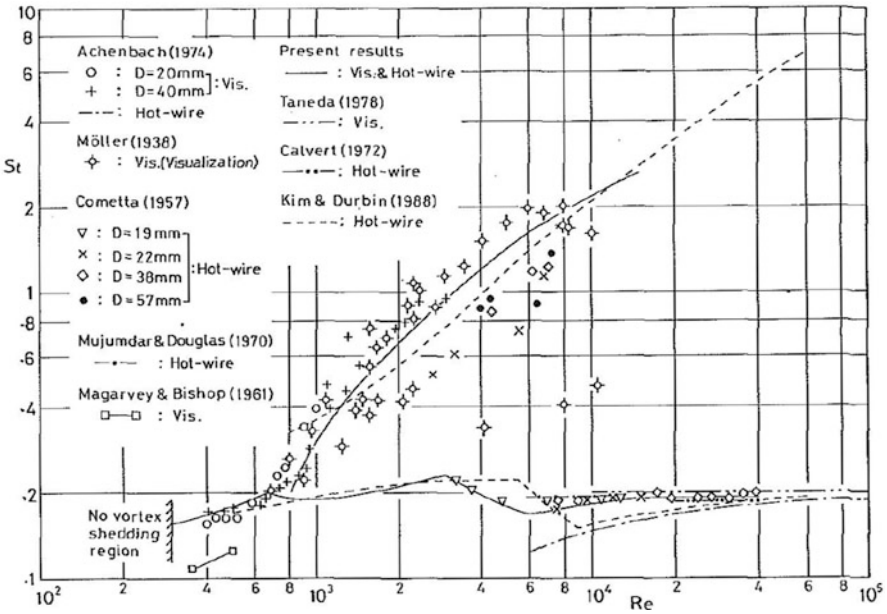

Fig. 6.11 Overview of results showing the experimentally obtained relationship between the Strouhal and Reynolds number [39, Fig. 3]

a *bending* natural frequency of the beam, resonance occurs and thus the amplitude of vibration significantly increases. It should be noted that there has been much work done on understanding the relationship between the Strouhal number and the Reynolds number, Re; again, an in-depth overview will not be realised here, but for the sake of completeness it should be looked at briefly such that flutter evolving from vortex shedding may also be explicated.

The relationship between the Strouhal and Reynolds[6] numbers somewhat resembles a piecewise function, in that there are regions where the Strouhal number is found to be independent of the Reynolds number, and elsewhere there appears a nonlinear relationship. Sakamoto and Haniu [39] pointed out that previous experimental work on vortex shedding from a spherical bluff body varied from researcher to researcher, and that discontinuities were found in the St vs. Re relationship. Through a series of flow visualisation and hot-wire experiments, they examined the Strouhal number for $10^3 < \mathrm{Re} < 10^4$. In Fig. 6.11, a comparison of their results against many previous results obtained is shown.

[6]The Reynolds number is a dimensionless number, which is the ratio of the fluid inertial forces to the viscous forces. Mathematically, it is defined as $\mathrm{Re} = \frac{uD}{\nu}$, where u is the flow velocity, d is the characteristic dimension of the immersed body, and ν is the kinematic viscosity of the fluid.

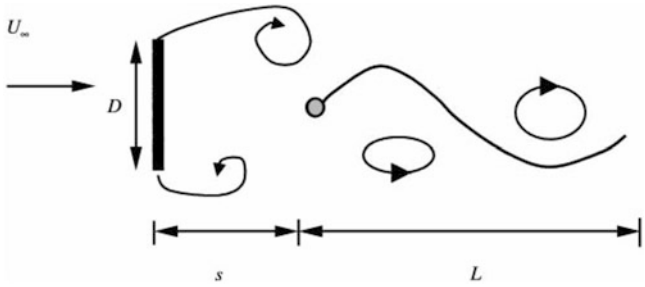

Fig. 6.12 The experimental setup schematic by Allen and Smits [2, Fig. 1]

It can be seen that for Re $>$ 800, two Strouhal numbers coexist for a given Re number—a high- and low-frequency mode of vortex shedding. Sakamoto and Haniu [39, p. 392] concluded that:

> . . .this coexistence of modes was due to the periodic fluctuation in the vortex tube formed by the pulsation of the vortex sheet separated from the surface of the sphere and in the turbulent wake with progressive wave motion respectively.

That said, there was found to be a higher power content in the lower-frequency Strouhal number [39, Fig. 5], and thus it is the mode of interest for the purpose of exciting an immersed beam.

EIE Flutter Energy Harvesting Examples

In 2001, Allen and Smits [2] investigated the concept of an "energy harvesting eel", whereby a thin, flexible beam was placed downstream of a vortex-shedding bluff body. They noted that in order for the vortices to influence the motion of the beam, the beam must have low bending rigidity, since a rigid splitter plate downstream of a bluff body was previously found to truncate the vortex sheet formation (see [20,38]). Allen and Smits [2] used a few different beam materials with different bending rigidities and differing lengths and conducted a Particle Image Velocimetry (PIV) flow visualisation investigation to determine the effect of the vortices impinging on the beam. A schematic of their setup is shown in Fig. 6.12; although the size of the bluff body D was varied in order to effectively change the Re number, the ratio s/D was kept constant at unity throughout the experiments.

Taylor et al. [43] conducted a similar investigation, whereby a PVDF-laden beam was placed behind a bluff body and immersed in a water flow. Experiments in a water tunnel were carried out to investigate the power output of the beam; however, most of the focus remained on optimising the electrical sub-system as opposed to examining the beam flutter characteristics. They calculated a maximum mechanical-to-electrical energy conversion efficiency of 37 %, given optimum circuit loading

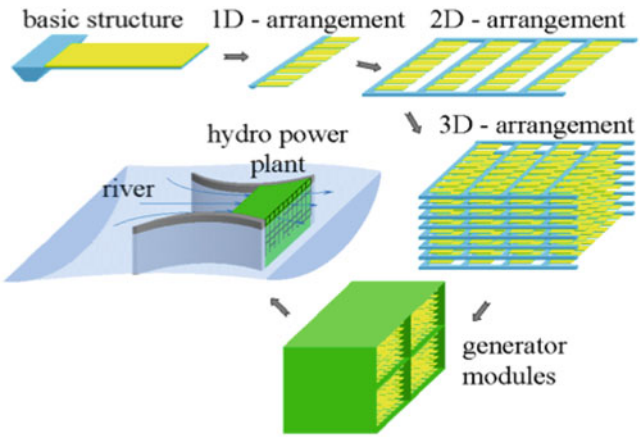

Fig. 6.13 The piezoelectric flapper array concept proposed by Pobering and Schwesinger [35, Fig. 5]

conditions and minimal mechanical losses. This connotes that when the electrical aspect is carefully considered along with the mechanical design, this technology displays much potential.

Pobering and Schwesinger [35] suggested a realisation of a flapper-harvester array in rivers and streams, as a replacement for water turbines (Fig. 6.13). They calculated that the power density of such a device could be up to 68.1 W/m^2, and compared this value to current wind turbine values of around 34 W/m^2.

Pobering and Schwesinger [35] accounted more for the structural–electrical feasibility of the piezoelectric device, rather than the vortex-shedding mechanisms that excite the system. A simple Rankine vortex model[7] was used to describe the vortices shed from the upstream bluff body of characteristic dimension, D. Mutual interaction effects between flappers were considered in the analysis but have been found elsewhere (e.g. [7, 26]) to be significant in terms of flutter frequency and output power.

Clamping Base Geometry

The leading-edge clamping conditions of the beam also play a major role in determining the magnitude of the flutter. As discussed previously in the vortex shedding overview, the maximum amplitude of flutter occurs when the vortex shedding frequency matched a bending natural frequency of the beam. If the

[7] A Rankine vortex is one that rotates at a constant angular velocity, ω, and has radius r_v. The velocity v for any $r < r_v$ is such that $v = \omega r$. For $r > r_v$, v decreases exponentially.

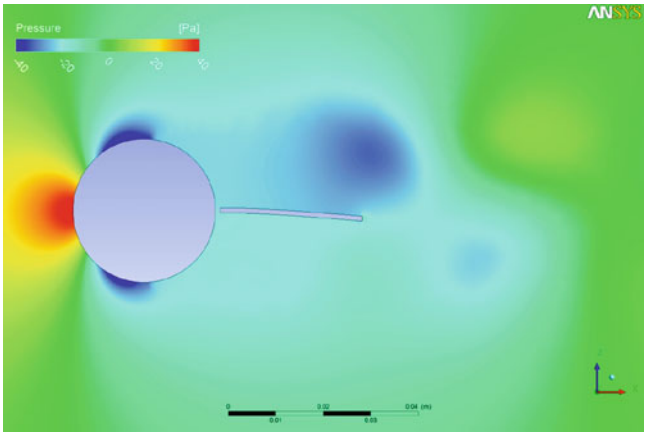

Fig. 6.14 A snapshot of a vortex shedding circular cylinder and flexible beam exhibiting EIE-type flutter, in CFD/FSI

geometry of the clamping base is significant in size, the vortex shedding off of the base may actually inhibit flutter by doing one of two things:

1. Delaying the cut-in speed.
2. Destructive interference, or anti-resonance.

Note that evaluation of the clamping base geometry constitutes the case where $s \to 0$, as depicted in Fig. 6.12 (p. 182). Work by Deivasigamani et al. [13] showed that the critical flutter speed of a given beam geometry would be delayed, for off-design conditions of the base clamping geometry. In that work, it was shown that the length, or stream-wise dimension of the clamp had little effect on the flutter characteristics of the beam; the width, or cross-stream dimension of the clamp caused changes in the critical flutter speed of the beam. An excellent method to conduct parametric studies in this facet of EIE-type flutter is using a Computational Fluid Dynamics (CFD)/FSI approach. The two-dimensional Navier–Stokes (N–S) equations may be readily and quickly solved for many cases of clamping-base-size to beam-length ratios, and while the results quantitatively may not give a very accurate solution,[8] qualitative flutter motions may be captured and assessed, as is illustrated in Fig. 6.14.

In addition, the FSI solutions may be extended to interact with a piezoelectric material; computational aero-mechanical–electrical interactions. This simply involves applying piezoelectric material properties to the fluttering beam behind the clamping base.

[8] Solving the two-dimensional N–S equations over a circular cylinder, for example, has shown gross over-prediction of the lift coefficient—even with significant mesh refinement, see Dong et al. [15].

6.2.3 Structural–Electrical Coupling

The phenomenon of piezoelectricity was first discovered in 1880 by Pierre and Jacques Curie during their study of the effects of pressure on the generation of electrical charge by crystals such as quartz, tourmaline and Rochelle salt. The term "piezoelectricity" was first given by W. Hankel, and the converse effect was mathematically deduced by Gabriel Lipmann from fundamental thermodynamic principles. However, piezoelectricity remained as a laboratory phenomenon until 1917, when Paul Langevin and his colleagues designed an ultrasonic submarine detector, which consisted of a transducer made of thin quartz crystals carefully glued between two steel plates, and a hydrophone to detect the returned echo. By emitting a high-frequency chirp from the transducer, and measuring the amount of time it takes to hear an echo from the sound waves bouncing off an object, one could calculate the distance to that object [55]. This success opened up the opportunities for piezoelectric materials in a variety of applications such as ultrasonic transducers, microphones, and accelerometers.

Piezoelectric Materials

There are a variety of piezoelectric materials in use currently, and the endeavour of this section is to introduce the reader to a few commonly used piezoelectric materials.

Early Discoveries

In 1935, Busch and Scherrer discovered piezoelectricity in potassium dihydrogen phosphate (KDP) and its isomorph. However in 1940–1943, unusually high dielectric properties were found in $BaTiO_3$. After this discovery, modifications of $BaTiO_3$ led to high voltage output.

Lead–Zirconate–Titanate (PZT)

In 1950, it was found that the PZT (Lead–Zirconate–Titanate) system could exhibit strong piezoelectric effects. Since then, the PZT system containing various additives has become the dominant piezoelectric ceramic for various applications [10]. A unit molecular cell of PZT is shown in Fig. 6.15.

PZTs are manufactured in strips and plates of various thicknesses based on the application. However, these strips have a specific stiffness which restricts its use for various applications that require flexibility of piezoelectric materials. Moreover, PZT strips are brittle in nature, and thus do not have the ability to handle large deformations.

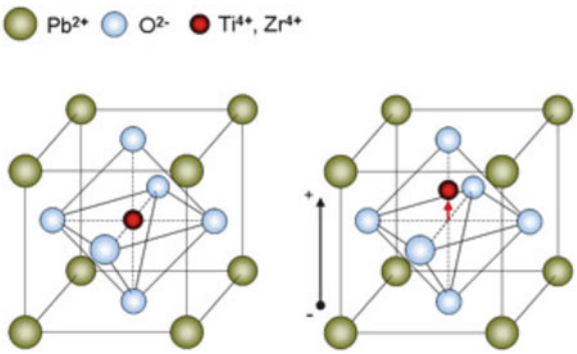

Fig. 6.15 The structure of a single PZT molecule [53]

Macro-fibre Composites

In order to overcome the above limitations, several forms of PZT have been developed for various applications, which are flexible to handle large amounts of strain. These PZTs are specially manufactured and are called Macro-fibre Composites (MFC). The MFC consists of rectangular piezo ceramic rods sandwiched between layers of adhesive, electrodes and polyimide film. The electrodes are attached to the film in an inter-digitated pattern, which transfers the applied voltage directly to and from the ribbon-shape rods. This assembly enables in-plane poling, actuation and sensing in a sealed and durable, ready-to-use package. As a thin, surface-conformable sheet it may be bonded to various types of structures or embedded in a composite structure. MFCs are very precisely engineered materials, having high energy densities and [thus] power outputs. However, they are very expensive due to the manufacturing complexities involved with the materials.

Polyvinylidene Fluoride (PVDF)

In 1969, strong piezoelectricity was observed in PVDF. Since then, PVDFs are used for various applications in place of PZTs due to their availability, cost and other piezoelectric parameters. PVDF has a glass transition temperature (T_g) of about $-35\,^{\circ}\mathrm{C}$ and is typically 50–60 % crystalline. To give the material its piezoelectric properties, it is mechanically stretched to orient the molecular chains and then poled under tension. PVDF exists in several forms: alpha (TGTG′), beta (TTTT), and gamma (TTTGTTTG′) phases, depending on the chain conformations as trans (T) or gauche (G) linkages. When poled, PVDF is a ferroelectric polymer, exhibiting efficient piezoelectric and pyroelectric properties. These characteristics make it useful in sensor and battery applications [54].

Since PVDFs are polymers, they may be manufactured to be very flexible compared to MFCs. Thus, PVDFs can be utilised for applications that require greater flexibility and low stiffness. Also, MFCs are made up of PZT fibres, which (as mentioned previously) are brittle and do not have the capability to handle large strains for a large number of cycles.

Piezoelectric Constitutive Relationships

Piezoelectric effects are classified into two categories, namely, the direct piezoelectric effect and converse piezoelectric effect. Direct piezoelectric effect is the instance where mechanical strain is converted to electrical charge; the converse piezoelectric effect is the opposite. Thus, it is essential to understand the mathematical relationship between electrical charge, displacement, mechanical stress and strain.

The electric displacement, D, and electric field strength, E, are related as

$$D = \epsilon E, \tag{6.4}$$

where ϵ is defined as the electric permittivity. Also, according to Hooke's law,

$$S = cT, \tag{6.5}$$

where S is mechanical strain, T is mechanical stress, and c is compliance (i.e. the inverse of elastic modulus). Thus, these two equations, which govern the electrical displacement and mechanical strain, are related in the coupling equations as

$$\{D\} = [d]\{T\} + [\epsilon]\{E\}, \tag{6.6}$$

$$\{S\} = [c]\{T\} + \left[d^t\right]\{E\}, \tag{6.7}$$

where d is defined as the piezoelectric coupling coefficient [16]. It is important to note that the terms in Eqs. (6.6) and (6.7) are matrices, since they are direction-dependent tensors. Thus, the values of electric displacement and strain could change based on the interaction between the mechanical and electrical behaviour in three orthogonal directions. The superscript, t, refers to the transposed matrix of d (indicating the converse piezoelectric effect). Additionally, we see from Eqs. (6.6) and (6.7) that it is the elastic modulus, electrical permittivity and piezoelectric coefficient that determine the ability of a piezoelectric material to convert mechanical energy into electrical energy and vice versa.

Energy Harvesting from Vibrations

As discussed in Sect. 6.2.3, the electrical charge developed in a piezoelectric material depends on mechanical strain. In order to harvest energy using piezoelectric materials, it is important that these materials are subjected to repetitive stress and strain. Before we look at the different forms of energy harvesting from vibrations investigated, it is important to understand some basic concepts behind vibrations of continuous beams.

Euler–Bernoulli Beam Theory

A beam undergoing transverse vibration is governed by the Euler–Bernoulli beam theory, which is written as

$$m\frac{\partial^2 y}{\partial t^2} + EI\frac{\partial^4 y}{\partial x^4} = F, \tag{6.8}$$

where m is the mass per unit length of the beam, EI is the bending stiffness, and F is the input forcing function. Thus the mechanical stress and strain induced from these vibrations are given by

$$T = \frac{Mz}{I} = -zE\frac{\partial^2 y}{\partial x^2}, \tag{6.9}$$

$$S = -z\frac{\partial^2 y}{\partial x^2}, \tag{6.10}$$

where M is the bending moment, I is the moment of inertia, and z is the distance from the neutral axis to the point of interest [46]. It is these stresses and strains experienced by the piezo that get converted into electrical energy, as governed by the coupling equations in Eqs. (6.6) and (6.7).

Power Available from Vibrations

The equation of motion for analysing forced vibrations of a lumped parameter system may be written as

$$\begin{aligned} m\ddot{z} + c\dot{z} + kz &= -m\ddot{y}, \\ \ddot{z} + \frac{c}{m}\dot{z} + \frac{k}{m}z &= -\ddot{y}, \\ \ddot{z} + 2\delta\omega_n\dot{z} + \omega_n^2 z &= -\ddot{y}, \end{aligned} \tag{6.11}$$

where the over-dots denote the derivative with respect to time, $\delta = \frac{c}{2\sqrt{mk}}$ is the damping ratio, and $\omega_n = \sqrt{\frac{k}{m}}$ is the natural frequency. Let us now examine the Laplace transform of a function:

$$\begin{aligned} \mathscr{L}\big(z(t)\big) = Z(s) &= \int_0^\infty e^{-st} z(t)\mathrm{d}t, \\ Z(s) &= \left[\frac{e^{-st}z(t)}{-s}\right]_0^\infty - \int_0^\infty \frac{e^{-st}\dot{z}(t)}{-s}\mathrm{d}t, \\ Z(s) &= \left[\frac{z(0)}{s}\right]_0^\infty + \frac{1}{s}\mathscr{L}\big(\dot{z}(t)\big). \end{aligned} \tag{6.12}$$

Now, rearranging terms gives

$$\mathscr{L}\big(\dot{z}(t)\big) = s\mathscr{L}\big(z(t)\big) - z(0) = sZ(s) - z(0). \tag{6.13}$$

Similarly,

$$\mathscr{L}\big(\ddot{z}(t)\big) = s^2 Z(s) - sZ(s) - z(0), \tag{6.14}$$

$$\mathscr{L}\big(\ddot{y}(t)\big) = s^2 Y(s) - sY(s) - y(0). \tag{6.15}$$

Now, substituting Eqs. (6.14) and (6.15) into Eq. (6.11) with initial position at 0 yields

$$s^2 Z(s) + 2\delta\omega_n s Z(s) + \omega_n^2 Z(s) = -s^2 Y(s). \tag{6.16}$$

Rearranging it yields

$$\left|\frac{Z(s)}{Y(s)}\right| = \frac{s^2}{s^2 + 2\delta\omega_n s + \omega_n^2},$$

$$Z(s) = \frac{s^2}{s^2 + 2\delta\omega_n s + \omega_n^2}\mathscr{L}\big(Y \sin\omega t\big). \tag{6.17}$$

Using the Laplace formula for sine, we have

$$Z(s) = Y\left(\frac{s^2}{s^2 + 2\delta\omega_n s + \omega_n^2}\right)\left(\frac{\omega}{s^2 + \omega^2}\right). \tag{6.18}$$

Now, applying the inverse Laplace transform by using partial fractions will yield

$$z(t) = \frac{\left(\frac{\omega}{\omega_n}\right)^2}{\sqrt{\left(1 - \left(\frac{\omega}{\omega_n}\right)^2\right)^2 + \left(\frac{2\delta\omega}{\omega_n}\right)^2}} Y \sin\omega t - \varphi. \tag{6.19}$$

Equation (6.19) is the position equation. If we differentiate, we obtain velocity v as

$$v = \dot{z}(t) = \frac{\left(\frac{\omega}{\omega_n}\right)^2}{\sqrt{\left(1 - \left(\frac{\omega}{\omega_n}\right)^2\right)^2 + \left(\frac{2\delta\omega}{\omega_n}\right)^2}} Y\omega, \tag{6.20}$$

and differentiating again we obtain the acceleration, a:

$$a = \ddot{z}(t) = \frac{\left(\frac{\omega}{\omega_n}\right)^2}{\sqrt{\left(1 - \left(\frac{\omega}{\omega_n}\right)^2\right)^2 + \left(\frac{2\delta\omega}{\omega_n}\right)^2}} Y\omega^2. \tag{6.21}$$

Note that the maximum values are taken by neglecting the sine and cosine functions. Therefore, the power in the vibrations is the product of force and velocity [36]:

$$P = m\ddot{z}(t)\dot{z}(t) = \frac{\left(\frac{\omega}{\omega_n}\right)^4 Y^2\omega^3 m}{\left(1-\left(\frac{\omega}{\omega_n}\right)^2\right)^2 + \left(\frac{2\delta\omega}{\omega_n}\right)^2}. \tag{6.22}$$

During resonance,

$$P = \frac{Y^2\omega^3 m}{4\delta^2}. \tag{6.23}$$

From the above analysis, three vital aspects of power extraction from vibrations are observed:

1. Power available from vibrations is directly proportional to the square of its vibration amplitude.
2. Power available from vibrations is directly proportional to the cube of its vibration frequency.
3. During resonance, the amplitude is at a maximum, hence the power available is at a maximum.

Electrical Load Matching

Piezoelectric materials may be electrically modelled as a combination of a capacitor (from which current is discharged) and a resistor through which the generated current flows. Thus, this RC internal circuit needs to be matched with optimum electrical resistance (i.e. electrical load) before it is connected to the electrical storage device, in order to obtain maximum power. Due to this electrical load matching, energy harvesting devices have the ability to output more power when matched to the optimum resistive load.

A simplified theoretical formula to arrive at the optimum electrical load is given by Eq. (6.24):

$$R_{L_{\text{opt}}} \approx \frac{1}{\omega C}, \tag{6.24}$$

where C is the capacitance of the piezoelectric material. Vibration of these piezoelectric materials induces an AC voltage, thus the output must be rectified in order to charge a battery, or to power any electronic devices. A typical circuit layout for a piezoelectric energy harvester is shown in Fig. 6.16.

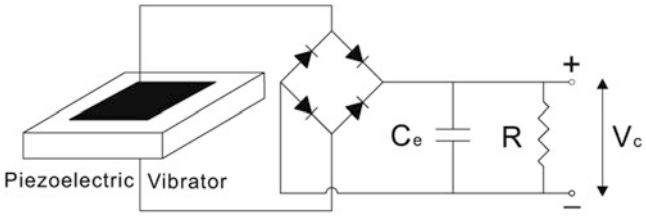

Fig. 6.16 A typical circuit, containing a piezoelectric vibrator [40, Fig. 3]

In order to evaluate the power output from a vibrating piezoelectric element, the following equation is used:

$$P = \frac{V_{\text{RMS}}^2}{R_L}, \tag{6.25}$$

where V_{RMS} is the root-mean-square voltage output from the piezo, and R_L is the load resistance in the energy capture circuit. Given a constant vibration frequency ω, the load resistance may be matched according to the capacitance of the piezoelectric material (which may be assumed constant). Thus, with the optimum load resistance, optimum power output is attained. However, given a variable vibration frequency over time, the load must be actively tuned to match ω. As the load resistance is changed, back-coupling occurs within the piezo element, and the subsequent output voltage also changes. Active resistance tuning for an autonomous system requires power input, and it remains to be seen whether the power input outweighs the power output from a piezo energy harvester. Furthermore, when dealing with flutter energy harvesters deployed in real-world atmospheric conditions, the vibration (flutter) frequency is *stochastic*, because the excitation force originating from the turbulent wind is stochastic. This will be discussed later on, but for now we concentrate our attention on a single piezoelectric leaf-stalk element, in order to further understand the electro-aero-mechanical dynamics.

6.2.4 Analysis of a Single Piezoelectric Leaf-Stalk

The objective with this type of energy harvesting system, and any energy harvesting system in general, is to generate maximum power. In extending the concept introduced by Dickson [14] (see Sect. 6.1), Li and Lipson [29] concentrated on understanding the dynamics of one discrete piezoelectric leaf-stalk system. They utilised a polyvinylidene-fluoride (PVDF) piezoelectric patch, coupled via a revolute hinge to a triangular, polymeric "leaf". They placed this leaf-stalk in a smooth, parallel flow, and increased the flow speed until the leaf-stalk started to flutter in Limit-Cycle Oscillations (LCO). Once fluttering, the time-varying strain on the PVDF element caused an AC voltage to be output.

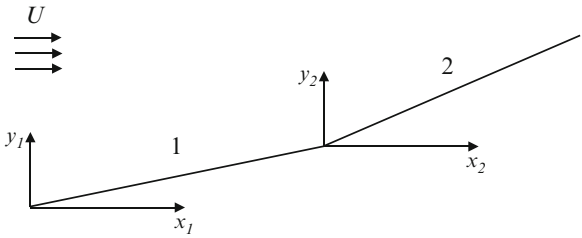

Fig. 6.17 The analytical model for determination of the hinge effect on the cantilever beam dynamics

Table 6.1 Beam properties utilised for the analytical, computational and experimental analyses

Property	Symbol	Value
Stiffness	EI	2.70×10^{-4} (N m^2)
Beam density	ρ_s	995 (kg/m^3)
Cross-sectional area	A	21 (mm^2)
Beam length	L	236 (mm)
Beam thickness	h	0.35 (mm)
Beam width	w	60 (mm)
Mass ratio	μ	1.19

Effect of a Revolute Hinge on Flutter Dynamics [12]

One main question that remained following the work by Li and Lipson [29] was the effect of the revolute hinge on the leaf-stalk flutter dynamics. Both Li and Lipson [29] and Bryant et al. [7] (elsewhere) found that by hinging a second element to the free end of the piezoelectric beam, the power output increased compared to a uniform beam case. Li and Lipson [29] suggested that the trailing element functioned to increase vibration amplitude in two ways:

1. It acted like an added mass to the piezoelectric beam.
2. It augmented the impinging pressure force by adding surface area.

Deivasigamani et al. [12] undertook an analytical, numerical and experimental investigation into the dynamic effect of a hinge interconnecting two identical beam elements. The leaf-stalk geometry was not modelled, in order that the hinge's effect on the beam dynamics was isolated and identified. The analytical model is shown as a schematic, in Fig. 6.17, and the beam mechanical and geometric properties used are listed in Table 6.1.

Analytical Hinged Beam Model

Euler–Bernoulli beam theory was utilised to extract the undamped, free-vibration natural frequencies of the clamped-hinged-free beam. If Euler–Bernoulli beam theory is applied for both beam elements 1 and 2, we have

$$m\frac{\partial^2 y_1}{\partial t^2} + EI\frac{\partial^4 y_1}{\partial x_1^4} = 0, \tag{6.26}$$

$$m\frac{\partial^2 y_2}{\partial t^2} + EI\frac{\partial^4 y_2}{\partial x_2^4} = 0. \tag{6.27}$$

Refer to Eq. (6.8) for variable definitions. The variable separable method was then utilised to solve Eqs. (6.26) and (6.27), so that

$$y_1 = Y_1(x)T_1(t), \tag{6.28}$$

$$y_2 = Y_2(x)T_2(t), \tag{6.29}$$

where $Y_i(x)$ is the ith space function and $T_i(t)$ is the ith time function. The transient behaviour of the beam was ignored, because the steady-state LCO of the beam were of interest. Thus, the general solutions of the space functions for both beam elements become

$$Y_1 = C_1\cos\beta x + C_2\sin\beta x + C_3\cosh\beta x + C_4\sinh\beta x, \tag{6.30}$$

$$Y_2 = C_5\cos\beta x + C_6\sin\beta x + C_7\cosh\beta x + C_8\sinh\beta x, \tag{6.31}$$

where $C_{1,2,\ldots,8}$ are constants and $\beta^4 = \dfrac{\rho_s A\omega^2}{EI}$, such that

$$\omega_i = (\beta_i L)^2\sqrt{\frac{EI}{\rho_s AL^4}}. \tag{6.32}$$

ω_i is the ith natural frequency, A is the beam cross-sectional area, and $\beta_i L = \lambda_i$, the ith eigenvalue of the system. Should the reader be interested in the remainder of the eigenvalue extraction process, see Deivasigamani et al. [12]. A comparison of the hinged-beam natural frequencies was made to the standard natural frequencies of a clamped-free beam [6], the eigenvalues of which are the roots of Eq. (6.33):

$$\cos(\lambda)\cosh(\lambda) = -1. \tag{6.33}$$

A modal natural frequency ratio, R_i, is defined in Eq. (6.34), and plotted in Fig. 6.18 for the 2nd through 4th modes of vibration. In this analysis, the hinge non-dimensional position along the beam, denoted by $\eta = x/L$, was varied and R_i subsequently examined. Due to the presence of a hinge, the fundamental (i.e. first) vibration mode of the beam was a rigid body mode[9]; thus $R_1 = 0$ for all η, and hence this mode was ignored

[9] A mode of vibration with zero strain.

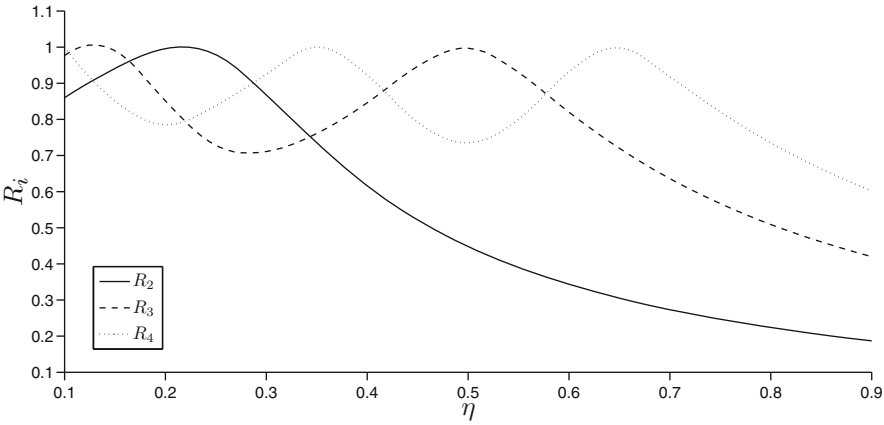

Fig. 6.18 Analytical R_i as a function of non-dimensional hinge position, η

$$R_i = \frac{\omega_{\text{hinge}_i}}{\omega_{\text{uniform}_i}}, \tag{6.34}$$

where ω_{hinge_i} is the ith hinged-beam natural frequency and $\omega_{\text{uniform}_i}$ is the ith uniform-beam natural frequency.

Computational Hinged Beam Model

In order to corroborate the analytical model, a finite element modal analysis was carried out involving the exact same beam geometry and boundary conditions as specified in Fig. 6.17 and Table 6.1. The computational model, with the hinge at $\eta = 0.5$, is displayed in Fig. 6.19.

In a modal analysis in ANSYS®, the shifted Block Lanczos algorithm is used by default [3] to directly extract the eigenvalues and eigenvectors of a structural model containing rigid-body modes. The interested reader may find details of the algorithm in Grimes et al. [21]. As with the analytical model, the 2nd through 4th modes were extracted, as well as the uniform-beam vibration modes. $R_{i\,\text{comp}}$ was evaluated at discrete beam hinge locations and compared with the analytical modal solution, as shown in Fig. 6.20.

The normalised mode shapes for the second vibration mode are shown in Fig. 6.21 for two hinge position cases: (1) where R_2 is maximum at $\eta = 0.2$ (Fig. 6.21a) and (2) where R_2 is minimum at $\eta = 0.9$ (Fig. 6.21b).

The hinge introduced an additional degree of freedom to the system, giving the beam greater flexibility. When $\eta = 0.2$, the hinge did not affect the mode shape (Fig. 6.21a) greatly, therefore rendering $R_2 \approx 1$. However, as the hinge was moved towards the free end, the first beam length increased, permitting greater flexibility; consequently, R_2 decreased. This is because the trailing element became shorter

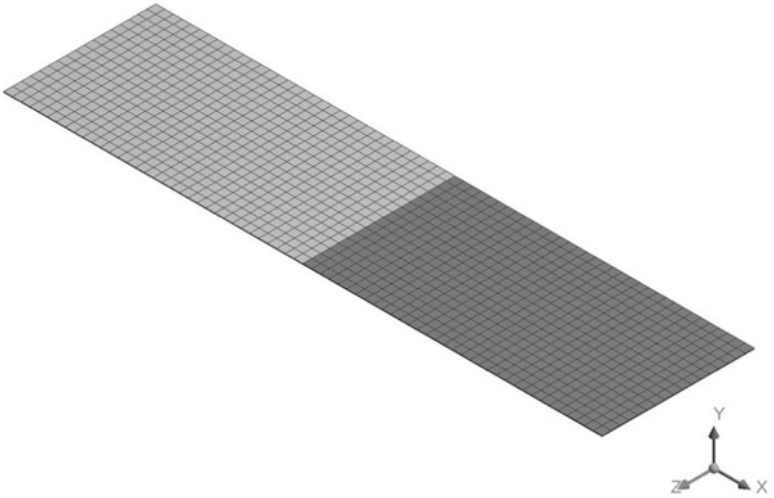

Fig. 6.19 The meshed computational model in ANSYS® Mechanical™(Release 13.0)

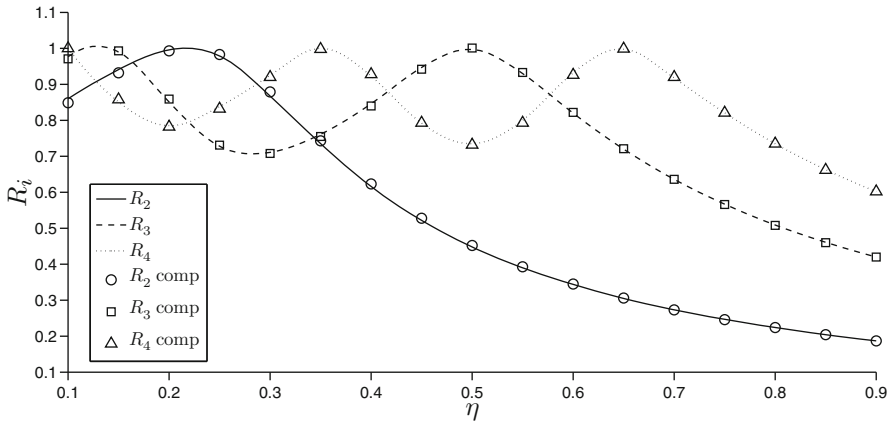

Fig. 6.20 $R_{i_{\text{comp}}}$ and R_i comparison

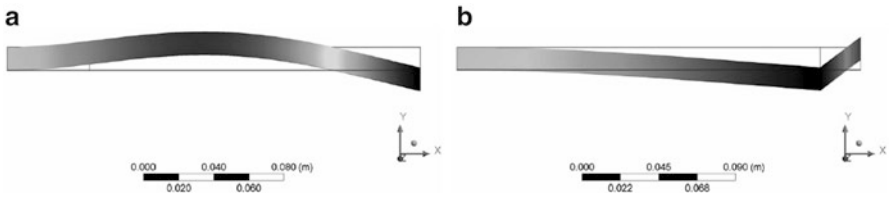

Fig. 6.21 The hinge positions which give (**a**) maximum R_2 ($\eta = 0.2$) and (**b**) minimum R_2 ($\eta = 0.9$). The undeformed wireframe of each beam is included for reference. Note the axes orientation

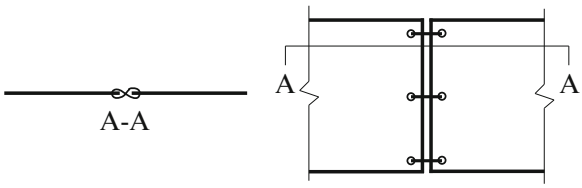

Fig. 6.22 *Side*- and *top*-view illustration of the hinge sewing method

and stiffer compared to the leading element. Also, the hinge was located at a node of maximum displacement for the case where $\eta = 0.9$ (Fig. 6.21b).

Experimental Hinged Beam Testing

The experiments were carried out in similar fashion to Li and Lipson [29]—smooth, parallel flow conditions. The RMIT University Aeronautical wind tunnel was used because of the low turbulence intensity ($\approx$0.5 %) values achieved. Nine identical polypropylene beams were fashioned (with mechanical properties listed in Table 6.1 on p. 192), each with one unique hinge position, ranging from $\eta = 0.1$ to 0.9. The revolute hinges were constructed by sewing threads with an "8" pattern at the top, middle and bottom to couple the beam elements (Fig. 6.22). This hinge construction technique was chosen as it was the most ideal solution for replicating a zero-mass hinge, and the "8" pattern ensured that the thread did not loosen during beam flutter. The effect of the hinge mass on the beam flutter characteristics was evaluated elsewhere, see McCarthy et al. [31].

A base stand was securely fastened into the wind tunnel test section, and a steel strip having a height of 600 mm, a stream-wise dimension of 12 mm, and a transverse dimension of 1.75 mm, was clamped to the base stand at the top, and bolted to the wind tunnel floor at the bottom. The beams were then clamped at the leading edge using another shorter steel strip fastened to the longer one, so that the transverse dimension (the width) of the base clamping system became 3.5 mm. The effects of the transverse clamping base dimension, in general, were discussed in Sect. 6.2.2; for the experiments conducted it was found that the clamping width had negligible influence on the critical flutter speed of the polypropylene beams. For more details of the experimental setup, see Deivasigamani et al. [12].

In previous work by Argentina and Mahadevan [4], two scaling laws were derived from a theoretical aeroelastic analysis of a two-dimensional beam fluttering in an ideal, parallel, potential flow. These scaling laws related the critical flutter speed and flutter frequency of an immersed beam to simple mechanical and geometric parameters. Later, these scaling laws were experimentally validated for highly three-dimensional beams in real-world flows, refer to Deivasigamani et al. [13]. Argentina and Mahadevan [4] found that the flutter frequency of a beam immersed in a parallel flow scales as

$$\omega \sim \sqrt{\frac{\rho_f u^2}{\rho_s h L}}. \tag{6.35}$$

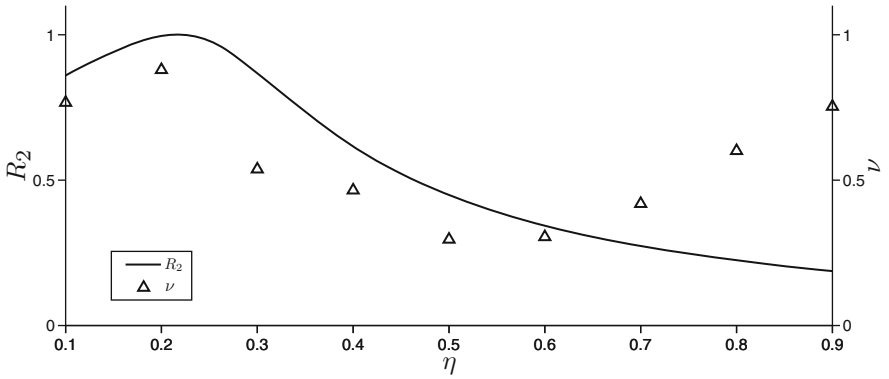

Fig. 6.23 R_2 and ν plotted against η

Also, when the flutter frequency is equated to the *lowest* flexible mode of vibration (i.e. ignoring all rigid body modes), Argentina and Mahadevan [4] found that the critical flutter speed, u_c, scales as

$$u_c \sim \sqrt{\frac{Eh^3}{\rho_f L^3}}. \tag{6.36}$$

In previous spectral analyses, workers discovered that maximum power was contained in the lowest flexible bending mode of vibrations [1, 23]. By Eqs. (6.35) and (6.36), it may be deduced that the natural frequency of a cantilever beam is directly related to its critical flutter speed in a parallel flow. Additionally, for the mass ratio (see Sect. 6.2.2) of the beams used here, it was expected that the flutter frequency would be approximately equal to the natural frequency, since it was found previously that unsteady lift effects did not significantly influence flutter [47]. Therefore, the critical flutter speed each polypropylene beam was evaluated for $\eta = 0.1$–0.9. We define a normalised critical flutter speed as

$$\nu = \frac{u_{c\,\text{hinge}}}{u_{c\,\text{uniform}}}, \tag{6.37}$$

where $u_{c\,\text{hinge}}$ is the critical flutter velocity of the hinged beam and $u_{c\,\text{uniform}}$ represents the critical flutter velocity of the uniform beam. The experimental ν trend obtained, along with R_2 as a function of η, are displayed in Fig. 6.23.

When the hinge was at $\eta = 0.1$, the first beam element was observed to remain rigid, while the second element fluttered as a uniform hinged-free beam in the wind tunnel. In the case of the hinge at $\eta = 0.2$, virtually no discontinuity was observed at the hinge position, and the entire system fluttered as a uniform cantilever beam. This is evidenced from the normalised critical flutter speed value, $\nu \approx 0.9$ (Fig. 6.23),

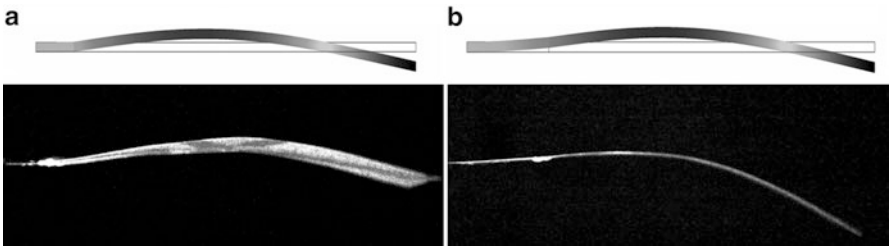

Fig. 6.24 Experimental and computational mode shape comparison for (**a**) a hinge at $\eta = 0.1$ and (**b**) a hinge at $\eta = 0.2$. Both beams were fluttering in the lowest flexible bending mode, λ_2

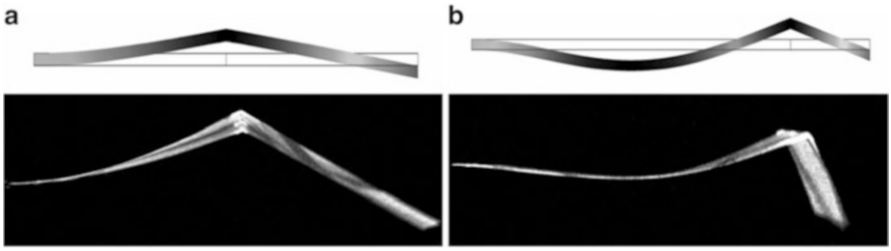

Fig. 6.25 Experimental and computational mode shape comparison for (**a**) a hinge at $\eta = 0.5$ and (**b**) a hinge at $\eta = 0.8$. When the hinge was at $\eta = 0.5$, flutter was in the λ_2 mode. When the hinge was at $\eta = 0.8$, flutter occurred in the λ_3 mode

and was elucidated previously in Fig. 6.21a from the mode shape. As the hinge was shifted towards $\eta = 0.5$, the critical flutter speed decreased monotonically. It is evident from Fig. 6.23 that for $0.1 \leq \eta \leq 0.5$, v has the same trend as R_2. This was due to flutter occurring in the lowest flexible bending mode for these hinge positions, suggesting that the scaling law in Eq. (6.36) indeed holds for these hinge positions. In Fig. 6.24, images of the mode shapes captured in the wind tunnel, and the computational mode shapes are compared for $\eta = 0.1$ and 0.2.

For $\eta > 0.5$, v started to increase and deviate from the R_2 trend. For these hinge positions, it was noticed that the specimens began to flutter in higher-order mode shapes, and not the lowest flexible bending mode. This phenomenon occurred due to the relative stiffness and length between the leading and trailing elements. When the hinge position was beyond $\eta = 0.5$, the hinged beam was able to flutter in higher-order modes because the leading element became longer compared to the trailing element. In Fig. 6.25, the mode shapes are compared for $\eta = 0.5$ and 0.8.

The hinge enhanced system stability by transitioning flutter occurrence into higher-order modes and thus delaying flutter onset. This transitional behaviour has been previously observed by Watanabe et al. [47] for both the flutter frequency and the critical flutter speed, for a varying mass ratio of a uniform beam. Indeed, the modal flutter transitions are depicted in Fig. 6.26.

It was proved in Sect. 6.2.3 that the power output of a piezoelectric element is proportional to the vibration amplitude squared and vibration frequency cubed.

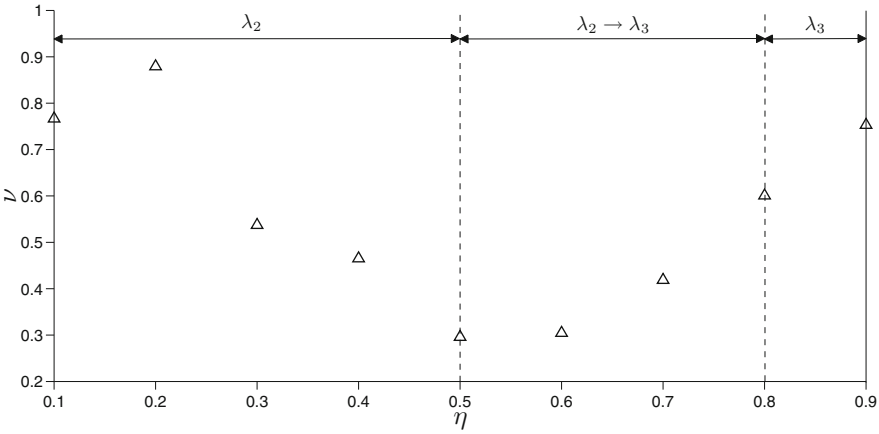

Fig. 6.26 The distinct regions in which the flutter mode changed from λ_2 for $\eta \leq 0.5$, to a transitional combination of modes for $0.5 < \eta < 0.8$, to λ_3 for $\eta \geq 0.8$

Placing the hinge near the leading edge of the beam delays flutter onset, causes lower-frequency and higher-amplitude vibrations; placing the hinge halfway along the beam gives the lowest cut-in wind speed and largest flutter amplitudes. Finally, placing the hinge near the trailing edge of the beam gives an increased cut-in wind speed compared to a hinge at the halfway point; however, the vibration frequencies are much higher and amplitudes much lower.

Effect of Leaf Geometry on Power Output [31]

In both continuance and furtherance of Li and Lipson's [29] work, McCarthy et al. [31] examined the effect of changing the polymeric-leaf geometry on the power output of the piezo. Li and Lipson [29] evaluated many leaf shapes and found that a triangularly shaped leaf gave the highest power output, though it was not known why. The results of their leaf shape analysis are shown in Fig. 6.27.

Once the leaf shape was chosen, no other modifications to the leaf were made throughout the remainder of their analysis. Thus, the leaf used by Li and Lipson [29] constituted the *baseline* leaf design for the parametric analysis conducted by McCarthy et al. [31]. Two leaf geometric parameters were varied, each one varied while keeping the other constant: (1) the leaf area with constant aspect ratio and (2) the leaf aspect ratio with the best-performing leaf area (i.e. the leaf area that rendered maximum power output). The PVDF piezoelectric stalk was identical to the one used in Li and Lipson [29].[10]

[10]Measurement Specialties, Inc., LDT1-028K/L type.

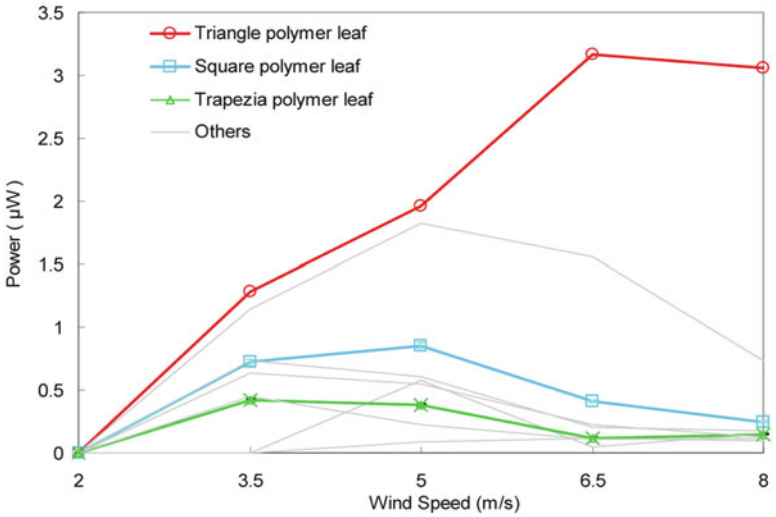

Fig. 6.27 The power output evaluated for a range of leaf shapes [29]

Increased Power Output of Triangular Leaf

Smoke-wire flow visualisation is used widely in the fluid mechanics discipline as a quick and readily available method to determine the flow behaviour around solid objects. Bryant et al. [8] performed smoke flow visualisation around their fluttering piezoelectric energy harvester, to determine the behaviour of the trailing-edge vortices. The geometry of their harvester is shown in Fig. 6.28; note that the leaf they used was rectangular.

The flow immediately surrounding the harvester—particularly, flow induced around the leaf—could be the cause of the increased power output for the triangular leaf. Observe the differences in flow between Bryant et al.'s [8] harvester (Fig. 6.29), and flow visualisation of a harvester with the same leaf geometry as Li and Lipson [29] (Fig. 6.30).

The major difference between the rectangular leaf and the triangular leaf is the presence of out-of-plane cone vortices for the triangular leaf case. These out-of plane vortices, unlike the in-plane vortices observed in the case of the rectangular leaf, induce torsion of the leaf—hence, torsion of the piezoelectric stalk. Therefore, in addition to the cyclic bending stresses, the piezo stalk with the triangular leaf experiences cyclic torsional stresses as a result of the induced pressure gradients, caused by the out-of-plane cone vortices.

Leaf Area Parametric Analysis

The leaves used for the experiments were made from 0.35 mm-thick polypropylene, which has an elastic modulus of 1,261 MPa and a density of 995 kg/m^3.

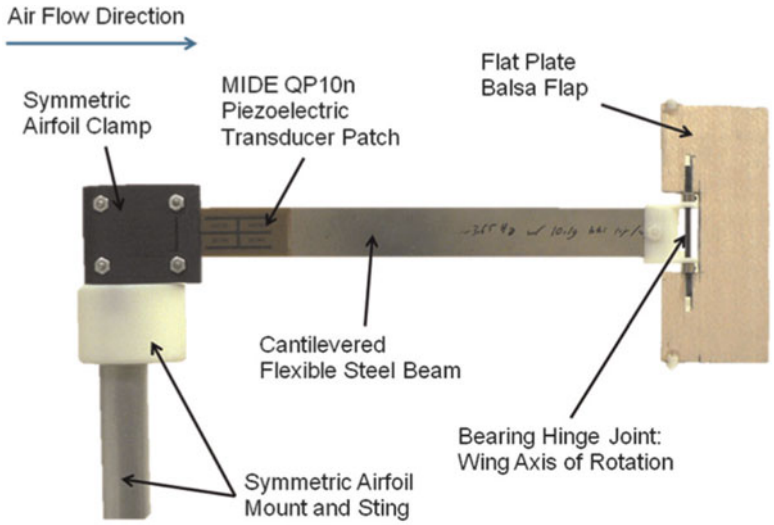

Fig. 6.28 The energy harvester used by Bryant et al. [8]

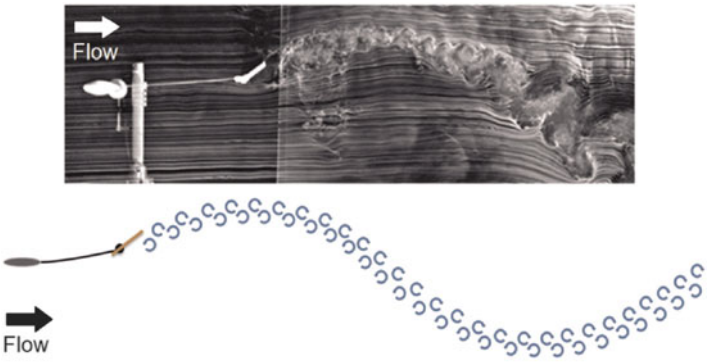

Fig. 6.29 Smoke flow visualisation of Bryant et al.'s [8] energy harvester

The clamping base and test stand setup in the wind tunnel was similar to the one utilised for the hinge analysis experiments in Sect. 6.2.4; an image of the experimental setup used in these tests is shown in Fig. 6.31.

Four leaf areas were chosen; the baseline leaf had an area $A = bh/2$, and aspect ratio $AR = h/b$ (b = base and h = height), while three other leaf areas were selected relative to the baseline leaf area. The aspect ratio was constant at unity. Table 6.2 displays the leaf dimensions and areas used.

The energy capture circuit used facilitated passive resistance tuning and power output analysis, for details refer McCarthy et al. [31]. The power output in 0.1-s intervals (P_i) was calculated using Eq. (6.25) (p. 191), and the total average power over a 30-s data acquisition window was calculated as

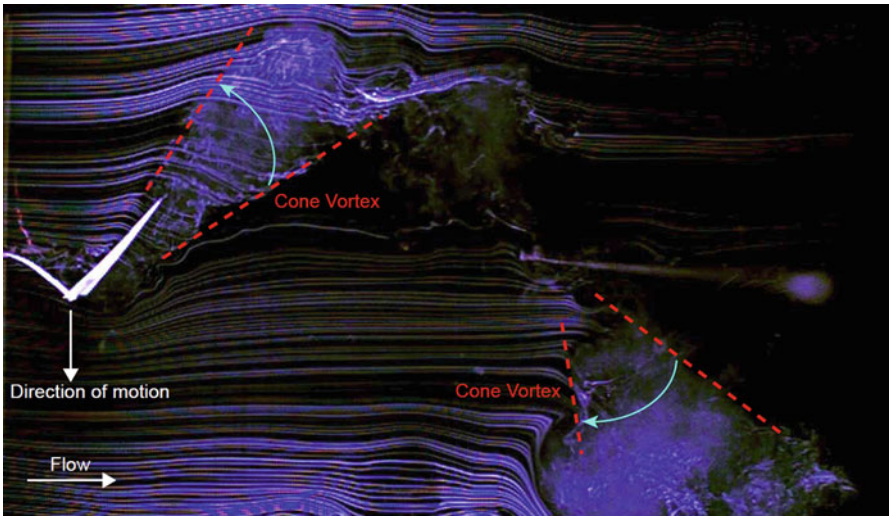

Fig. 6.30 Smoke flow visualisation of an energy harvester in the RMIT University Aeronautical wind tunnel. The *blue arrows* show the vortex rotation direction

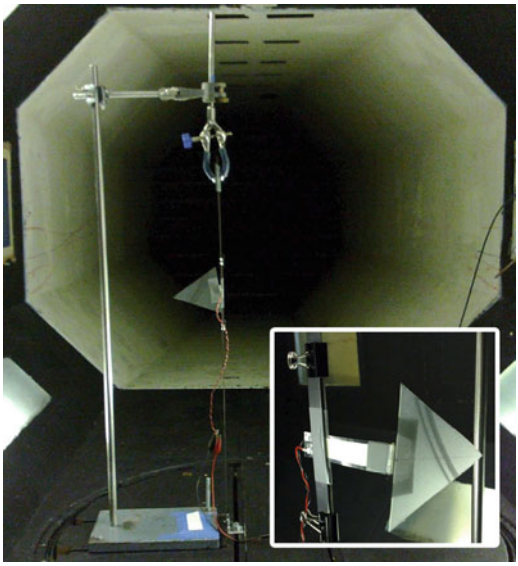

Fig. 6.31 Wind tunnel experimental setup. *Inset*: leaf-stalk close-up [31]

Table 6.2 Dimensions and areas of four leaves used in the parametric analysis

Dimensions (b cm × h cm)	Area (cm^2)
6 × 6	18
8 × 8 (baseline)	32
10 × 10	50
12 × 12	72

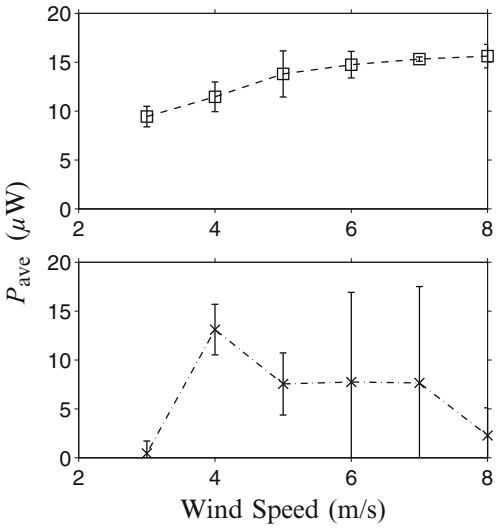

Fig. 6.32 Comparison of leaf area output power deviation. □– –, 8 × 8 cm; ×–·–, 12 × 12 cm

$$P_{\text{ave}} = \frac{1}{300}\sum_{i=1}^{300} P_i\,. \tag{6.38}$$

The wind speed testing range was chosen based on average measured urban wind speeds [41], where this type of technology would potentially be deployed.

In order to determine whether, during the testing, the leaf-stalks were transitioning from LCO to chaotic flutter (see Sect. 6.2.2), the output power deviation was monitored. As mentioned previously, maximum bending energy was found to be in the LCO flutter, rather than the chaotic flutter—thus it would be undesirable from a power output perspective for the leaf-stalks to transition to the chaotic flutter regime. It was observed in the tests that the 6 × 6 and 8 × 8 cm leaf cases did not show signs of chaotic flutter; however, it may be seen in Fig. 6.32 that the 12 × 12 cm leaf case fluttered chaotically for the wind speeds greater than 4.0 m/s.

The results for all four leaf areas are shown in Fig. 6.33. Flutter of the 6×6 cm leaf-stalk was delayed due to the smaller surface area. The smaller leaf presents less area for the free-stream flow to influence, and thus less pressure force is exerted on the leaf-stalk for a given wind speed. The 10×10 cm leaf initially showed a similar trend to that of the two smaller leaf-stalks, but at a wind speed of 6.0 m/s the power substantially decreased. At this wind speed, the 10×10 cm leaf-stalk had transitioned into the third flutter regime, where spontaneous snap-through events were seen to occur throughout the 30-s data collection window. Given further wind speed increase, the power output increased monotonically for the 10×10 cm leaf-stalk, but the stochastic nature of the flutter presented larger error and thus prohibited extrapolation beyond the maximum wind speed of 8.0 m/s.

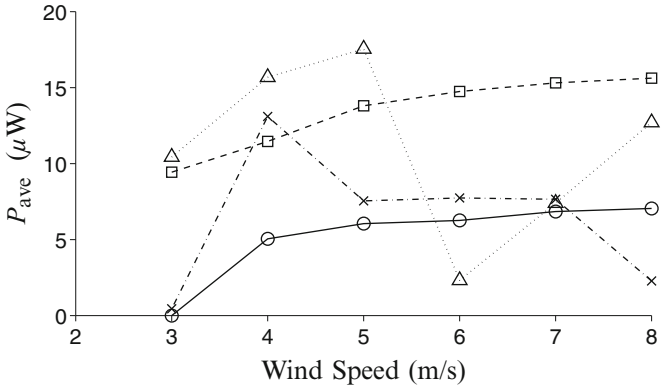

Fig. 6.33 Leaf area variation results. ◯—, 6 × 6 cm; □– –, 8 × 8 cm; △ ⋯, 10 × 10 cm; ×–·–, 12 × 12 cm

Increasing the leaf area while keeping the aspect ratio constant has two geometric effects: (1) the leaf gets longer and (2) the leaf gets wider. As mentioned previously in Sect. 6.2.2, it was found that lengthening a beam decreased the critical flutter speed and flutter frequency. It is also known that a two-dimensional (i.e. infinite cross-stream dimension) beam is always less stable than a three-dimensional beam [18]. These two effects may be seen in Figs. 6.32 and 6.33, whereby the larger leaf-stalks tended to cut-in at the minimum wind speed (though the 12×12 cm leaf-stalk cut-in earlier than 3 m/s), and the larger leaf-stalks also showed an accelerated tendency to unstable, chaotic flutter regime where power output is lower.

Leaf Aspect Ratio Parametric Analysis

The 8×8 cm leaf aspect ratio was subsequently varied, because it gave the highest power output with the lowest deviation. Four aspect ratios were tested: 0.25, 0.86 (equilateral triangle), 1 (baseline) and 4. Geometrically, varying the aspect ratio means that the length and width of the triangle change inversely, i.e. as the length increases, the width decreases and vice versa. The power output deviation is compared for the leaves with aspect ratios 0.25 and 4 in Fig. 6.34. None of the leaf-stalks transitioned into the third flutter type during the experiments, which suggests that area quantity—not area distribution, is a factor in determining the flutter regime of the leaf-stalk for this range of wind speeds. Further flow speed increase would eventually cause transition to the third flutter type. The power output results for all four aspect ratios are shown in Fig. 6.35.

The leaf-stalk with an aspect ratio of 4 did not start fluttering until around 5.0 m/s. This seems contradictory to previous work, which stated that a longer beam should cut-in sooner. Rather, the critical flutter speed of the leaf-stalk with an aspect ratio of 4 (i.e. the longest leaf) is the highest among all the other leaf-stalks. This may indicate that the stabilising effect of a smaller width on the critical flutter speed

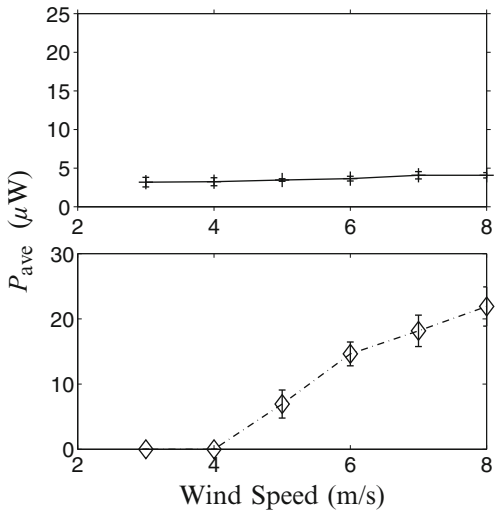

Fig. 6.34 Comparison of leaf aspect ratio power output deviation. +—, 0.25; ◇–·–, 4

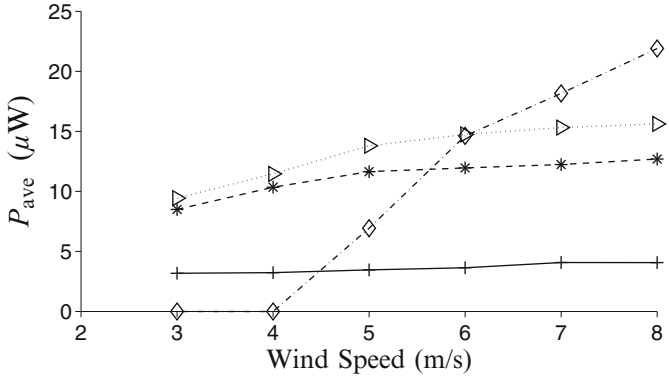

Fig. 6.35 Leaf aspect ratio variation results. +—, 0.25; ∗– –, 0.86; ▷ ···, 1; ◇–·–, 4

could be more significant than the destabilising effect of increasing length. The leaf-stalk with an aspect ratio of 0.25 began to flutter prior to reaching the 3.0 m/s minimum wind speed. It is interesting to note that in Fig. 6.35 the leaf-stalk with an aspect ratio of 0.25 output approximately constant power over a range of wind speeds, while the leaf-stalk with an aspect ratio of 4 output power approximately linearly-increasing for wind speeds from 4.0 to 8.0 m/s. To explain this behaviour, we examine the geometric and mass properties of a triangle. The triangular leaf is considered to be two-dimensional, since the thickness $\ll (b, h)$. The mass moment of inertia of a thin triangular plate rotating about its base is given as [25]

$$I_b = \frac{mh^2}{6}, \tag{6.39}$$

where m is the leaf mass. As the aspect ratio increases, h increases and hence I_b about the hinge increases, for a constant area. A consequence of a larger moment of inertia about the hinge is that more energy is required to initiate flutter of the system, in addition to the stabilising effect of the smaller width—hence the delayed flutter onset of the leaf-stalk with an aspect ratio of 4. However, a larger moment of inertia also means that there is inherently more rotational energy in the system, which translates to a higher power output.

6.3 Concluding Remarks

Energy harvesters, based on fluttering piezoelectric elements, are still in the incubation phase of development, with on-going research focused on maximising their (relatively low) power outputs. A significant issue for such energy harvesting systems of the future will be their power output compared with conventional wind generators, which have efficiencies that can typically extract up to 50 % of the available energy in an unbounded fluid stream (i.e. approaching the theoretical Betz limit of 59.3 %). Aside from considerations of energy efficiency conversion, other key considerations that challenge the viability of all systems are to do with return on investment and include considerations of payback time, reliability in the field (including under arduous climatic conditions of extreme winds, rain and icing) and maintenance costs.

Work to date has focused on laboratory-based fluttering element(s) in smooth fluid streams (usually air) where the element(s) are aligned with the stream direction. It has been demonstrated that for optimum geometries and spacing the combined power output of two or more aligned systems can be greater than the sum of systems in isolation. However if such systems are to be used outdoors it must be noted that atmospheric winds close to the ground are highly turbulent and turbulence intensities can be as high as 50 % in built-up areas. Associated with this turbulence are short-term fluctuations of the approach flow angles which offer challenges to harvesting systems in terms of local alignment, ultraviolet-based material degradation and fatigue, but may also offer opportunities to extract turbulent energy that is not present in smooth flow streams. Depending on geographic location the mean wind direction can vary from 0° to 360°, so decisions will have to be made as to whether such systems are self-aligning with mean wind direction. Further improvements in energy harvesting may come from local positioning around buildings where it has been shown that over-speed areas can be found which have about 50 % increase in flow speeds for a restricted range of approach flow angles compared with the local atmospheric wind speed [28]. Since the power developed by energy harvesting systems is highly dependent upon wind speed, and their use will generally be coupled to powering ULP devices on buildings (e.g. LED lighting and sensor networks), positioning systems on, or around buildings may find the earliest in-field applications.

Acknowledgements This work is funded by an Australian Research Council linkage scheme (grant no. LP100200034) in conjunction with Fabrics & Composites Science & Technology Pty. The authors would also like to thank Mr. Phred Peterson for the smoke-flow imagery.

List of Symbols

A	Cross-sectional area
a	Acceleration
AR	Aspect ratio
b	Leaf base length
C	Capacitance
c	Compliance or damping
$C_{1,2,3,\ldots,8}$	Constants in the general solutions of the space functions, Y_1 and Y_2
D	Characteristic dimension of bluff body or electric displacement
d	Piezoelectric coupling coefficient
E	Electric field strength or elastic modulus $\left(\frac{1}{c}\right)$
EI	Bending stiffness
F	Input forcing function
f	Vortex shedding frequency
h	Beam thickness or leaf height
I	Moment of inertia
I_b	Moment of inertia of an object rotating about its base axis
k	Stiffness
L	Beam length
$\mathscr{L}$	Laplacian operator
M	Bending moment
m	Mass per unit length of the beam, or mass
N	Number of discretisation points
P	Power
P_{ave}	Average power
P_i	Instantaneous power in an ith second interval
R_L	Load resistance
$R_{L_{\text{opt}}}$	Optimum load resistance
r	Radius
r_v	Rankine vortex radius
Re	Reynolds number
R_i	ith analytical natural frequency ratio
$R_{i\,\text{comp}}$	ith computational natural frequency ratio
S	Mechanical strain
s	Distance from beam leading-edge to upstream bluff body, or Laplacian coordinate
St	Strouhal number

T	Mechanical stress
t	Time, or when superscript, denotes the transpose of a matrix
T_g	Glass transition temperature
$T_i\,(t)$	ith time function in variable separable method
u	Fluid stream-wise velocity component
u_c	Critical flutter speed
u_q	Quenching speed
V_{RMS}	Root-mean-square voltage
v	Velocity or cross-stream velocity component
w	Beam width
$x,\ y,\ z$	Cartesian coordinates
$x_i,\ y_1,\ z_i$	ith local coordinates
$Y_i\,(x)$	ith space function in variable separable method
$Y(s),\ Z(s)$	Laplace transform of a function
z	Distance from beam neutral axis to point of interest

Greek Symbols

β_i	$\sqrt[4]{\rho_s A\omega_i^2/EI}$
δ	Damping ratio
ϵ	Electric permittivity
η	Non-dimensional hinge position, x/L
λ	Eigenvalue
λ_i	ith mode shape eigenvalue
μ	Mass ratio
ν	Kinematic viscosity or normalised critical flutter speed
φ	Phase difference
ρ_f	Fluid density
ρ_s	Beam density
ω	Angular frequency or angular velocity
ω_n	nth natural frequency

Subscripts

i	Index
Hinge	Hinged beam
Uniform	Uniform beam
Comp	Computational

References

1. Alben S, Shelley MJ (2008) Flapping states of a flag in an inviscid fluid: bistability and the transition to chaos. Phys Rev Lett 100(7):074,301-1–4
2. Allen JJ, Smits AJ (2001) Energy harvesting eel. J Fluids Struct 15(3–4):629–640
3. ANSYS® (2010) Mechanical, Release 13.0. No. Theory Reference: Eigenvalue and Eigenvector Extraction in Help System, ANSYS, Inc.
4. Argentina M, Mahadevan L (2005) Fluid-flow-induced flutter of a flag. Proc Natl Acad Sci U S A 102(6):1829–1834
5. Billah K, Scanlan R (1991) Resonance, tacoma narrows bridge failure, and undergraduate physics textbooks. Am J Phys 59(2):118–124
6. Blevins RD (1979) Formulas for natural frequency and mode shape. Van Nostrand Reinhold Company, New York. ISBN: 0-442-20710-7
7. Bryant M, Mahtani R, Garcia E (2011) Synergistic wake interactions in aeroelastic flutter vibration energy harvester arrays. In: ASME conference on smart materials, adaptive structures and intelligent systems (SMASIS2011), September 18–September 21. American Society of Mechanical Engineers, Scottsdale
8. Bryant M, Mahtani RL, Garcia E (2012) Wake synergies enhance performance in aeroelastic vibration energy harvesting. J Intell Mater Syst Struct 23(10):1131–1141
9. CAB (1961) Aircraft Accident Report—Braniff Airways, Inc., Lockheed Electra N9705C. Tech. Rep. USCOMM-DC-27267 Airways, Inc., Lockheed Electra N9705C, Civil Aeronautics Board
10. Cady WG (1964) Piezoelectricity: an introduction to the theory and applications of electromechanical phenomena in crystals. Dover Publications, New York
11. Connell BSH, Yue DKP (2007) Flapping dynamics of a flag in a uniform stream. J Fluid Mech 581:33–67
12. Deivasigamani A, McCarthy J, John S, Watkins S, Coman F, Trivailo P (2012a) Flutter of cantilevered interconnected beams with variable hinge positions. J Fluids Struct 38:223–237
13. Deivasigamani A, McCarthy J, Watkins S, John S, Coman F (2012) Flow-induced flutter of slender cantilever high-compliance plates. In: 28th international congress of the aeronautical sciences (ICAS 2012), Brisbane, September 23–September 28, p 863
14. Dickson R (2008) New concepts in renewable energy. Lulu Enterprises, Inc., Raleigh
15. Dong S, Karniadakis G, Ekmekci A, Rockwell D (2006) A combined direct numerical simulation-particle image velocimetry study of the turbulent near wake. J Fluid Mech 569:185–207
16. Dragan D (1998) Ferroelectric, dielectric and piezoelectric properties of ferroelectric thin films and ceramics. Rep Prog Phys 61(9):1267–1324
17. van Dyke M (1982) An album of fluid motion. The Parabolic Press, Stanford
18. Eloy C, Souilliez C, Schouveiler L (2007) Flutter of a rectangular plate. J Fluids Struct 23:904–919
19. Encraft (2009) Final report (warwick microwind trial project). Tech. Rep. http://www.warwickwindtrials.org.uk/2.html. Viewed 28 Dec 2011
20. Gerrard JH (1966) The mechanics of the formation region of vortices behind bluff bodies. J Fluid Mech 25:401–413
21. Grimes RG, Lewis JG, Simon HD (1994) A shifted block lanczos algorithm for solving sparse symmetric generalized eigenproblems. SIAM J Matrix Anal Appl 15(1):228–272
22. Hariri M, John S, Trivailo P (2009) Modelling piezoelectric actuation during structural flutter. In: ASME conference on smart materials, adaptive structures and intelligent systems (SMASIS2009), vol 1, September 21–September 23. American Society of Mechanical Engineers, Oxnard, pp 33–43
23. Hobeck J, Inman DJ (2011) Energy harvesting from turbulence-induced vibration in airflow: artificial piezoelectric grass concept. In: 2011 ASME conference on smart materials, adaptive structures and intelligent systems (SMASIS2011), September 18–September 21. American Society of Mechanical Engineers, Scottsdale

24. Huang L (1995) Flutter of cantilevered plates in axial flow. J Fluids Struct 9:127–147
25. Industrial Press (2008) Properties of bodies. In: Machinery's handbook, 28th edn. Industrial Press Inc., New York, pp 222–245
26. Jun Z, Childress S, Libchaber A, Shelley M (2000) Flexible filaments in a flowing soap film as a model for one-dimensional flags in a two-dimensional wind. Nature 408:835–839
27. Kornecki A, Dowell EH, O'Brien J (1976) On the aerodynamic instability of two-dimensional panels in uniform incompressible flow. J Sound Vib 47(2):163–178
28. Ladani R, Watkins S, Ei Wei KL (2012) Flow mapping around a building: with emphasis on wind turbine siting over building rooftops. J Wind Eng Ind Aerodyn (submitted for publication)
29. Li S, Lipson H (2009) Vertical-stalk flapping-leaf generator for wind energy harvesting. In: ASME conference on smart materials, adaptive structures and intelligent systems (SMASIS2009), vol 2, September 21–September 23. American Society of Mechanical Engineers, Oxnard, pp 611–619
30. Lord R (1878) On the instability of jets. Proc Lond Math Soc 10(1):4–13
31. McCarthy J, Deivasigamani A, John S, Watkins S, Coman F (2012) The effect of the configuration of the amplification device on the power output of a piezoelectric strip. In: ASME conference on smart materials, adaptive structures and intelligent systems (SMASIS2012), September 19–September 21. American Society of Mechanical Engineers, Stone Mountain, p 7951
32. Naudascher E, Rockwell D (1980) Oscillator-model approach to the identification and assessment of flow-induced vibrations in the system. J Hydraul Res 18:59–82
33. Naudascher E, Rockwell D (1994) Flow-induced vibrations: an engineering guide. A. A. Balkema, Rotterdam
34. Païdoussis M (1998) Fluid–structure interactions—slender structures and axial flow, vol 1. Elsevier Academic Press, London
35. Pobering S, Schwesinger N (2004) A novel hydropower harvesting device. In: International conference on MEMS, NANO and smart systems (ICMENS 2004), August 25–August 27. IEEE Computer Society, Banff, pp 480–485
36. Priya S (2007) Advances in energy harvesting using low profile energy harvesters. J Electroceram 19:165–182
37. Raju M (2008) Energy harvesting: ULP meets energy harvesting. www.ti.com/corp/docs/landing/cc430/graphics/slyy018_20081031.pdf
38. Roshko A (1954) On the drag and shedding frequency of two-dimensional bluff bodies. Tech. Rep. 3169, NACA
39. Sakamoto H, Haniu H (1990) A study on vortex shedding from spheres in a uniform flow. Trans ASME J Fluids Eng 112(4):386–392
40. Shu YC, Lien IC (2006) Analysis of power output for piezoelectric energy harvesting systems. Smart Mater Struct 15:1499–1512
41. Sustainable Energy Authority Victoria (2003) Victorian wind atlas. Cartographic Material
42. Tang L, Paidoussis MP (2007) On the instability and the post-critical behaviour of two-dimensional cantilevered flexible plates in axial flow. J Sound Vib 305:97–115
43. Taylor GW, Burns JR, Kammann SM, Powers WB, Welsh TR (2001) The energy harvesting eel: a small subsurface ocean/river power generator. IEEE J Ocean Eng 26(4):539–547
44. Theodorsen T (1935) General theory of aerodynamic instability and the mechanism of flutter. Tech. Rep. No. 496, National Advisory Committee for Aeronautics
45. Thorpe S (1971) Experiments on the instability of stratified shear flows: miscible fluids. J Fluid Mech 46(2):299–319
46. Timoshenko SP (1953) History of strength of materials. McGraw-Hill, New York
47. Watanabe Y, Isogai K, Suzuki S, Sugihara M (2002) A theoretical study of paper flutter. J Fluids Struct 16:543–560
48. Watanabe Y, Suzuki S, Sugihara M, Sueoka Y (2002) An experimental study of paper flutter. J Fluids Struct 16:529–542
49. Webb A (2007) The viability of domestic wind turbines for urban Melbourne. Tech. Rep. Alternative Technology Association

50. Wilson A (2009) The folly of building-integrated wind. http://www.buildinggreen.com/auth/article.cfm/2009/4/29/The-Folly-of-Building-Integrated-Wind, viewed (2 Jan 2012)
51. Yamaguchi N, Sekiguchi T, Yokota K, Tsujimoto Y (2000) Flutter limits and behaviors of a flexible thin sheet in high-speed flow—II: experimental results and predicted behaviors for low mass ratios. ASME J Fluids Eng 122:74–83
52. Yamaguchi N, Yokota K, Tsujimoto Y (2000) Flutter limits and behaviors of a flexible thin sheet in high-speed flow—I: analytical method for prediction of the sheet behavior. ASME J Fluids Eng 122:65–73
53. YTC America Inc. (2008) Structure of PZT. JPEG, http://www.ytca.com/lead_free_piezoelectric_ceramics, viewed (28 Nov 2012)
54. Zhang QM, Bharti V, Kavarnos G, Schwartz M (2002) Poly-vinylidene fluoride (PVDF) and its copolymers. In: Encyclopedia of smart materials, vols 1–2. Wiley, New York, pp 807–825
55. Zhu X (2009) Piezoelectric materials: structure, properties and applications. Nova Science Publishers, Inc., New York, pp 1–36

Chapter 7
Experimental and Finite Element Nonlinear Dynamics Analysis of Formula SAE Impact Attenuator

Toh Yen Pang and Hoy Tristian

Abstract Energy absorption and weight are major concerns in the design of an impact attenuator. To reduce the costs involved in the design and development of a new attenuator, it is important to minimise the time spent in the development and testing phase. The aim of this paper is to report on a study that used computer dynamic simulation to analyse the energy absorption and damage in a new impact attenuator. All initial requirements of the new attenuator were set in accordance with the 2011 Formula SAE rules. In this study, a nonlinear dynamic finite element was used to simulate an FSAE impact attenuator crash against a rigid barrier. Geometrical and material nonlinearities were performed using ABAQUS/Explicit commercial code. The numerical model was verified by experimental tests. Agreement between the numerical simulations and the test results showed that finite element analysis could be used effectively to predict the energy absorption and damage performance of an impact attenuator.

7.1 Introduction

As part of the 2011 Formula SAE Regulations, the Rules Committee has added specific criteria that are mandatory for the participating teams. They must fit impact attenuators to all competing vehicles at a Formula SAE event [1]. The attenuator is required by the rules of the competition to be tested with a total of 300 kg vehicle crashed into a rigid, non-yielding impact barrier at velocity of 7.0 ms^{-1}. The total energy absorbed by the attenuator must meet or exceed 7,350 J, and the average deceleration of the vehicle should not to exceed 20 g, with a peak deceleration less than or equal to 40 g.

T.Y. Pang (✉) • H. Tristian
School of Aerospace, Mechanical and Manufacturing Engineering, RMIT University, Bundoora, VIC, 3083 Australia
e-mail: tohyen.pang@rmit.edu.au; hoy.tristan@gmail.com

R.N. Jazar and L. Dai (eds.), *Nonlinear Approaches in Engineering Applications 2*,
DOI 10.1007/978-1-4614-6877-6_7,

The RMIT Racing team has designed and produced an impact attenuator that is made of 5083-H321 Aluminium and attached rigidly to the chassis. The material has mechanical and forming properties and can readily be welded [2], which make it ideal for this application.

The final design was then subjected to an impact crash to evaluate the damage and to verify the effectiveness of the structure's energy absorption. Due to the high costs and significant time requirements of conducting full-scale physical testing, there is a further need to develop more refined analytical tools to investigate the ultimate energy absorption behaviour of the attenuator. For cost reasons, it is important to reduce the time spent on the development and testing phase. Computer simulation of tests can significantly reduce the time and cost required involved in finalising an attenuator design. High-speed computers and commercial finite element method (FEM) packages facilitate the development of these tools through refined three-dimensional FEM.

The objective of this paper is to evaluate by FEM the absorbed energy and the damage to the impact attenuator. The FEM results are compared with experimental data obtained by means of full-scale testing.

The next section describes the detailed FEM formulation to solve the nonlinearity of governing equations of motion for the dynamic contact problem. The equations of motion are integrated using the explicit central difference integration rule. The penalty method is adopted to enforce the contact constraints and to compute the contact force in the analysis. The numerical simulation of the impact attenuator and full-scale impact verification results are discussed in detail in the following section, followed by conclusion.

7.2 Theoretical Background

7.2.1 Equilibrium Equation for Bodies in Contact

A contact between two deformable bodies is considered here. The dynamic boundary formulation for a system consisting of body with contact can be expressed as:

$$W^{inertia} + W^{damp} + W^{\text{int}} = W^{ext} + W^{cont} \tag{7.1}$$

where the terms denote the virtual kinetic forces, internal forces, external forces and contact forces, respectively.

When two elastic-impact bodies at time t are in contact, the principle of virtual work can be written as [3–5]:

$$\int_{\tau_1}^{\tau_2} \left(\delta E_\alpha + \delta T_\alpha + \delta C_\alpha - \delta W_\alpha - \delta \prod_{\alpha}^{cont} \right) dt = 0 \tag{7.2}$$

and

$$\delta E_\alpha = \int\limits_{V^{(\alpha)}} \delta\left(\varepsilon^{(\alpha)}\right) : \sigma^{(\alpha)} dV \tag{7.3}$$

$$\delta T_\alpha = \int\limits_{V^{(\alpha)}} \delta u^{(\alpha)} \cdot \rho \ddot{u}^{(\alpha)} dV \tag{7.4}$$

$$\delta C_\alpha = \int\limits_{V^{(\alpha)}} \delta u^{(\alpha)} \cdot c \dot{u}^{(\alpha)} dV \tag{7.5}$$

$$\delta W_\alpha = \int\limits_{V^{(\alpha)}} \rho f^{(V_\alpha)} \cdot \delta u^{(\alpha)} dV + \int\limits_{S_\sigma^{(\alpha)}} f^{\left(S_\sigma^{(\alpha)}\right)} \cdot \delta u^{(\alpha)} dS \tag{7.6}$$

The relevant variables above are: τ_1, τ_2 denote time instant; $\delta E\alpha$, $\delta T\alpha$, $\delta W\alpha$ are virtual kinetic, internal and external forces, respectively; V denotes a volume occupied by a part of the body in the current configuration; S denotes the surface bounding in this volume; ρ is the material density; $f^{(V_\alpha)}$ and $f^{\left(S_\sigma^{(\alpha)}\right)}$ are the components of externally applied forces per unit volume and externally applied surface traction per unit surface area, respectively; σ is the Cauchy stress tensor field, ε is its conjugate strain tensor; u is the displacement vector in the body and $\delta \prod_\alpha^{cont}$ represents virtual contact work dependent upon the contact force exerted on the contact surface. Prefix δ designates an arbitrary, virtual and compatible variation.

In a general contact interface, the weak form equality with the active set of constraints within an increment solution step for Eq. (7.2) can be written as:

$$\sum_{\alpha=1}^{2} \left(\int\limits_{V^{(\alpha)}} \sigma : \delta u^{(\alpha)} dV + \int\limits_{V^{(\alpha)}} c \dot{u} \delta u^{(\alpha)} dV - \int\limits_{V^{(\alpha)}} \rho^{(\alpha)} \left(f^{(V_\alpha)} - \ddot{u}^{(\alpha)} \right) \delta u^{(\alpha)} dV \right.$$
$$\left. - \int\limits_{S_\sigma^{(\alpha)}} f^{\left(S_\sigma^{(\alpha)}\right)} \cdot \delta u^{(\alpha)} dS \right) - \delta \prod_{\alpha}^{cont} = 0 \tag{7.7}$$

where $\delta \prod_\alpha^{cont}$ is 'contact contribution' associated with the active constraint set and initial conditions that a user defined.

7.2.2 Contact Constraints

A variety of numerical methodologies have been proposed in the literature to deal with the contact constraints [5–9], among them, the enforcement of the constraints using Lagrange multiplier methods and penalty methods. Lagrange multiplier methods introduce additional variables (the Lagrange multipliers) to enforce directly and exactly the contact constraint. Despite the obvious advantage of the exact enforcement of the constraint condition, the method poses some difficulties due to the additional effort required to solve the multipliers. The penalty methods avoid the need for additional variables by introducing an approximation of the constraint conditions [8, 10], this method was chosen for the study reported here.

In the penalty method, the contribution to the virtual work due to contact can be written as follows [8]:

$$\delta \prod^{cont} \left(\mathrm{u}^{(\alpha)}; \delta \mathrm{u}^{(\alpha)}\right) = \int_{S_c} \varepsilon_N \bar{g}_N \delta \bar{g}_N dA + \int_{S_c} t_T \cdot \delta g_T dA, \qquad \varepsilon_{\mathrm{N}} > 0 \tag{7.8}$$

where $\delta \bar{g}_N$ and δg_T are the variations in gap and tangential displacement, t_T is the tangential stress vector determined from the constitutive law of frictional slip and ε_N is the penalty parameter.

7.2.3 Contact Kinematics

When two bodies coming into contact is considered, any contact surface involved in the problem is assigned as slave or master. The master contact point of the master surface, $S_c^{(1)}$, is at node (1), and the slave contact point of the slave surface, $S_c^{(2)}$, is at node (2) in Fig. 7.1. The normal vector $\bar{n}^1$ is used to define the distance between the master surface node and the slave node. $\bar{x}^1$ is the deformation of the master surface and x^2 is the deformation of the slave surface.

The gap (g_N) for slave node (2) is defined as the distance between current position of node x^2 and the master surface ($S_c^{(1)}$):

$$g_{\mathrm{N}} = \left(x^2 - \bar{x}^1\right) \cdot \bar{\mathrm{n}}^1 \tag{7.9}$$

The mathematical condition for non-penetration is:

$$g_N \geq 0 \tag{7.10}$$

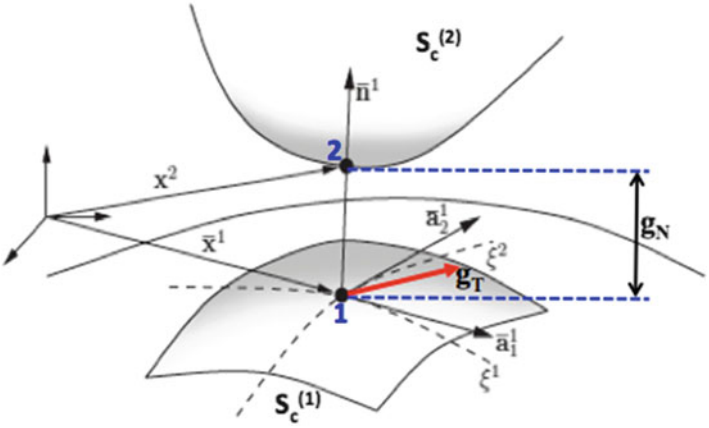

Fig. 7.1 Geometrical description of contact between two deformable bodies [5]

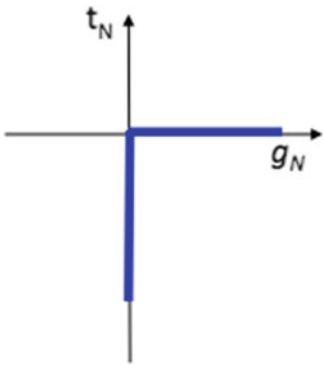

Fig. 7.2 Contact force versus normal gap

7.2.4 Normal Contact Constraints

When the penalty method is used to calculate contact force, some interpenetration is allowed. In this case, the contact force (t_N) is expressed as a function of the normal gap intensity:

$$t_N = \varepsilon_N g_N \tag{7.11}$$

where ε_N is the normal penalty parameter. Contact takes place when $g_N = 0$ and $t_N < 0$ (Fig. 7.2). The penalty parameter value can be seen as the stiffness of the surface to penetration. If there is a gap between the contacting bodies, then the relation of $g_N > 0$ and $t_N = 0$ holds. This leads to the statements:

$$g_N \geq 0; t_N \leq 0; t_N g_N = 0 \tag{7.12}$$

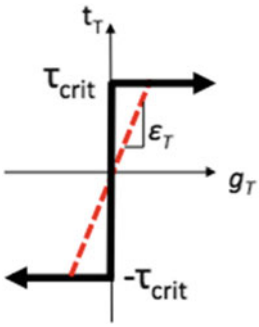

Fig. 7.3 Tangential contact and Coulomb friction conditions

which are known as the Kuhn–Tucker–Karush condition. Figure 7.2 and Eq. (7.12) lead to a non-smooth contact law for the normal contact pressure [5].

7.2.5 Tangential Contact Constraints

When the friction is modelled, tangential relative displacement must be considered. The contacts in tangential directions have two distinctive conditions, i.e. a stick condition or a slip condition. In the stick condition, two contact bodies stick to each other; there is no sliding between two bodies occurs and the tangential relative velocity is equal to zero. When the velocity is zero, the tangential relative displacement is also zero. Hence, the stick condition can be obtained from [5, 7]:

$$\dot{g}_T = 0 \Leftrightarrow g_T = 0 \tag{7.13}$$

where g_T denotes the relative displacement in a tangential direction. Note that in the stick condition, there is no need to distinguish between the normal and tangential directions. In this case, the normal gap is closed:

$$g_{\mathrm{N}} = \left(x^2 - \bar{x}^1\right) \cdot \bar{\mathrm{n}}^1 = 0 \tag{7.14}$$

The sliding condition occurs when there is relative tangential movement between two contact bodies, and this is classically described by the law of Coulomb, which takes the form:

$$\|t_T\| \leq \tau_{crit}, \ \|g_N\| \geq 0, \ (\|t_T\| - \tau_{crit}) \|g_T\| = 0 \tag{7.15}$$

where τ_{crit} is a threshold of tangential contact traction for tangential slip (shown in Fig. 7.3). If the frictional model is characterized by Coulomb's law, then $\tau_{crit} = \mu t_N$, where μ is the sliding friction coefficient. In general, the friction coefficient depends upon different parameters such as the surface roughness, the relative sliding

velocity ($\dot{g}_T$) between the contacting bodies, the contact normal pressure t_N, and the temperature θ (see [5] for more discussion).

7.2.6 Governing Equation of Equilibrium

The governing matrix notation of Eqs. (7.7) and (7.8) yields:

$$M\ddot{u}_{(t)} + c\dot{u}_{(t)} + [K + K_c]\, u_{(t)} = F^{ext}\left(u_{(t)}\right) + F^{cont}\left(u_{(t)}\right) \tag{7.16}$$

In Eq. (7.16) all quantities are evaluated at the initial conditions, where: $\ddot{u}$, $\bar{u}$ and u are the global vectors of unknown accelerations, velocities and displacements; F^{ext} and F^{cont} are the global vectors of external and contact forces resulting from the definitions of virtual external and contact works; M, c and $[K + K_c]$ are the global mass, damping and stiffness matrices derived by manipulations with the virtual inertial, damping and internal works in the same expression.

This equation can be transformed into a first order algebraic differential equation as:

$$\ddot{u}|_{(t)} = (\boldsymbol{M})^{-1} \cdot \left(\boldsymbol{F^{ext}} - I\right)\Big|_{(t)} \tag{7.17}$$

where $\mathbf{M}$ is the mass matrix, $\mathbf{F^{ext}}$ is the applied load vector and

$$I = c\dot{u}_{(t)} + [K + K_c]\, u_{(t)} + F^{cont}(u) \tag{7.18}$$

I is the sum of the damping, nodal internal force vector and the contact forces. The subscript $\ldots|_{(t)}$ denotes the quantity has to be evaluated at time t. The initial values (at time $t = t_0$) of velocity and acceleration are set to zero unless the user specifies them.

7.2.7 Explicit Time Integration Schemes

This section presents the explicit time integration solution procedure for predicting the frictional contact configuration considering both material and geometrical nonlinearities. The explicit dynamics analysis algorithm is based on the implementation of the central difference scheme together with the diagonal or "lumped" element mass matrices. The equations of motion for the body and for the acceleration are integrated through time, using the central difference integration rule [11] that calculates the change in velocity assuming that the acceleration is constant. This change in velocity is added to the velocity from the middle of the previous increment to determine the velocities at the middle of the current increment:

$$\dot{u}|_{(t+\frac{\Delta t}{2})} = \dot{u}|_{(t-\frac{\Delta t}{2})} + \frac{\left(\Delta t|_{(t+\Delta t)} + \Delta t|_{(t)}\right)}{2}\ddot{u}_{(t)} \tag{7.19}$$

The initial half-step lagging velocity is calculated from the initial velocity, assuming the initial acceleration is constant over the lagging half-step. The calculated velocities will then be added to the displacements at the beginning of the increment to determine those at the end of the increment [11]:

$$u|_{(t+\Delta t)} = u|_{(t)} + \Delta t|_{(t+\Delta t)}\,\dot{u}|_{(t+\frac{\Delta t}{2})} \tag{7.20}$$

The explicit integration operator is conditionally stable, where the time step is subjected to a limitation via Eq. (7.17), which requires no iterations and no tangent stiffness matrix [12].

For nonlinear problems, the computational efficiency of the explicit procedure is based upon the critical time step of the time incrementation scheme. The critical time step depends upon:

$$\Delta t = \frac{L_e}{c_d} \tag{7.21}$$

where L_e is the element dimension and c_d is the dilatational wave speed of the material.

7.3 Modelling of Impact Attenuator

The commercial FE program, ABAQUS [13], was adopted for modelling of crash between the attenuator and the rigid barrier as described in the physical experimental testing. In order to model the crash for this experiment, nonlinear behaviour in material and geometry was considered.

7.3.1 Geometry Models

The geometry of the crash attenuator is shown in Fig. 7.4, where the smaller circular cut-outs have diameters of 50 mm and the larger cut-outs have 60 mm. The cut-outs have also been strategically placed to initiate buckling while also reducing the structure's weight. With the cut-outs, it can be predicted that the initial crumple zone will form closer to the rear of the structure because the moment created during impact will be greatest in this area, combined with the fact that this cross section has the largest amount of removed material and, therefore, will carry the highest stresses during impact.

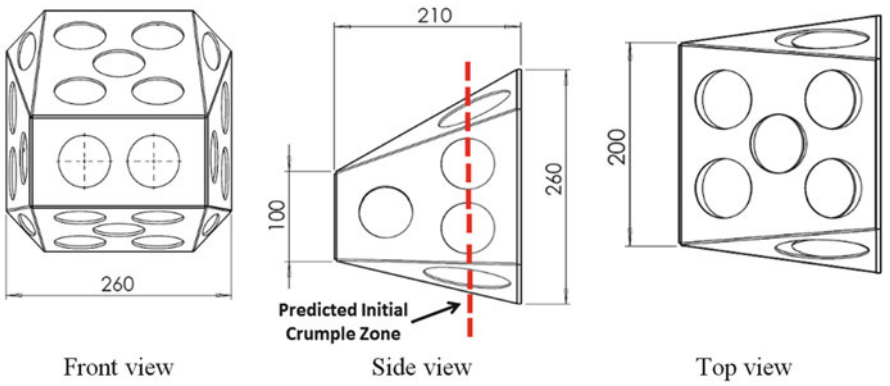

Fig. 7.4 Geometry description of the impact attenuator

7.3.2 Material Models

The material used in the structure is commercially available 5083-H321 aluminium plate. A 4 mm section has been utilized for the base and 3 mm sections for the protruding sections that undergo deformation. This material features high, corrosive resistance and is easily welded and provides a light-weight alternative for the racing setting [2]. The aluminium plate was modelled as an elastic plastic material. It was expected that work hardening of the material would play a significant role in a real world model, and so the material's work-hardening properties would have to be included in the computational model. The material work hardening is described by [14]:

$$\sigma_f = K\left(\varepsilon^{pl}\right)^n \tag{7.22}$$

where Young's modulus, $E = 70.3$ GPa, Poisson's ratio, $\nu = 0.33$, initial yield stress $= 315$ MPa, constant, $K = 550.4$ MPa, constant, $n = 0.223$, density $= 7{,}833$ kg/m^3.

7.3.3 Boundary Conditions and Loadings

For this analysis, the impact attenuator was positioned 1 mm away from a discrete rigid wall. As noted earlier, the test is required to simulate the crash structure's effectiveness as if it were attached to a 300 kg vehicle travelling at 7 ms^{-2}. Hence, the impact attenuator simulates attachment to a chassis of mass 300 kg by using a point mass, which is located in the centre of the mass of the chassis. The centre of the point mass was fixed at a reference point, which was coupled to the rear face of the attenuator that allows even dissipation of the kinetic energy over the model's dimensions.

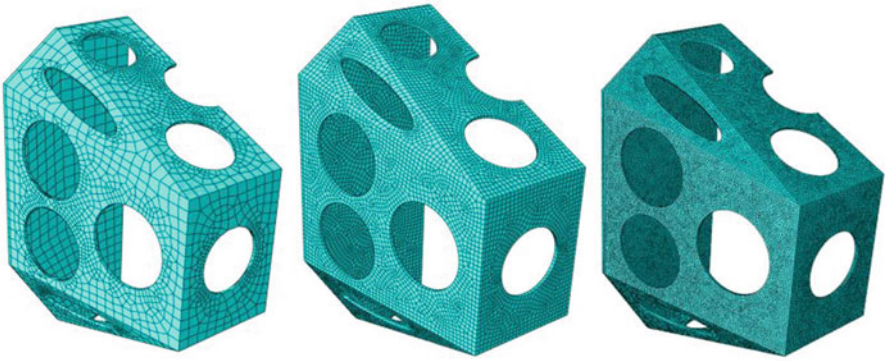

Fig. 7.5 Mesh convergence studies with course, medium and fine mesh size.

The predefined fields were used to prescribe the initial velocity of the structure and the mass at 7 ms^{-1} moving towards the discrete rigid wall. The boundary conditions of the rigid wall were fixed in all degrees of freedom; the attenuator and point mass were free to move only in the *Z*-direction. Symmetric constraints are imposed on the symmetric plane of the model to reduce the computational time.

7.3.4 Contact Modelling

The surface-to-surface contact approach was used for discretizing the contacting surfaces between the rigid wall and the attenuator. The penalty contact algorithm available in ABAQUS/Explicit was used to enforce the contact constraints. The commonly used Coulomb model that assumes a constant coefficient of friction of 0.45 was used to describe the friction between the contacting surfaces.

7.3.5 Mesh Convergence Study

A mesh convergence study was carried out to choose the appropriate mesh size. Several mesh sizes of the attenuator were performed (Fig. 7.5) to ensure the mesh model is accurate enough to produce reliable results for the energy absorption behaviour and deformations of the attenuator. The mesh convergence studies showed that the force-displacement response at the contact point was almost convergent for mesh size 5 mm. Therefore, it was decided to select a medium mesh size, with dimensions of 5 mm × 5 mm mesh, for the mesh of the whole structure. With these considerations, 18,619 elements were used for the attenuator.

7.4 Experiment Sled Test

The sled apparatus used in the physical test consisted of a steel channel welded to provide a rigid face to attach the attenuator (Fig. 7.6). This was then bolted to a thick plate with rear re-enforcements to increase rigidity. The remainder of the 300 kg required for the simulation was added in the form of attachable weights bolted to the base plate behind the crush zone. An accelerometer was placed behind the steel plate to capture the deceleration data. A high-speed camera was also used to capture the deformation of the attenuator during the crash. The physical test was conducted at the APV Engineering and Testing Services, which is fully accredited for impact testing. The sled test and attenuator before and after deformation are shown in Fig. 7.7.

7.5 Results

7.5.1 Time History Plot

Data and high-speed photographs from the physical test were used to verify the results obtained from the computer simulations. Figure 7.8 shows the comparison of the simulation results, in terms of acceleration-time curves, with those from the physical experiments conducted at APV Engineering and Testing Services.

Fig. 7.6 The sled apparatus used in the crash test

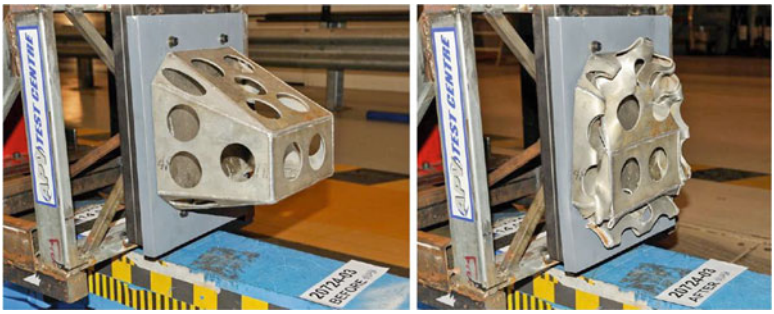

Fig. 7.7 The impact attenuator before and after the crash testing

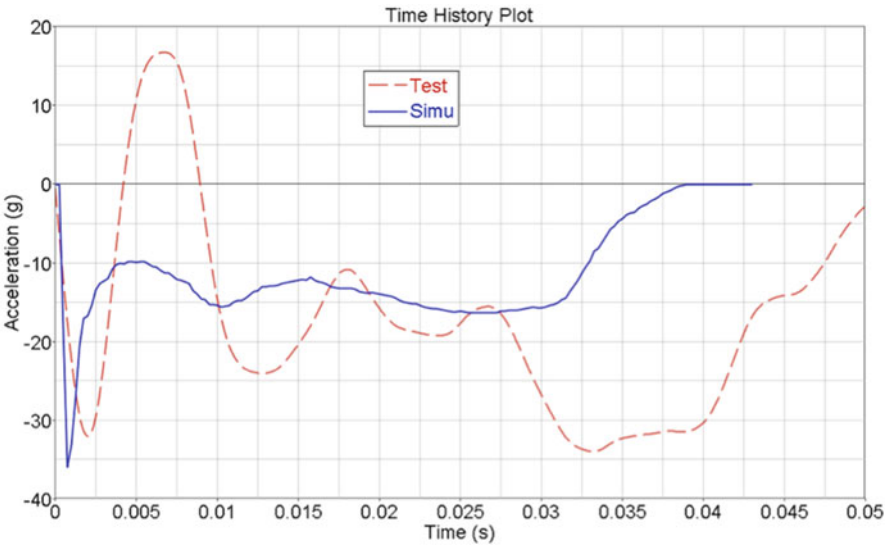

Fig. 7.8 Experimental (*red line*) and simulated (*blue line*) acceleration-time responses of the attenuator impacts against a rigid barrier

The model response correlated well with the experimental results: the contact timing, slopes of the loading, and peak accelerations of the attenuator model in the simulation were consistent with those in the physical tests. However, the model gave poor results for the unloading phase and folding of the attenuator's structure after 0.5 ms when compared with the experimental results. The finite element predictions for the first and second peak axial crush accelerations were 35 and 15 g; the corresponding experimental values were 32 and 24 g. The energy absorbed by impact attenuator model was 12 kJ, compared with 7.4 kJ in the experiment.

7.5.2 *Deformation and Energy Absorption of the Attenuator*

Figure 7.9 shows the deformation of the attenuator in the physical test and in the numerical modelling. When the attenuator made initial contact with the rigid barrier during the impact test, the flat front face of the aluminium structure caused a small contact area of the attenuator to be compressed (Fig. 7.9). When the attenuator continued moving toward the rigid barrier, the material around the circular cut-out on the bottom surface was highly stressed and compressed (Fig. 7.9), which caused the bottom face's material to buckle and deform. Immediately after the bottom face material collapsed, the top surface started to deform (Fig. 7.9). The attenuator continued to deform until the whole structure collapsed completely (Fig. 7.9). The results of FE analysis and experiment were in agreement.

The initial crumple zone is designed to initiate buckling, and the maximum stress of 450 MPa was observed as in Fig. 7.9. As soon as the material started to buckle, it caused instability in the neighbouring structure. In this case, the folding collapse started and spread to the neighbouring structure until it bottomed out (Fig. 7.9).

7.6 Discussion

Nonlinear analyses of the FSAE impact attenuator were carried out with ABAQUS explicit code, which simultaneously considered two nonlinearities: material nonlinearity (plastic behaviour), and geometric nonlinearity (changing in contact conditions and large displacements). The dynamic contact between the rigid barrier and the attenuator was modelled using the surface-to-surface contact interaction. Self-contact was also included as it is necessary for simulating collapsing structures.

The mesh density applied to the deformable crash structure had a large impact on the accuracy of the results. A high mesh density or "fine mesh" will provide the most accurate results but at the expense of large computational costs; a low mesh density or 'coarse mesh' will provide less accurate results but at a relatively low computational cost. Therefore, a mesh convergence study was conducted to find an acceptable compromise between the accuracy of the simulations results and the computational cost.

The attenuator model was validated using physical impact test data. Good correlations were observed between the simulated and experimental acceleration-time responses; however, poor results were observed for the unloading phase and folding of the attenuator's structure after the first peak. The dynamic finite element analysis initially predicted a much stiffer behaviour of the attenuator than that observed by the experiment. As the deformation progressed and the attenuator underwent significant deformation, the difference between the FE prediction and the experimentally observed behaviour became more evident (Fig. 7.8). The discrepancies in the results may be attributed to the inaccuracies in the geometry of the attenuator model. The position and size of the cut-outs varied slightly because

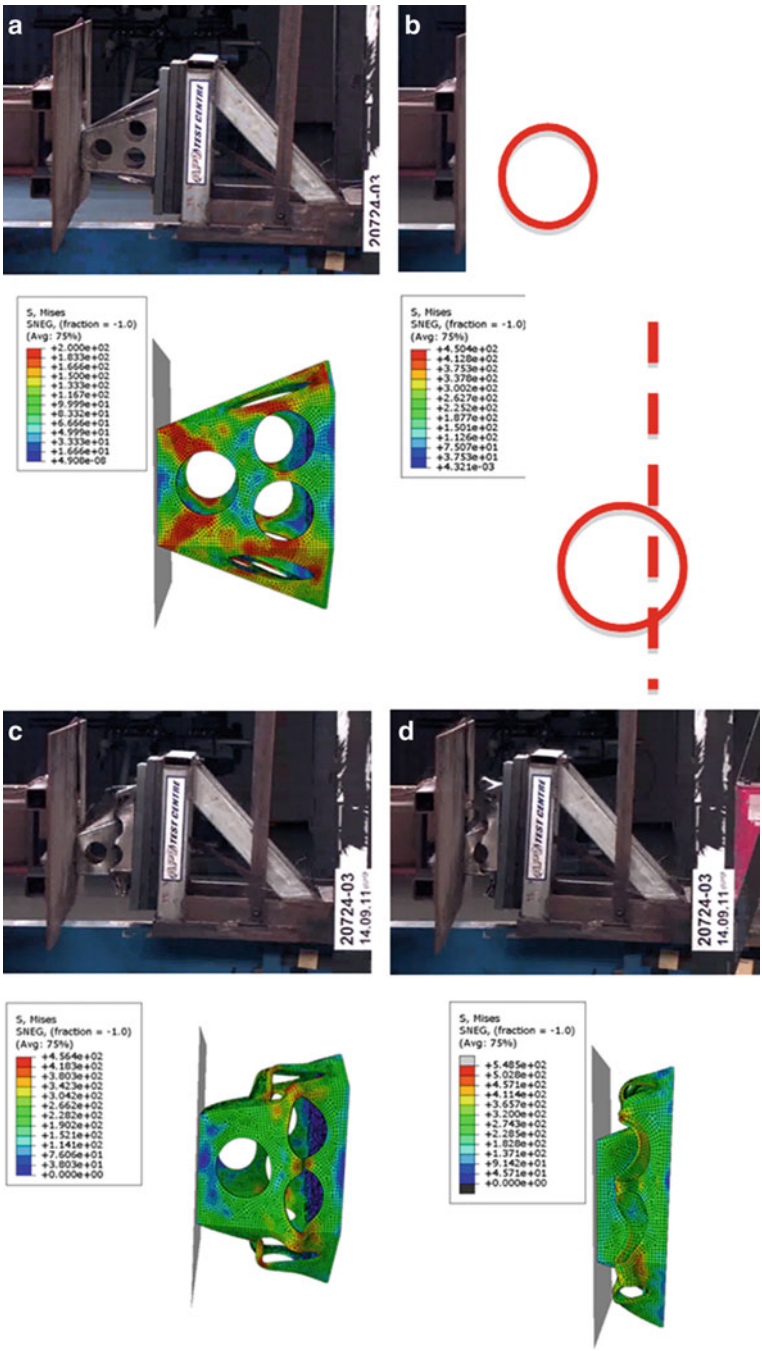

Fig. 7.9 Deformation and von Mises stress contours of attenuator as compared with physical sled test

the computational geometry was a re-creation of the attenuator used in the sled test. Again, the differences between the physical and computational models were small.

The aluminium plate was modelled during the crushing process as an elastic–plastic material with work-hardening properties. The aluminium's plastic material properties were chosen to conform to the literature [14–17]; hence, it was expected that the theoretical material properties would be quite different from findings in previously reported physical experiments [14–17]. Although it is known that the finite element material properties approximate a real engineering structure [18], they were deemed acceptable for the purposes of this study. The attenuator model did crush and collapse in a similar way seen in the physical sled test (Fig. 7.9).

7.7 Summary

The dynamic response of an impact attenuator during the crash test is highly nonlinear due to the elastic–plastic behaviour of the aluminium material and large deformation of the structure during contact. A nonlinear dynamic finite element with a reasonable mesh size was used to estimate the dynamic response and energy absorption of the attenuator model. The finite element results were verified by comparing the simulated results with the physical sled test. The simulation and experimental results agreed on the collapsing behaviour and the buckling location of the attenuator. However, there were discrepancies between the simulation and experiment results; hence, further investigations are needed to refine the model in terms of material definition and geometry description.

Acknowledgements This experiment and design were based on works supported by the RMIT University 2011 Formula SAE team. The authors would like to thank Daniel Tonini for his contribution in this study.

List of Symbols

τ_1, τ_2	Time instant
$\delta E\alpha$	Virtual kinetic force
$\delta T\alpha$	Internal force
$\delta W\alpha$	External forces
V	Volume occupied by a part of the body in the current configuration
S	The surface bounding in the volume
ρ	Material density
$f^{(V_\alpha)}$	Externally applied forces per unit volume
$f^{(S_\sigma^{(\alpha)})}$	Externally applied surface traction per unit surface area
σ	Cauchy stress tensor field
ε	Conjugate strain tensor

u	Displacement
$\ddot{u}$	Accelerations
$\bar{u}$	Velocities
$\delta \prod_{\alpha}^{cont}$	Virtual contact work
δ	Arbitrary, virtual and compatible variation
$\delta \bar{g}_N$	Variation in gap
δg_T	Variation in tangential displacement
g_N	Gap
g_T	Relative displacement in a tangential direction
$\bar{g}_T$	Relative sliding velocity
t_T	Tangential stress vector
t_N	Contact force
τ_{crit}	Threshold of tangential contact traction for tangential slip
ε_N	Penalty parameter
$\bar{n}^1$	Normal vector
$\bar{x}^1$	Deformation of the master surface
X^2	Deformation of the slave surface
$\mathrm{S}_c^{(1)}$	Master surface
$S_c^{(2)}$	Slave surface

References

1. SAE International (2010) 2011 Formula SAE® Rules, USA
2. Askeland DR, Phule PP (2006) The science and engineering of materials, 5th edn. Thompson, Toronto
3. Asano N (1981) Principle of virtual work for two elasto-impact bodies in separate state and its application to finite element method. Bull JSME 24:1123–1129
4. Asano N (1983) Virtual work principles for two elastoimpact contact bodies. Bull JSME 26:1687–1695
5. Wriggers P (2002) Computational contact mechanics. Wiley, West Sussex
6. Jiang L, Rogers RJ (1988) Combined Lagrangian multiplier and penalty function finite element technique for elastic impact analysis. Comput Struct 30:1219–1229
7. Vulovic S, Zivkovic M, Grujovic N, Slavkovic R (2007) A comparative study of contact problems solution based on the penalty and Lagrange multiplier approaches. J Serbian Soc Comput Mech 1:174–183
8. Weyler R, Oliver J, Sain T, Cante JC (2012) On the contact domain method: a comparison of penalty and Lagrange multiplier implementations. Comput Methods Appl Mech Eng 205–208:68–82
9. Wu SR (2009) A variational principle for dynamic contact with large deformation. Comput Methods Appl Mech Eng 198:2009–2015
10. Wang F-J, Wang L-P, Cheng J-G, Yao Z-H (2007) Contact force algorithm in explicit transient analysis using finite-element method. Finite Elements Anal Design 43:580–587
11. Dassault Systèmes (2010) Abaqus 6.10 theory manual. Dassault Systèmes Simulia Corp., Providence
12. Choi HH, Hwang SM, Kang YH, Kim J, Kang BS (2002) Comparison of implicit and explicit finite-element methods for the hydroforming process of an automobile lower arm. Int J Adv Manuf Technol 20:407–413

13. Simulia Inc. (2010) ABAQUS/Explicit user's manual. Version 6.10. Dassault Systèmes, Providence, RI
14. Mahmudi R (1997) Stress-state dependence of work-hardening behavior in aluminium alloy sheet. J Mater Process Technol 72:302–307
15. Akbarpour MR, Ekrami A (2008) Effect of ferrite volume fraction on work hardening behavior of high bainite dual phase (DP) steels. Mater Sci Eng A 477:306–310
16. Isaac Samuel E, Choudhary BK (2010) Universal scaling of work hardening parameters in type 316L(N) stainless steel. Mater Sci Eng A 527:7457–7460
17. Zare A, Ekrami A (2011) Effect of martensite volume fraction on work hardening behavior of triple phase (TP) steels. Mater Sci Eng A 528:4422–4426
18. Bathe KJ (1996) Finite element procedures. Prentice Hall, Upper Saddle River

Chapter 8
Nonlinear Vehicle Seat BSR Characterization Using CAE Methodology

M. Tatari, M. Fard, N. Nasrollahzadeh, and M. Mahjoob

Abstract The noise and vibration of a poor automotive seat aggravate the interior cabin noise and discomfort. The automotive seat structural noise and vibration is caused by the transmission of the power train or road vibration into the seat. The characterization of seat structural dynamics behavior in early design phase assists to effectively improve the NVH quality of the seat. The seat nonlinear buzz, squeak, and rattle (BSR) noise are the major issues which are directly linked to the NVH quality of the vehicle. For this purpose, a practical CAE (computer-aided engineering) concept modeling method is introduced and developed for full BIW (body-in-white) and seat separately. Here, the seat concept model is employed to allow designing the seat structure modifications as well as examining the effects of the modifications on the rattle noise. Comparisons of the results of the simulation and experiment validate the developed seat CAE model. Three modifications are proposed to optimize the dynamics of the seat structure to prevent the seat rattle noise. These modifications are designed to shift or decrease the seat torsion resonance and vibration level, respectively. The results verified that by modification the seat structural dynamics, the nonlinear events such as rattle noise and in general BSR noise can be reduced or controlled accordingly.

M. Tatari • N. Nasrollahzadeh • M. Mahjoob
School of Mechanical Engineering, College of Engineering,
University of Tehran, Tehran, Iran
e-mail: m.tatari@ut.ac.ir; n.nasrolahzadeh@ut; mmahjoob@ut

M. Fard (✉)
School of Aerospace, Mechanical and Manufacturing Engineering,
RMIT University, Melbourne, VIC 3083, Australia
e-mail: mohammad.fard@rmit.edu.au

R.N. Jazar and L. Dai (eds.), *Nonlinear Approaches in Engineering Applications 2*,
DOI 10.1007/978-1-4614-6877-6_8,

8.1 Introduction

Squeak and rattle in the automobile industry are terminologies to describe short duration transient noises that are generated by the relative motion or impacts between vehicle parts. In other words, in general, BSR noise is a high frequency audible phenomenon resulting from two distinct forms of noise: (a) caused by friction between elements under forced road excitation (buzzes, squeaks) and (b) caused by loose or overly flexible elements with the potential for impact with other elements (rattles). The mechanisms involved in generating squeak and rattle noise are mainly nonlinear. This nonlinearity and complexity make it very difficult to simulate in a CAE analysis. Therefore, there are no predictive CAE tools available in the industry thus far. Most CAE methods focus on preventive tools. Some researches in the squeak and rattle preventive methods [1, 2] have been established at Ford in past years. But here, it is shown that there is a strong link between the structural dynamics and the rattle noise so that the rattle noise can be predicted and controlled from the structural analysis in early design phase.

The vehicle seat BSR (buzz, squeak, and rattle) noise is one of the major issues which is directly linked to the NVH (noise, vibration, and harshness) quality of the vehicle. Predicting and improving the seat BSR noise in early design phase is still challenging. This is mainly due to the complexity, nonlinearity, and uncertainty of the impact mechanism at joints contributed to the rattle. Controlling BSR is becoming essential with the trend toward using lightweight materials combined with the increase in number of the seat sub-components such as electronic gadgets [3]. According to a market survey, squeaks and rattles are the third most important customer concern in cars after 3 months of ownership [4]. Furthermore, upcoming electric cars will highlight the importance of the BSR issues [5]. BSR is generally caused by loose or overly flexible elements under excitation. Modern advances in the vehicle noise and vibration control engineering have reduced the transmission of the vibration or noise from different sources such as powertrain or road into the passenger cabin [5]. Predicting and controlling BSR in the early design phase is important to be investigated (Hagiwara and Ma 1992 [14]). As for rattle simulation, it includes complicated periodical nonlinear impact and needs a special CAE model to directly simulate these phenomena [6]. Finite element analysis is almost utilized in analyzing the vibratory dynamics of these systems, though the full nonlinearity of the problem with the transient impacts is not accounted for the analysis. In the above analysis the resonant frequencies and mode shapes from the linear finite element model are used to extract the local dynamics of the components in terms of a simple multi-degree of freedom spring mass model. Then, characterization of the seat dynamics is the based method for predicting and controlling of the BSR noise.

The use of computer-aided engineering can be considered as a useful tool for BSR detection in the early design phase. However, BSR is not easily evaluated by CAE methods due to its wide range of causes and the inherent complexity of the related problems; but those BSR noises that emanating from the structural vibrations

can easily be identified and controlled. In the past, vehicle product evaluation from the BSR perspective was so time- and cost consuming, but, nowadays, with the technological advancement CAE models are the fast tool in the NVH analysis. Despite the fact that automotive advanced CAE model is developed by detailed and accurate geometry data, concept model can be created in early design phase where there is no enough detailed and constrained design data. For accurate NVH analysis, one needs a fairly simple but reliable concept model to identify and predict dynamic behavior of the structures. Recently, several methodologies have been developed for automotives concept modeling [7, 8]. The common objective of all these methodologies is to enhance functional performances in order to shorten the vehicle development and time-to-market process. BSR noises can be managed and controlled by modification of this concept model in virtual domain and then implemented in practice. The basic idea of this tool is to find the location of seat resonant frequencies and its corresponding structural mode shapes. Experimental test setup is designed to measure the seat radiated noise when it goes under vibration excitation.

This chapter shows that the seat rattle noise can be predicted and controlled in early design phase by managing the seat structural dynamics. Experiments are designed to first characterize the seat resonant frequencies/mode-shapes and second to measure the seat rattle noise. It is shown that the rattles of the seat components can be reduced by modifying the seat structural dynamics. Such upfront knowledge about the seat rattle can greatly assist to provide robust solutions for preventing or controlling the seat rattle in early design phase [5]. The structural dynamics of the seat is also characterized by using the developed CAE (computer-aided engineering) model of the seat [9]. The concept modeling method is used for the CAE modeling of the seat structure [7, 8]. The model is developed to allow us to probe the effects of seat-structure modifications on the rattle noise. Comparisons of the results of the simulation and experiment validate the developed CAE model. The experiment and simulation results show that the seat has two structural resonances in low frequency range (<50 Hz); one at around 31 Hz, which is the seat torsion and the other at around 48 Hz, which is the seat fore-aft bending. The noise measurement result reveals that the seat generates high level of the rattle noise when the seat excitation vibration is close to the seat structure torsion resonance (31 Hz). We have further confirmed that the occurrence of the rattle is related to the seat structural dynamics and it can be controlled by modifying the structure. Three modifications are proposed by using the seat CAE model. One modification is frequency shifting by increasing the stiffness of such members. Another modification is done by sensitivity analysis. Sensitivity analysis indicates which members have an important role in the torsion mode. Last modification is dynamic damper. The vibration level is reduced by using this type of damper. It can be concluded that by changing the seat resonant frequencies, the rattle noise and in general BSR noise can be changed accordingly. Consequently, for the seat system which has an identifiable structural dynamics, the BSR noise can be managed and controlled in early design phase by using the seat CAE model. Furthermore, such early phase modifications of the seat

structure are more robust than merely tuning the joints associated with BSR. In fact, the proposed modifications of the structure control the seat resonances and therefore transfer less vibration into the sub-components which are vulnerable to rattle.

8.2 CAE Simulation and Concept Modeling

In order to create a concept model, the first step is to decide about the layout and functional components of the structure [10]. Generally, in concept modeling three major parts should be simplified and modeled.

8.2.1 Beam-Like Structures

The most primary parts are beam-like structures or main members that define the frame body of the vehicle. Beam-like components are those members that have small cross sections in comparison with their lengths. Main members of the BIW such as doorsill, pillars, and the frame of seat structure are modeled using beam elements. Since the shape of the cross sections is considered similar to the corresponding sections at the physical model, calculated properties of the beam elements such as bending and torsional moments of inertia reflect good approximation in accordance with real members. The cross section of 1D elements is created approximately like real members by accounting the effect of all shell elements (outer skin and inner reinforcements) involving beam-like structures. Concept and advanced model of a beam-like structure is shown in Fig. 8.1.

Beam-Like Structure Cross Section Properties

In order to compute the cross section properties, at first we need centroid coordinate. Then moment of inertia about the centroid axes will be calculated. This moment will be transformed to the global centroid coordinate set using coordinate axes

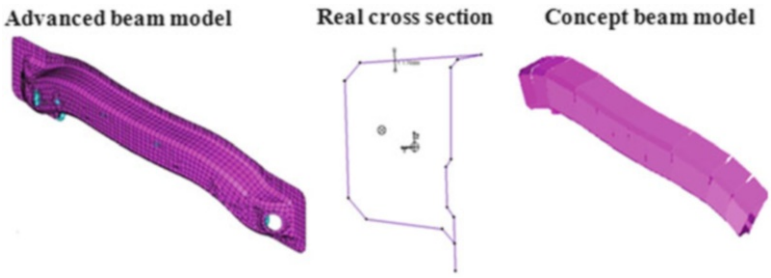

Fig. 8.1 Detailed model (*left*) and concept model of a selected beam (*right*)

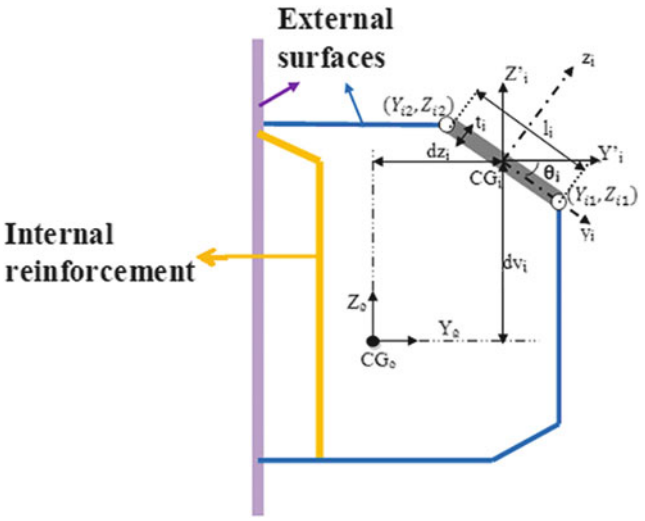

Fig. 8.2 Selected beam cross section and needed geometrical data to calculate its properties

rotation laws. Finally the transmission law is employed to compute each moment of inertia separately. The mentioned procedures are conducted in MATLAB software. In this section these properties are derived with parametric formula for arbitrary cross section depicted in Fig. 8.2.

- Centroid coordinate:

$$Y_O = \frac{\sum \frac{Y_{i1}+Y_{i2}}{2} t_i l_i}{\sum t_i l_i} \tag{8.1}$$

$$Z_O = \frac{\sum \frac{Z_{i1}+Z_{i2}}{2} t_i l_i}{\sum t_i l_i} \tag{8.2}$$

- Specify local coordinate axes and their angles to global coordinate axes:
- Cross section area calculation and i_{th} section moment of inertia:

$$A_i = t_i l_i \tag{8.3}$$

$$Iyy|_i = \frac{1}{12} t_i \, l_i^3 \, Izz|_i = \frac{1}{12} l_i \, t_i^3 \tag{8.4}$$

$$I_{Z_i}{}' = \frac{Izz|_i + Iyy|_i}{2} + \frac{Izz|_i - Iyy|_i}{2} \cos(2\theta) \tag{8.5}$$

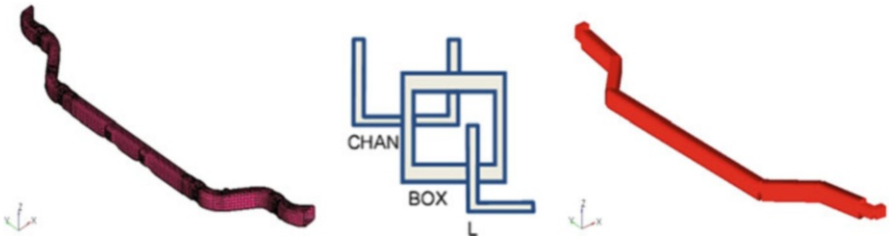

Fig. 8.3 Beam-like structures modeling using standard profiles in the library of finite element software

Fig. 8.4 Sample standard cross section

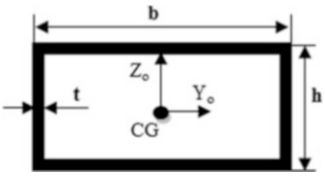

$$I_{Y_i}{}' = \frac{Izz|_i + Iyy|_i}{2} - \frac{Izz|_i - Iyy|_i}{2}\cos(2\theta) \tag{8.6}$$

$$I_{ZY_i}{}' = \frac{Izz|_i - Iyy|_i}{2}\sin(2\theta) \tag{8.7}$$

- The contribution of i_{th} section moment of inertia about centroid:

$$I_{Y_o^i} = I_{Y_i'} + A_i d_{yi}^2 \quad and \quad I_{Y_O} = \sum_i I_{Y_o^i} \tag{8.8}$$

$$I_{z_o^i} = I_{Z_i'} + A_i d_{Zi}^2 \quad and \quad I_{Z_O} = \sum_i I_{Z_o^i} \tag{8.9}$$

$$A_O = \sum_i A_i \tag{8.10}$$

Standard Cross Sections Deficiency

Although previous researches didn't mention to the selection procedure of the beam-like cross sections, it is not easy to have a standard section that satisfies all the properties of original one. In other words, it's only possible for members like Fig. 8.3 that has a standard cross section. Usually we need to neglect one cross section property (product moment of inertia); because of symmetrical geometry this property is equal to zero. For a special case and make it clear to you, using a rectangular profile with thickness t (Fig. 8.4), three principal properties of a cross section (I, J, A) will be calculated. For this reason the Eq. (8.11) must have real answers ($t \ll b, h$).

$$\begin{cases} 2t\left[(b-t)+(h-t)\right] = A_O \\ 1/12(bh^3 - \left((b-2t)\,(h-2t)^3\right) = I_{Y_O} \\ 1/12(hb^3 - \left((h-2t)\,(b-2t)^3\right) = I_{Z_O} \end{cases} \tag{8.11}$$

Though the calculation of the moment of inertia in accordance with the above equation is possible, considering the torsional moment of inertia in this equation makes it more complicated. For beams with arbitrary cross sections, calculation of the moment of inertia in accordance with Eqs. (8.12) and (8.13) will be complicated. Furthermore, if you can compute that, it is rare to find standard cross section that satisfies all calculated properties. One reason is that torsional moment of inertia (and warping function) heavily depends on the shape of cross section. Above materials show deficiencies of standard cross sections and make clear advantages of arbitrary cross sections.

$$\mathrm{J} = \mathrm{I_Y} + \mathrm{I_Y} - \int_{\mathrm{A}} \left(\mathrm{Z}\frac{\partial \varphi}{\partial \mathrm{y}} - \mathrm{y}\frac{\partial \varphi}{\partial \mathrm{z}}\right) \mathrm{dA} \tag{8.12}$$

In Eq. (8.12) $\varphi\,(\mathrm{y}, \mathrm{z})$ is warping function that can be computed based on the elasticity theory from the differential equation (8.13). $\mathrm{n_z}$ and $\mathrm{n_y}$ are normal unit vector of the beam cross section.

$$\begin{aligned} &\frac{\partial^2 \varphi}{\partial \mathrm{y}^2} + \frac{\partial^2 \varphi}{\partial \mathrm{z}^2} = 0 \\ &\left(\frac{\partial \varphi}{\partial \mathrm{y}} - \mathrm{z}\right) \mathrm{n_z} + \left(\frac{\partial \varphi}{\partial \mathrm{z}} - \mathrm{y}\right) \mathrm{n_y} = 0 \end{aligned} \tag{8.13}$$

8.2.2 Joints Modeling

Joints are in secondary order of importance and they connect beam-like structure to each other. Panels are other major components that perfect the layout of the structure. In NVH concept modeling analysis, preparing the concept joints is a critical issue. Usually, model reduction methods (static or dynamic) are exploited to reduce the FE model computation time and cost. According to the characteristics of the model and analysis requirements, an appropriate model reduction method [11] such as Guyan, CMS, and SEREP has to be selected. Then the large FE model is condensed in a few degrees of freedom by the method specified transformation matrix (TC) according to Eqs. (8.14)–(8.16), where subscripts A is representative of all DOFs, subscripts i stands for the DOFs that are going to be omitted, and subscripts b are those that will be kept after model reduction [10]. Since the concept joints connect the concept beam-like structures (1D beam elements) to each other in their terminal nodes, the detailed joints are condensed into a reduced description of the stiffness and mass matrices at the boundary nodes.

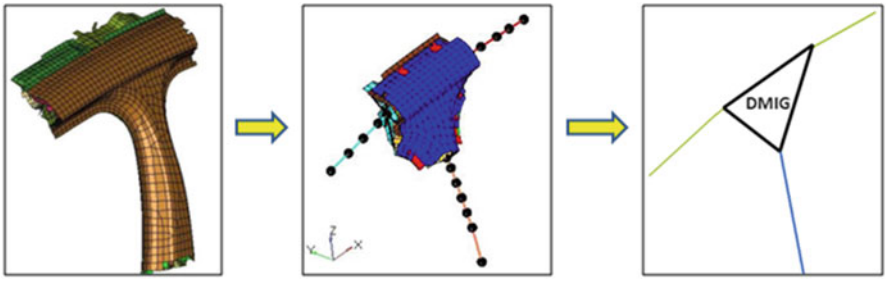

Fig. 8.5 Steps of reducing detail model joint to concept condensed joint in order to connect beam elements

$$\{x_A\} = \begin{Bmatrix} x_i \\ x_b \end{Bmatrix} = [T_{Condensation}]\{x_b\} \tag{8.14}$$

$$[K_C] = [T_C]^T [K_A][T_C] \tag{8.15}$$

$$[M_C] = [T_C]^T [M_A][T_C] \tag{8.16}$$

Here, both Guyan [11] and CMS[1] [12] model reduction are tested for reducing and generating concept joints; the results for both have a little discrepancy in low frequency range. Therefore, as the aim of the concept modeling is focusing on global modes of the structure that are usually below 100 Hz, Guyan method is used to prepare concept joints. Neglecting the inertia effects in calculating reduced model, Guyan method is also called static condensation. Equation (8.17) is the general form of the static finite element model, in which the internal and boundary DOFs are reordered to make the calculation process straightforward. Then by a little manipulation on block rows of this equation [11], the Guyan condensation matrix (TG) can be extracted according to Eq. (8.18).

$$\begin{bmatrix} K_{ii} & K_{ib} \\ K_{bi} & K_{bb} \end{bmatrix} \begin{Bmatrix} x_i \\ x_b \end{Bmatrix} = \begin{Bmatrix} F_i \\ F_b \end{Bmatrix} \tag{8.17}$$

$$[T_G] = \begin{bmatrix} [-{K_{ii}}^{-1} K_{ib}] \\ [I_{bb}] \end{bmatrix} \tag{8.18}$$

The procedures of converting advanced joint model to concept joints are illustrated in Fig. 8.5.

[1]Component mode synthesis.

Table 8.1 The effects of the important panels on the BIW torsional stiffness (W/O denotes "without")

	W/O roof panel	W/O front windshield	W/O rear windshield	Final concept model
Torsion resonant frequency	36.21 Hz	39.99 Hz	44.04 Hz	48.82 Hz

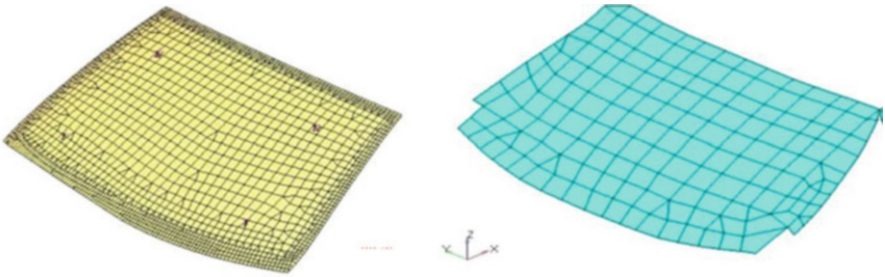

Fig. 8.6 The detailed or advanced (*left*) and the concept model (*right*) for the front windshield

8.2.3 Panels Modeling

Although most of the panels have a decisive role on the automotive structural dynamics at high frequencies (>100 Hz), efficacy of the special panels such as the roof and the platform tunnel in vehicle body cannot be neglected. In other words, BIW structural mode shapes and resonance frequencies are directly linked to such panels [13]. Table 8.1 investigates the influence of the roof panel, front windshield, and rear windshield in the first torsion mode of BIW.

The concept panels are simply created using shell elements (2D elements) by some principal nodes of the real panel provided that the shape of the panel is approximately kept. Figure 8.6 depicts the concept panels of the front windshield of the BIW. Finally the attachment of panels and beams is conducted by interpolation and rigid elements (e.g., RBE2 and RBE3 in NASTRAN [14]).

8.2.4 BIW Concept Modeling

In order to construct the BIW concept model, 45 different beam properties with similar cross section properties (correspond to advanced CAE model) are created. The main members of the platform, engine compartment, front and rear bumper reinforcements, pillars, rail roofs, etc. are modeled with 1D elements.

In addition, by taking advantages of the Guying reduction, 20 concept joints (DMIG Superelements) are employed to make developed BIW concept model as similar and reliable as possible to the advanced CAE model. Moreover, panels

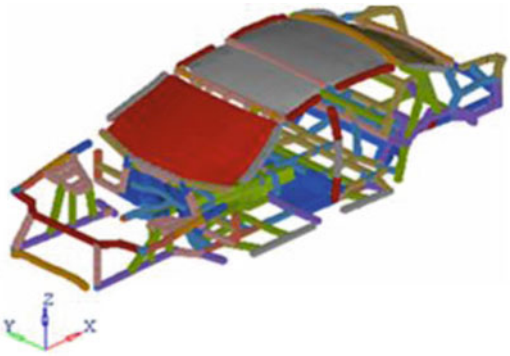

Fig. 8.7 BIW concept model

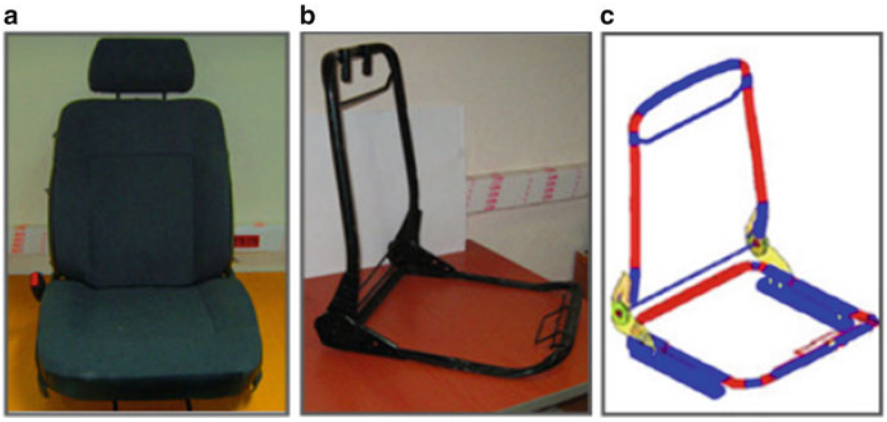

Fig. 8.8 The vehicle seat used in this research (**a**), the main frame of the seat structure (**b**), and its CAE concept model (**c**)

such as roof, platform tunnel, front windshield, and rear glass are simply created with rough enough 2D shell elements and added to concept beam and joints. It is important to note that RBE2 and RBE3 elements have been used to combine beams and shell elements in the BIW concept modeling. Figure 8.7 demonstrates the BIW concept model.

8.2.5 The Seat Concept Modeling

A selected vehicle seat (Fig. 8.8) is modeled by using above FE methods and CAE techniques. The model of the seat must be correlated with its corresponding test data and it will be used instead of the seat. In other words, the model is developed to characterize the major seat structural dynamic behaviors such as resonant frequencies and corresponding mode shapes [14].

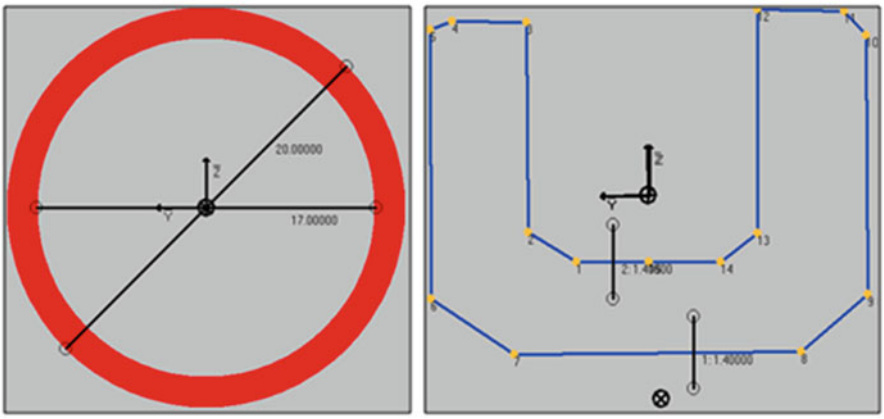

Fig. 8.9 The standard (*left*) and nonstandard (*right*) sample cross section in the seat structure modeling

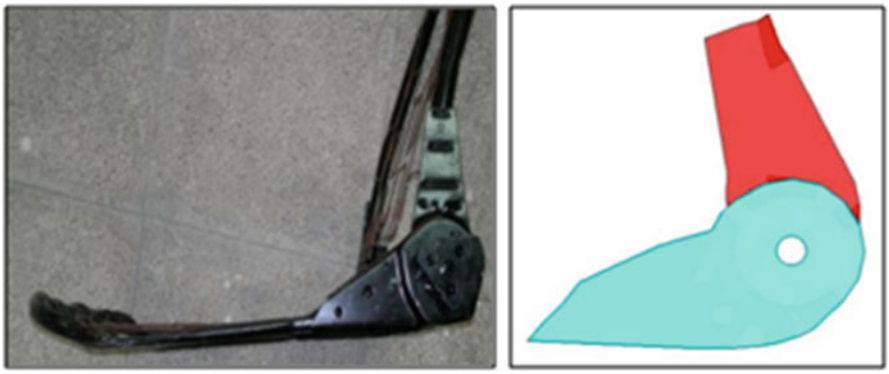

Fig. 8.10 The real (*left*) and modeled joint (*right*)

The cross sections of 1D elements include both standard and nonstandard cross section and are calculated approximately like real members by accounting the effect of all shell elements involving beam-like structures. The samples of these cross sections are shown in Fig. 8.9.

The main joint of the seat structure and its model (with detailed) are illustrated in Fig. 8.10.

Seat rails and structure are attached to each other using interpolation elements (RBE in Nastran). This is mainly due to that, when we use node to node connection, seat structure stiffness is increased dramatically. Figure 8.11 shows this attachment in detail.

It is important to note that 2D elements have been employed to model the concept joint. Steel properties have been used in modeling as listed in Table 8.2.

Fig. 8.11 Physical and finite element model of the seat, rails and structure conjunction is conducted via RBE element

Table 8.2 Steel properties in concept model

Young modulus	210 MPa
Poisson's ratio	0.3
Density	7.9×10^{-6} kg/mm^3

Table 8.3 Information of the advanced and concept model for the seat structure

Advanced model information	Numbers	Concept model information	Numbers
2D shell element	10792	1D beam element	554
1D beam element	50	Interpolation and rigid element	36
Concentrated mass	20	Concentrated mass	24
Spot weld element	360	Super element	2
Weight	7.120 kg	Weight	7.156 kg
Solution time	3 min	Solution time	20 s

Taking all the above-mentioned materials about concept modeling into consideration, a concept model for the seat structure is derived. The seat members such as back rest, side members are simplified using beam modeling approximation. In addition, by taking advantages of the Guyan reduction, two concept joints (DMIG Superelements) are employed to make developed seat concept model as easy and reliable as possible. Weight of the structure is about 7,156 g. The seat structure and its concept model are demonstrated in Fig. 8.8. As a result of the seat concept model Table 8.3 represents all its characteristics and compares it with the advanced seat model.

Weight of the complete seat is 13,150 g. Therefore we need to add the cushion weight, 5,994 g, to the whole seat structure as the nonstructural mass. The whole seat is shown in Fig. 8.8 (left). In the next step, model validating will be conducted using experimental modal analysis (EMA).

8.3 Characterization of the Seat Dynamics

8.3.1 Experimental Modal Testing

Experimental modal analysis is utilized to characterize the seat structural resonant frequencies and its corresponding mode shapes. Impact hammer test, which is a common method in modal testing, was used to extract the seat structural resonances and mode shapes. The modal test setup consisted of a hammer, charge amplifier, three axial accelerometers, and data logger. The seat structure was suspended from bungee cords (elastic ropes) to allow the seat system to be nearly free in six axes. Therefore, the seat modal characteristics were measured in the free–free boundary condition. The mounting of the accelerometers to the different parts of the seat frame was done using adhesive wax [9]. To obtain proper mode shapes, thirteen points of the seat frame were measured. Test setup for the seat modal test is demonstrated in Fig. 8.12.

Fixture Dynamics

A fixture is generally used for this type of testing. The seat modal characteristics can be easily affected by the fixture structural properties. Therefore, modal analysis

Fig. 8.12 Test setup to obtain modal characteristic of the seat

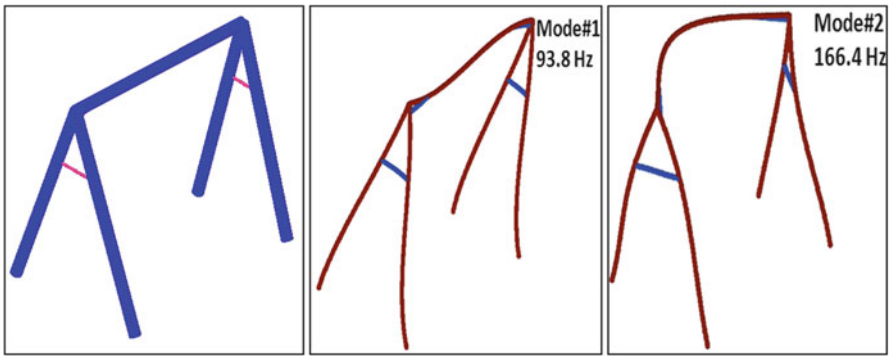

Fig. 8.13 Fixture finite element model (*left*), first mode shape at 93.8 Hz (*middle*) and second mode shape at 166.4 Hz (*right*)

of the fixture is conducted using HyperWorks and Nastran software. Figure 8.13 shows the first and second mode shapes of the fixture at its corresponding natural frequencies. The first and second natural frequencies are 93.8 and 166.4 Hz, respectively. Cabin input excitations due to road inputs usually occur at frequencies up to 40 Hz because the tires and suspension act as low-pass filters [5].

As we will show, the fixture resonance frequencies are completely far from the seat natural frequencies. In other words, it is concluded that the fixture structure does not have a major effect on the seat.

8.3.2 Simulation and Experimental Results

Due to the fact that NVH performance is investigated through dynamic response behavior for the structures, the validation of the developed NVH concept model is conducted in dynamic domain by taking their eigenvalues and eigenvectors into consideration. To put it in another way, fundamental resonance frequencies and mode shapes are considered as dynamic indicators and compared between advanced CAE model and concept model. Three criteria of natural frequency, MAC (modal assurance criteria), and frequency response function (FRF) have been used to validate the developed seat concept model. For example, the first torsion mode shape of the seat happened in 31 Hz for the experiment which has a less than 3 % error with concept model of the seat. Figure 8.14 illustrates this mode shape for the seat concept model and experimental test.

Following the comparison of the experiment and simulation results, the values of the resonant frequencies and the values of MAC (modal Assurance Criteria) [15] have been compared (Table 8.4) between the experiment and the simulation. Taking the above-mentioned materials into consideration, the natural frequencies error percent (Δ %) and MAC of the concept and advanced models are computed

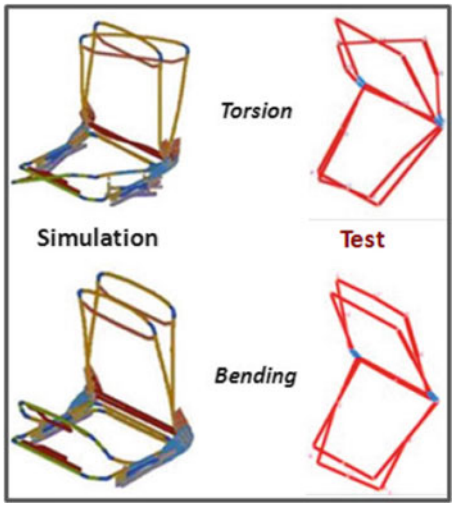

Fig. 8.14 Seat structural dynamics: torsion modes (*top*) and bending modes (*bottom*) from simulation (*left*) and experiment (*right*) are similar

Table 8.4 Comparison of the seat resonant frequencies and corresponding mode shapes between the experiment and simulation

Mode number	Resonance of experimental test (Hz)	Resonance of concept models (Hz)	Error (Δ)%	MAC
1	31	31	2.9	0.96
2	47.2	48	1.6	0.91

to validate the developed NVH concept model. The MAC index between similar modes of two models is calculated by Eq. (8.19), in which φ_A and φ_C are the matrix of eigenvectors for the experimental results and concept model, respectively, and superscript T denotes the transpose of a vector. The eigenvectors are constructed by using main structure nodes in the test and corresponding nodes in the concept model (a total of thirteen nodes).

$$MAC_{A,C}|_k = \frac{\left(\{\Phi_A\}_k^T \{\Phi_C\}_k\right)^2}{\left(\{\Phi_A\}_k^T \{\Phi_A\}_k \{\Phi_C\}_k^T \{\Phi_C\}_k\right)} \tag{8.19}$$

A MAC value equal to unity indicates a 100 % similarity between the vibration mode shape obtained from the simulation and that of obtained from the experiment. The MAC values, in the Table 8.4, for the two seat torsion and fore-aft bending modes are found to be above 0.9, which indicates a good consistency between the modes of the developed model and the test data. Comparison of the values of torsion and fore-aft bending resonant frequencies indicates very low discrepancies ($\Delta < 3$ %). Table 8.5 demonstrates the high accuracy of this concept modeling method for BIW.

To further validate the developed model, the inertance FRFs are compared, between the test data and corresponding simulation data, when the seat is excited

Table 8.5 Dynamic results (mode shape and natural frequency) of the BIW concept and advanced models

Mode number	Resonance of advanced model (Hz)	Resonance of concept model (Hz)	Error (Δ)%	MAC
1	35.48	34.75	2.06	0.95
2	41.36	41.98	1.50	0.97
3	45.75	45.46	0.63	0.85
4	48.88	48.11	1.60	0.71
5	50.07	50.04	0.06	0.88

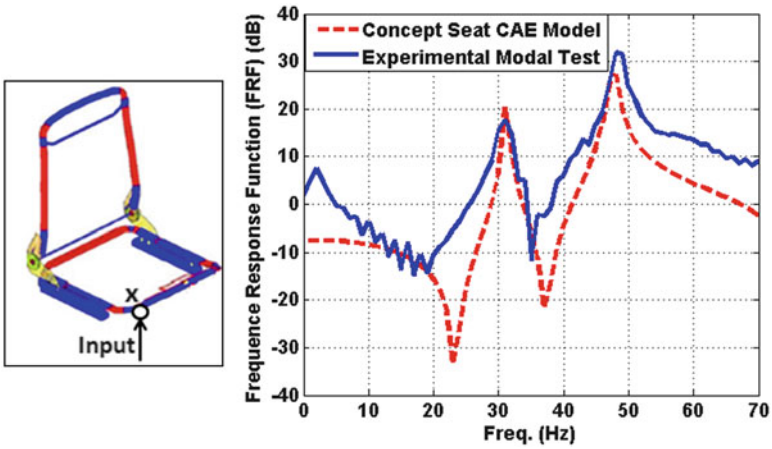

Fig. 8.15 Comparison of the inertance FRF at point "X" between the simulation and experiment (*right*). The measurement point "X" is also illustrated (*left*)

at one specified point on its frame (Fig. 8.15). Note that, here, the inertance FRF indicates the FRF which its output is measured at input point or its input and output points are same. The input and output are both measured at point "X" that is shown in Fig. 8.15. The similarity between the FRF graphs from the test and simulation (Fig. 8.15) further validates the developed model.

8.4 Rattle Noise Mechanism and Causes

In this section, an analytical expression that provides a measure of rattle frequency and intensity, referred to as the "rattle factor," is derived for the simple lumped mass mechanical model depicted in Fig. 8.16. There is some level of preload in the spring that tries to preserve contact in the face of the internal forcing caused by the base motion, z(t) [16]. The "rattle factor" measure will subsequently be generalized to more complex structures such as different components of the seat. The system shown in Fig. 8.16 is excited by random input and is undergoing intermittent rattle,

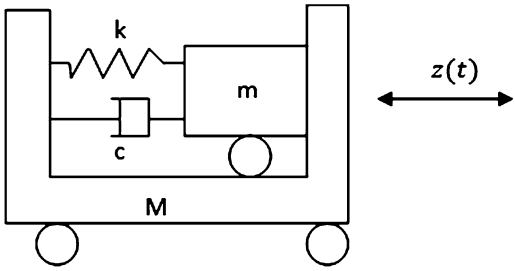

Fig. 8.16 Generic rattle mechanism excited by random input

there are (often relatively short) bursts of activity, during which the system is trying to re-achieve its original rest state, separated by spans of relatively quiescent behavior. A measure of rattle, the average frequency between events, is defined. Considering the average of the durations T_b^i, the rattle factor is defined to be:

$$R = \frac{1}{E[T_b^i]} = \frac{1}{\text{expected event time}} \tag{8.20}$$

where E[x] is the expected value of x. A small value of R (rattle factor) corresponds to infrequent rattle events of short duration. Moreover, smaller values of R correspond to rattle of less severity. Therefore in nonlinear engineering structure achieving to the minimum value of R is desired. Note that this measure is used simply because of the difficulties in computing analytical expressions for information about the details of the settle-out events.

8.4.1 BSR Causes

We can divide the main causes of the BSR noises into four major groups as follows.

Manufacturing Issue

Dimensional control is an important factor in a manufacturing process. It determines part-to-part variation and clearance between two parts. An insufficient clearance is one of the major causes of squeak and rattle problems in the automotive parts.

Assembly Issues

Parts are assembled together using many fasteners, screws, bolts, and seals. Improper assembling of these parts (e.g., insufficient clamp load) or missing parts always causes squeak and rattle problems.

Material Compatibility Issues

In the case of not frictionally compatible contact squeak problems tend to develop. Temperature sensitive materials are extremely exposed to squeak generation.

Non-robustness of Local Part Design

Automotive OEM companies use many local parts (e.g., fasteners and latch and striker) designed and developed by suppliers. Squeak and rattle propensity is heavily relied on the design and installation of these parts.

8.4.2 Noise Measurement

The effectiveness of the seat structural properties on the noise generation will be presented. There are four different types of vibration in use for BSR lab tests: random vibration (sometimes called PSD control since the target is a power spectral density level as a function of frequency), sinusoidal (sine) vibration, sine-on-random (SineOnRandom), and time history replication (often called road loads in the vehicle industry) [16]. Here, the seat is excited by sinusoidal input (between 10 and 80 Hz) and the generated noise is measured at four different points using microphones. The noise measurement system consisted of microphone, electromagnetic shaker, amplifier, data logger.

Here is a brief summary of what was done to seat that came to the BSR detection:

1. Suspend seat from the fixture (via elastic ropes)
2. Create realistic vibration having vertical, longitudinal, and pitch motions and also lateral and roll motions
3. Use ultra-quiet electro-magnetic exciters to reproduce sinusoidal signal to find BSR issues
4. Record microphone measurements and quantify noises against an evolving pass/fail criterion
5. Find and fix root causes of excessive noise
6. Use a disciplined process to feedback findings and undertake corrective actions

Background noise was retained below 36 dBA at the running condition of the vibration shaker. The temperature and humidity were kept at 22.5 °C and 35 %, which was reported to cause dimensional variation in the components, especially those containing elastomers. Test setup for noise measurement and four selected points are illustrated in Fig. 8.17.

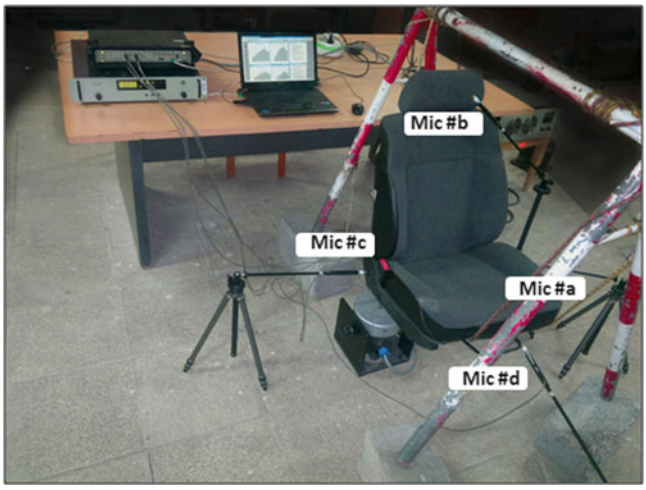

Fig. 8.17 Test setup and four selected points for measuring the sound pressure level

8.4.3 Noise Source Identification

The radiated sound pressure levels (SPLs) are measured when the seat is under the excitation, at four points, which has already been named "a" to "d" in Fig. 8.17. The results show that when the excitation frequency approaches to the seat torsion resonant frequency (31 Hz), the components of the seat near the seat belt buckle start rattling [17]. Accordingly, comparison of the SPLs measured by four microphones indicates that the microphone #c, shown in Fig. 8.17, received higher SPL than the other three microphones. Figure 8.18 compares the SPLs obtained from the four microphones when the seat is excited by a single sine input with 31 Hz frequency (equal to the seat torsion resonance). As it is observed, the rattle causes higher noise level (here 70 dB SPL) mainly at frequencies below 2,500 Hz. Note that even the seat is excited by a single sine vibration, the rattle noise can be occurred in a wide frequency range. Furthermore, the rattle noise is also functions of additional physical properties such as the contact surface and materials of the rattling parts [4].

By decreasing or increasing the excitation frequency from 31 to 25 Hz or 35 Hz, the rattle noise is also considerably decreased (Figs. 8.19 and 8.20). In other words, a wide band rattle noise is seen when the seat is excited at its resonance frequency. This confirms that the occurrence of the seat subcomponents rattle is linked to the seat resonant frequency, so that by changing the excitation frequency away from the seat structural resonance, the rattle noise can be controlled.

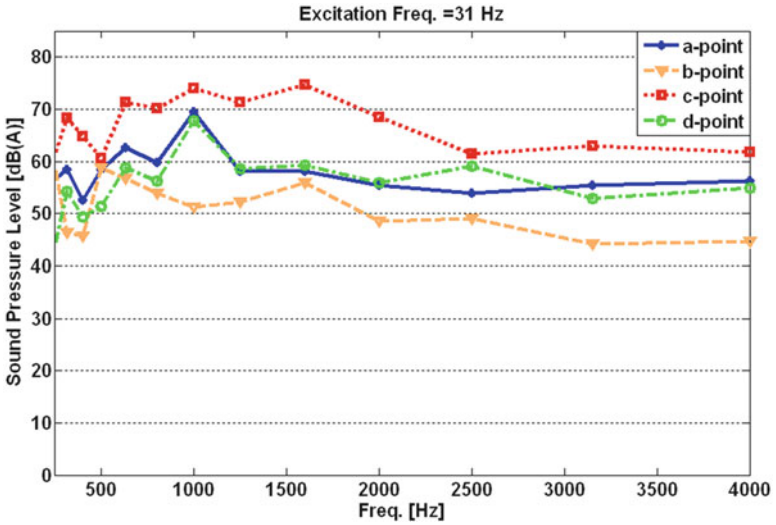

Fig. 8.18 SPL at four selected points when the seat excited at its 31 Hz resonant frequency

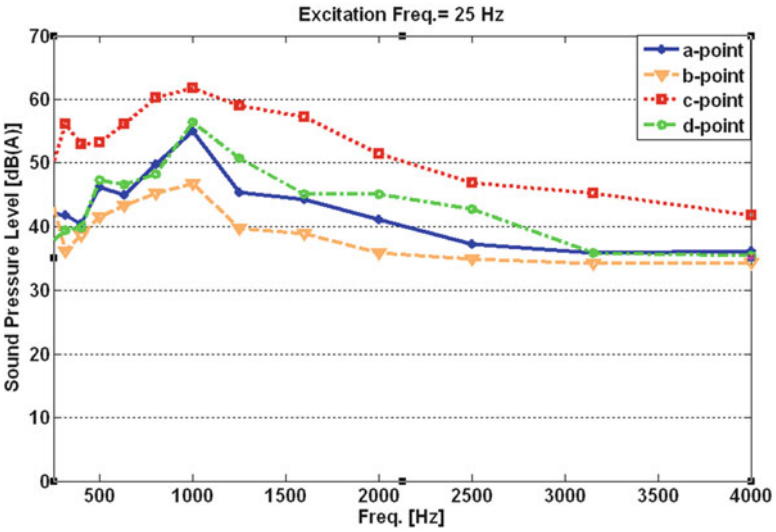

Fig. 8.19 SPL at four selected points when the seat excited at its 25 Hz resonant frequency

According to the measured data and their analysis, the major source of the seat noise was identified as region around c-point (seat belt) in seat structure. A wide band rattle noise is seen when the seat is excited at its resonance frequency. It is important to note that when the seat is excited at its resonance frequency and critical point, the rattle noise level will be increased (Fig. 8.21).

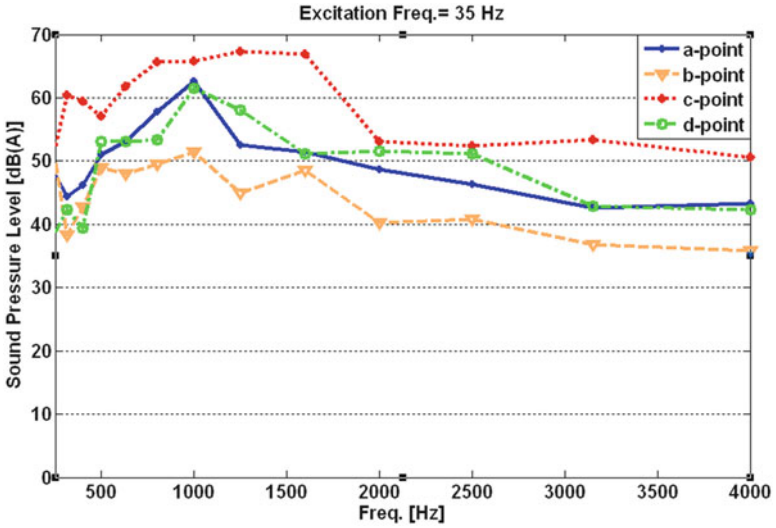

Fig. 8.20 SPL at four selected points when the seat excited at its 35 Hz resonant frequency

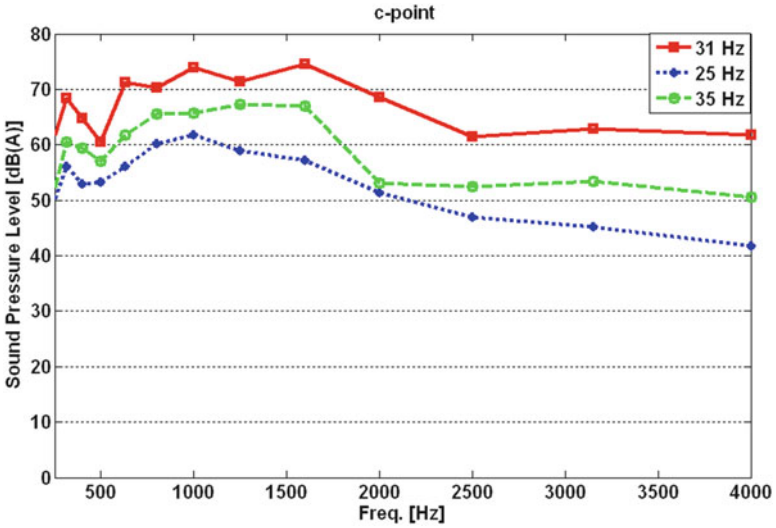

Fig. 8.21 Comparison of the seat radiated SPLs when excitation frequency is equal to resonance frequency (31 Hz) with those of neighboring frequencies (25 and 35 Hz)

8.5 Seat Structure Optimization

As explained in the previous section, seat structure has a large contribution on the noise generation because of the structural deficiencies. Two main sources of the disturbance in the vehicle are engine and road input. The idle engine vibration has frequency range 10 up to 33 Hz. On the other hand, tires and suspension system act

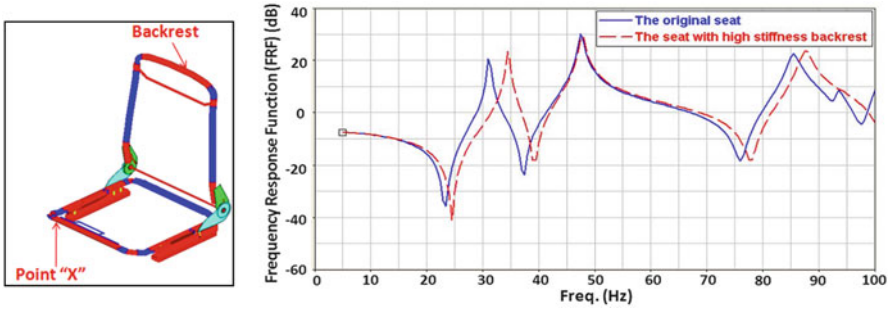

Fig. 8.22 Frequency response function (FRF) graph for point "X" shows first resonance frequency is increased about 3 Hz when it has stiffener backrest

as low-pass filters. Therefore, the first resonance frequency, torsion mode at 31 Hz, must be shifted or its vibration level be reduced. For this purpose, we propose three methods based on the developed CAE concept model.

8.5.1 Stiffness Variation

Stiffness directly affects dynamical properties of the structures. The young modulus of one seatback member (shown in Fig. 8.22) is changed from 2.1×10^8 to 2.1×10^{10} N/mm^3. The first resonance frequency is shifted to 34.57 Hz by stiffness variation method. Although this cannot be easily implemented in real, the computed FRF in Fig. 8.22 shows influence of the backrest stiffness on the first torsion resonance.

8.5.2 Sensitivity Analysis

Sensitivity analysis can be conducted to identify the effects of beam properties such as area and moments of inertia of the cross section in predefined NVH characteristics. For example here, the natural frequency of the first torsion mode for the seat-only structure is selected and the effects of seat components parameters are calculated when they are increased 20 % in their values. The components of the seat and the results of the sensitivity analysis are presented in Fig. 8.23 and Table 8.6, respectively. The results reveal that the property of the seatback beam is generally more effective than the other parts. After member 3, the cross sections of the 1, 2, and 6 members have an important role on the first torsion mode. Therefore, the cross sections have been changed and are listed in Table 8.7. After reducing the cross sections in accordance with Table 8.7, the weight of the seat decreased about 540 g and first natural frequency increased to 33.3 Hz.

New cross sections are listed in Table 8.7.

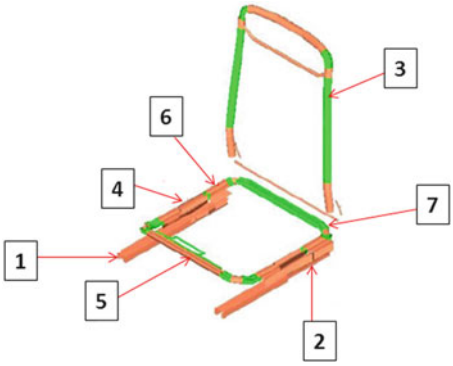

Fig. 8.23 Seat component number considered for sensitivity analysis

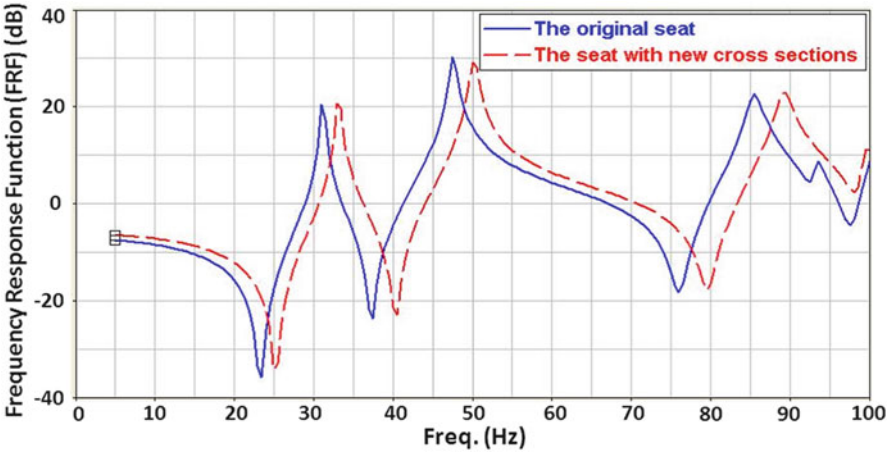

Fig. 8.24 Resonance frequencies that increased by reducing some cross sections according to Table 8.7

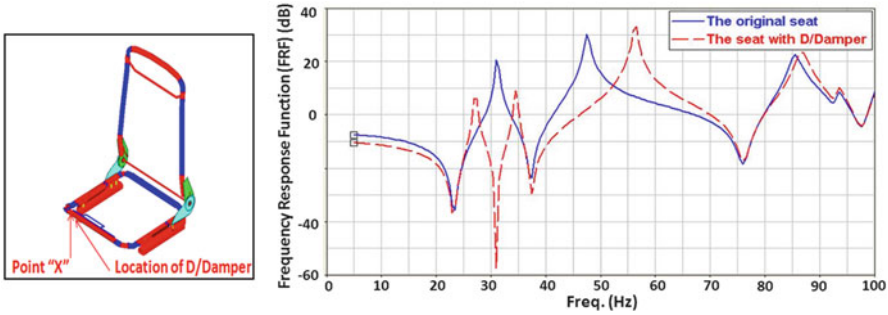

Fig. 8.25 Frequency response function (FRF) indicates reduced vibration level around first torsion mode after employing the D/Damper (D/Damper denotes Dynamic damper)

Table 8.6 The sensitivity of the first seat torsion mode to different seat components is shown in Fig. 8.23

Component number	A	I_1	I_2	I_{12}	J
1	−0.51	0	0.006	0	0.067
2	−0.51	0.014	0.006	0	0
3	−2.28	1.13	0.58	0	1.37
4	−0.31	0.004	0.086	0	0.27
5	−0.4	0.016	0.04	−0.02	0.35
6	−0.51	0.017	0.82	0	1.75
7	−0.16	0.03	0.14	0	0.008

Table 8.7 Original and new cross sections with their component number

Component number	Original cross section (mm^2)	New cross section (mm^2)
1	240	200
2	117	80
3	144	90
6	127	90

8.5.3 Dynamic Damper

Dynamic damper is a combination of the mass and spring that can be attached to the structures and divide one resonance into two resonances with lower vibration level. In the seat structure, dynamic damper reduced the vibration level about 12 dB. Dynamic damper mass was 1 kg and its stiffness was calculated using Eq. (8.21).

$$\sqrt{\frac{k}{m}} = 31.9\ Hz = 31.9 * 2 * \pi \left(\frac{rad}{s}\right) \overset{m=1\ Kg}{\rightarrow} k \approx 40\frac{kN}{m} \tag{8.21}$$

It can be seen from the above figure that dynamic damper decreased the vibration level (12 dB) and divided the frequency 31.9 Hz into two frequencies of 27.2 and 34.6 Hz.

8.6 Summary and Outlook

A method is presented for the seat concept modeling to predict the dynamic behavior of the seat. In the early vehicle design phase, without access to any detailed data, it is required to develop a concept CAE model based on the initial design information and predecessor seat data. In this study, the members of the seat structure are modeled and approximated using beam elements. Also, for shortening the solution time, the Guyan reduction is used to condense detailed joints properties in their boundary nodes to connect concept beams. Dynamic comparison between model

and experiment is performed to confirm the validity of the developed NVH concept model. The value of resonance frequencies and MAC showed that these concept models reflect good enough correlation with the experimental test in low frequency range (below 60 Hz).

The automotive seat modal test results show that seat has major structural mode shapes in low frequency range. These fundamental mode shapes can cause transmitting a high level of vibration to the car occupant, especially when these seat modes occur at frequencies near the engine input frequencies. These vibrations at low frequency range can easily produce annoying BSR noise in the vehicle cabin. Therefore, controlling the BSR noise needs to focus on the seat structural dynamics and characterize its characteristics.

A noise measurement technique was used to automatically detect the potential source regions of BSR on the seat subject to sinusoidal signal excitation with 5 Hz discrepancy between 10 and 80 Hz. After measuring the sound pressure level, the main source of seat rattle is identified. When the input frequency changed from 25 or 35 Hz to 31 Hz, the first seat structural mode was excited and it caused to produce rattle noise. The most important characteristics of the identified source mechanisms included relative movements such as impact induced phenomena, and slip–stick between two parts in the frequency range from 300 to 1,200 Hz. Rattles were found to be more dominant than squeaks.

Seat structure has a large contribution on the noise generation because of the structural vibration and generally low frequency forces (below 40 Hz) translate from the road to the seat through the tires and suspensions. Therefore, for BSR noise reduction, structural mode must be controlled. As a solution, the first seat resonance frequency (31.9 Hz) must be shifted up or its vibration level be reduced. Three different methods were proposed. These methods are: increasing the seatback stiffness, sensitivity analysis and using mass damper. As the experimental test shows, these solutions can effectively reduce seat rattle noise from the structure.

References

1. Kuo EY (1998) Up-front squeak and rattle prevention using CAE models. In: The 4th ISSAT, International Society of Science
2. Kuo EY, Mehta PR, Geck PE (2002) High mileage squeak and rattle robustness assessment for super-duty cab weight reduction using high-strength steel and adhesive bonding. SAE Trans 111(2):637–647
3. Cerrato-Jay G, Gabiniewicz J, Gatt J, Pickering DJ (2001) Automatic detection of buzz, squeak and rattle events. SAE Trans 110(6):1763–1770
4. Kavarana F, Rediers B (2001) Squeak and rattle-state of the art and beyond. Sound Vib 35(4):56–65
5. Gosavi SS (2005) Automotive buzz, squeak and rattle (BSR) detection and prevention. SAE paper, no. 2005-26: 056
6. Her JY, Hsieh SR, Moore J (1997) Quantitative identification of vehicle rattle sources using CAE and experimental tools. Paper presented at the Proceedings of the 1997 American Society of Mechanical Engineers Design Engineering Technical Conferences

7. Donders S, Takahashi Y, Hadjit R, Van Langenhove T, Brughmans M, Van Genechten B, Desmet W (2009) A reduced beam and joint concept modeling approach to optimize global vehicle body dynamics. Finite Elem Anal Design 45(6):439–455
8. Mundo D, Hadjit R, Donders S, Brughmans M, Mas P, Desmet W (2009) Simplified modelling of joints and beam-like structures for BIW optimization in a concept phase of the vehicle design process. Finite Elem Anal Design 45(6):456–462
9. Fard M (2011) Structural dynamics characterization of the vehicle seat for NVH performance analysis. SAE paper 501: 2011
10. Fard M, Nasrolahzadeh N, Tatari M, Mahjoob M (2012) Automotive body-in-white concept modeling method for the NVH performance optimization. In: ISMA conference, Leuven, 17–21 September 2012
11. Guyan R (1965) Reduction of mass and stiffness matrices. AIAA J 3(2):380
12. Bampton MCC, Craig RR Jr (2012) Coupling of substructures for dynamic analyses. AIAA J 6(7)
13. Nasrolahzadeh N, Fard M, Tatari M, Mahjoob M (2013) Automotive concept modeling: optimization of the vehicle NVH performance. In: Proceedings of the FISITA 2012 world automotive congress lecture notes in electrical engineering, vol 201, pp 365–376
14. Hagiwara I, Ma Z-D (1992) Development of eigenmode and frequency response sensitivity analysis methods for coupled acoustic-structural systems, JSME International Journal, Series III, 35(2):229–235
15. Ewins DJ (1984) Modal testing: theory and practice. Research Studies Press Ltd, Taunton
16. Trapp M, Chen F (2011) Automotive buzz, squeak and rattle: mechanisms, analysis, evaluation and prevention. Butterworth-Heinemann, Elsevier
17. Tatari M, Fard M, Nasrolahzadeh N, Mahjoob M (2013) Charactrization of the automotive seat structural dynamics. In: Proceedings of the FISITA 2012 world automotive congress lecture notes in electrical engineering, vol 201, pp 541–552

Chapter 9
Parametric Segmentation of Nonlinear Structures in Visual Data: An Accelerated Sampling Approach

Reza Hoseinnezhad and Alireza Bab-Hadiashar

Abstract In many image processing applications, identification of nonlinear structures in image data is of particular interest. Examples include fitting multiple ellipse patterns to image data, estimation and segmentation of multiple motions in subsequent images in video, and fitting nonlinear patterns to cell images for cancer detection in biomedical applications. This chapter introduces a novel approach to calculate a first order approximation for point distances from general nonlinear structures. We also propose an accelerated sampling method for robust segmentation of multiple structures. Our sampling method is substantially faster than random sampling used in the well-known RANSAC method as it effectively makes use of the spatial proximity of the points belonging to each structure. A fast high-breakdown robust estimator called Accelerated-LKS (A-LKS) is devised using the accelerated search to minimize the kth order statistics of squared distances. A number of experiments on homography estimation problems are presented. Those experiments include cases with up to eight different motions and we benchmark the performance of the proposed estimator in comparison with a number of state-of-the-art robust estimators. We also show the result of applying A-LKS to solve ellipse fitting and motion segmentation in practical applications.

9.1 Introduction

Fitting nonlinear models to image data is a common yet challenging task in many image processing applications. Examples include machine perception of surrounding environment by 3-D range data segmentation using planes, cylindrical and spherical object models [1–11], ellipse fitting in various applications (such

R. Hoseinnezhad (✉) • A. Bab-Hadiashar
School of Aerospace, Mechanical and Manufacturing Engineering, RMIT University, Bundoora, VIC 3083, Australia
e-mail: rezah@rmit.edu.au; abh@rmit.edu.au

R.N. Jazar and L. Dai (eds.), *Nonlinear Approaches in Engineering Applications 2*,
DOI 10.1007/978-1-4614-6877-6_9,

as gait periodicity detection [12], landmark localization in neuroimages [13], skin colour [14] and nuclear buds [15] detection, gestational age estimation in ultrasound images [16]) and detection and fitting of nonlinear motion models to a dataset of point matches (that may include erroneous mismatches) in 3-D reconstruction and motion tracking applications [17–24].

When we fit one or more instances of a model to a set of data points, each instance is called a *structure*. To estimate the parameters of one of those structures, a common approach is to define a measure of goodness that captures the *distance* from each data point to the multi-dimensional manifold defined by a hypothesized model (a structure with hypothesized parameters). The best model parameters are then found via analysis of the distances for various hypotheses. In presence of outliers (data points not belonging to any structure) a *robust estimation* scheme is often used to ensure that the outcome is not biased by the influence of those outliers [25].

In the computer vision literature, definition of appropriate distances and finding nonlinear robust fitting solutions have been studied for different applications [26]. This chapter presents an attempt to move away from application-dependent metrics and introduces a generic and universally applicable distance measure. The proposed measure is intended to suit common robust fitting methods in a general nonlinear fitting and segmentation scenario. We also propose a new method for parametric segmentation of multiple nonlinear structures with significantly faster rate of convergence compared with current existing methods.

The rest of this chapter is organized as follows. The problem of multi-structure nonlinear detection and segmentation is stated in Sect. 9.2, with examples presented in the context of ellipse, homography and fundamental matrix fitting. The common approach to solve the problem is to turn it into an optimization problem as discussed in Sect. 9.3. The optimization cost function is usually formulated in terms of distances. Section 9.4 outlines the concept of geometric distance followed by our proposed universally applicable measure for geometric distance. Our proposed accelerated sampling method is then presented in Sect. 9.5 where we detail the cost function optimization part of A-LKS and the analysis of the proposed sampling method. Simulation results are presented in Sect. 9.6. Section 9.7 concludes the chapter.

9.2 Problem Statement

To formulate the problem, we start by assuming that n measurements are given as a set of data points denoted by $\{\mathbf{x}_i\}_{i=1}^{n}$. Each measurement $\mathbf{x}_i$ represents an exact value $\mathbf{x}_{i0}$ perturbed by noise,

$$\mathbf{x}_i = \mathbf{x}_{i0} + e_i \tag{9.1}$$

where e_i is a sample of Gaussian white noise with the noise power σ^2,

$$e_i \sim \mathcal{N}(0, \sigma^2).$$

There are an unknown number of structures, each containing some data points to which a parametric nonlinear model is fitted. The model is the same for all structures but each structure has different parameters. The model is denoted by the general form,

$$g(\mathbf{x_0}, \Theta, \alpha) = 0 \tag{9.2}$$

where $\mathbf{x_0}$ is the exact data locations, $\Theta = [\theta_1 \ \cdots \ \theta_p]^\top$ is the parameter vector and α is a scalar parameter.

In general, parameters can be scaled by an arbitrary constant and there are only p degrees of freedom in choosing those parameter values. However, most applications involve models with *linear* parameters as:

$$g(\mathbf{x_0}, \Theta, \alpha) = \theta_1 f_1(\mathbf{x}_0) + \cdots + \theta_p f_p(\mathbf{x}_0) + \alpha = 0 \tag{9.3}$$

in which the parameters are constrained by following conditions to guarantee the uniqueness of their values,

$$\alpha > 0 \qquad \text{and} \qquad ||\Theta|| = 1. \tag{9.4}$$

The general problem in this framework is to find the number of such structures in the data, estimate their parameters, and segment the data between those structures. For every structure, data points that belong to that structure are called *inliers* and the rest of data points are called *outliers*. Of those, the ones that belong to another structure in that data set are called *pseudo* outliers and the rest are called *gross* outliers. To show the application of this general framework, a number of common special cases are presented in the following section.

9.2.1 Ellipse Fitting

In a two-dimensional image space, the data points are the coordinates of pixels in the image. The problem is to find the number of ellipses that can be fitted to the ensemble of the given pixels. This problem is a common part of many pattern recognition tasks in AI and robotic applications. Each ellipse has its own Θ and α parameters and is defined by the following nonlinear formula:

$$\theta_1 x_1^2 + \theta_2 x_1 x_2 + \theta_3 x_2^2 + \theta_4 x_1 + \theta_5 x_2 + \alpha = 0 \tag{9.5}$$

where $\mathbf{x} = [x_1 \ x_2]^\top$ denotes the coordinates of a pixel on the ellipse (one of the data points). In order to guarantee that the above conic section is an ellipse, we need to enforce the constraint $\theta_2^2 - 4\theta_1\theta_3 < 0$ in addition to the constraints given in (9.4). In this case the parameter space is five-dimensional ($p = 5$), i.e. five pairs of point coordinates (x_1, x_2) are sufficient to specify a possible parameter estimate. Such a solution is called a *model candidate*.

A circle fitting problem is a special case of ellipse fitting, in which circular patterns are the instances of fitting the following model

$$\theta_1(x_1^2 + x_2^2) + \theta_2 x_1 + \theta_3 x_2 + \alpha = 0. \tag{9.6}$$

We note that both the circle and ellipse equations follow the general form of (9.3) where the parameter space has three to five degrees of freedom.

9.2.2 Homography Estimation

When a planar object undergoes a general motion in the 3-D space, its motion can be modelled by a *homography* model [26]. Assume two images, called the pre-motion and post-motion images, taken before and after the motion occurs. Consider a pixel (x_1, x_2) in the pre-motion image matching the pixel (x_1', x_2') in the post-motion image. The homography model is then parametrized by a 3×3 matrix denoted by H in such a way that:

$$\omega \begin{bmatrix} x_1' \\ x_2' \\ 1 \end{bmatrix} = H \begin{bmatrix} x_1 \\ x_2 \\ 1 \end{bmatrix} \tag{9.7}$$

where ω is the (unknown) scale of perspective projection. Eliminating ω from the system of equations (9.7) leads to the following simultaneous nonlinear equations:

$$\begin{aligned} h_{11}x_1 + h_{12}x_2 + h_{13} - h_{31}x_1x_1' - h_{32}x_2x_1' - h_{33}x_1' = 0 \\ h_{21}x_1 + h_{22}x_2 + h_{23} - h_{31}x_1x_2' - h_{32}x_2x_2' - h_{33}x_2' = 0 \end{aligned} \tag{9.8}$$

in which h_{ij} denotes the i-by-j element of the homography matrix H. We note that each of the two equations in (9.8) is in the general form of (9.3). There are nine elements in the homography matrix, including eight independent ones (considering the scale). Each matching pair of pixels, $[x_1 \ x_2 \ x_1' \ x_2']^\top$, results in two equations. Therefore, a model candidate is given by $p = 4$ pairs of matching pixels.

9.2.3 Fundamental Matrix

When a non-planar object undergoes a general motion in the 3-D space, its matching pixels in the pre-motion and post-motion images do not satisfy the homography model (9.7) [26]. A more general model for such motions is called the *fundamental matrix* model. In this model, the motion is fully parametrized by a 3×3 fundamental

matrix denoted by F which is of rank 2, and for which, every pair of matching pixels $(x_1, x_2), (x_1', x_2')$ in the pre-motion and post-motion images satisfies the following equation:

$$[x_1' \; x_2' \; 1] \; F \; [x_1 \; x_2 \; 1]^\top = 0. \tag{9.9}$$

This model can be rewritten in the general form of (9.3) as:

$$\theta_1 x_1 x_1' + \theta_2 x_2 x_1' + \theta_3 x_1' + \theta_4 x_1 x_2' + \theta_5 x_2 x_2' + \theta_6 x_2' + \theta_7 x_1 + \theta_8 x_2 + \alpha = 0 \tag{9.10}$$

where the parameters $\{\theta_i\}_{i=1}^8$ and α are the elements of the fundamental matrix:

$$F = \begin{bmatrix} \theta_1 & \theta_2 & \theta_3 \\ \theta_4 & \theta_5 & \theta_6 \\ \theta_7 & \theta_8 & \alpha \end{bmatrix}. \tag{9.11}$$

Disregarding the rank-2 constraint, fundamental matrix estimation involves estimating 8 independent parameters, and the dimension of data and parameter spaces is $p = 8$. The rank-2 constraint is usually imposed by finding the closest rank-2 matrix to the estimated fundamental matrix as follows. Given the putative rank-3 estimated matrix, the smallest (in magnitude) singular value of this matrix is replaced with zero and the rank-2 matrix is reconstructed using the singular vectors of original rank-3 matrix.

9.3 Parametric Segmentation

Most of the methods developed for solving the problem stated in Sect. 9.2 are *sequential* solutions [26]. The parameters of a single structure are estimated, its inliers are segmented and removed from the dataset, and the estimation, segmentation and removal steps are repeated until only gross outliers are remained in the dataset.

The first step (parameter estimation) is commonly implemented using a *robust* estimation routine that is tolerant to outliers. In multi-structure segmentation scenario, a small ratio of data points would necessarily belong to each single structure. Therefore, *high breakdown* robust estimators (tolerant to large ratios of outliers) need to be employed. Such estimators usually employ an *optimization search* at their core, exploring the parameter space for the winning model candidate (Θ^*, α^*) that minimizes a cost function $C(\Theta^*, \alpha^*)$.

The most common approach to define meaningful cost functions is to express the cost as a function of the distances $\{d_i\}_{i=1}^n$ of the data samples $\{\mathbf{x}_i\}_{i=1}^n$ from the p-dimensional manifold defined by the equation $g(\mathbf{x}, \Theta, \alpha) = 0$. The location and shape of this manifold in the data space depends on the values chosen for the parameters, and so does every distance d_i.

The cost function of the least squares estimator is simply the sum of all the squared distances:

$$C_{\mathrm{LS}}(\Theta, \alpha) = \sum_{i=1}^{n} [d_i(\Theta, \alpha)]^2 . \tag{9.12}$$

The rationale behind this choice of cost function is that the best parameter value is intuitively the one corresponding to the manifold that is *closest* to the data points. Minimization of this cost function would of course be meaningful only when *all* the data points are around a *single* structure, i.e. when there are no pseudo or gross outliers. However, in presence of multiple structures and gross outliers, an alternative cost function is needed.

The problem of devising meaningful cost functions for robust estimation in presence of large ratios of outliers has been visited in many papers and numerous cost functions have been devised for various applications [1–3, 6–10]. One of the simplest and most effective cost functions is the least kth order statistics function used in the adaptive least kth order statistics (ALKS) estimator [2], and defined as:

$$C_{\mathrm{LKS}}(\Theta, \alpha) = d_{k:n}(\Theta, \alpha) \tag{9.13}$$

where $d_{k:n}(\Theta, \alpha)$ is the kth order statistics of the distances (kth smallest distance out of n distances). Minimizing this cost function would result in a fit that is closest to k data points no matter where other data points are, i.e. the estimator is tolerant to outliers even if they include $n - k$ points of the whole dataset.

In practice, the minimum size of a structure that would be of interest in a particular application is known. For instance, in an ellipse fitting problem, an absolute minimum of the number of points on a structure is $p = 5$ although we may have a minimum size of $k = 10$ or even $k = 20$ points. In a range segmentation application, we may be only interested in cylindrical structures for which at least $k = 30$ range measurements are segmented as inliers. In a motion segmentation application, we may be only looking for motions that contain at least $k = 20$ pairs of matching pixels from our dataset.

The above-mentioned practical necessity justifies and determines the input parameter k in the LKS cost function. In order to perform robust segmentation, two important questions need to be addressed:

1. What would be a practically meaningful definition for the distance of a point from a nonlinear manifold?
2. What is an accurate and computationally efficient way to search the parameter space for the minimum point of a given cost function?

We will address these two questions in following sections.

9.4 Geometric Distance

The most commonly distance measure, used for parametric data segmentation in imaging applications, is the *geometric* distance, i.e. the minimum Euclidean distance of a point in the data space from the points on the manifold corresponding to the nonlinear structure. Formulas of geometric distance have been separately derived for different applications. Here, we present a unified approach to compute a first-order approximation of the geometric distance for a nonlinear manifold.

Let us start from the simple case of segmentation of nonlinear structures in a two-dimensional data space. Figure 9.1 shows an instance of the geometric distance of a measurement point (x_1, x_2) from a general manifold defined by the nonlinear equation (9.2). By definition, for a given structure, inlier and outlier data points are identified based on how large their distances are from that structure. Appropriately, the cost function of a robust estimator should intrinsically return large values for large distances even if those are not calculated accurately. More precisely, a distance formula is required to be more accurate for the points closer to the structure (with smaller distances) compared to ones that are much further away.

Consider a point $P(x_1^P, x_2^P)$ in a small distance d from the manifold given by the equation $g(x_1, x_2, \theta, \alpha) = 0$. We denote the closest point on the manifold to the point P, by $Q(x_1^Q, x_2^Q)$. The equation of the line passing through the point Q and tangent to the manifold is given by:

$$\frac{\partial g}{\partial x_1}\Big|_Q (x_1 - x_1^Q) + \frac{\partial g}{\partial x_2}\Big|_Q (x_2 - x_2^Q) = 0 \tag{9.14}$$

and the distance of the point $P(x_1^P, x_2^P)$ from this lines is given by:

$$d = \frac{\left| \frac{\partial g}{\partial x_1}\big|_Q (x_1^P - x_1^Q) + \frac{\partial g}{\partial x_2}\big|_Q (x_2^P - x_2^Q) \right|}{\sqrt{\left(\frac{\partial g}{\partial x_1}\big|_Q\right)^2 + \left(\frac{\partial g}{\partial x_2}\big|_Q\right)^2}}. \tag{9.15}$$

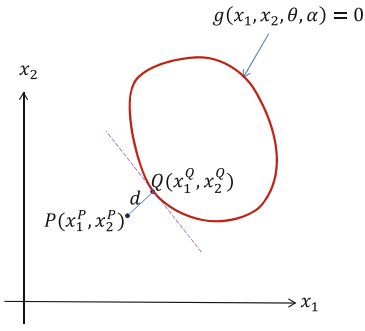

Fig. 9.1 A 2D representation of the geometric distance

To simplify the computation of the above distance, we note that the numerator is the first-order Taylor's series approximation to $g(x_1^P, x_2^P, \theta, \alpha)$ and in the denominator, with first-order approximation, we replace the partial derivative terms with partial derivatives at the point P,

$$d = \frac{\left|g(x_1^P, x_2^P, \theta, \alpha)\right|}{\sqrt{\left(\frac{\partial g}{\partial x_1}\big|_P\right)^2 + \left(\frac{\partial g}{\partial x_2}\big|_P\right)^2}}. \tag{9.16}$$

In a general case involving m-dimensional data points, a similar approach can be followed.[1] The equation of the hyperplane that is tangent to the structure defined by (9.2) is given by:

$$\nabla g\Big|_Q \cdot (\mathbf{x} - \mathbf{x}^Q) = 0 \tag{9.17}$$

and the geometric distance is:

$$d = \frac{\left|\nabla g|_Q \cdot (\mathbf{x}^P - \mathbf{x}^Q)\right|}{\left|\left|\nabla g|_Q\right|\right|} \tag{9.18}$$

where $||\cdot||$ denotes the 2-norm. The numerator can be first-order approximated by $g(\mathbf{x}^P, \Theta, \alpha)$ and the denominator by $\left|\left|\nabla g|_Q\right|\right|$, i.e.

$$d = \frac{\left|g(\mathbf{x}^P, \Theta, \alpha)\right|}{\left|\left|\nabla g|_P\right|\right|}. \tag{9.19}$$

In ellipse fitting with models formulated by (9.5), the geometric distance is:

$$d(x_1, x_2, \Theta, \alpha) = \frac{|\theta_1 x_1^2 + \theta_2 x_1 x_2 + \theta_3 x_2^2 + \theta_4 x_1 + \theta_5 x_2 + \alpha|}{\sqrt{(2\theta_1 x_1 + \theta_2 x_2 + \theta_4)^2 + (\theta_2 x_2 + 2\theta_3 x_2 + \theta_5)^2}}. \tag{9.20}$$

In homography estimation, using the model given by the two manifolds in Eq. (9.8), for each pair of matching pixels, (x_1, x_2) and (x_1', x_2'), two distances can be calculated, each corresponding to one manifold:

[1] It is important to note that the dimension of data space is not always equal to the dimension of the parameter space denoted by p in this chapter. More precisely, p is the minimum number of data points that can specify a unique model candidate, which is not necessarily equal to the dimension of the data points. For instance in the fundamental estimation problem, each data point includes a pair of matching pixels and the dimension of each data point is 4, but the dimension of the parameter space is 8.

$$d_1 = \frac{|h_{11}x_1 + h_{12}x_2 + h_{13} - h_{31}x_1x_1' - h_{32}x_2x_1' - h_{33}x_1'|}{\sqrt{(h_{11} - h_{31}x_1')^2 + (h_{12} - h_{32}x_1')^2 + (h_{31}x_1 + h_{32}x_2 + h_{33})^2}} \tag{9.21}$$

$$d_2 = \frac{|h_{21}x_1 + h_{22}x_2 + h_{23} - h_{31}x_1x_2' - h_{32}x_2x_2' - h_{33}x_2'|}{\sqrt{(h_{21} - h_{31}x_2')^2 + (h_{22} - h_{32}x_2')^2 + (h_{31}x_1 + h_{32}x_2 + h_{33})^2}}. \tag{9.22}$$

The two distances can be combined into one scalar in different ways. One way is to consider the smaller among the two as the distance. A common choice is the root mean square of the two distances,

$$d = \sqrt{d_1^2 + d_2^2}. \tag{9.23}$$

In fundamental matrix estimation, the geometric distance is directly found by applying (9.19) to the model (9.10),

$$d = \frac{\left|[x_1' \; x_2' \; 1] \; F \; [x_1 \; x_2 \; 1]^\top\right|}{\sqrt{\left(\frac{\partial r}{\partial x_1}\right)^2 + \left(\frac{\partial r}{\partial x_2}\right)^2 + \left(\frac{\partial r}{\partial x_1'}\right)^2 + \left(\frac{\partial r}{\partial x_2'}\right)^2}}. \tag{9.24}$$

where

$$r = [x_1' \; x_2' \; 1] \; F \; [x_1 \; x_2 \; 1]^\top. \tag{9.25}$$

This distance is referred to as Sampson distance in the computer vision literature.

9.5 Optimization

As it was mentioned in Sect. 9.3, robust parametric segmentation solutions usually involve solving an optimization problem. The parameter space is searched for the minimum point of a cost function that is usually formulated as a function of distances of the data points from a hypothesized model candidate. In a p-dimensional parameter space, an ensemble of p data points (termed a "p-tuple" in the literature [3]) corresponds with a candidate model. One possible approach to solve the optimization problem is an *exhaustive search* of the sample space in which the cost function is computed for the model candidates corresponding to *all* possible p-tuples. Having n data points, such a search would involve examining

$$N_{\text{exhaustive}} = C_n^p = \frac{n!}{p!(n-p)!} \tag{9.26}$$

p-tuples which is a huge number for practical data size n.

A common approach that was initially introduced as part of the Random Sample Consensus (RANSAC) [27] method in about three decades ago is *random sampling*. In this search method, a number of randomly selected p-tuples are examined and the one that results in the smallest cost is chosen as the model candidate. If the number of the p-tuples randomly selected is N, then with a probability of:

$$P_{\text{success}} = 1 - \left[1 - (1 - \epsilon')^p\right]^N \tag{9.27}$$

at least one of them is a *good* p-tuple (i.e. all its samples belong to the inlier structure), where ϵ' is the ratio of outliers. Thus, for a given success probability P_{success}, at least:

$$N = \left\lceil \frac{\log(1 - P_{\text{success}})}{\log(1 - (1 - \epsilon')^p)} \right\rceil \tag{9.28}$$

p-tuples should be randomly examined where $\lceil . \rceil$ means rounding up to the next integer.

When the ratio of inliers to each structure is small, the number of random p-tuples given by (9.28) is substantial and the computational load of segmentation is too high for real-time (or near real-time) applications [28–30]. For instance, in case of having eight homography motions with almost equal number of matching points and 10% mismatches, at least 28,748 random 4-tuples are required to ensure 99% success probability. The computational cost is higher in case of general motions modelled by eight fundamental matrices, requiring at least 20,191,937 random 8-tuples.

In this chapter, we introduce a method to accelerate the sampling. Our proposed approach specially useful when the points belonging to each structure are not sparse but spatially close to each other. This method can be used to optimize the cost function of many estimators, and it requires far less random p-tuples (compared to random sampling) in case of parametric segmentation of multiple structures. Using our optimization search to minimize the kth order statistics of squared distances, we develop a new estimator called Accelerated Least kth order Statistics (A-LKS). Our experiments show that in terms of estimation error, A-LKS performs similar to the state of the art in high breakdown robust estimators, but it runs substantially faster when segmentation of several structures is involved.

9.5.1 Related Work

Tordoff and Murray [31] have tackled the computational cost issues of random sampling by devising a guided sampling technique in which the p-tuples are randomly chosen using a Monte-Carlo method according to the matching probabilities. In another effort, the "preemptive RANSAC" suggested by Nister [32] preemptively prioritizes a large number of random p-tuples and depending on the available time,

the cost function is computed and compared for a portion of them. However, in the examples presented by Tordoff and Murray[31] and Nister[32] to benchmark the performance of their methods, the number of p-tuples required to obtain accurate fits is still close to the theoretical number given by Eq. (9.28).

Alternative approaches to random sampling include the gradient-based search over a Grassman manifold in the p-dimensional space of parameter vectors implemented within pbM-estimator [33], and an iterative search based on reweighted least-squares used in High Breakdown M-estimator (HBM) [29, 30]. In cases involving multiple motions, the iterative search within both pbM and HBM need to be repeated for a number of times each starting from a random p-tuple. The number of repetitions needs to be tuned off-line by trial-and-error.

A number of modified versions of RANSAC have also appeared in the literature. Some recent examples include LO-RANSAC [34], randomized RANSAC [35] and BEEM [36]. These methods follow RANSAC in that they assume the availability of a scale (or error threshold) to determine the inliers for each hypothetical fit. Such a threshold is not always available. For instance, in motion estimation, the scale of noise mainly depends on the point matching techniques utilized to find corresponding points. In this chapter, we are interested only in estimators that work without any knowledge of the scale of measurement noise. Indeed, in many such estimators, the scale is either estimated within the estimation procedure or can be separately calculated upon its completion.

Our accelerated sampling method requires a small number of random samples—far less than the theoretical number given by Eq. (9.28). The search process does not need the scale of noise or any other threshold to determine inliers. Indeed, a theoretical stopping criterion is formulated and used to determine the minimum required number of p-tuples for a given success probability.

9.5.2 Accelerated Search

With recent increases in the reliability and sophistication of data measurement methods and equipment, the chances of having widely erroneous measurement data have substantially decreased. As such, in most image processing applications, a very large portion of measurement data are simply usable data. In robust segmentation framework this means that the ratio of gross outliers is small while the ratio of *pseudo* outliers is large particularly in challenging scenarios when several structures exist in a dataset.

The main reason for the large number of random samples is that in Eq. (9.28) many p-tuples include points from different structures and are simply discarded because they are not *good* samples. Our sampling method starts from the premise that there are some information in those p-tuples that can be utilized to effectively direct the search toward the optimum point of the cost function.

The fit given by a so-called bad sample is usually made up of points belonging to different structures. When we segment the data points that are inlier to a bad fit,

they would actually be the union of subsets of inliers to several structures. We would expect each of such subsets of inlier data points to be spatially close to each other and could be separated from others.

The flowchart of the proposed accelerated sampling algorithm is shown in Fig. 9.2. The algorithm comprises two levels of nested random sampling. First, n_1 random p-tuples are chosen. Each p-tuple corresponds to a parameter estimate for which an inlier–outlier dichotomy is conducted. The inliers are then clustered into separate groups of data points and the largest group is found. If the group contains sufficient data points, then in the inner level of random sampling, n_2 random p-tuples are selected from the points in the group. The total number of random samples will be no more than $N = n_1 n_2$.

For a given n_1 and n_2, the probability of having at least one "good" p-tuple can be computed as follows. Each of the n_1 random p-tuples in the first round of sampling contains p inliers or pseudo outliers (belonging to different structures) with a probability of $(1-\epsilon)^p$ where ϵ is the ratio of gross outliers.[2] Such a p-tuple corresponds to a fit for which an inlier–outlier dichotomy can be calculated. The inliers to the fit are clustered into groups and the largest group is selected for a second round of random sampling. If at most n_{occ} structures can be simultaneously occluding each other, and in the worst scenario they contain an equal number of points in the data (the smallest possible ratio of inliers), each of the n_2 random samples selected in the second round will be a good sample (with all points belonging to one structure) with a probability of $(1/n_{\text{occ}})^p$. Therefore, the probability of having at least one good sample in the second round is given by:

$$P_2 = 1 - \left[1 - \left(\frac{1}{n_{\text{occ}}}\right)^p\right]^{n_2}. \tag{9.29}$$

The overall success probability is then given by:

$$\begin{aligned} P_{\text{success}} &= 1 - [1 - (1-\epsilon)^p P_2]^{n_1} \\ &= 1 - \left[1 - (1-\epsilon)^p \left\{1 - \left[1 - \left(\frac{1}{n_{\text{occ}}}\right)^p\right]^{n_2}\right\}\right]^{n_1} \end{aligned} \tag{9.30}$$

and for a given n_2 and success probability, the minimum number of random samples required to be examined throughout the search is:

$$\begin{aligned} N &= n_2\, n_1 \\ &= n_2 \left\lceil \frac{\log(1 - P_{\text{success}})}{\log\left(1 - (1-\epsilon)^p \left\{1 - \left[1 - \left(\frac{1}{n_{\text{occ}}}\right)\right]^{n_2}\right\}\right)} \right\rceil. \end{aligned} \tag{9.31}$$

[2] It is important to note that ϵ is the ratio of *gross* outliers and in the presence of several structures, it is far less than ϵ' in Eqs. (9.27) and (9.28) which equals the sum of gross and pseudo outlier ratios. In the presence of n_{obj} structures with an equal number of inliers, $\epsilon' = \epsilon + (1-\epsilon)(1-1/n_{\text{obj}})$. For instance, if $\epsilon = 5\%$ of data are gross outliers and there are $n_{\text{obj}} = 8$ structures, we have $\epsilon' = 88\%$.

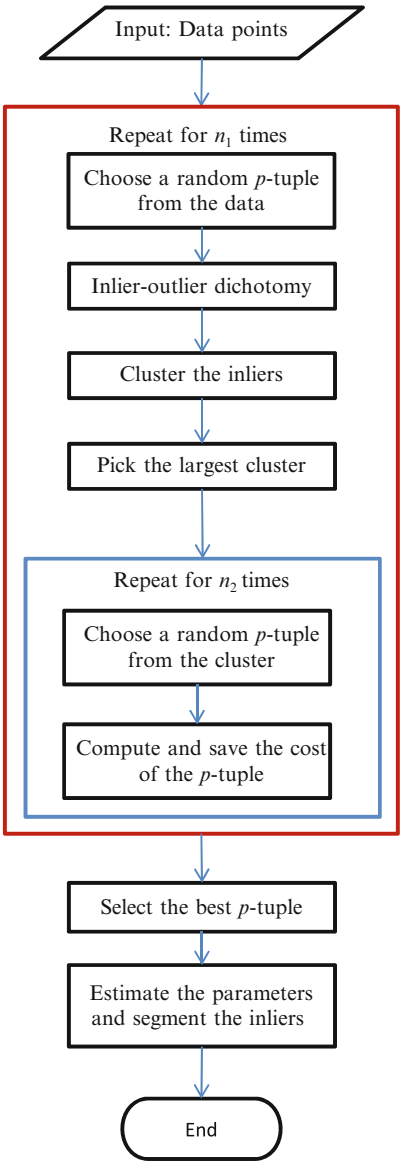

Fig. 9.2 The proposed accelerated sampling algorithm

In order to demonstrate the reduction of number of samples compared to the traditional random sampling, we have plotted the number of samples given by (9.31) versus the ratio of gross outliers (mismatches in case of motion segmentation), compared with the number of random samples required by RANSAC-based methods given by (9.28) for several number of motions. Figure 9.3a, b shows the plots for

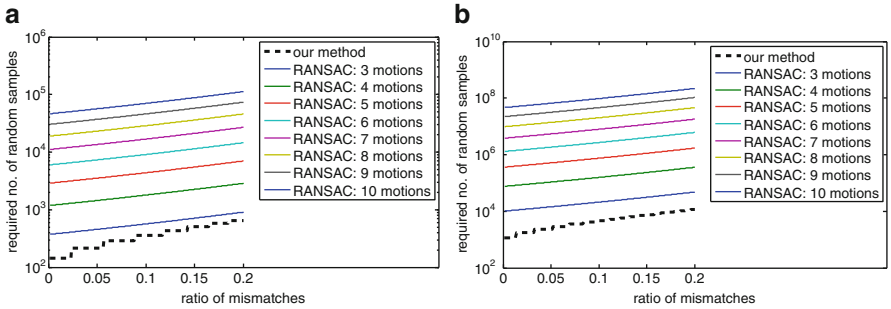

Fig. 9.3 Comparison of the number of random samples required by our guided search compared to theoretical number of random samples as used by a RANSAC-type estimator for cases involving estimation of various numbers of (**a**) homography motions (**b**) fundamental matrix motions

homography ($p = 4$) and fundamental matrix ($p = 8$) estimation. In both cases, it is assumed that no more than two moving objects can occlude each other ($n_{\text{occ}} = 2$). Noting the logarithmic scale on vertical axes, the plots show drastic reductions in the number of random samples, especially in cases where numerous motions are involved.

Remark 1. The above results are independent of the clustering technique used in the method, and any of the modern clustering methods can be employed. In our simulations we have used the Mean Shift method [37]. The mean shift algorithm is a nonparametric clustering technique which does not require prior knowledge of the number of clusters and does not constrain the shape of the clusters.

Remark 2. As it was mentioned before, only a *sufficiently large* group of points are subjected to a second round of sampling and if no such group results from clustering, the optimization procedure simply skips to process the next p-tuple of the first round of random sampling. In practice, a minimum size for the structure is assumed available (denoted by $k_{\min}$) and a group is considered sufficiently large if it contains at least $k_{\min}$ data points.

Remark 3. In deriving the formulas (9.30) and (9.31), we have assumed that for any of the n_1 random samples that contains no gross outliers, clustering of the inliers to the fit returned by the p-tuple will result in at least one sufficiently large group. It is noted that for some random samples that include *marginal* points on the edge of structures, this condition may not be satisfied, but we believe that such marginal points constitute a small fraction of points. Indeed, the inaccuracy can be compensated for by treating such points like gross outliers via increasing the ratio ϵ in Eq. (9.31). It is important to note that in practice, the actual ratio of gross outliers is small and despite the above-mentioned addition, a relatively small ϵ will be practically sufficient in most applications.

9.6 Simulation Results

To realize a high breakdown robust estimation scheme, we have used the proposed accelerated sampling method to optimize the kth order statistics of squared distances. We call the complete estimator as Accelerated Least kth order Statistics or A-LKS for short. In a number of experiments, we have compared the performance of A-LKS with MSSE [3], Adaptive Scale Sample Consensus (ASSC) estimator [38] and High-Breakdown M-estimator (HBM) [29].

To obtain an inlier–outlier dichotomy for a given parameter estimate, we have employed the specific routine suggested by Bab-Hadiashar and Suter within the Modified Selective Scale Estimator (MSSE) [3]. The procedure is described as follows. Having a set of distances $d_1, \ldots, d_n$, the distances are sorted in ascending order and the following unbiased scale estimates are computed:

$$\hat{\sigma}_k = \left[\sum_{i=1}^{k} d_{i:n}^2 / (k-p) \right]^{1/2} \quad ; \quad k = k_{\min}, \ldots, n \tag{9.32}$$

where $k_{\min}$ is a known lower bound for the number of points in a single structure and $d_{i:n}$ denotes the ith sorted distance. Then the smallest index $k^{'}$ is found for which $d_{(k'+1):n} > 4\,\hat{\sigma}_{k'}$. Finally, an inlier–outlier dichotomy is obtained by labelling all the points associated with distances $\{d_{1:n}, \ldots, d_{k':n}\}$ as inliers and the rest as outliers. This segmentation method has been chosen because it has been shown to have the best performance in terms of consistency [39] and finite sample bias [40].

Our first set of simulations involve segmentation of 4–8 homography motions. Each simulation includes 100 runs, each involving randomly generated homography motions for 4–8 objects which appear as squares in image 1 and evolve to a generally irregular quadrilateral in image 2. For each motion, 100 correct matches are found and the pixel coordinates are synthetically corrupted with noise. Those points as well as a total of 50 random mismatches are taken as measurements. A sample of the measurements generated in an experiment involving six motions is shown in Fig. 9.4a.

In each simulation, the measurements are processed by a robust motion segmentation method and two quantities are recorded: the processing time taken by the method for segmentation of the first motion, and the number of matches computed for that motion. The number of samples for each method and number of motions are averaged over the 100 runs, and the results shown in Fig. 9.4b. It is observed that in terms of segmentation accuracy, the performance of A-LKS is similar to other methods examined in the experiments.

Figure 9.4c shows the average computation times for each method plotted versus the number of motions involved. It is observed that the computation time of A-LKS (the number of required random samples) does not vary with the number of motions. The computation times of other estimators substantially increase with the number of motions because the outlier ratio ϵ' in Eq. (9.28) increases. Quantitatively,

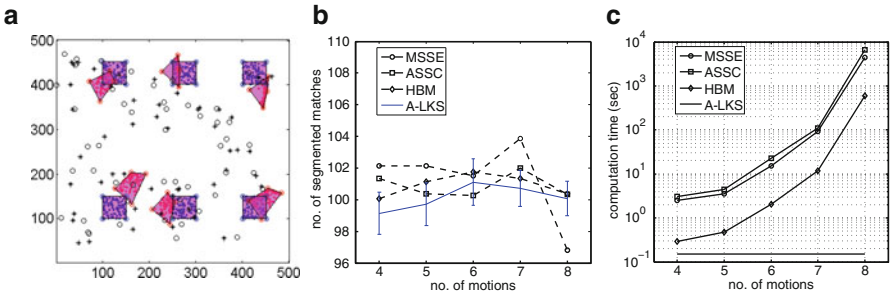

Fig. 9.4 (**a**) A sample of synthetic data generated in the experiment. The *blue points* in the squares move to *red points*. The *black points* marked with "*asterisk*" and "*open circle*" symbols represent the mismatches in images 1 and 2, respectively. (**b**) Average number of segmented inliers to the first estimated motion returned by the examined techniques. For A-LKS, the error bars are also shown. (**c**) Average computation times required to segment the first motion

the computation time of A-LKS is observed to be 10–1,000 times faster than other methods. The computation advantage gained via using A-LKS is especially substantial when numerous motions exist.

We have also examined the performance of the proposed method for segmenting multiple homographies using real data experiments. In the first experiment, shown in Fig. 9.5a, b, two images include three moving books. In the second experiment, shown in Fig. 9.5c, d, two images of the national library of Belarus at Minsk from two different perspectives include four moving planar surfaces. Using the well-known SIFT method [41], we first found a number of matching pixels between the corresponding images (shown by red crosses in Fig. 9.5a, c) and then used those points as data points for the A-LKS to estimate the parameters of, and segment based on the estimated motions. The results are shown in Fig. 9.5b, d which demonstrate that different motions in those experimented are correctly segmented.

We have also examined A-LKS in practical applications where circular or elliptic patterns need to be segmented and their parameters estimated. As it was mentioned in Sect. 9.2, the input image needs to be first processed and its edges detected. The outcome of edge detection is a black and white (binary) image and the pixels forming the edges are used as data points to segment the elliptic or circular patterns. An example is shown in Fig. 9.6a where a road image is taken by a camera mounted on an autonomous car, and various signs need to be detected and followed by the car. The sign in the image is the "one-way" sign and the first step in its detection is the detection of its elliptic perimeter. Figure 9.6b shows the binary image generated by the Canny edge detection method and the ellipse pattern detected and segmented by the A-LKS is highlighted by red dots.

Figure 9.6c, d demonstrates another example of ellipse fitting in a biomedical application where in a grey scale image of blood cells, the cells are needed to be segmented before statistics of their characteristics (e.g. radius) can be evaluated. The results of circle segmentation using the A-LKS are shown in Fig. 9.6d.

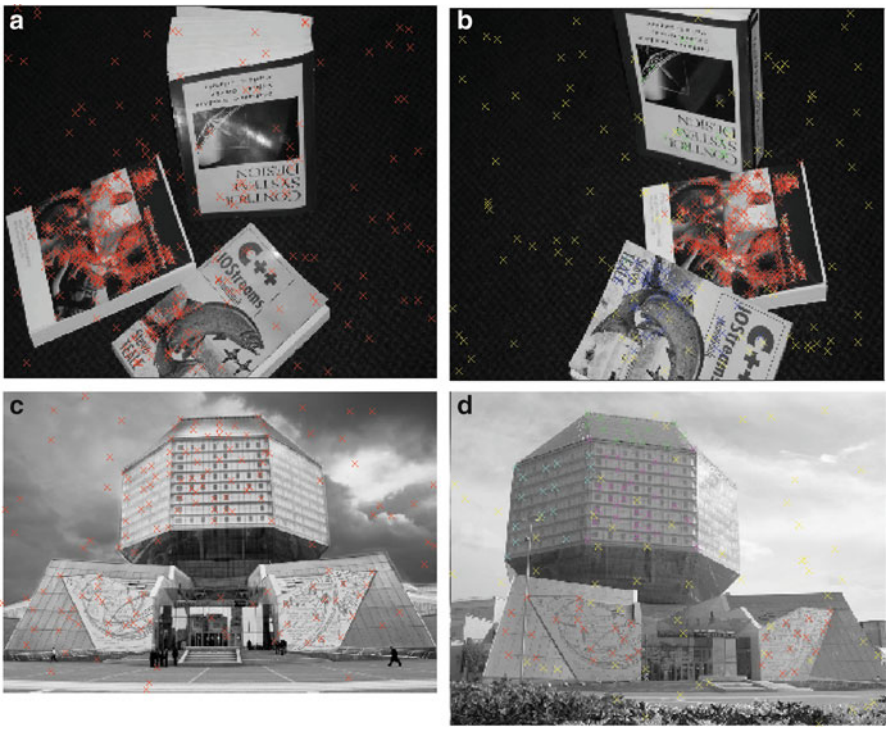

Fig. 9.5 Results of homography estimation: (**a**, **b**) Three books are placed on a table, an image is taken, then they are moved and the second image is taken. Matching pixels between the two images are found (*red crosses* in image (**a**)) and used as data points to find the homographies and segment them. (**c**, **d**) Two different images of the national library of Belarus from two angles. Different planar surfaces on the building undergo different homography motions which are segmented as shown in *different cross colours* in (**d**)

9.7 Conclusions

This chapter presented the general problem of parametric segmentation of multiple nonlinear structures existing in visual data. We introduced a unified formula for the distance of a data point from any model candidate. We also presented a new accelerated method for searching the parameter space for best model candidates that minimize a cost function. Our simulations showed that our method can segment several nonlinear structures in various applications with accuracies comparable to the state of the art; however, the speed of our method if far greater. This significant increase in the speed of computation makes our method an ideal candidate for computer vision applications where several nonlinear patterns need to be segmented and parametrically estimated in real time.

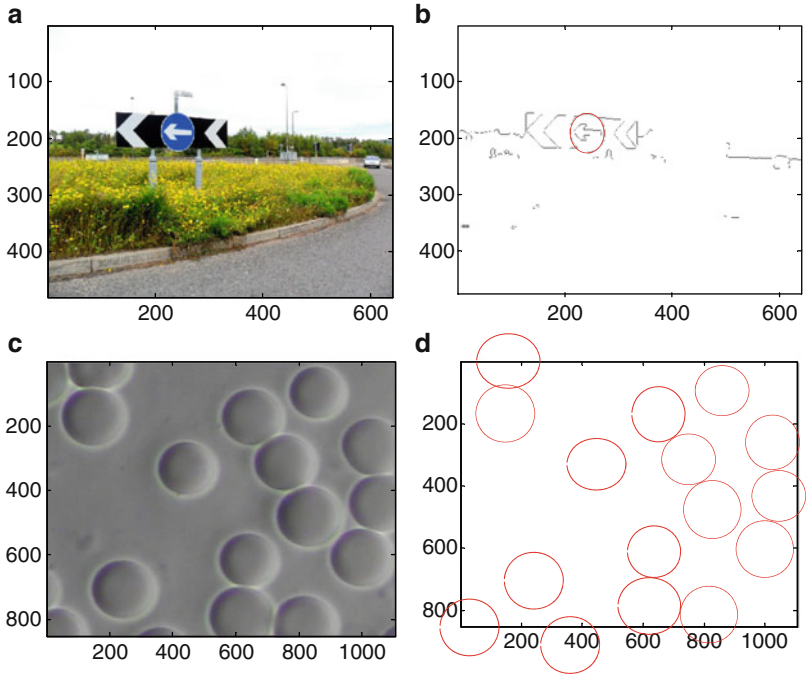

Fig. 9.6 (**a**) A road image taken by a camera mounted on an autonomous car which needs to detect and follow the road signs. (**b**) The binary image produced via applying Canny edge detection to the road image. The elliptic perimeter of the road sign has been detected and segmented by A-LKS and is highlighted in red in the image. (**c**) An image of blood cells. In a biomedical application, we need to know some statistics of the blood cells such as their number or distribution of their radii (**d**) The blood cells are segmented by A-LKS

References

1. Yu X, Bui TD, Krzyzak A (1994) Robust estimation for range image segmentation and reconstruction. IEEE Trans PAMI 16(5):530–538
2. Lee KM, Meer P, Park RH (1998) Robust adaptive segmentation of range images. IEEE Trans PAMI 20(2):200–205
3. Bab-Hadiashar A, Suter D (1999) Robust segmentation of visual data using ranked unbiased scale estimator. Robotica 17:649–660
4. Bab-Hadiashar A, Suter D (2000) Range and motion segmentation. In: Bab-Hadiashar A, Suter D (eds) Data segmentation and model selection for computer vision. Springer, New York, pp 119–142
5. Bab-Hadiashar A, Gheissari N (2004) Model selection for range segmentation of curved objects. In: Springer-Verlag lecture notes on computer science (LNCS), vol 3021 (European conference on computer vision - ECCV 2004). Springer, Prague, pp 83–94
6. Bab-Hadiashar A, Gheissari N (2006) Range image segmentation using surface selection criterion. IEEE Trans Image Process 15(7):2006–2018
7. Ding Y, Ping X, Hu M, Wang D (2005) Range image segmentation based on randomized Hough transform. Pattern Recogn Lett 26(13):2033–2041

8. Min J, Bowyer KW (2005) Improved range image segmentation by analyzing surface fit patterns. Comput Vis Image Understand 97(2):242–458
9. Wang H, Suter D (2004) MDPE: a very robust estimator for model fitting and range image segmentation. Int J Comput Vis 59(2):139–166
10. Han F, Tu Z, Zhu SC (2004) Range image segmentation by an effective jump-diffusion method. IEEE Trans Pattern Anal Mach Intell 26(9):1138–1153
11. Hesami R, Bab-Hadiashar A, Hoseinnezhad R (2010) Range segmentation of large building exteriors: a hierarchical robust approach. Comput Vis Image Understand 114(4):475–490
12. Ben MWYR X (2012) Dual-ellipse fitting approach for robust gait periodicity detection. Neurocomputing 79:173–178
13. Volkau I, Puspitasari F, Ng TT, Bhanu Prakash KN, Gupta V, Nowinski WL (2012) A simple and fast method of 3D registration and statistical landmark localization for sparse multi-modal/time-series neuroimages based on cortex ellipse fitting. Neuroradiol J 25(1):98–111
14. Sun JG, Zhou YC (2012) Skin color detection method based on direct least square ellipse fitting in CrCbCg space. Advanced Materials Research. 2012;366:28–31.
15. Zhang C, Sun C, Pham TD, Vallotton P, Fenech M (2010) Detection of nuclear buds based on ellipse fitting. In: DICTA 2010, pp 178–183
16. Marhaban MH, Kaid RS, Mohd SB (2010) Automatic estimation of gestational age in ultrasound images based on direct least-squares fitting of ellipse. IEEJ Trans Electr Electron Eng 5(5):569–573
17. Torr PHS (1998) Geometric motion segmentation and model selection. Philos Trans R Soc A 1321–1340
18. Hajder L, Chetverikov D (2006) Weak-perspective structure from motion for strongly contaminated data. Pattern Recogn Lett 27(14):1581–1589
19. Vidal R, Ma Y, Soatto S, Sastry S (2006) Two-view multibody structure from motion. Int J Comput Vis 68(1):7–25
20. Qian G, Chellappa R, Zheng Q (2005) Bayesian algorithms for simultaneous structure from motion estimation of multiple independently moving objects. IEEE Trans Image Process 14(1):94–109
21. Schindler K, Suter D (2006) Two-view multibody structure-and-motion with outliers through model selection. IEEE Trans Pattern Anal Mach Intell 28(6):983–995
22. Basah SN, Bab-Hadiashar A, Hoseinnezhad R (2009) Conditions for motion-background segmentation using fundamental matrix. IET Comput Vis 3(4):189–200
23. Bartoli A, Sturm P (2004) Nonlinear estimation of the fundamental matrix with minimal parameters. IEEE Trans Pattern Anal Mach Intell 26(3):426–432
24. Tsui CC (2004) An overview of the applications and solutions of a fundamental matrix equation pair. J Franklin Inst 341(6):465–475
25. Chin TJ, Yu J, Suter D (2012) Accelerated hypothesis generation for multistructure data via preference analysis. IEEE Trans Pattern Anal Mach Intell 34(4):625–638
26. Hartley R, Zisserman A (2003) Multiple view geometry in computer vision. Cambridge University Press, New York
27. Fischler MA, Bolles RC (1981) Random sample consensus: a paradigm for model fitting with applications to image analysis and automated cartography. Commun Assoc Comput Mach 24(6):381–395
28. Hesami R, Bab-Hadiashar A, Hosseinnezhad R (2007) A novel hierarchical technique for range segmentation of large building exteriors. In: Bebis G (ed) Third international symposium on visual computing (ISVC07). LNCS, vol 4842/2007. Springer, Lake Tahoe, pp 75–85
29. Hoseinnezhad R, Bab-Hadiashar A (2007) A novel high breakdown M-estimator for visual data segmentation. In: ICCV. IEEE, Rio de Janeiro
30. Hoseinnezhad R, Bab-Hadiashar A (2011) An M-estimator for high breakdown robust estimation in computer vision. Computer vision and image understanding (CVIU) 115(8):1145–1156

31. Tordoff B, Murray DW (2002) Guided sampling and consensus for motion estimation. In: ECCV, Copenhagen, pp 82–69
32. Nister D (2005) Preemptive RANSAC for live structure and motion estimation. Mach Vis Appl 16(5):321–329
33. Subbarao R, Meer P (2006) Subspace estimation using Projection based M-estimators over Grassman manifolds. In: Horst Bischof ALAP (ed) 9th European conference on computer vision (ECCV'06). Springer, Graz, pp 301–312
34. Chum O, Matas J, Kittler J (2003) Locally optimized RANSAC. In: Michaelis B, Krell G (eds) 25th DAGM symposium. Lecture notes in computer science (LNCS), vol 2781. Springer, Magdeburg, pp 236–243
35. Chum O, Matas J (2008) Optimal randomized RANSAC. PAMI 30(8):1472–1482
36. Goshen L, Shimshoni H (2008) Balanced exploration and exploitation model search for efficient epipolar geometry estimation. PAMI 30(7):1230–1242
37. Comaniciu D, Meer P (2002) Mean shift: a robust approach toward feature space analysis. PAMI 24(5):603–619
38. Wang H, Suter D (2004) Robust adaptive-scale parametric model estimation for computer vision. IEEE Trans PAMI 26(11):1459–1474
39. Hoseinnezhad R, Bab-Hadiashar A (2007) Consistency of robust estimators in multi-structural visual data segmentation. Pattern Recogn 40:3677–3690
40. Hoseinnezhad R, Bab-Hadiashar A, Suter D (2010) Finite sample bias of robust estimators in segmentation of closely spaced structures: a comparative study. J Math Imaging Vis 37(1):66–84
41. Lowe DG (2004) Distinctive image features from scale-invariant keypoints. IJCV 60(2):91–110

Chapter 10
Parametric Resonance: Application on Low Noise Mechanical and Electromechanical Amplifiers

Naser Nasrolahzadeh, Mohammad Fard, and Milad Tatari

Abstract Due to the growing demand for low noise signal amplification, developing mechanical and electromechanical parametric amplifiers is a topic of interest. Parametric amplification in mechanical domain refers to the method for amplifying the dynamic response of a mechanical sensor by modulating system parameters such as effective stiffness. Most of the studies in this regard have been focused on truncating equation of motion such that only linear terms remain. In this chapter, mathematical models of mechanical and electromechanical parametric amplifiers in the literature are reviewed. Then, the effect of nonlinearity is investigated by including a cubic nonlinearity on the governing equation of a classical degenerate parametric amplifier. To this end, the method of multiple scales (perturbation) has been utilized to calculate steady state solution of the nonlinear Mathieu-type equation. In addition, by determining the nature of singular points, stability analysis over the steady state response is performed. All the frequency response curves demonstrate a Duffing-like trend near the primary resonance of the system; however, the number of stable solutions changes with the parameters of the system. Furthermore, performance metrics of the system is analyzed in the presence of nonlinearity. The findings indicate that even very small nonlinearity term can dramatically decrease system performance as well as changing the relative phase in which maximum gain occurs.

N. Nasrolahzadeh (✉) • M. Tatari
School of Mechanical Engineering, College of Engineering, University of Tehran, Tehran, Iran
e-mail: n.nasrolahzadeh@ut.ac.ir; m.tatari@ut.ac.ir

M. Fard
School of Aerospace, Mechanical and Manufacturing Engineering, RMIT University, Melbourne, VIC, 3083, Australia
e-mail: mohammad.fard@rmit.edu.au

R.N. Jazar and L. Dai (eds.), *Nonlinear Approaches in Engineering Applications 2*,
DOI 10.1007/978-1-4614-6877-6_10,

10.1 Introduction

Parametric resonance occurs in mechanical systems with external excitation when parameters of the system are at certain values. Mathematically, the equations of motion for these systems are considered as the equation with time-dependence coefficients. In the mechanical context, this means stiffness, mass, or force is changing periodically. In fact, the word "parametric" refers to parameter-dependent behavior of the system [1]. Therefore, in these systems resonances are directly connected to certain values of the parameters. It seems that Faraday [2] was the first researcher who observed parametric resonance. According to his studies, a vertically oscillating fluid with forcing frequency close to the natural frequencies of the system generates horizontal waves. A pendulum with oscillating support can be considered as a classical example of parametric resonance, where the equation of motion leads to the Mathieu [3] equation in its linear form. A great majority of studies in this regard have been conducted to model parametrically excited systems [4, 5]. This has been done on various cases including, swing, ship, pendulum and structures. In addition, controlling the vibration of the system due to parametric resonance is another subject that has a long history. For instance, Oueini and Nayfeh [6] suggested a nonlinear feedback law to control the first mode vibrations of a cantilever beam that is under principal parametric excitation. Vibration suppression of a cantilever beam when it is excited externally as well as parametrically was investigated by Eissa and Amer [7]. Similarly, they used a control law based on cubic velocity feedback to deal with the problem of vibration suppression. Although the resonance phenomenon is usually considered as a threat in mechanical applications, the concept can be utilized as an effective tool to develop mechanical and electromechanical parametric amplifiers. Parametric amplification is a well-established concept in the field of electrical engineering and has been widely implemented; however, the technique has not received enough attention in mechanical engineering context.

In mechanical and electromechanical applications, parametric amplification refers to the method for amplifying the dynamic response of a mechanical sensor by modulating system parameters, including mass, stiffness, and damping [8]. In this approach, a system parameter such as spring constant that is effective in the vibration behavior of the sensor is controlled by parametric pumping to amplify the response amplitude of the system which is directly excited. Basically, there are two types of parametric amplifiers; degenerate and nondegenerate amplifiers. The former refers to those systems where the pumping frequency is tuned at twice of the direct excitation signal. The latter is used for the system when pumping signal is locked at frequencies that are different from twice of the direct signal. In addition, frequency of the direct excitation should be sufficiently close to the values that cause resonance response. It is worth mentioning that in a nonlinear system, the resonance response exists at the natural frequency of the system as well as its harmonics (e.g., sub-harmonics and super harmonics). Parametrically excited beams are very good cases in point to study parametric amplification in mechanical and

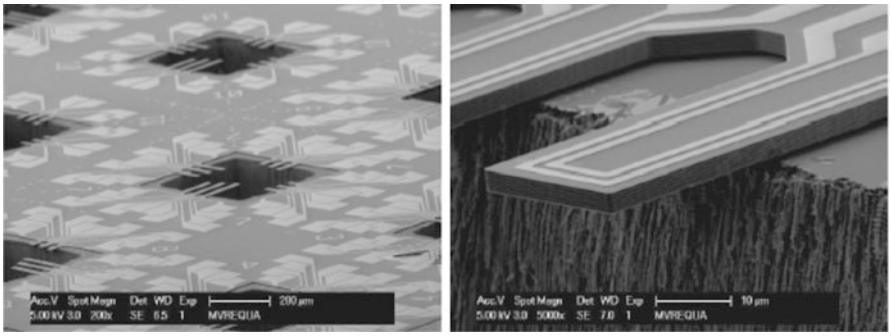

Fig. 10.1 Parametrically excited microbeams in a mass sensing device [10]

electromechanical sensors. In fact, microbeams are the most important element in almost all MEMS (Fig. 10.1). Jazar et al. [9] reviewed all important forces that affect the dynamic behavior of microbeams in MEMS and then formulated the equation of motion of the microbeam. Actually, the outcome of this study is the most general mathematical model for microbeams in MEMS. The model considers all attributes and therefore is somewhat complicated. However, this model can be simplified in different application when some terms are ignorable or a special case is going to be studied.

Classically, mechanical measurements are firstly converted to electrical signals by means of transducers and then the signal is electrically amplified. However, in some cases such as atomic force microscopy it is required to amplify the mechanical motion to improve the detection sensitivity. In fact, mechanical parametric amplification is mainly functional when the inherently noisy electrical amplifiers affect the measurement accuracy [11]. Therefore, in order to accomplish low noise signal amplification, various studies have been recently conducted on this topic to develop mechanical and electromechanical resonators, especially in MEMS/NEMS [8, 9, 11–17]. In different reported works in the literature, parametric amplification has been effectively implemented when the mechanical spring constant is modulated at twice the resonance frequency by external electrostatic forces [11, 18] or mechanical pumping [19]. Rugar and Grutter [11] were among the first researchers who study the parametric amplification in mechanical domain. They investigated noise squeezing as well as low noise amplification in a micro-cantilever beam. All other works in this regard are based on this study, where parametric amplifiers were investigated for torsional micro-resonators [16, 20], coupled micro-resonators [13], electric force microscope [21], and micro-cantilevers [8, 19]. Rhoads et al. [22] analytically and experimentally studied a macro-scale cantilever beam as a pure mechanical amplifier. In this degenerate amplifier, the base excitation was considered at transverse as well as axial directions. The analysis of this model is investigated by truncating the governing equation of motion of the system such that only linear terms remain. While the above-mentioned cases are fairly well understood in the linear domain, the impact of nonlinearities on different

parametric amplifiers has recently drawn many researchers attention [23]. Although in the linear analysis, the response of the system shows great performance and boundless gain for the amplifier, in a practical situation, as it was observed in experimental test of a macro-scale cantilever beam [22], the growth of the response is limited. This discrepancy between linear analysis and experimental results can be a result of inherit nonlinearities in the system that are not considered in the linearized equation of motion. Jazar et al. [9, 17] studied the dynamic behavior of an electrically actuated microcantilever. The study analyzes the steady state motion of the microcantilever with and w/o initial polarization and for linear and nonlinear condition (e.g., small and large vibration amplitude).

The main aim of this chapter is studying the behavior of the mechanical and electromechanical parametric amplifiers. Therefore, some mathematical models of mechanical and electromechanical parametric amplifiers in the literature are reviewed. To accomplish the analysis of these mathematical models, it is firstly required to acquire the necessary background about perturbation method. Therefore, the method of multiple scales is reviewed by solving a nonlinear forced oscillator as well as the Mathieu equation. Then, the nonlinear model of a classical degenerate parametric amplifier is introduced and the method of multiple scales is utilized to deal with the problem. In the next step, the stability analysis of the system is investigated. After that, in the results and discussion section, the outcomes of the perturbation solution are demonstrated and described; finally conclusion section will close the chapter.

10.2 Analytical Modeling of Mechanical and Electromechanical Parametric Amplifiers

In this section, the modeling process of some conducted studies regarding mechanical and electromechanical parametric amplifiers is briefly reported. In the scope of MEMS amplifiers, usually, the effective stiffness of the resonator is modulated electrostatically in such a way that parametric excitation arises. However, in macroscale cases base excitation can be used for this purpose. Therefore, reviewing some studies will help to get involved with the subject as well as understanding its applications.

Jazar et al. [9] have defined all important forces that affect the dynamic behavior of microbeams in MEMS and then formulated the equation of motion of the microbeam. According to this conducted study the general non-dimensionalized equation of motion of the microbeam is as following:

$$\ddot{Y} + \left(\zeta + a_6 \tfrac{r}{1+r^2}\right)\dot{Y} + \left(1 + b_3 - a_7 \tfrac{r}{1+r^2}\right) Y + \alpha Y^3 + a_4 Y^2 \dot{Y} + a_5 (1 - Y) Y = \tfrac{1}{(1-Y)^2}[(\mu + \lambda) + 2\sqrt{2\mu\lambda}\sin(r\tau) - \lambda\cos(2r\tau)] \tag{10.1}$$

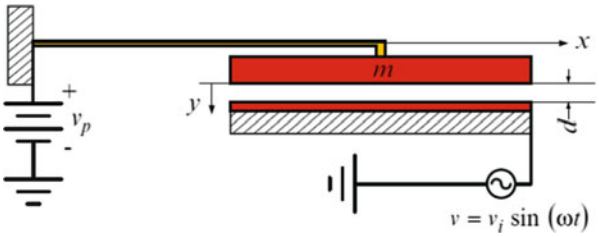

Fig. 10.2 Schematic of electrically actuated microcantilever [9]

where Y stands for the lateral motion, τ represents time, a_i are constant that can be calculated from the geometry and properties of the beam, b_3 and α are the terms for initial stretch and nonlinear stiffness, $r = \frac{\omega}{\omega_1}$, μ and λ are, respectively, representatives of the polarization (v_p) and modulating (v) voltages in nondimensenalized form (Fig. 10.2).

This equation considers the most important forces that affect the dynamic behavior of the electrically actuated microbeam. These are inertia, rigidity, electrostatic, viscous, internal tension, squeeze film, and thermal forces. Enthusiastic readers can find detailed procedure to extract the general equation of motion (10.1) in [9]. There are some other less important forces such as fringing, van der Waals, and Casimir that are in secondary level in comparison with the considered forces. Moreover, the equation can be pruned to (10.2) if one neglects squeeze-film $\{a_6 \frac{r}{1+r^2}\dot{Y} + a_7 \frac{r}{1+r^2} Y\}$, thermal forces $\{a_4 Y^2 \dot{Y} + a_5 (1-Y) Y\}$, and initial stretch.

$$\ddot{Y} + \zeta\dot{Y} + Y + \alpha Y^3 = \frac{1}{(1-Y)^2}((\mu+\lambda) + 2\sqrt{2\mu\lambda}\sin(r\tau) - \lambda\cos(2r\tau) \tag{10.2}$$

Assuming no polarization voltage, the governing equation is more simplified as following:

$$\ddot{Y} + \zeta\dot{Y} + Y + \alpha Y^3 = \frac{1}{(1-Y)^2}(\lambda - \lambda\cos(2r\tau) \tag{10.3}$$

By expanding the electrostatic term in series form as (10.4), the complexity of this equation of motion can be reduced.

$$\frac{1}{(1-Y)^2} = 1 + 2Y + 3Y^2 + 4Y^3 + 5Y^4 + \ldots \tag{10.4}$$

A simple linear analysis requires expansion of the series up to $O(Y^2)$ provided that the term αY^3 is also neglected from the left-hand side. On the other hand, in nonlinear analysis, due to the third order term of Y in the left-hand side, it

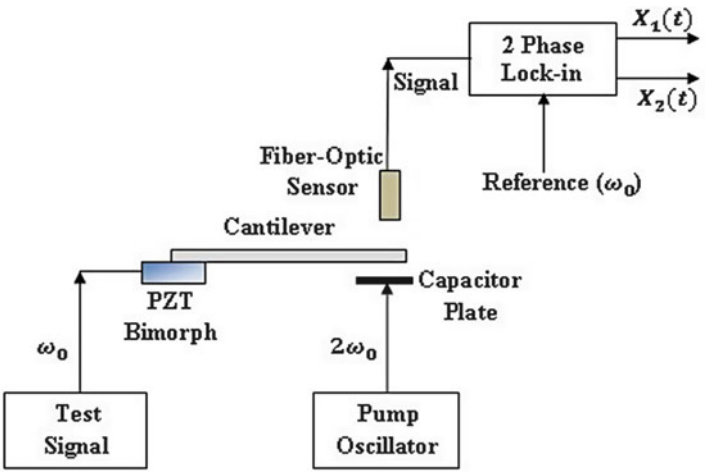

Fig. 10.3 The block diagram of an electromechanical parametric amplifier. Cantilever resonator is pumped by electrostatic force of the capacitor plate and the piezoelectric bimorph is used for the direct excitation [11]

is reasonable to expand the series term up to $O(Y^4)$. However, many researchers have neglected nonlinear terms of the electrostatic force while they have considered the cubic nonlinearity for stiffness of the microbeam. Although this assumption reduces the accuracy of the model, but gives a straightforward nonlinear Mathieu-type equation that eases investigation of the dynamic behavior of the system. In this condition, the microbeam is simply modeled as a mass, varying stiffness, and damper system.

Rugar and Grutter [11] were among the first researchers who mentioned the parametric amplification in mechanical domain. In the accomplished work by them according to Fig. 10.3, the silicon microbeam is pumped electrically and a piezoelectric bimorph is used for the direct excitation. The parametric modulation is carried out by means of a capacitor with time-varying voltage V (t) on it. Thus, the effective stiffness of the beam is expressed as follows:

$$k(t) = k_0 + k_p(t) \quad \text{and} \quad k(p) = \frac{\partial F_e}{\partial x} = \frac{1}{2}\frac{\partial^2 C}{\partial x^2}\,(V(t))^2 \tag{10.5}$$

where F_e represents electrostatic force, C stands for the electrode-cantilever capacitance, and x is the displacement of the beam.

The equation of motion of the cantilever beam was considered as a single degree of freedom mass, damper, and time-varying stiffness oscillator as follows:

$$m\ddot{x} + \frac{m\omega_0}{Q}\dot{x} + \left(k_0 + k_p(t)\right)x = F(t) \tag{10.6}$$

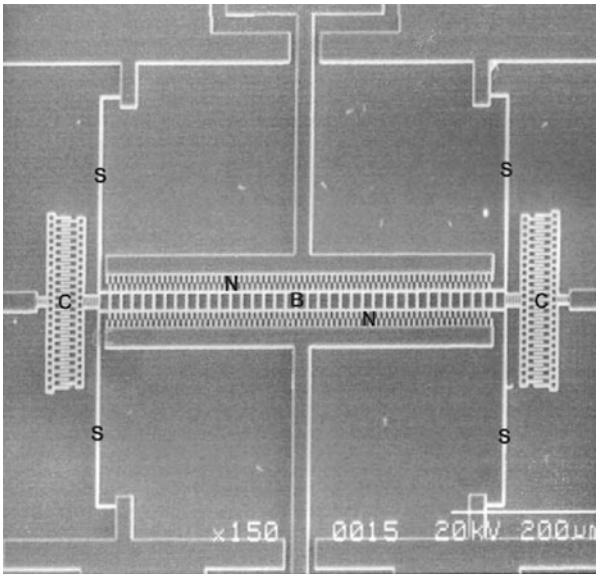

Fig. 10.4 An in-plane parametrically excited oscillator. In this micrograph S indicates the folded beam springs, C demonstrates the two sets of interdigitated comb finger banks, B shows on the backbone, and N exhibits non-interdigitated comb fingers [18]

where F (t) = $F_0 \cos(\omega_0 t + \phi)$ is the direct excitation signal, $k_p(t) = \Delta k \sin 2\omega_0 t$, Q is the quality factor of resonance, x is the cantilever displacement, and ω_0 is the unforced resonance frequency of the cantilever beam, that is ${\omega_0}^2 = \frac{k}{m}$. Expressing the damping factor c as $\frac{m\omega_0}{Q}$ is conventional because the right condition for the occurrence of parametric resonance can be intuitively understood [10]. Generally speaking, increasing quality factor broadens the region of instability.

Zhang et al. [18] investigated an in-plane parametrically excited mass sensor with electrostatic force as the driving force. Figure 10.4 depicts a scanning electron micrograph of the oscillator. As it can be seen, there are two sets of parallel interdigitated comb finger banks on either end of the backbone and two sets of non-interdigitated comb fingers on each side. Applying a time-varying voltage to the non-interdigitated fingers as pumping signal leads to modulation of the stiffness of the system and parametric resonance.

In order to derive equation of motion of the sensor, similar to the previous case, a simple mass, spring, and damper system was considered as follows:

$$m\ddot{x} + c\dot{x} + F_k(x) = F_e(t, x) \tag{10.7}$$

$$F_k(x) = k_1 x + k_2 x^3 \tag{10.8}$$

$$F_e(x, t) = -\left(kr_1 x + kr_2 x^3\right) {V_A}^2 (1 + \cos(\omega t)) \tag{10.9}$$

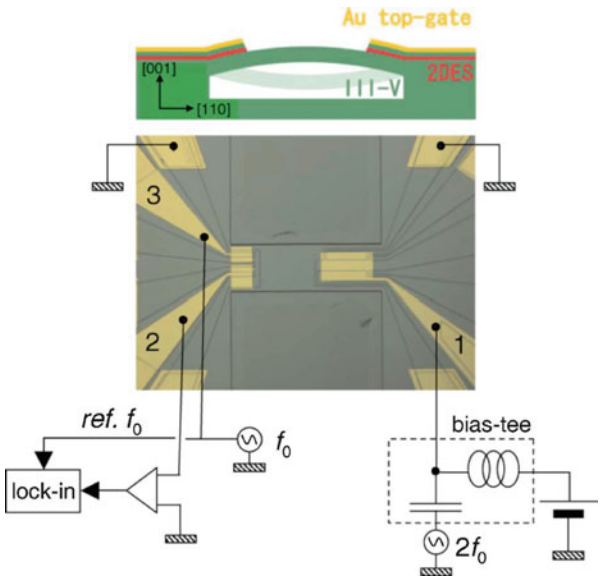

Fig. 10.5 An out-of-plane electromechanical microbeam oscillator. Three Schottky electrodes at clamped points for parametric pumping (gate 1), resonance detection (gate 2), and direct excitation (gate 3) [12]

where the letter k is used for the mechanical stiffness and kr represents electrostatic stiffness. Finally they have reported the following non-dimensional expression for the normalized equation of motion of the sensor.

$$x'' + \zeta x' + (\beta + 2\delta \cos(2\tau))x + (\delta_3 + \delta'_3 \cos(2\tau))x^3 = 0 \tag{10.10}$$

Here, prime stands for derivative with respect to τ. Note all the Greek letters coefficient in this nonlinear Mathieu equation are of small order (e.g., O(ε)), but the β that is O(1).

Mahboob et al. [12] investigated a electromechanical oscillator as it is shown in Fig. 10.5. As it is observed, the resonator is a clamped–clamped microbeam with Schottky contacted two-dimensional electron systems (2DES) in clamped points. In this parametric amplifier, the stiffness modulating transducer is integrated into the mechanical element that can reduce the size of the resonator. The excitation of the oscillator is accomplished when an AC voltage is applied between the top gate and the 2DES. In fact, the piezoelectric effect leads to bending of the beam and resonance at the frequency of the applied voltage which is compatible with the fundamental mode of the beam.

In this case also the electromechanical resonator has been simplified as a mass, damper, and time-varying spring system. Thus, similar to the previous works, the governing equation of this parametric amplifier is reported to be as:

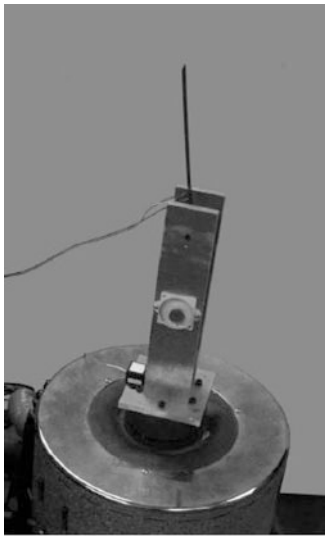

Fig. 10.6 A base excited cantilever beam as a macroscale mechanical parametric amplifiers [22]

$$\ddot{x} + \frac{\omega_0}{Q}\dot{x} + {\omega_0}^2\left(1 + \sqrt{2}C\,\lambda\,\sin(2\omega_0 t)\right)x = \eta\ \sin(\omega_0 t + \phi) \tag{10.11}$$

where the $\sqrt{2}C\lambda\,\sin(2\omega_0 t)$ is pumping signal that is implemented from gate 1 (see Fig. 10.5), the $\eta\ \sin(\omega_0 t + \phi)$ is direct excitation signal via gate 3 that arises primary resonance of the beam.

Rhoads et al. [22] studied the macroscale mechanical parametric amplifiers in the case of a base excited cantilever beam. In this degenerate amplifier, the base excitation, according to Eq. (10.12), was considered at transverse (v_p) as well as axial (u_p) directions (Fig. 10.6).

This is carried out by installing the cantilever beam on a shaker that generates two sinusoidal signals as follows:

$$x_p = A\cos(\Omega t + \Phi) + B\cos(2\Omega t) \tag{10.12}$$

$$u_p = x_p \sin\alpha,\ v_p = x_p\cos\alpha \tag{10.13}$$

where the signal with frequency Ω is used for direct excitation and the signal with frequency 2ω is used for parametric pumping. By using energy method that can be found in detail in [22] the governing equation of motion of the system for the first mode is reported as:

$$\begin{aligned}\ddot{z} + 2\varepsilon\zeta\dot{z} + (1 + \varepsilon\lambda_2\Omega^2\cos(2\Omega t) + \varepsilon\lambda_1\Omega^2\cos(\Omega t + \Phi))z \\ = \varepsilon\eta_1\Omega^2\cos(\Omega t + \Phi) + \varepsilon\eta_2\Omega^2\cos(2\Omega t)\end{aligned} \tag{10.14}$$

As evident, this equation of motion is also similar to other reviewed cases in which stiffness of the mechanical resonator is modulated by a pumping signal. Therefore, the study of a general equation of motion similar to (10.6), (10.10), (10.11), and (10.14) might be useful to understand the effects of different parameters of the system on the behavior of mechanical and electromechanical parametric amplifiers. In the next sections, the general form of a classical degenerate parametric amplifier will be investigated.

10.3 Mathematical Background

In this section, prerequisite math to deal with governing equations of mechanical parametric amplifiers are introduced. For the sake of investigating these systems, one needs to have an appropriate knowledge about solving weakly nonlinear oscillators via perturbation techniques. There are various perturbation methods including Poincare, multiple scale, averaging and harmonic balance. These methods are vastly applied on oscillating systems in order to solve their nonlinear equations of motion. There is no denying that the perturbation method is useful in the case of weak nonlinearity and the resulting analytical solution is an approximation around the corresponding linear system. Due to popularity of the method of multiple scales in comparison with others, we review its basic concepts to solve weakly nonlinear equations. The enthusiastic readers can acquire deep understanding of perturbation technique by studying perturbation methods by Nayfeh [24].

10.3.1 The Method of Multiple Scales

The main idea of this method is that the expansion of the response is the function of multiple independent variables. This is carried out by introducing fast-scale and slow-scale variables and treating them as independent variables. It is carried out by letting:

$$T_n = \varepsilon^n t \quad \text{for} \quad n = 0, 1, 2, \ldots \tag{10.15}$$

Here, T_0 is a fast time scale and T_1 is a slow time scale describing variation in the response of the system. Thus, the derivative with respect to t can be expressed in the new scales by using partial derivatives as follow:

$$\frac{d}{dt} = \frac{dT_0}{dt}\frac{\partial}{\partial T_0} + \varepsilon\frac{dT_1}{dt}\frac{\partial}{\partial T_1} + \ldots = D_0 + \varepsilon D_1 + \ldots \tag{10.16}$$

where $D_{k=}\frac{\partial}{\partial T_k}$, subsequently we have:

$$\frac{d^2}{dt^2} = D_0{}^2 + 2\varepsilon D_0 D_1 + \ldots \tag{10.17}$$

Now, one can express the response (x) in the form of new variables according to

$$x(t,\varepsilon) = x(T_0, T_1, \ldots, T_n, \varepsilon) = \sum_{i=0}^{n} \varepsilon^i x(T_0, T_1, \ldots, T_n) + O(\varepsilon^{n+1}) \tag{10.18}$$

It is worth mentioning that the number of independent variables is corresponding to the expansion order. In other words, when we expand the response to $O(\varepsilon^3)$, the T_0, T_1 and T_2 time scales are required.

In order to use the method of multiple scale for solving equations of motion such as (10.11), it might be a wise decision to start with a directly excited oscillating systems. It is mainly because one needs to understand the different resonance cases that can be occurred in a nonlinear oscillating system under direct excitation (e.g., primary resonance, sub-harmonic and super harmonic cases). Then, we can apply the method on a simple parametrically excited system to solve the Mathieu equation. Due to the time-varying coefficient of the mathematical model regarding parametric amplifiers, this could be a useful step to acquire the required insight into their Mathieu-type nature. Finally, the combined excitation that arises in the degenerate parametric amplifiers can be easily managed.

10.3.2 Direct Excitation for System with Cubic Nonlinearity

Forced vibration of an oscillating system with governing equation such as (10.19) is investigated. This can be the representative of a slightly damped motion of a particle that is attached to a spring with hardening nonlinearity. For the sake of simplicity, the natural frequency of the system is considered to be unity.

$$\ddot{x} + x + 2\varepsilon\zeta\dot{x} + \varepsilon\alpha x^3 = \varepsilon\eta\cos\Omega t \tag{10.19}$$

By expressing approximate solution of the system in different time scales according to the multiple scales method and expanding the response to the order of $O(\varepsilon^2)$, we have:

$$x(t,\varepsilon) = x_0(T_0, T_1) + \varepsilon x_1(T_0, T_1) + O(\varepsilon^2) \tag{10.20}$$

Now, by applying new variables time derivatives and separating the terms of the resultant equation in accordance with their orders, one can obtain following equations for $O(1)$ and $O(\varepsilon)$.

$$O(1): \quad D_0^2 x_0 + x_0 = 0 \tag{10.21}$$

$$O(\varepsilon): \quad D_0^2 x_1 + x_1 = -2D_0 D_1 x_0 - \alpha x_0^3 - 2\zeta x_0 + \eta \cos(\Omega T_0) \tag{10.22}$$

The solution of Eq. (10.21) can be expressed as:

$$x_0 = \frac{1}{2} A(T_1) e^{iT_0} + cc. \tag{10.23}$$

where $A(T_1)$ is a complex-valued quantity and cc. stands for complex conjugate of the first term. By using the above expression for x_0 in the second equation, the undetermined function $A(T_1)$ is obtained. This can be accomplished when the expressions which produce secular term in Eq. (10.22) are put equal to zero. The process of eliminating secular terms depends on the frequency of the direct excitation. Up until now, we have not assumed the excitation frequency to be equal to a predefined value. This value is important for solving the above perturbation problem because different values for Ω lead to different responses. In fact, in a nonlinear system, the resonance response exists at the natural frequency of the system as well as its harmonics. Generally speaking, there are three cases that may occur:

- Primary Resonance Case: it refers to the situation when excitation frequency is near to the natural frequency of the system ($\Omega \cong \omega$).
- Sub-Harmonic Resonance Cases: it arises when excitation frequency is near the integer multiples of the natural frequency ($\Omega \cong \mathbf{n}\omega$ and $\mathbf{n} = 2, 3, \ldots$).
- Super-Harmonic Resonance Cases: it is opposite concept to the previous case and occurs when the frequency of the driving excitation is close to an integer fraction of the natural frequency ($\cong \frac{\omega}{\mathbf{n}}$ and $\mathbf{n} = 2, 3, \ldots$).

It is worth mentioning that as the nonlinearity of the system grows to higher orders, the effects of sub-harmonic and super-harmonic cases will be more noticeable. In this place, the solution is progressed for the case of primary resonance. Therefore, by substituting x_0 in Eq. (10.22) as well as assuming $\Omega = 1 + \varepsilon\sigma$, where $\sigma = O(1)$, we will have:

$$D_0^2 x_1 + x_1 = \{-(2i\left(A' + \zeta A\right) + 3\alpha A^2 \bar{A}) \exp(iT_0) - \alpha A^3 \exp(3iT_0) + \frac{\eta}{2} \exp(i(T_0 + \sigma T_1))\} + cc \tag{10.24}$$

where prime denotes the derivative with respect to T_1 (e.g., $A' = D_1 A$) and $\bar{A}$ is complex conjugate of A. The secular term is eliminated when the terms that are the coefficient of $\exp(iT_0)$ are put equal to zero, thus:

$$2i\left(A' + \zeta A\right) + 3\alpha A^2 \bar{A} + \frac{\eta}{2} \exp(i\sigma T_1) = 0 \tag{10.25}$$

Now by expressing A in polar form as

$$A = \frac{1}{2} a\,(T_1)\, e^{i\beta(T_1)} \tag{10.26}$$

where a and β are real values; by substituting it into Eq. (10.25), one can separate real and imaginary parts that lead to a set of differential equation as follows:

$$a' = -a\zeta + \frac{\eta}{2} \sin\left(\sigma T_1 - \beta\right) \tag{10.27}$$

$$a\beta' = \frac{3\alpha}{8} a^3 - \frac{\eta}{2} \cos\left(\sigma T_1 - \beta\right) \tag{10.28}$$

Finally, the first approximate solution can be expressed as $x_0 + O(\varepsilon)$, in which the a and β are calculated from steady state solution of Eqs. (10.27) and (10.28).

10.3.3 Parametric Excitation of Linear Systems

We will apply the method of multiple scales on the Mathieu equation where natural frequency is a time-varying parameter according to Eq. (10.29). This parametrically excited linear oscillator can simulate small amplitude oscillations of a swing whose natural frequency is varying periodically in time.

$$\ddot{x} + \left(\omega^2 + \varepsilon\lambda \cos nt\right) x = 0 \tag{10.29}$$

The Mathieu equation is very interesting for researchers [1, 14, 25] because an instability phenomenon occurs when natural frequency of the system (ω) and frequency of the excitation (n) are tuned at certain values. Here, we consider a special case that is $n = 2$. In this case when $\omega^2 \neq m^2$, $m = 1, 2, 3$, the equilibrium $x = 0$ is stable near $\varepsilon = 0$; however, for some cases when $\omega^2 \cong k^2$, the solution is unstable [1, 4]. In this place, the case $m = 1$ that leads to $\omega^2 = 1 + \varepsilon\sigma$ when $\sigma = O(1)$ is studied. This is mainly because we will investigate the degenerate parametric amplifiers in the next section. It is important to recall that in these types of amplifiers, the frequency of the parametric excitation is tuned at twice of the natural frequency of the system that is so-called principal resonance case of the system. Thus, Eq. (10.30) is solved by the method of multiple scales in order to discuss about σ and ε parameters for which the instability phenomenon arises.

$$\ddot{x} + (1 + \varepsilon\sigma + \varepsilon\lambda \cos 2t)\, x = 0 \tag{10.30}$$

By expanding the response to the order of $O(\varepsilon^2)$, we have:

$$x\,(t, \varepsilon) = x_0\,(T_0, T_1) + \varepsilon x_1\,(T_0, T_1) + O(\varepsilon^2) \tag{10.31}$$

By substituting (10.31) into (10.30) and separating the terms of O(1) and O(ε), one can obtain:

$$\mathrm{D}_0^2 \mathrm{x}_0 + \mathrm{x}_0 = 0 \tag{10.32}$$

$$D_0^2 x_1 + x_1 = -2D_0 D_1 x_0 - (\sigma + \lambda \cos(2T_0))\, x_0 \tag{10.33}$$

The solution of Eq. (10.32) is:

$$\mathrm{x}_0 = \frac{1}{2}\mathrm{A}(\mathrm{T}_1)\, \mathrm{e}^{\mathrm{iT}_0} + \mathrm{cc}. \tag{10.34}$$

In this step, by using this solution in the second equation and expressing the cosine term in its exponential form, we find:

$$\begin{aligned} D_0^2 x_1 + x_1 = \{ & -i A' \exp(i T_0) - \frac{1}{2} A\sigma \exp(i T_0) \\ & - \frac{A}{4}\lambda \exp(3i T_0) - \frac{\bar{A}}{4}\lambda \exp\{i\,(T_0)\} + cc \end{aligned} \tag{10.35}$$

The solution for x_1 is periodic when the secular terms are eliminated from the above equation, which implies that:

$$-i A' - \frac{A}{2}\sigma - \frac{\bar{A}}{4}\lambda = 0 \tag{10.36}$$

Now by expressing $\mathrm{A} = \mathrm{a} + \mathrm{ib}$ and substituting it into Eq. (10.36), one can separate real and imaginary parts that lead to a set of differential equation as follows:

$$a' = \left(-\frac{\sigma}{2} + \frac{\lambda}{4}\right) b \tag{10.37}$$

$$b' = \left(\frac{\sigma}{2} + \frac{\lambda}{4}\right) a \tag{10.38}$$

The solutions of this set of equation are proportional to $\mathrm{e}^{(\mp s T_1)}$, where $\mathrm{s} = \frac{1}{2}\sqrt{\frac{\lambda^2}{4} - \sigma^2}$. Hence, we find that solution is unstable or periodic solution does not exist when $|\sigma| < \lambda/2$.

10.3.4 The Mathieu Equation with Viscous Damping

Since there is always an amount of damping in the mechanical systems, a small viscous damping term can be considered in the Mathieu equation as:

$$\ddot{x} + \varepsilon\zeta\dot{x} + (1 + \varepsilon\sigma + \varepsilon\lambda\cos 2t)\, x = 0 \tag{10.39}$$

If the solving procedure is repeated for this case, one finds that the following terms that produce secular terms should be eliminated:

$$-iA' - \frac{A}{2}\sigma - \frac{\bar{A}}{4}\lambda - i\frac{A}{2}\zeta = 0 \tag{10.40}$$

Similar to the last case, if we take A = a + ib, then

$$a' = -\frac{\zeta}{2}a + \left(\frac{\lambda}{4} - \frac{\sigma}{2}\right)b \tag{10.41}$$

$$b' = \left(\frac{\lambda}{4} + \frac{\sigma}{2}\right)a - \frac{\zeta}{2}b \tag{10.42}$$

This leads to $s = -\frac{\zeta}{2} \mp \frac{1}{2}\sqrt{\frac{\lambda^2}{4} - \sigma^2}$ that is the zeros of the characteristics equation; the characteristics equation is calculated from:

$$\begin{vmatrix} s + \frac{\zeta}{2} & -\frac{\lambda}{4} + \frac{\sigma}{2} \\ -\frac{\lambda}{4} - \frac{\sigma}{2} & s + \frac{\zeta}{2} \end{vmatrix} = 0 \tag{10.43}$$

Thus, the trivial solution is stable when $\zeta > 0$ and $\lambda^2 < 4\left(\zeta^2 + \sigma^2\right)$. As evident, when the damping term is omitted that leads to previous condition for undamped system. The critical condition ($\lambda = 2\sqrt{\zeta^2 + \sigma^2}$) demonstrates the curve in the (σ, λ) plane that separate stable and unstable solutions; Fig. 10.7 depicts the instability bounds with and without damping in the (σ, λ) plane for different values of damping. As it can be seen, when $0 < \zeta < \frac{\lambda}{2}$, the instability region has been shifted up, and for $\zeta > \frac{\lambda}{2}$ the instability domain does not appear.

10.4 System Model

According to governing equations of motion for reviewed mechanical and electromechanical parametric amplifiers in Sect. 10.2, the general form of governing equation for a linear degenerate amplifier may be expressed as Eq. (10.44).

$$\ddot{z} + 2\varepsilon\zeta\dot{z} + z + \varepsilon\lambda\cos(2\Omega t)\, z = \varepsilon\eta\cos(\Omega t + \Phi) \tag{10.44}$$

where z represents the mechanical resonators displacement, λ is the pumping signal amplitude, ζ considered for linear dissipation effects, η *and* Ω represent direct excitation signal amplitude and frequency, t represents non-dimensional time

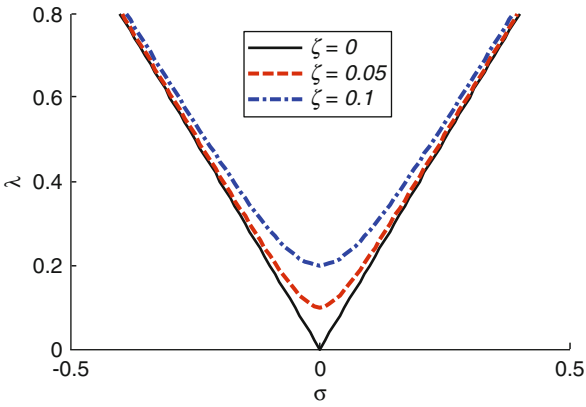

Fig. 10.7 First order approximation of instability bounds without and with damping

variable, Φ stands for relative phase parameter which is necessary for amplifier tuning. This simple equation is a good case in point to investigate the effects of different parameters in the response and performance of the different parametric amplifiers.

Similarly, nonlinear parametric amplifiers can be studied by this equation provided that compatible term of nonlinearity to be added to the linear equation. Since the cubic nonlinearity is a typical nonlinear term in mechanical cases, especially structural vibrations, the basic equation is amended by a cubic nonlinear term as Eq. (10.45), where α is a parameter for highlighting the order of effective nonlinearity in the system. In addition, for the sake of simplification of the analysis and according to the conducted studies [18], each of nonlinearity, dissipation, and excitation terms has been considered to be O (ε). It is indisputable that perturbation method has proved its effectiveness for these forms of equation. It should be noted that this problem is investigated in [23] by the method of averaging. Here, similar to previous cases in this chapter, the method of multiple scales is used to deal with the problem. Furthermore, the stability analysis of the steady state solution is studied.

$$\ddot{z} + 2\varepsilon\zeta\dot{z} + z + \varepsilon\lambda\cos(2\Omega t)\, z + \varepsilon\alpha z^3 = \varepsilon\eta\cos(\Omega t + \Phi) \tag{10.45}$$

10.4.1 Perturbation Solution

By expanding z as the following expression and substituting it into Eq. (10.45), one can obtain Eqs. (10.47) and (10.48) for terms with same order.

$$z(T_0, T_1) = Z_0(T_0, T_1) + \varepsilon Z_1(T_0, T_1) + \ldots \tag{10.46}$$

$$O(1) : D_0^2 Z_0 + Z_0 = 0 \tag{10.47}$$

$$O(\varepsilon): D_0^2 Z_1 + Z_1 = -2D_0 D_1 Z_0 - \lambda Z_0 \cos(2\Omega T_0) - \alpha Z_0^3 - 2\zeta Z_0 + \eta \cos(\Omega T_0 + \Phi) \tag{10.48}$$

The solution of Eq. (10.42) can be expressed as:

$$\mathrm{Z}_0 = \frac{1}{2}\mathrm{A}(\mathrm{T}_1)\,\mathrm{e}^{\mathrm{iT}_0} + \mathrm{cc} \tag{10.49}$$

where A (T_1) is a complex quantity and cc. stands for complex conjugate of the first term. In addition, for the sake of investigating system behavior around its natural frequency, a detuning parameter (σ) is defined, and direct excitation frequency is considered to be $\Omega = 1 + \varepsilon\sigma$. By taking this measure the frequency response curves of the system can be extracted. These curves are very useful for demonstrating response variation with parameters of the system. With this in mind and substituting (10.49) into Eq. (10.48), one can find the expressions which produce secular terms are eliminated if:

$$-2i\left[A' + \zeta A\right] - \frac{1}{2}\lambda \bar{A} e^{i2\sigma T_1} - 3\alpha A^2 \bar{A} + \frac{1}{2}\eta e^{i(\sigma T_1 + \Phi)} = 0 \tag{10.50}$$

Consider $A(T_1)$ in polar form as (10.51) in order to manage Eq. (10.50).

$$\mathrm{A} = \frac{1}{2}\mathrm{a}(\mathrm{T}_1)\,\mathrm{e}^{\mathrm{i}\beta(\mathrm{T}_1)} \tag{10.51}$$

where a and β are real-valued quantities. Substituting (10.51) into Eq. (10.50), one can separate real and imaginary parts; then, a little manipulation over two equations yields:

$$a' = -\frac{1}{4}\lambda a \sin 2(\sigma T_1 - \beta) - a\zeta + \frac{1}{2}\eta \sin(\sigma T_1 - \beta + \Phi) \tag{10.52}$$

$$a\beta' = \frac{1}{4}\lambda a \cos 2(\sigma T_1 - \beta) + \frac{3\alpha}{8}a^3 - \frac{1}{2}\eta \cos(\sigma T_1 - \beta + \Phi) \tag{10.53}$$

Next, by letting $\gamma = \sigma T_1 - \beta$, Eqs. (10.52) and (10.53) will be transformed into an autonomous system, the results can be expressed as:

$$a' = -\frac{1}{4}\lambda a \sin 2\gamma - a\zeta + \frac{1}{2}\eta \sin(\gamma + \Phi) \tag{10.54}$$

$$a\gamma' = a\sigma - \frac{1}{4}\lambda a \cos 2\gamma - \frac{3\alpha}{8}a^3 + \frac{1}{2}\eta \cos(\gamma + \Phi) \tag{10.55}$$

With Eqs. (10.54) and (10.55) in hand, the steady state solution for the system of interest can be obtained by setting $(a', \gamma') = (0, 0)$. Generally, one may find a

closed form expression solution for pumping off (i.e., $\lambda = 0$) situation in parametric amplifiers; however, steady state solution of the considered degenerate amplifier when $\lambda \neq 0$ should be evaluated numerically.

10.4.2 Stability Analysis

In order to study the stability of steady state motion, one can impose a small perturbation to steady state solution and investigate the results by determining the nature of singular points [4]; therefore, we let,

$$a = a_0 + a_1 \tag{10.56}$$

$$\gamma = \gamma_0 + \gamma_1 \tag{10.57}$$

where a_0 & γ_0 represent the singular point and a_1 & γ_1 are small perturbations over them. By substituting given expression for a & γ into Eqs. (10.54) and (10.55) and knowing that a_0 & γ_0 satisfy steady state solution as well as neglecting nonlinear terms, the following equations can be obtained.

$$a'_1 = -\left(\zeta + \frac{1}{4}\lambda \sin 2\gamma_0\right) a_1 + \left(\frac{1}{2}\eta \cos(\gamma_0 + \Phi) - \frac{1}{2}\lambda a_0 \cos 2\gamma_0\right) \gamma_1 \tag{10.58}$$

$$\gamma'_1 = -\left(\frac{3}{4}\alpha a_0 + \frac{\eta}{2{a_0}^2} \cos(\gamma_0 + \Phi)\right) a_1 + \left(\frac{1}{2}\lambda \sin 2\gamma_0 - \frac{\eta}{2a_0} \sin(\gamma_0 + \Phi)\right) \gamma_1 \tag{10.59}$$

These equations can be demonstrated in matrix form such that,

$$\begin{Bmatrix} a'_1 \\ \gamma'_1 \end{Bmatrix} = \begin{bmatrix} \mathrm{T}_1 & \mathrm{T}_2 \\ \mathrm{T}_3 & \mathrm{T}_4 \end{bmatrix} \begin{Bmatrix} a_1 \\ \gamma_1 \end{Bmatrix} \tag{10.60}$$

where

$$\mathrm{T}_1 = -\left(\zeta + \frac{1}{4}\lambda \sin 2\gamma_0\right) \tag{10.61}$$

$$\mathrm{T}_2 = \left(\frac{1}{2}\eta \cos(\gamma_0 + \Phi) - \frac{1}{2}\lambda a_0 \cos 2\gamma_0\right) \tag{10.62}$$

$$\mathrm{T}_3 = -\left(\frac{3}{4}\alpha a_0 + \frac{\eta}{2{a_0}^2} \cos(\gamma_0 + \Phi)\right) \tag{10.63}$$

$$\mathrm{T}_4 = \left(\frac{1}{2}\lambda \sin 2\gamma_0 - \frac{\eta}{2a_0} \sin(\gamma_0 + \Phi)\right) \tag{10.64}$$

As it is clear, the stability of the steady state motion of an expression like $\{X'\} = [A]\{X\}$ depends on the eigenvalues of the A matrix; thus, by evaluating eigenvalues (s) for the T matrix in (10.60), the nature of singular points will be revealed. Hence, one needs to solve the following determinant:

$$\begin{vmatrix} s + \zeta + \frac{1}{4}\lambda \sin 2\gamma_0 & -\frac{1}{2}\eta \cos(\gamma_0 + \Phi) + \frac{1}{2}\lambda a_0 \cos 2\gamma_0 \\ \frac{3}{4}\alpha a_0 + \frac{\eta}{2a_0{}^2} \cos(\gamma_0 + \Phi) & s - \frac{1}{2}\lambda \sin 2\gamma_0 + \frac{\eta}{2a_0} \sin(\gamma_0 + \Phi) \end{vmatrix} = 0 \tag{10.65}$$

$$s^2 - (T_1 + T_4)\, s + (T_1 T_4 - T_2 T_3) = 0 \tag{10.66}$$

$$s = \frac{(T_1 + T_4) \pm \sqrt{(T_1 + T_4)^2 - 4\,(T_1 T_4 - T_2 T_3)}}{2} \tag{10.67}$$

According to the above equation, the steady state motion is unstable if $(T_1 + T_4) > 0$ or $(T_1 T_4 - T_2 T_3) < 0$. Having been calculated from (10.67) for a specific singular point, a complex s with negative real part means a stable solution (e.g., Stable focus); otherwise the steady state solution is unstable (e.g., Saddle point).

Similar to all linear parametrically excited systems, wedge of instability appears for the unforced linear equation of motion of the system. To extract this wedge of instability near principal resonance case, one needs to investigate Eq. (10.68).

$$\ddot{z} + 2\varepsilon\zeta\dot{z} + z + \varepsilon\lambda \cos(2\Omega t)\, z = 0 \tag{10.68}$$

By repeating the procedure of solving according to the method of multiple scales, one finds two equations that are identical to Eqs. (10.54) and (10.55), but in which α and η are put equal to zero. As it is clear, in this condition trivial solution will be appeared, and stability analysis of the trivial solution will reveal the bounds of instability. In fact, in the case of Eq. (10.68) the secular terms are eliminated as long as:

$$-2i\left[A' + \zeta A\right] - \frac{1}{2}\lambda \bar{A} e^{i 2\sigma T_1} = 0 \tag{10.69}$$

Considering

$$A = \frac{1}{2}(p - iq) e^{i\sigma T_1} \tag{10.70}$$

where p and q are real. By substituting (10.70) into Eq. (10.69) and separating real and imaginary parts, one obtains:

$$p' = -\zeta p + \left(-\sigma - \frac{\lambda}{4}\right) q \tag{10.71}$$

$$q' = \left(\sigma - \frac{\lambda}{4}\right) p - \zeta q \tag{10.72}$$

Calculating eigenvalues of the coefficient matrix of these set of equations leads to:

$$s = -\zeta \mp \sqrt{\frac{\lambda^2}{16} - \sigma^2} \tag{10.73}$$

That implies the trivial solution is stable if:

$$\lambda^2 < 16(\zeta^2 + \sigma^2) \tag{10.74}$$

10.5 Results and Discussion

10.5.1 Frequency Response Curves

In the first place, the steady state solution of the linear system ($\alpha = 0$) is calculated for different parameters of the system. As it can be seen in Fig. 10.8, amplitude of the system is grown by increasing the effects of pumping signal, and it becomes boundless when the pumping signal violates linear stability threshold ($\lambda = 4\sqrt{\zeta^2 + \sigma^2}$). Figure 10.9 demonstrates the effects of damping and direct excitation on the amplitude of the amplifier. As it is expected, by increasing the direct excitation, the response of the system is magnified; and more damping reduces the amplitude of the amplifier.

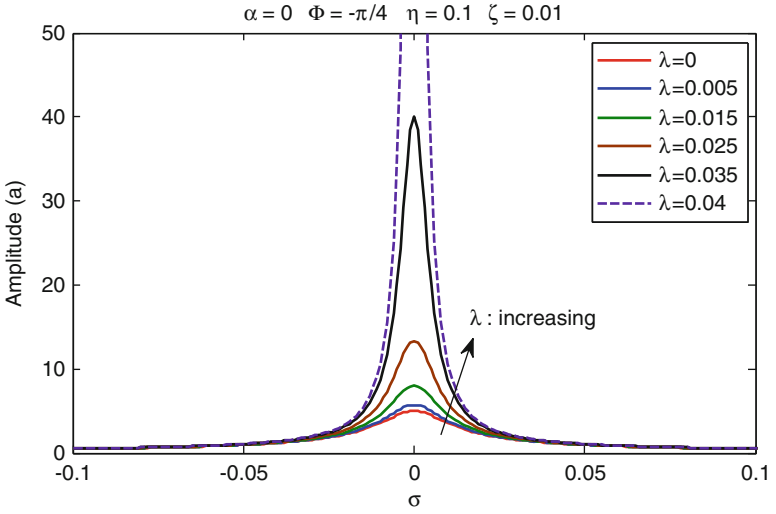

Fig. 10.8 Linear frequency response—increasing pumping signal leads to boundless amplitude

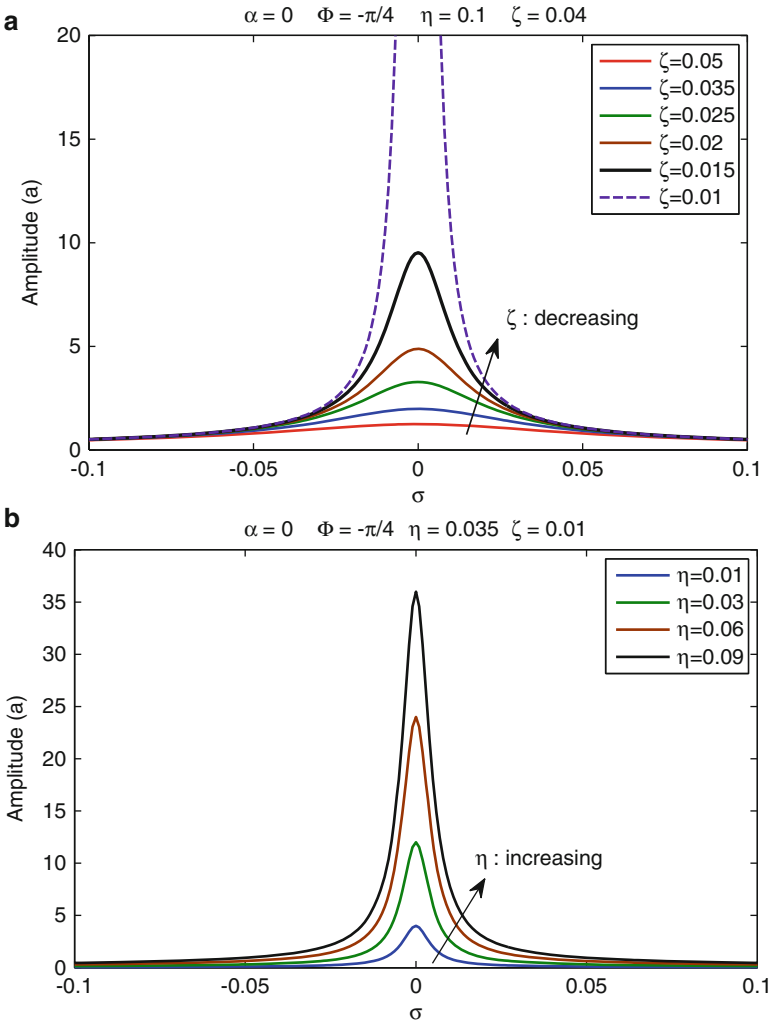

Fig. 10.9 Linear frequency response—effects of different damping (**a**) and direct excitation (**b**)

There is no denying that for nonlinear system many stable and unstable solutions can exist. Therefore, to investigate the nature of this solution, the phase portraits of the system have been numerically calculated by solving Eqs. (10.54) and (10.55) with different initial values for a & γ. Figure 10.10 shows the phase plane diagrams for 3 different pumping signals when the detuning parameter is 0.1 ($\sigma = 0.1$). As it can be observed the number of stable and unstable solutions varies for different pumping amplitudes. While for $\lambda = 0.035$ there are two stable and one unstable solution, one can see three stable and two unstable solution for the $\lambda = 0.055$ and 0.09. For example consider phase plane diagram that has been illustrated in

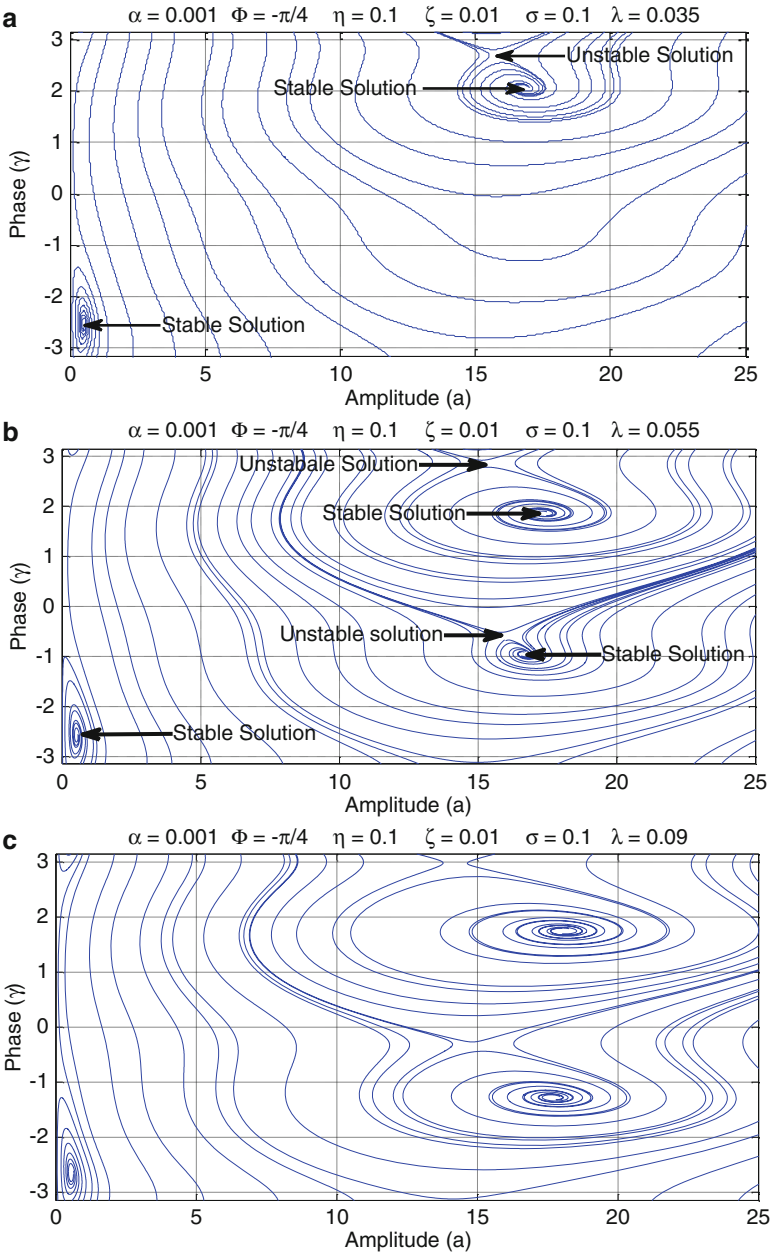

Fig. 10.10 Phase portraits of the nonlinear amplifier at $\sigma = 0.1$. (**a**) $\lambda = 0.035$, (**b**) $\lambda = 0.055$, (**c**) $\lambda = 0.09$

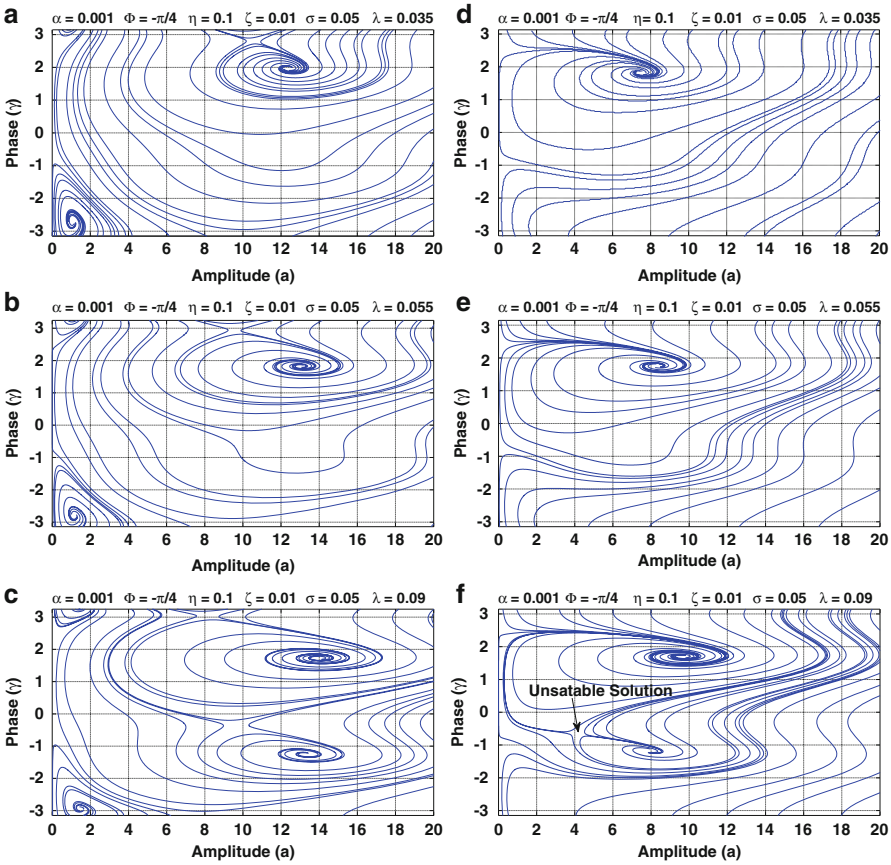

Fig. 10.11 Phase plan diagrams of the system for different parameters. (**a**) $\sigma = 0.05,\ \lambda = 0.035$, (**b**) $\sigma = 0.05,\ \lambda = 0.055$, (**c**) $\sigma = 0.05,\ \lambda = 0.09$, (**d**) $\sigma = 0.01,\ \lambda = 0.035$, (**e**) $\sigma = 0.01,\ \lambda = 0.055$ and (**f**) $\sigma = 0.01,\ \lambda = 0.09$

Fig. 10.10, by tracking the solution routes in the phase plane diagrams, one can find three stable foci which are the feasible steady state solutions, one of the stable solutions has very small amplitude while two others have large amplitude. These stable solutions are almost identical in amplitude, but they have different phase.

Figure 10.11 depicts the phase portrait with same pumping signals when detuning parameter is 0.05 and 0.01. Again, there is no equal number of stable and unstable solutions for different pumping signals as well as detuning parameters. In order to investigate this phenomenon, it is a good idea to plot frequency response curves of the system for different pumping signals to have all steady state solution in a frequency range.

When both a' & γ' are considered equal to zero in (10.54) and (10.55), the steady state solutions for the system of interest can be extracted. Figures 10.12,

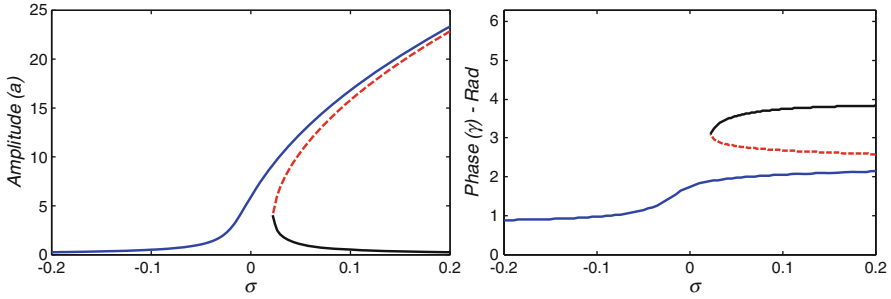

Fig. 10.12 Amplitude and phase frequency response in steady state mode when pumping amplitude is under its parametric instability threshold, ($\Phi = -\frac{\pi}{4}$, $\zeta = 0.01$, $\alpha = 0.001$, $\eta = 0.1$ & $\lambda = 0.035 < 4\zeta$). *Solid lines*: stable solution branches; *dashed line*: unstable solution branch

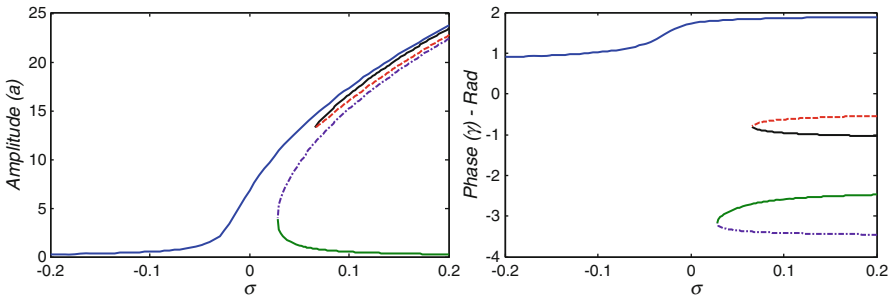

Fig. 10.13 Amplitude and phase frequency response in steady state mode when pumping amplitude is slightly above its parametric instability threshold ($\Phi = -\frac{\pi}{4}$, $\zeta = 0.01$, $\alpha = 0.001$, $\eta = 0.1$ & $\lambda = 0.055 > 4\zeta$). *Solid lines*: stable solution branches; *dashed line*: unstable solution branches

10.13, and 10.14 depict the amplitude and phase of the steady state solution for different parameters of the system. As expected, due to the cubic nonlinearity, the frequency response curves demonstrate a Duffing-like trend near their resonance frequency that is $\sigma = 0$. Note that frequency response curves have been calculated for three different conditions. In the first place, the steady state solutions are obtained when parameters are set in such a way that pumping amplitude is under principal resonance instability threshold, that is $\lambda = 4\sqrt{\zeta^2 + \sigma^2}$. Then, by keeping other parameter in their previous values, the pumping signal is magnified slightly and well above the instability threshold.

As it can be observed from Fig. 10.12 for under instability threshold condition (i.e., $\lambda < 4\zeta$ when $\sigma = 0$), the steady state solution has three branches in a frequency band that means different steady state solutions in frequency response regime. By evaluating corresponding eigenvalues for the solutions, it is revealed that the upper and lower branches are stable solutions for this region and the middle branch is unstable steady state solution that cannot be achieved in the reality. Furthermore, Figs. 10.13 and 10.14 show that when the pumping amplitude

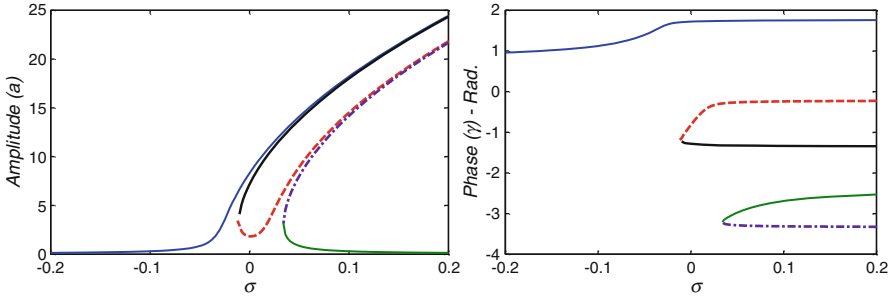

Fig. 10.14 Amplitude and phase frequency response in steady state mode when pumping amplitude is far above its parametric instability threshold $\Phi = -\frac{\pi}{4}$, $\zeta = 0.01$, $\alpha = 0.001$, $\eta = 0.1$ & $\lambda = 0.09 > 4\zeta$. *Solid lines*: stable solution branches; *dashed line*: unstable solution branches

is slightly and far above instability threshold, the frequency response solutions have five distinct branches. Therefore, they can represent five different steady state solutions; however, the stability analysis for these conditions leads to three stable solutions which are feasible and two unstable stationary points. As it is clear from Figs. 10.13 and 10.14, over a wide frequency range the amplitude of two upper stable branches is almost equal, while they have completely different phase. The other interesting phenomena about steady state solution with parameters above instability threshold is that the higher the pumping signal amplitude, the wider frequency range to have three stable solutions.

Figures 10.15 and 10.16 show the effects of nonlinear term in the amplitude of the steady state solution. As it can be seen, by increasing the order of nonlinear term, the amplitude of the amplifier is decreased, regardless of variation of pumping signal. It also leads to smaller frequency range for five steady state solutions when the pumping signal is above the linear stability threshold (Fig. 10.16).

10.5.2 System Performance Metrics

An important parameter for evaluating system performance is the gain of the parametric amplifier which is defined according to Eq. (10.75). Parametric amplifier's gain is the ratio of the steady state amplitude with pumping signal to amplitude without pumping signal. In order to study the effects of different parameters on performance of the amplifier, the gain of the system can be evaluated by changing parameters. To this end, a specific parameter of the system such as relative phase (Φ) can be considered as variable, then by keeping other parameters as constant values, the gain is extracted. This procedure can be managed for all parameters of the system, including pumping, damping, nonlinearity, and detuning.

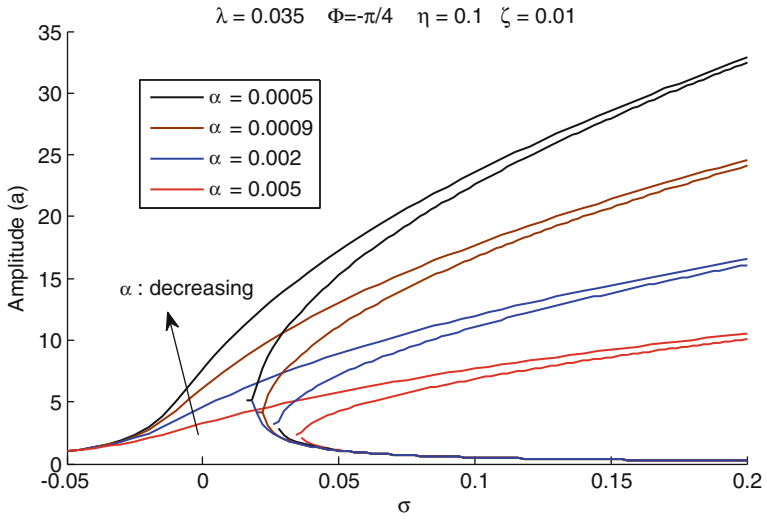

Fig. 10.15 The impact of nonlinear term on the frequency response curves when pumping signal is under linear instability threshold

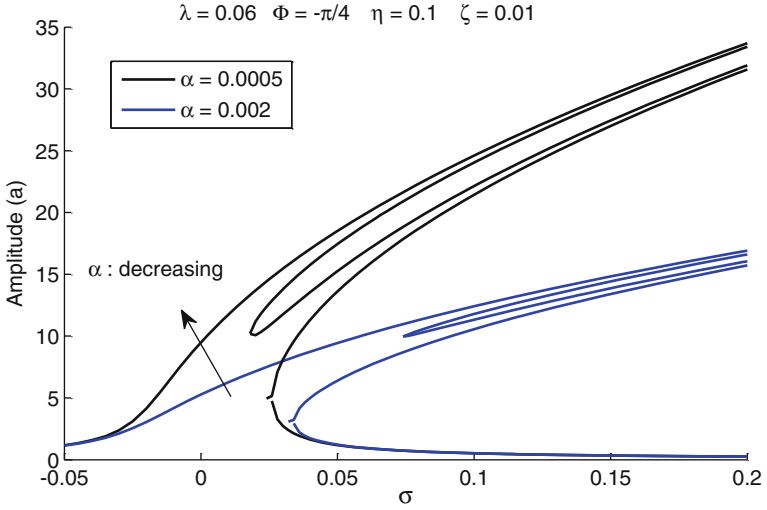

Fig. 10.16 The effects of nonlinear term in the amplitude of the steady state solution when pumping signal is above linear instability threshold

$$G = \frac{a_{pump\ on}}{a_{pump\ off}} \tag{10.75}$$

Firstly, the gain is calculated for linear system to examine the effects of parameters such as damping and relative excitation phase. Figure 10.17 illustrates

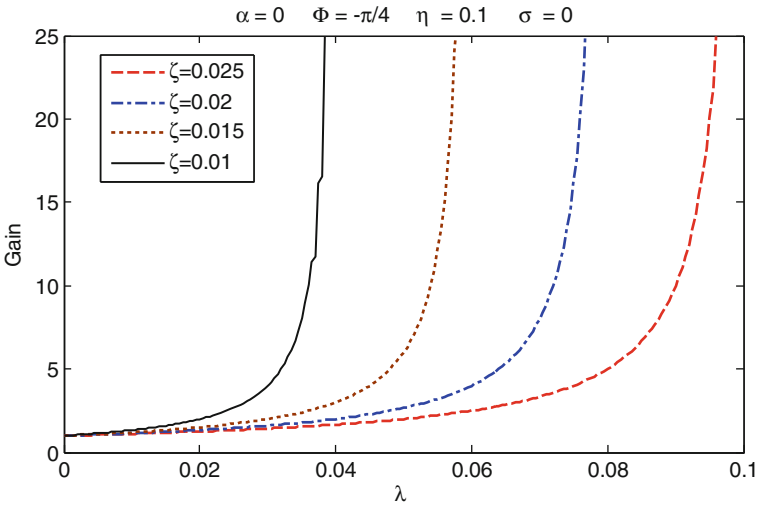

Fig. 10.17 The effects of pumping signal and damping on the gain of the linear system (instability restricts pumping signal)

the effects of pumping signal and damping on the gain of the system. It is clear from this figure that the gain becomes boundless when the pumping signal reaches to instability threshold. Moreover, as it can be observed, damping term does not have an effective impact on gain, but with higher damping, the pumping signal should and can be more increased to result in a better gain. Figure 10.18 shows the effects of relative phase excitation (Φ) on gain of the linear system for different pumping signal. According to the graphs of Fig. 10.18, the excitation phase can change the gain of the system in different orders. Although the excitation phase is not such important parameter in small pumping levels, it has a great role to play when the amplitude of pumping signal is large enough and close to instability threshold. This outcome can be discussed from another point of view, in which the pumping signal is kept constant and the damping parameter is varied. In fact, when the damping decreases, the required pumping signal for high gain value that arises near instability threshold reduces. Figure 10.19 demonstrates the results for this case.

In the second place, the effect of nonlinearity is examined on system performance; Fig. 10.20 shows the gain of the amplifier for nonlinearity with different orders. Calculated gains indicate that the more the level of nonlinearity, the less the effectiveness of the amplifier. Undoubtedly, as it can be seen from the results, even very small nonlinearity term can dramatically decrease system performance; therefore, analysis results with linear approximation may significantly be different for an even slightly nonlinear system. In addition, the finding reveals that nonlinear amplifiers can work well over instability threshold constraint which was previously predicted for linear systems. Furthermore, there is no denying that as long as pumping amplitude is strong enough, large gains still can be acquired.

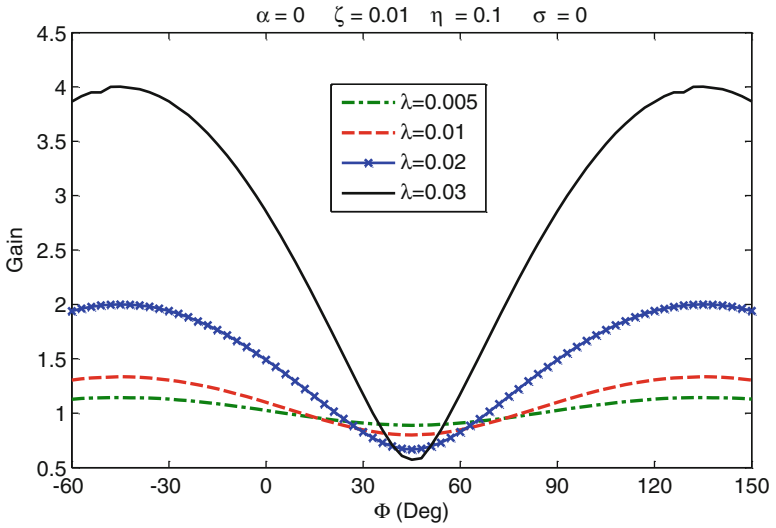

Fig. 10.18 The effects of pumping signal and relative phase excitation on the gain of the linear system (relative phase is important when the pumping signal amplitude is large enough)

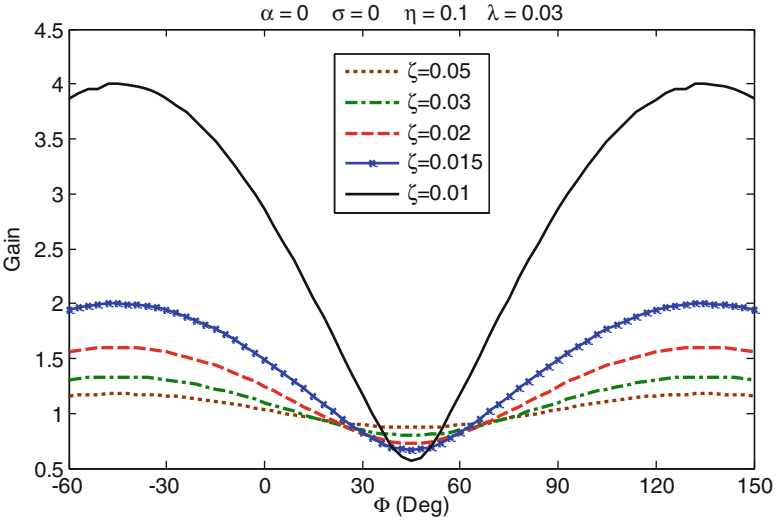

Fig. 10.19 The effects of damping and relative phase excitation on the gain of the linear system (relative phase is important when the pumping signal amplitude is close to instability threshold)

The impact of relative phase is also examined for different nonlinearity orders. According to Fig. 10.21, the more the order of nonlinearity, the more distortion occurs in the gain of the amplifier. In fact, the nonlinearity term change the phase in which maximum gain occurs that is due to the imposed asymmetry on the gain versus relative phase axis diagram. In addition, investigation of different

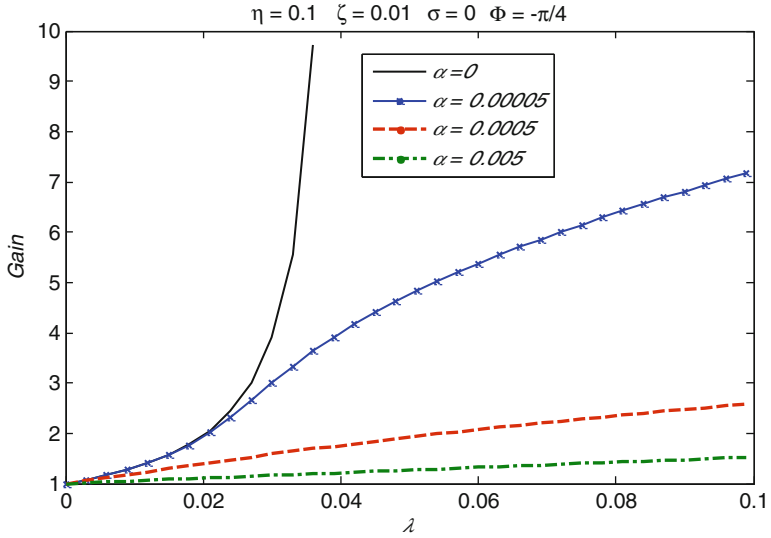

Fig. 10.20 The effects of nonlinearity and pumping signal on the gain of the amplifier (meaningful nonlinear amplifiers gain over linear instability threshold that is $\boldsymbol{\lambda} > 4\zeta$)

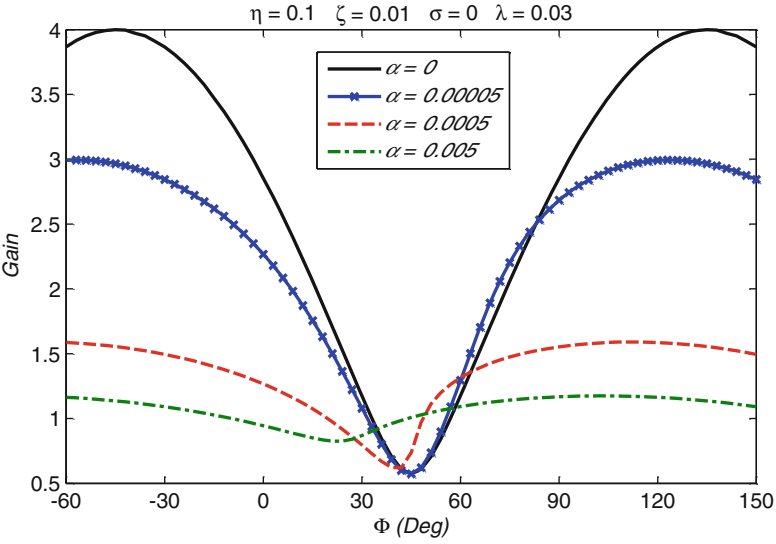

Fig. 10.21 Gain vs. relative phase for different nonlinearity orders (as the order of nonlinearity increases, much distortion arises)

detuning parameter for system performance has revealed small changes in system performance. According to Fig. 10.22, in low pumping signal amplitude region (e.g., $\lambda < 0.04$), small positive detuning from resonance frequency leads to higher

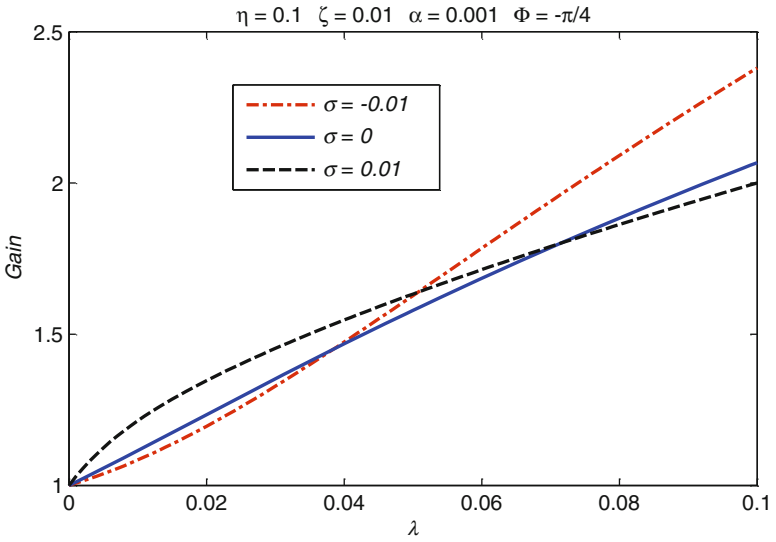

Fig. 10.22 Gain vs. pumping signal (small improvement on system performance by tuning σ)

system gain. In contrast, in high pumping signal amplitudes (e.g., $\lambda = 0.08$), the outcome from slight negative detuning provides better performance than working at resonance frequency ($\sigma = 0$).

10.6 Conclusion

Governing equations of motion for mechanical and electromechanical parametric amplifiers in the literature were reviewed. According to them, a general equation of motion for a nonlinear classical degenerate parametric amplifier was considered. The study of the parametric amplifier with a cubic nonlinearity was accomplished by means of the method of multiple scales. The stability analysis for the steady state motion of the nonlinear degenerate parametric amplifier as well as trivial solution of the unforced linear system was conducted. All the steady state solutions demonstrated a Duffing-like behavior in their frequency response curves. In addition, the stable solution branches were switched to three when pumping amplitude was increased over the instability threshold constraint for the unforced linear system. Furthermore, the effects of nonlinearity, relative phase, pumping signal amplitude, and detuning parameters were investigated on system performance. The findings indicate that even very small nonlinearity term can dramatically decrease system performance as well as changing the relative phase in which maximum gain occurs. The paper attempted to show that nonlinear amplifiers are stable and can be realized

when there is no alternative to avoid working in nonlinear range; nevertheless, nonlinearities limit the maximum gains of parametric amplifiers compared with classical linear amplifiers.

Key Symbols

m	Mass
k	Stiffness
c	Damping
Q	Quality factor
t, τ	Time
x, z, y	Lateral displacement of the resonator
V	Excitation voltage
F_e	Electrostatic force
r	Dimensionless excitation frequency
ω_i	i-th resonance frequency
λ	Pumping signal amplitude
η	Direct excitation amplitude
Φ	Relative phase of direct excitation
ζ	Linear dissipation
α	Coefficient of cubic nonlinearity for stiffness
Ω	Frequency of the direct excitation
σ	Detuning parameter
a	Amplitude of amplifier response
γ	Phase of amplifier response
ε	Small positive value

References

1. Verhulst F (2009) Perturbation analysis of parametric resonance. Encyclopedia of complexity and systems science. Springer, New York, pp 6625–6639
2. Faraday M (1831) On a peculiar class of acoustical figures; and on certain forms assumed by groups of particles upon vibrating elastic surfaces. Philos Trans R Soc Lond 121:299–340
3. Mathieu E (1868) Mémoire sur le mouvement vibratoire d'une membrane de forme elliptique. J Math 13:137–203
4. Nayfeh AH, Mook DT (1955) Nonlinear oscillations. Wiley, New York
5. Hyun S, Yoo H (1999) Dynamic modelling and stability analysis of axially oscillating cantilever beams. J Sound Vib 228(3):543–558
6. Oueini S, Nayfeh H (1999) Single-mode control of a cantilever beam under principal parametric excitation. J Sound Vib 224(1):33–47
7. Eissa M, Amer Y (2004) Vibration control of a cantilever beam subject to both external and parametric excitation. Appl Math Comput 152(3):611–619

8. Ono T, Wakamatsu H, Esashi M (2005) Parametrically amplified thermal resonant sensor with pseudo-cooling effect. J Micromech Microeng 15(12):2282
9. Jazar RN (2011) Nonlinear mathematical modeling of microbeam MEMS. Nonlinear approaches in engineering applications. Springer, New York, pp 69–104
10. Requa MV (2006) Parametric resonance in microcantilevers for applications in mass sensing. Ph.D. Thesis, University of California, Santa Barbara
11. Rugar D, Grütter P (1991) Mechanical parametric amplification and thermomechanical noise squeezing. Phys Rev Lett 67(6):699–702
12. Mahboob I, Yamaguchi H (2008) Piezoelectrically pumped parametric amplification and Q enhancement in an electromechanical oscillator. Appl Phys Lett 92(17):173109–173109-3
13. Olkhovets A et al (2001) Non-degenerate nanomechanical parametric amplifier. In: The 14th IEEE international conference on micro electro mechanical systems, (MEMS 2001), IEEE, pp 298–300
14. Napoli M et al (2003) Understanding mechanical domain parametric resonance in microcantilevers. In: The sixteenth annual international conference on micro electro mechanical systems, (MEMS-03), Kyoto, IEEE, pp 169–172
15. Hu Z et al (2010) An experimental study of high gain parametric amplification in MEMS. Sens Actuators A Phys 162(2):145–154
16. Baskaran R, Turner KL (2003) Mechanical domain coupled mode parametric resonance and amplification in a torsional mode micro electro mechanical oscillator. J Micromech Microeng 13(5):701
17. Jazar R et al (2009) Effects of nonlinearities on the steady state dynamic behavior of electric actuated microcantilever-based resonators. J Vib Control 15(9):1283–1306
18. Zhang W, Baskaran R, Turner KL (2002) Effect of cubic nonlinearity on auto-parametrically amplified resonant MEMS mass sensor. Sens Actuators A Phys 102(1):139–150
19. Dana A, Ho F, Yamamoto Y (1998) Mechanical parametric amplification in piezoresistive gallium arsenide microcantilevers. Appl Phys Lett 72(10):1152–1154
20. Carr DW et al (2000) Parametric amplification in a torsional microresonator. Appl Phys Lett 77(10):1545–1547
21. Ouisse T et al (2005) Theory of electric force microscopy in the parametric amplification regime. Phys Rev B 71(20):205404
22. Miller NJ, Shaw SW, Feeny BF (2008) Mechanical domain parametric amplification. J Vib Acoust 130:061006–1
23. Rhoads JF, Shaw SW (2010) The impact of nonlinearity on degenerate parametric amplifiers. Appl Phys Lett 96(23):234101–234101-3
24. Nayfeh AH (2000) Perturbation methods. Wiley, New York
25. Ng L, Rand R (2002) Bifurcations in a Mathieu equation with cubic nonlinearities. Chaos Solitons Fractals 14(2):173–181

Index

A
Accelerated least kth order statistics (A-LKS), 262, 266–268, 270
Accelerated sampling method
  algorithm, 264–265
  bad sample, 263
  probability, 264
  pseudo outliers, 263
  RANSAC-type estimator, 265, 266
Aeromechanical–electrical interaction, 170
Alben, S., 174
Allen, J.J., 178
Amer, Y., 274
ANSYS®, 190, 191
Apkarian, P., 137
Argentina, M., 172, 192, 193
Azimuth-elevation dual axis trackers, 39, 47–48

B
Bab-Hadiashar, A., 267
Beam-like structures
  body-in-white, 230
  cross section properties, 230–231
  detailed model and concept model, 230
  standard cross sections deficiency, 232–233
Best, A., 31
Bilinear damper, 19, 22
Body-in-white (BIW) concept model, 235–236
Bryant, M., 188, 196, 197
Buckled motion
  sectioning points, 73, 76–77
  wave forms and phase diagrams, 73–75
Busch, G., 181
Buzz, squeak, and rattle (BSR) noise. *See* Vehicle seat BSR noise

C
Car bicycle model
  angular oscillations, 7–9, 11
  with damping, 5
  decoupling condition, 4–5
  degree-of-freedom systems, 2
  front oscillations, 7–10
  mode shapes, 4
  parameters, 3
  rear oscillations, 7, 9–10
  specification, 6
Cebon, D., 32
Chaotic motion
  sectioning points, 77, 80
  wave form and phase diagram, 77–79, 81–83
Chen, W., 137
Chen, Y., 37
Chong, K., 37
Clamping base geometry
  FSI solutions, 180
  role, 179
  vortex shedding circular cylinder and flexible beam, 180
Collector-centered frame C, light-tracker
  azimuth-elevation dual axis tracker, 47–48
  orientation of panel-fixed C-frame, 46, 47
  tip-roll dual axis tracker, 46–47
Computer-aided engineering (CAE) methodology, vehicle seat
  beam-like structures
    BIW, 230
  cross section properties, 230–232
  detailed model and concept model, 230
  standard cross sections deficiency, 232–233
  BIW concept model, 235–236
  joints modeling

R.N. Jazar and L. Dai (eds.), *Nonlinear Approaches in Engineering Applications 2*,
DOI 10.1007/978-1-4614-6877-6, © Springer Science+Business Media New York 2014

Computer-aided engineering (CAE) methodology, vehicle seat *(cont.)*
conversion, 234
DOF, 233
Guyan method, 234
reduction method, 233
panels modeling, 235
seat concept modeling
vs. advanced model, 238
FE methods and CAE techniques, 236
physical and finite element mode, 238
standard and nonstandard sample, 237
steel properties, 238
structure, 237
Connell, B.S.H., 173, 175, 176
Contact constraint
contact force *vs.* normal gap, 213–214
Lagrange multiplier methods, 212
penalty methods, 212
tangential contact and Coulomb friction conditions, 214–215
Contact kinematics, 212–213
Contact modelling, 218
Cool Robot, 36
Crolla, D., 31
Curie, P.J., 181

D
Dai, L., 64, 68
Deivasigamani, A., 180, 188, 189, 192
Dickson, R., 168, 169, 187
Dowell, E.H., 64, 65
Duan, G., 137
Dynamic damper, 250

E
Earth-centered frame E, light-tracker, 45
Earth-surface frame S, light-tracker, 45–46
Eissa, M., 274
Electrically actuated microcantilever, 277
Electromechanical microbeam oscillator, 280
Electromechanical parametric amplifiers
base excited cantilever beam, 281
block diagram, 278
damper system, 279
electrically actuated microcantilever, 277
forces, 277
Mathieu equation, 280
microbeam, 276
oscillator, 280
parametric modulation, 278
SEM, 279
Ellipse fitting model, 255–256
Energy harvesting system
fluid-structure interaction, 165–169
piezoelectric energy harvesters
fluid-structure coupling, 170–180
physics interactions, 170
single piezoelectric leaf-stalk, 187–202
structural–electrical coupling, 181–187
Euler–Bernoulli beam theory, 183–184
Explicit time integration schemes, attenuator, 215–216
Extraneously-induced excitation (EIE)
clamping base geometry
FSI solutions, 180
role, 179
vortex shedding circular cylinder and flexible beam, 180
definition, 176
experimental setup, 178
flapper-harvester array, 178–179
particle image velocimetry, 178
Rankine vortex model, 179
vortex shedding
bluff body, 176
Reynolds number, 177
Strouhal number, 176

F
Faraday, M., 274
Fei, J., 137
Finite element method (FEM)
fixture dynamics, 240
impact attenuator, 210
joints modeling, 233
seat rails and structure, RBE element, 237–238
vibration in plate, 149–150
Flat motion, 84–87
Flat ride tuning. *See* Smart flat ride tuning
Fluid-structure coupling
extraneously-induced excitation, 176–180
movement-induced excitation flutter, 170–176
Fluid-structure interaction (FSI)
Bernárd–von-Kármán vortex shedding, 166
definition, 166
filament flapping, 167
flag flapping, 166
flutter, 167 (*see also* Flutter)
Kelvin–Helmholtz instability, 166–167
piezoelectric tree, 168, 169
potential flow components, 168
ULP technologies, 169

Flutter
analytical potential flow methods, 168
characteristics, 168
extraneously-induced excitation, 176–180
MIE (*see* Movement-induced excitation (MIE) flutter)
movement-induced excitation, 170–176
plates (*see* Plates, flutter behavior of)
Formula SAE impact attenuator
ABAQUS explicit code, 221
aluminium material, 223
boundary conditions and loadings, 217–218
contact constraints, 212–214
contact kinematics, 212–213
contact modelling, 218
deformation and energy absorption, 221, 222
equilibrium equation for bodies, 210–211
experiment sled test, 219, 220
explicit time integration, 215–216
finite element method, 210
geometry models, 216–217
governing equation of equilibrium, 215
material models, 217
mesh convergence study, 218
normal contact constraints, 213–214
RMIT Racing team, 210
tangential contact constraints, 214–215
time history plot, 219–220
FSI. *See* Fluid-structure interaction (FSI)
Fundamental matrix model, 256–257
Fuzzy sliding mode control (FSMC) strategy, 88
control input, 90, 93–95
rule, 89
selected point, 90, 95
wave form and phase diagram, 90–93

G
Garrick, E.I., 64, 67
Generalized sliding surface control (G_{SS}) designs
closed-from, 119–120
control law, 116–119
nominal system's trajectory, 114
sliding surface definition, 115
tracking error signal, 115
triple pendulum, 121–131
Geometry models, impact attenuator, 216–217
Grimes, R.G., 190
Gross outliers, 255
Grutter, P., 275, 278
Guest, J.J., 2, 30, 32
Guyan, R., 234
Guyan method, 234

H
Haniu, H., 177, 178
Hankel, W., 181
Hariri, M., 172
High breakdown robust estimator, 257
Hinged beam model
analytical model
Euler–Bernoulli beam theory, 188
nondimensional hinge position, 190
steady-state LCO, 189
computational model
ANSYS® and Mechanical™, 191
Block Lanczos algorithm, 190
hinge positions, 191
R_i comparison, 191
uniform-beam vibration, 190
experimental testing
and computational mode shape comparison, 194
hinge placing, 195
hinge sewing method, side-and top-view, 192
parallel flow scales, 192
polypropylene beam, 193
R_2 and v plot, 193
Homogeneous transformation matrix
4-by-4 matrix, 42
compound, 44
coordinate transformation, 42
decomposition of, 43–44
inverse, 44
Homography model, 256
Horizontal axis tracker, 38
Huang, L., 168, 171–173
Hydragas systems, 32
Hydrolastic systems, 32

I
Illuminance, light-tracking kinematics, 40–41
Impact attenuator. *See* Formula SAE impact attenuator

J
Jazar, R.N., 43, 275, 276
Jiang, J., 137
Joints modeling
conversion, 234
DOF, 233

Joints modeling *(cont.)*
Guyan method, 234
reduction method, 233
Jun, Z., 167, 172, 175

K
King, R., 31
Kornecki, A., 171
Kuo, C.L., 88

L
Langevin, P., 181
Lead-zirconate-titanate (PZT)
macrofibre composites, 182
strips and plates, 181
structure, 182
Leaf area parametric analysis
dimensions and areas, 198
energy capture circuit, 197
LCO flutter, 199
leaf area variation, 200
output power deviation comparison, 199
wind tunnel experimental setup, 198
Leaf aspect ratio parametric analysis
aspect ratio variation results, 201
power output comparison, 201
Legnani, G., 43
Li, S., 187, 188, 195, 196
Light-tracking kinematics
compound homogeneous transformation
coordinate frames, 42
matrix, 42–44
motion of target and tracker, 41
coordinate frames and transformation
collector-centered frame C, 46–48
Earth-centered frame E, 45
Earth-surface frame S, 45–46
moving platform body frame B, 48–50
illuminance computation, 40–41
light vectors in spherical coordinate system, 41
mobile robot carrying photovoltaic panels
dual-axis tracking system, 51
illuminance received by collector panel, 52–54
multiple light emitter case, 56–59
reference frames, 51–52
single light emitter case, 56–58
trajectory constraint, 50–51
radiant energy sources, 40
Sun-tracker, 37
types of tracker
dual axes trackers, 39
rotational degree-of-freedom, 37
single axis trackers, 38
Light vectors, spherical coordinate system, 41
Limit-cycle flapping (LCO), 173, 187, 189, 199
Linear suspension
near flat ride solution
constant stiffness ratio, 16–17
design chart, 17, 21
front and rear suspensions, 12–13
smart suspension, 17–18
spring ratio, 15
no flat ride solution, 11–12
Lipson, H., 187, 188, 192, 195, 196
Liu, G.P., 137
Lumped mass system, OEC
actuation forces, 146–148, 150
control gain matrix, 148
displacement of masses, 146, 148–149
operating eigenvalues, 143–144
settling time and overshoot, 145
springs and dampers, 142–143
Lyapunov exponent spectrum
asymptotic state, 70
definition, 71
maximum Lyapunov exponent, 71
orthonormal vectors, 72
stochastic Mathieu oscillator, 71

M
Macrofibre composites (MFC), 182
Macroscale mechanical parametric amplifiers, 281
Mahadevan, L., 172, 192, 193
Mahboob, I., 280
Material models, impact attenuator, 217
Mathieu, E., 274
Mathieu equation
mechanical and electromechanical parametric amplifiers, 280
parametric excitation, linear systems, 285
with viscous damping, 286–287
McCarthy, J., 192, 195, 197
Mechanical parametric amplifiers. *See* Electromechanical parametric amplifiers
Mindlin plate theory, 149
Mobile robot carrying photovoltaic panels
dual-axis tracking system, 51
illuminance received by collector panel, 52–54

multiple light emitter case
brightness comparison, 59
orientation of mobile tracker, 56, 58
pitch angle *vs.* time, 55, 57
position of mobile tracker, 56, 58
positions of lights, 56–57
yaw angle *vs.* time, 58–59
reference frames, 51–52
single light emitter case
brightness comparison, 55, 58
orientation of mobile tracker, 55–56
pitch angle *vs.* time, 55, 57
position of mobile tracker, 55–56
yaw angle *vs.* time, 55, 57
trajectory constraint, 50–51
Modal assurance criteria (MAC), 240–241
Model candidate, 255–257, 261
Movement-induced excitation (MIE) flutter
critical flutter speed
fluid-to-structure mass ratio, 172
types, 171
in vacuo mode shapes, 172
definition, 171
mass ratio
calculation, 172
definition, 172
experimental results, 173
LCO, 173
normalised power spectrum *vs.* frequency, 174–175
tail displacement *vs.* time, 173, 175
time-varying beam deformation, pressure and vorticity, 174
subcritical bifurcation and hysteresis, 175–176
Moving platform body frame B, light-tracker, 48–50
Murray, D.W., 262, 263

N
Naudascher, E., 171, 176
Nayfeh, A.H., 71, 274, 282
Nister, D., 262, 263
Nominal multibody systems
actual unconstrained system, 107–110
controlled actual system, 109–112
generalized sliding surface controller designs
closed-from, 119–120
control law, 116–119
nominal system's trajectory, 114
sliding surface definition, 115
tracking error signal, 115
planar pendulum
angular responses, 106
control force, 106, 108
control requirement, 104
energies in Newtons, 105–107
generalized sliding surface control, 121–131
masses suspended from rods, 102–103
total energy, 103
trajectory of mass, 105
system description, 100–102
uncertainties in mechanical system dynamics, 112–114
Noncirculatory aerodynamic theory, 171
Nonlinear dampers
force-velocity characteristics
bilinear damper, 19, 22
opposite cycle model, 22, 25
real damper, 18, 21
front and rear suspensions, 22–23, 25
ideal model, 20, 22
linear *vs.* opposite cycle, 22, 26
near flat ride solution
ideal nonlinear damping, 24, 28–29
spring ratio *vs.* τ, 23–24, 27
stiffness ratio, 24, 27
Nonlinear oscillations, fluttering plate. *See* Plates, flutter behavior of
Nonlinear structures
geometric distance
2D representation, 259
homography estimation, 260
Sampson distance, 261
Taylor's series, 260
optimization
accelerated search, 263–266
exhaustive search, 261
probability, 262
p-tuples, 261–262
random sampling, 263
RANSAC, 262
parametric segmentation
cost function, 258
least kth order statistics function, 258
robust estimation, 257
problem statement
ellipse fitting, 255–256
exact value perturbed by noise, 254
fundamental matrix, 256–257
homography estimation, 256
inliers and outliers, 255
pseudo and gross outliers, 255
robust estimation, 254

Nonlinear structures *(cont.)*
simulation
A-LKS, 268
computation times, 267–268
ellipse fitting, 268, 270
homography estimation, 268–269
inlier–outlier dichotomy, 267
structure, 254

O
Odhams, A., 32
Olley, M., 1, 11, 25–30
Orthogonal eigenstructure control (OEC)
applicability, 161
closed-loop linear system, 138
control gain matrix, 139, 141
eigenvalues and eigenvectors, 140
schematic represenattion, 141–142
singular value decomposition, 139
system of lumped masses
actuation forces, 146–148, 150
control gain matrix, 148
displacement of masses, 146, 148–149
operating eigenvalues, 143–144
settling time and overshoot, 145
springs and dampers, 142–143
vibration isolation in plate
actuators on nodes 19 and 26, 158–161
actuators on nodes 19 and 33, 156–158
damping matrix, 150
failed middle actuator, 152–154
failed outer actuator, 154–156
Mindlin plate theory, 149
nodes of finite element model, 149–150
three working actuators, 150–151
Oueini, R., 274

P
Païdoussis, M., 168
Panels model, 235
Parametric resonance
atomic force microscopy, 275
degenerate and nondegenerate amplifiers, 274
direct excitation with cubic nonlinearity, 283–285
frequency response curves
amplitude and phase frequency response, 296–297
damping and direct excitation, 292–293
linear stability threshold, 297, 298
phase portraits, 293–295
pumping signal, 292
Mathieu equation with viscous damping, 286–288
mechanical and electromechanical parametric amplifiers
base excited cantilever beam, 281
block diagram, 278
damper system, 279
electrically actuated microcantilever, 277
forces, 277
Mathieu equation, 280
microbeam, 276
oscillator, 280
parametric modulation, 278
SEM, 279
method of multiple scales, 282–283
microbeams, 275
parametric excitation of linear systems, 285–286
pendulum, 274
perturbation method, 282
system model
cubic nonlinearity, 288
linear degenerate amplifier, 287
perturbation solution, 288–290
stability analysis, 290–292
system performance metrics
gain *vs.* pumping signal, 301–302
gain *vs.* relative phase, 300–301
nonlinearity, 299, 301
parametric amplifier gain, 297–298
pumping signal and damping, 299
relative phase excitation, 299–300
Parametric segmentation, nonlinear structures
cost function, 258
least kth order statistics function, 258
robust estimation, 257
Periodicity ratio (PR) method
chaotic motion, 70
definition, 68
periodic points, 69
Poincare map, 68
quasiperiodic response, 68
Periodic motion
sectioning points, 77, 84
wave form and phase diagram, 77, 80
Piezoelectric energy harvesters
fluid-structure coupling
extraneously-induced excitation, 176–180
movement-induced excitation flutter, 170–176
physics interactions, 170

properties, 169
single piezoelectric leaf-stalk, 187–202
Piezoelectric tree, 168, 169
Pilbeam, C., 31
Plates, flutter behavior of
2D plate motion
assumptions, 66
nondimensionalization, 66
ordinary differential equations, 67
supersonic flow, 65
FSMC strategy, 88
control input, 90, 93–95
rule, 89
selected point, 90, 95
wave form and phase diagram, 90–93
Lyapunov exponent spectrum
asymptotic state, 70
definition, 71
maximum Lyapunov exponent, 71
orthonormal vectors, 72
stochastic Mathieu oscillator, 71
PR method
chaotic motion, 70
definition, 68
periodic points, 69
Poincare map, 68
quasiperiodic response, 68
system motions detection
buckled motion, 73–75, 77
chaotic motion, 77–80
flat motion, 84–87
Jacobi matrix, 72–73
Lyapunov exponents, 73
periodic motion, 77, 80, 84
PR method, 73
Pobering, S., 179
Polyvinylidene fluoride (PVDF), 182
Primary resonance, 284
Pseudooutliers, 255

Q
Quasisteady lifting line theory, 171

R
Randall, J., 36
Random Sample Consensus (RANSAC), 262–263
Rankine vortex model, 179
Rattle noise mechanism
BSR causes
assembly issues, 243
local part design, nonrobustness of, 244
manufacturing issue, 243
material compatibility issues, 244
noise measurement, 244–245
noise source identification
c-point, 246–247
sound pressure levels, 245
test setup, 245
torsion resonant frequency, 245–246
rattle factor, 242–243
Reed, W.H., 64
Reynolds number, 177, 178
Rhoads, J.F., 275, 281
RMIT Racing team, 210
Rockwell, D., 171, 176
Rong, H., 71
Rowell, H.S., 2, 30, 32
Royce, H., 25, 26
Rugar, D., 275, 278

S
Sakamoto, H., 177, 178
Sansoni, P., 36
Scherrer, P., 181
Schwesinger, N., 179
Seat concept modeling
beam-like structures, 230–233
BIW concept modeling, 235–236
characteristics and compares, 238
FE methods and CAE techniques, 236
joints modeling, 233–235
panels modeling, 235
physical and finite element mode, 238
real and modeled joint, 237
standard and nonstandard sample, 237
steel properties, 238
Seat dynamics
BIW concept and advanced models, 241–242
experimental modal testing
fixture dynamics, 239–240
impact hammer test, 239
test setup, 239
inertance FRF, 242
modal assurance criteria, 240
NVH concept model, 240, 241
resonant frequencies and mode shapes, 241
torsion and bending modes, 240–241
Seat structure optimization
dynamic damper, 250
engine and road input, 247
sensitivity analysis, 248–250
stiffness variation, 248
Seo, C.J., 137

Sharp, R., 31
Shelley, M.J., 174
Shubov, M.A., 64
Singh, M.C., 64
Single piezoelectric leaf-stalk
  geometric parameters
    leaf area parametric analysis, 196–200
    leaf aspect ratio parametric analysis, 200–202
    triangular leaf, 196–198
  PVDF element, 187
  revolute hinge effect
    analytical beam model, 188–190
    computational beam model, 190–192
    experimental beam testing, 192–195
Sipcic, S.R., 64
Smart flat ride tuning
  car bicycle model
    angular oscillations, 7–9, 11
    with damping, 5
    decoupling condition, 4–5
    degree-of-freedom systems, 2
    front oscillations, 7–10
    mode shapes, 4
    parameters, 3
    rear oscillations, 7, 9–10
    specification, 6
  definition, 1–2
  near flat ride solution for ideal, nonlinear damper
    ideal nonlinear damping, 24, 28–29
    spring ratio *vs.* τ, 23–24, 27
    stiffness ratio, 24, 27
  near flat ride solution for linear suspension
    constant stiffness ratio, 16–17
    design chart, 17, 21
    front and rear suspensions, 12–13
    smart suspension, 17–18
    spring ratio, 15
  no flat ride solution for linear suspension, 11–12
  nonlinear damper
    bilinear damper, 19, 22
    front and rear suspensions, 22–23, 25
    ideal model, 20, 22
    linear *vs.* opposite cycle, 22, 26
    opposite cycle model, force-velocity characteristics, 22, 25
    real damper, force-velocity characteristics, 18, 21
  Olley investigations
    bicycle car model for vibrations, 28, 30
    bouncing table rig, 27
    Cadillac k_2 rig, 30–31
    history, 25
    Hydrolastic systems, 32
    pitch suppression, 31
    Rolls-Royce type, 26
    rules of practice, 29–30
    suspension stiffness and damping rates, 27
    vehicle vibration response spectra, 31
Smits, A.J., 178
Sound pressure levels (SPL), 245–247
Static condensation, vehicle seat, 234
Strouhal number, 176, 177
Structural-electrical coupling
  discovery, 181
  electrical load matching
    circuit layout and equation, 186–187
    formula, 186
    load resistance, 187
  energy harvesting from vibrations
    Euler–Bernoulli beam theory, 183–184
    power availablity, 184–186
  lead–zirconate–titanate, 181–182
  macrofibre composites, 182
  piezoelectric effect, 183
  polyvinylidene fluoride, 182
Subharmonic resonance, 284
Super-harmonic resonance, 284
Suter, D., 267

T

Tacoma Bridge disaster, 168
Tang, X., 137
Tao, G., 136
Taylor, G.W., 178
Theodorsen, T., 168
Tilt axis tracker, 38
Tilt-roll dual axis trackers, 39
Tordoff, B., 262, 263
Triple pendulum
  angular responses, 106
  control force, 106, 108
  control requirement, 104
  energies in Newtons, 105–107
  generalized sliding surface control
    angular response, 122, 125
    closed-form equation of motion, 121
    constrained trajectories, 122, 124
    control forces of actual pendulum, 126, 128–129
    displacement and velocity errors, 122, 126–127, 130–131
    location of actual masses, 121–122
    probability density function, 121, 123

total control force, 123
uncertainties in actual system, 121
masses suspended from rods, 102–103
total energy, 103
trajectory of mass, 105

U
Uncertain nonlinear multibody mechanical systems. *See* Nominal multibody systems

V
Vehicle seat BSR noise
CAE methodology
beam-like structures, 230–233
BIW concept model, 235–236
joints modeling, 233–234
panels modeling, 235
seat concept modeling, 236–238
rattle noise mechanism
BSR causes, 243–244
noise measurement, 244–245
noise source identification, 245–247
rattle factor, 242–243
seat dynamics
BIW concept and advanced models, 241–242
fixture dynamics, 239–240
impact hammer test, 239
inertance FRF, 242
modal assurance criteria, 240
NVH concept model, 240, 241
resonant frequencies and mode shapes, 241
test setup, 239
torsion and bending modes, 240–241
seat structure optimization
dynamic damper, 250
engine and road input, 247
sensitivity analysis, 248–250
stiffness variation, 248
Vertical axis tracker, 38
Vibration in plate, OEC
actuators on nodes 19 and 26
actuation forces, 159–160
control gain matrix, 158
displacements of nodes, 159
eigenvalues of open-and closed-loop systems, 159–160
actuators on nodes 19 and 33
actuation forces, 157–158
control gain matrix, 156
displacements of nodes, 157
eigenvalues of open-and closed-loop systems, 157–158
damping matrix, 150
failed middle actuator
actuation forces, 153
displacements of nodes, 152–153
eigenvalues of open-and closed-loop systems, 154
failed outer actuator
actuation forces, 154–155
displacement of plate's middle node, 154, 156
eigenvalues of open-and closed-loop systems, 155–156
node displacements, 154–155
Mindlin plate theory, 149
moved closed-loop poles, 160–161
nodes of finite element model, 149–150
three working actuators
actuation forces, 150–151
displacements of nodes, 150
eigenvalues of open-and closed-loop systems, 151
Vortex shedding
bluff body, 176
experimental setup, 178
Reynolds number, 177
Strouhal number, 176

W
Wang, G., 137
Wang, R., 137
Watanabe, Y., 173, 175, 176, 194
Wolf, A., 71
Wong, C., 37

Y
Yamaguchi, N., 172, 173
Yang, Y., 137
Yue, D.K.P., 173, 175, 176

Z
Zhang, W., 279
Zhao, Q., 137